Deep multi-frequency radio observations of the SHADES fields and the nature of the faint radio populaton

EDUARDO IBAR

Institute for Astronomy
School of Physics and Astronomy

University of Edinburgh
Doctor of Philosophy

December 2008

This thesis is solely my own composition,
except where specifically indicated in the text.

Eduardo Ibar,
August 2008.

Abstract

The two SCUBA HAlf-Degree Extragalactic Survey (SHADES) fields are amongst the richest places in the sky in terms of multi-wavelength coverage. They comprise an eastern section of the Lockman Hole (LH) and the central portion of the Subaru-*XMM/Newton* Deep Field (SXDF).

In this thesis, I have obtained extremely deep, multi-frequency radio imaging of the SHADES fields using the Giant Metre-wave Radio Telescope (GMRT) and the Very Large Array (VLA), at 610 MHz and 1.4 GHz, respectively.

These data are used to analyse the nature of the sub-milliJansky (sub-mJy) radio population, which has been hotly debated in the last few years: are they powered by star-forming or nuclear activity? To tackle the problem, I employ different approaches making use of the large variety of multi-wavelength data in the SHADES fields.

I begin by analysing the spectral index, $\alpha_{1.4\mathrm{GHz}}^{610\mathrm{MHz}}$, of radio sources detected in the LH, to explore the dominant emission mechanism. Based on a robust $10\,\sigma$ detection criterion, I find a constant median spectral index of $\alpha_{1.4\mathrm{GHz}}^{610\mathrm{MHz}} \approx -0.6$ to -0.7 for sources between $S_{1.4\mathrm{GHz}} \approx 200\,\mu$Jy and 10 mJy. This result suggests that the galaxy population in the sub-mJy regime is powered by optically-thin synchrotron emission – star-forming galaxies or lobe-dominated active galactic nuclei (AGN).

Making use of X-ray observations in the LH, I show that the fraction of radio sources detected in the hard X-ray band (between 2 and 10 keV) decreases from 50 to 15 per cent between $S_{1.4\mathrm{GHz}} \approx 1$ mJy and $\lesssim 100\,\mu$Jy, which strongly suggests a transition from AGN to star-forming galaxies.

Based on the deep, multi-wavelength coverage of the SXDF, I explore the behaviour of the far-infrared (FIR)/radio correlation as a function of redshift. I combine the q_{24} factor – the logarithmic flux density ratio between *Spitzer* 24-μm and VLA 1.4-GHz flux densities – with available photometric redshifts and find strong evidence that the correlation holds out to $z \approx 3.5$. Based on M82-like k-corrections and using a high-significance ($S_{1.4\mathrm{GHz}} > 300\,\mu$Jy) radio sub-sample, I find a mean and scatter of $q_{24} = 0.71 \pm 0.47$. Monte-Carlo simulations based on these findings show that

fewer sources deviate from the correlation at fainter flux densities (i.e. fewer radio-loud AGN). I predict that the radio-loud fraction drops from 50 per cent at ~ 1 mJy to zero at $\lesssim 100\,\mu$Jy.

The validity of the FIR/radio correlation out to very high redshifts adds credibility to identifications of sub-millimetre (submm) galaxies (SMGs) made at radio wavelengths. Based on a sample of 45 radio-identified SMGs in the LH, I find a median radio spectral index of $\alpha_{1.4\mathrm{GHz}}^{610\mathrm{MHz}} = -0.72 \pm 0.07$, which suggests that optically-thin synchrotron is the dominant radio emission mechanism.

Finally, as an Appendix I include a theoretical treatment that constrains the average geometry of the dusty, torus-like structures believed to obscure a large fraction of the AGN population. I use the distribution of column densities (N_{H}) obtained from deep ~ 1 Msec X-ray observations in the *Chandra* Deep Field South. I find that to reproduce the wide observed range of N_{H}, the best torus model is given by a classical "donut"-shaped distribution with an exponential angular dependency of the density profile.

Acknowledgements

First of all, I want to thank the Particle Physics and Astronomy Research Council – PPARC (now the Science and Technology Facilities Council – STFC) and Fundación Andes for giving me the opportunity to complete this PhD at the University of Edinburgh. The funding has permitted a relatively comfortable stay in the United Kingdom without concerns of an economic nature. I have included all the research I have carried out during these last three years within this thesis.

This thesis could not have been completed without the unconditional support from my supervisors Rob Ivison and Philip Best. Their experience and valuable help have been essential for my inspiration during the entire process of my PhD.

I also thank Michele Cirasuolo for his close collaboration and sympathy all these years, Andy Biggs for his useful tips in data analysis, Peder Norberg for his useful discussions in statistics, and all my mates with whom I shared a good laugh within this time.

I acknowledge Dave Green, Ian Smail, Chris Simpson, Dharam Vir Lal, Paulina Lira, Loretta Dunne, Glenn Morrison, Frazer Owen, Mark Dickinson, Eleni Vardoulaki, Jim Dunlop, Omar Almaini, Ross McLure, Sebastien Foucaud and Steve Rawlings, for their help and useful comments on the different collaborations in which I was involved.

I would also like to thank my friends, Benedict Clark, Ross 'Dooch' Ellis, Stuart Borrows, Carolina Carrasco, Manu Alevantis, Erin Letovsky, Eduardo Matthies and Galvarino Cerón, who were always there for support and obviously for the great time during my stay in Edinburgh, cheers guys!

"Finalmente quiero agradecer a mi familia y a mis amigos que siempre me apoyaron durante todo este tiempo a la distancia. Ustedes saben bien que esos casi doce mil kilometros que nos separan, no se comparan en nada con lo cerca que los llevo en el corazón."

In memory of the people who suffered from the greed of the British saltpetre companies in the Atacama Desert, northern Chile.

"Dedicada de toda la gente que sufrió por la codicia de las compañías Británicas del salitre en el Desierto de Atacama, norte de Chile."

Contents

CHAPTER 1

Introduction

"Sentada en un balcón en el piso 17 en una noche semiestrellada,
me senti parte del burdo cuestionamiento de la ensoñación ególatra humana,
tratando de descifrar tan distinto mensaje que aquel infinito manto azul,
entregaba de día y de noche,
de formas tan contradictorias...
en su eterno diálogo con su platinada y eterna contrincante."

Constanza Valdebenito.

1.1 The radio Universe

The sky at radio wavelengths looks completely different to that seen by our eyes in the optical. Indeed, radio emission arises from completely different astrophysical mechanisms (highly-energetic and relativistic) than those that dominate the optical spectrum. Most radio sources are extragalactic, with some local sources in the Galactic plane. In the electromagnetic spectrum, radio observations are defined as those at frequencies, $\nu \lesssim 200\,\mathrm{GHz}$ ($\lambda \gtrsim 1.5\,\mathrm{mm}$), the frequency above which thermal radiation from cold dust rapidly overwhelms the radio power.

In astronomy, radio observations have been extremely useful to image what other wavelengths cannot see. It is possible to identify three main reasons why these observations can be more useful than those in other parts of the electromagnetic spectrum. First, radio interferometry (see Chapter 2) makes it possible to image at sub-arcsecond resolution. This implies

that the vast majority of local radio sources can be resolved, defining physical sizes and determining accurate positions. Second, extinction is not an issue at radio wavelengths, implying radio data can provide a clean estimate of the luminosity of high-redshift galaxies and dust-enshrouded objects. This property is particularly important in high-redshift studies such as those described later. The third is a property mentioned in §1.3.1 and it is related to star-forming galaxies: radio emission provides clear evidence of very recent star formation, not overwhelmed by emission from stellar populations older than 10^8 yr.

In early studies, mostly after World War II, radio observations were restricted to powerful (> 1 Jy)[1] radio sources, typically associated with optically bright quasars (Condon 1984; Willott et al. 2002) and rare, luminous galaxies ($L \approx 10^{25-29}\,\mathrm{W\,Hz^{-1}}$). Radio-loud quasars are usually hosted by massive elliptical galaxies and display magnificent radio structures: widely separated radio lobes on either side of an unresolved, usually fainter, central core (see Fig. 1.1).

It was not until the mid 1980s that the Westerbork Synthesis Radio Telescope (WSRT) and the Very Large Array (VLA) began to shed light on the mJy and sub-mJy radio sky (Windhorst et al. 1985; Mitchell & Condon 1985). These observations revealed a new radio population dominated by star-forming galaxies (spirals and irregulars) instead of massive elliptical galaxies. Recent deep radio observations, in combination with deep multi-wavelength coverage (spectroscopic and photometric), have shown that the sub-mJy radio sources are mostly a combination of star-forming galaxies and faint radio active galactic nuclei (AGN) (e.g. Simpson et al. 2006; Barger et al. 2007; Bondi et al. 2007; Padovani et al. 2007), although the relative contributions of these populations are not yet well known. One of the aims of this thesis is to present a detailed analysis of the nature of the faint radio population, combining different multi-wavelength observations in large ($\sim 1\,\mathrm{deg}^2$) surveys.

1.1.1 Radio number counts

Historically, the number of sources detected as a function of radio flux density is presented in its differential form, normalised to an Euclidean Universe (e.g. see Fig. 1.2). The number counts clearly reveal the appearance of a new radio population at sub-mJy flux densities (at 1.4 GHz). Population synthesis models use these counts to predict the evolution of the radio sources as a function of cosmic time (e.g. Dunlop & Peacock 1990; Hopkins et al. 2000; Jarvis & Rawlings 2004). These models show that normal star-forming galaxies, starburst galaxies and radio-quiet AGN (sources where the jet power is negligible compared to the central core) are mainly responsible for the sub-mJy counts, while the powerful (> 1 mJy) sources are mostly radio-loud AGN (sources with powerful jets and lobes – see Fig. 1.1). A short description of all the different source classifications is given in § 1.2.

The integral form of the number counts, $N(> S)$, is often parameterised by a simple power law, $k\,S^{-\gamma}$. This form provides a simple estimate of the number of sources expected to be

[1] $1\,\mathrm{Jy} = 10^{-26}\,\mathrm{W\,m^{-2}\,Hz^{-1}}$

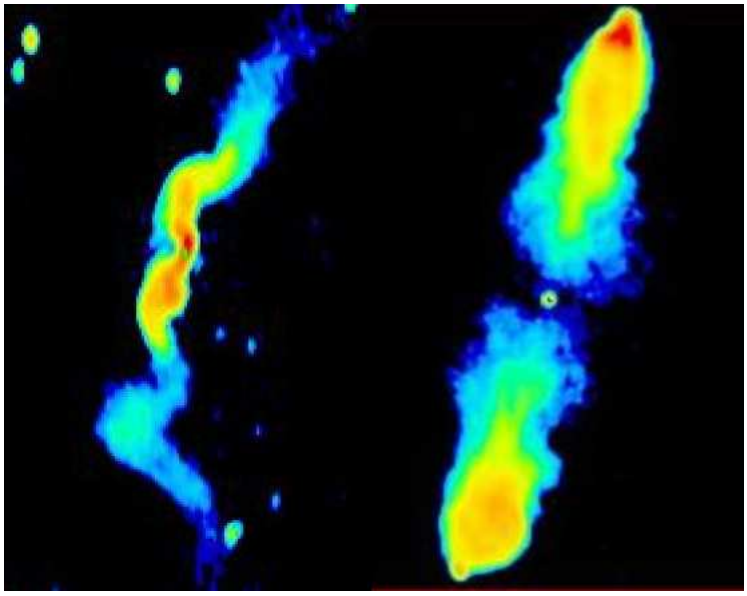

Figure 1.1: Two powerful radio-loud AGN; 3C31 (left) and 3C223 (right), a FR I and II source (see definition in § 1.2), respectively. In the image, red indicate higher surface brightness than blue. Image kindly provided by Philip Best.

observed to the flux limit of an observation. It is predicted that in the sub-mJy regime, down to a few tens of μJy, at an observing frequency of 1.4 GHz (Richards 2000):

$$N(>S_{1.4\mathrm{GHz}}) \approx 133\, S_{1.4\mathrm{GHz}}^{-1.38} \quad \mathrm{arcmin}^{-2} \tag{1.1}$$

where N is the expected number of sources per arcmin^2 above the specific flux density level $S_{1.4\mathrm{GHz}}$ in μJy. For example, in a 1-deg^2 image, the number of sources expected above 100 μJy is approximately 830, while across the whole sky we would expect $\sim$34 million sources.

1.1.2 The nature of sub-mJy radio sources

Very luminous, rare radio galaxies and quasars are known to dominate the bright (>mJy) source counts. The faint radio regime has been more controversial, since only extremely deep optical/near-infrared images are able to provide identifications. In Chapter 4, I show how very deep K-band observations (Cirasuolo et al. 2007), down to $K_{\mathrm{AB}} \approx 24$ in magnitude, have been able to identify $\sim$ 90 per cent of the faint radio population.

As population synthesis models suggest, based on the luminosity of well-known local radio emitters, it is possible to guess the sort of sources observed in redshift space for a given flux-limited observation. Garrett (2005) itemises seven classes of objects that may play a role in the faint number counts: (1) local, low-luminosity AGN, also classified as Seyfert galaxies, with radio luminosities of $L \approx 10^{23}\,\mathrm{W\,Hz^{-1}}$ such as M84 (a faint FR I; Bower et al.

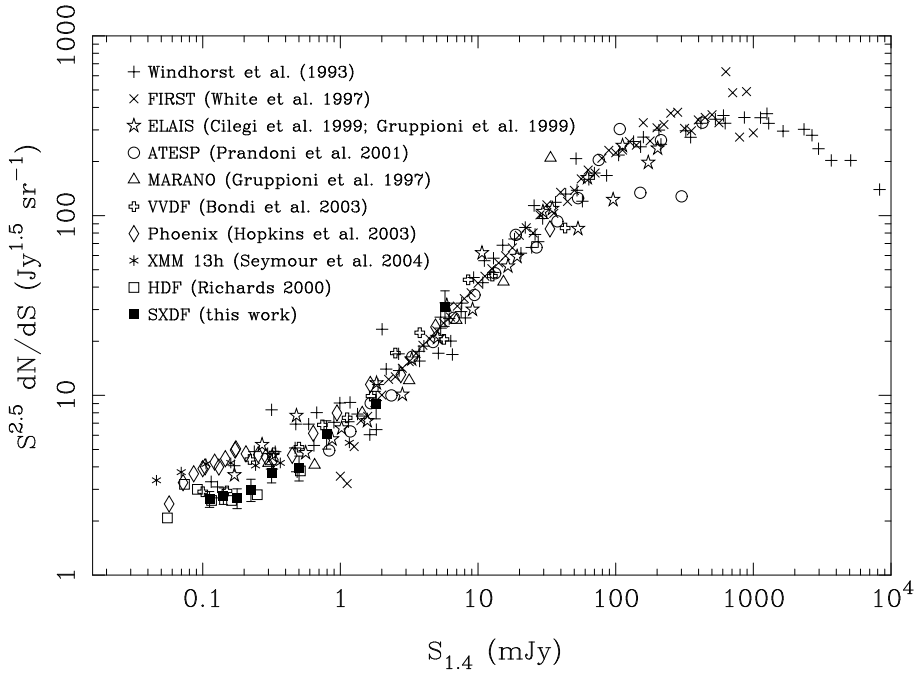

Figure 1.2: Differential number counts at 1.4 GHz normalised to an Euclidean universe. The figure is presented by Simpson et al. (2006), based on a large observational compilation (including the Subaru *XMM/Newton* Deep Field, part of the SHADES submm survey – see later), kindly provided by Nick Seymour.

1997); (2) normal, star-forming galaxies like the Milky Way, with luminosities in the range $L \approx 10^{18-21}\,\mathrm{W\,Hz^{-1}}$, and starburst systems like M82 or Arp 220 ($L \approx 10^{22-23}\,\mathrm{W\,Hz^{-1}}$); (3) the most numerous galaxy-scale objects in the Universe, dwarf irregular galaxies with $L \approx 10^{17-21}\,\mathrm{W\,Hz^{-1}}$; (4) powerful γ-ray bursts (GRBs) (e.g. GRB030329 – van der Horst et al. 2005) with extreme luminosities, $L \approx 10^{24}\,\mathrm{W\,Hz^{-1}}$; (5) violent hypernovae ($\gtrsim 50\,\mathrm{M_\odot}$ supernovae)[2] with $L \approx 10^{21-22}\,\mathrm{W\,Hz^{-1}}$ in individual starburst galaxies (e.g. in Arp 220 – Smith et al. 1998); (6) Galactic supernova remnants, such as SN 1993J (Chandra et al. 2004), with luminosities in the $L \approx 10^{17-21}\,\mathrm{W\,Hz^{-1}}$ range; and (7) radio binary systems seen during outburst, e.g. Cyg X3 ($L \approx 10^{17}\,\mathrm{W\,Hz^{-1}}$).

Fig. 1.3 suggests that the most likely contributors to the sub-mJy population, at least at moderate redshifts, are low-luminosity AGN and Arp 220-like starburst galaxies. With the present capabilities of radio telescopes, normal star-forming (or M82-like starburst) galaxies can be only detected up to moderate redshifts, $z \lesssim 0.2 - 0.4$. The contribution from dwarf irregular galaxies is negligible, as is that of Galactic objects (at least in radio observations away from the Galactic plane at 1.4 GHz). Finally, GRBs can be observed up to very high redshifts but these objects are rare and short-lived so make an insignificant contribution (Garrett 2005), though studies of radio transients are in their infancy.

[2] $1\,\mathrm{M_\odot} = 1.99 \times 10^{30}\,\mathrm{kg}$

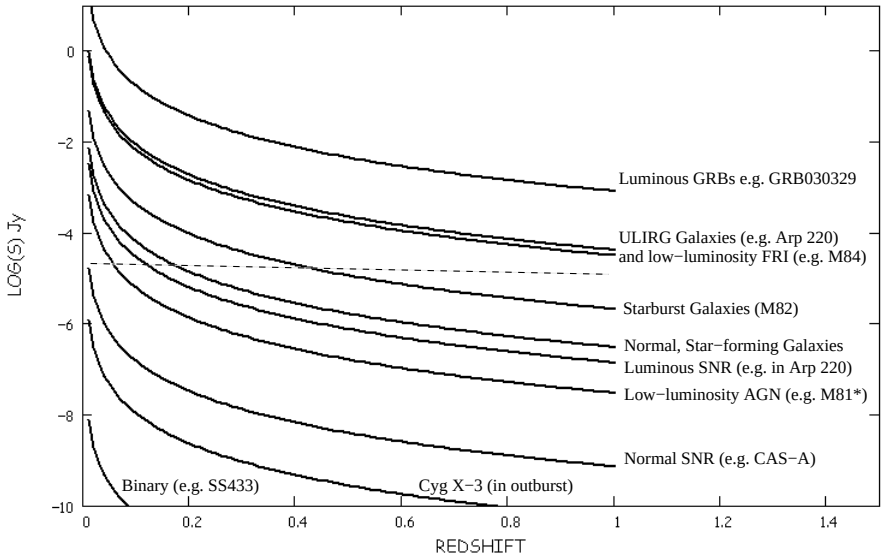

Figure 1.3: Flux density as a function of redshift for a variety of radio emitters (see text for details). The dashed line is the typical flux density limit reached in moderately deep radio observations (see Chapter 3). Image from Garrett (2005).

An extensive effort to clarify the nature of the faint radio sources has been made at optical wavelengths. Using spectroscopy, Gruppioni et al. (1999) found that 44 ± 16 per cent of radio sources with $200\,\mu\mathrm{Jy} < S_{1.4\mathrm{GHz}} < 1\,\mathrm{mJy}$ are early-type galaxies, although this was based on an incomplete ($\sim$50 per cent) sample. Ciliegi et al. (2005) found a late-type star-forming galaxy population (based on colour-colour plots) and extended the analysis to $S_{1.4\mathrm{GHz}} < 0.15\,\mathrm{mJy}$. For a highly spectroscopically complete sample, Barger et al. (2007) suggested that the bulk of $S_{1.4\mathrm{GHz}} \gtrsim 40\,\mu\mathrm{Jy}$ ($L_{1.4\mathrm{GHz}} < 10^{24}\ \mathrm{W\,Hz^{-1}}$) sources are indeed star-forming galaxies with strong Balmer lines and no broad or high-ionisation lines. However, based on the optical morphology of the sources, Padovani et al. (2007) find that the contribution from star-forming galaxies to the sub-mJy radio population is only about one third of the total, suggesting a very large fraction of radio-quiet AGN in this regime. The most radical result comes from Simpson et al. (2006), work that found no difference in colour-colour diagrams for the faint population with respect to bright (mJy) radio sources. They suggested a dominant radio-quiet AGN population at $100\,\mu\mathrm{Jy} < S_{1.4\mathrm{GHz}} < 300\,\mu\mathrm{Jy}$.

These results clearly show that different approaches have failed to find a consensus for the properties of faint radio emitters. A plausible scenario involves hybrid radio systems that display both AGN and star-forming characteristics.

1.2 Active galactic nuclei

An AGN is the very bright innermost region of a galaxy. It is believed to comprise a super-massive black hole ($M_{\rm BH} \approx 10^{6-9}\,{\rm M}_\odot$) devouring infalling material from an accretion disk. The typical scales for the accretion disk are few tens of Astronomical Units (AU)[3], a scale which precludes direct observation with current telescopes, even in the nearest AGN. Most of our knowledge of these monsters has come from spectroscopic analysis.

The extreme gravitational potential surrounding the super-massive black hole implies that the vast majority of the energy ($\sim 10^{37-41}$ W) is released by the accretion disk in the optical and ultraviolet (UV) wavelength range (Elvis et al. 1994). The continuum AGN power is remarkably constant over perhaps 15 decades of frequency – from γ-rays to radio –, presents variations in ~ 1 hr timescales and is often significantly polarised.

1.2.1 Historical classifications

In 1943, Carl K. Seyfert reported a sample of galaxies with very bright nuclei displaying broad emission lines in a wide range of ionisation states (Seyfert 1943). Today these objects (AGN) are categorised as either Seyfert 1 or Seyfert 2, depending on the detection of broad emission lines (H I, He I, He II with $\gtrsim 1000\,{\rm km\,s^{-1}}$), or their absence ($\lesssim 1000\,{\rm km\,s^{-1}}$), respectively. The broadening of the emission lines is produced by Doppler effects in regions with strong gravitational fields, near the galactic nucleus (the broad-line region – BLR). Narrow forbidden lines (e.g. [O III] and [S II]) coming from colder regions (the narrow-line region – NLR) are observed in both types of Seyfert galaxies. Often the continuum emission from the accretion disk in Seyfert 1 galaxies overwhelms the emission of the whole galaxy.

In the radio domain, the brightest extragalactic radio source in the sky is Cygnus A at redshift, $z = 0.057$. In general, these radio-loud galaxies are extremely powerful sources at cosmological distances, with typical radio luminosities of $10^{23-28}\,{\rm W\,Hz^{-1}}$ at 1.4 GHz. Evidence for broad and narrow emission lines have been also found, necessitating new classifications: broad-line radio galaxies (BLRGs) and narrow-line radio galaxies (NLRGs). Despite the obvious similarities with Seyfert galaxies, there are differences: (1) Seyfert galaxies are relatively radio-quiet compared to radio galaxies; (2) Seyferts are usually associated with spiral galaxies while bright radio emitters are instead associated with giant elliptical galaxies.

In the early 1960s, the discovery of highly redshifted emission lines from powerful point-like radio sources (e.g. 3C 273 at $z = 0.367$; Schmidt 1963) introduced a new class of very distant sources – quasars (QSOs). These are the most powerful sources in the Universe and have typical bolometric luminosities of $\sim 10^{38-41}$ W.

The basic division for radio galaxies is between "radio quiet" and "radio loud". Radio-loud sources usually consist of a radio core, one or two jets and two dominant radio lobes. Radio-quiet sources are less luminous at radio wavelengths by a factor 10^{3-4}, consisting of a

[3] $1\,{\rm AU} = 150 \times 10^9$ m

weak radio core and faint and diffuse radio jets. Spirals and Seyfert galaxies are sometimes seen to have "S-shaped" kpc-scale radio structures, possibly due to jets disrupted by a high-density interstellar medium (ISM), or simply by a lower efficiency for the core ejection. In fact, all Seyfert galaxies are low-redshift radio-quiet AGN, whereas QSOs are radio-loud AGN.

1.2.2 Radio jets from AGN

Baade & Minkowski (1954) were the first to use the term "jet" to describe a collimated fluid ejected from the nucleus of M87. Jets emits synchrotron radiation and have been extensively observed at radio wavelengths (e.g. Bridle & Perley 1984). High-resolution radio images have resolved jets into a series of knots, moving away from a central core (see Fig. 1.4) – typically from the central region of a massive elliptical galaxy. The material ejected from the central AGN is believed to be associated with a dynamic interaction between the accretion disk and the magnetic fields, around the super-massive black hole. The simplest model assumes a continuous flow of well-collimated material ejected at relativistic velocities, powered by the energy of accretion and/or by the extraction of rotational kinetic energy from the black hole. The jet traps and confines a twisted magnetic field within the plasma. Both the strength of the magnetic field and the energy of the charged particles decrease as a function of time while the jet expands. The fact that jets can be extended on scales from a parsec (pc)[4] to hundreds of kpc is evidence for a very stable alignment in the central core, and for non-destructive instabilities in the plasma. The large distances suggest a secondary mechanism of acceleration for the relativistic particles in order to keep the structure "alive".

Fanaroff & Riley (1974) classified radio sources according to their jet/lobe structure. They defined FR II sources as those characterised by powerful hotspots (bright and compact knots – see right source in Fig. 1.1) at larger distances from the central core than FR I sources (e.g. left source in Fig. 1.1, and top in Fig. 1.4). In general, FR I sources have weaker radio emission and lack the powerful hotspots observed in FR II sources. The transition between these two classes occurs at approximately $P_{1.4\mathrm{GHz}} \sim 10^{25}\,\mathrm{W\,Hz^{-1}}$.

In terms of the spectral energy distribution, the mean radio spectral index, measured between 178 and 750 MHz for a sample of $z < 0.5$ FR I and FR II AGN, has been found to be $\alpha = -0.74 \pm 0.19$ and -0.79 ± 0.14 (where $S \propto \nu^{\alpha}$), respectively (Laing et al. 1983). Approximately 40 per cent of jets have radio spectral indices (around 1.4 GHz) between $-0.6 < \alpha < -0.7$ and $\geq$90 per cent are between $-0.5 < \alpha < -0.9$ (Bridle & Perley 1984). Spectral gradients along most jets are small, but they steepen away from the core and the bright knots (Charlesworth & Spencer 1982; Burns et al. 1983).

[4] 1 pc = 3.09×10^{16} m

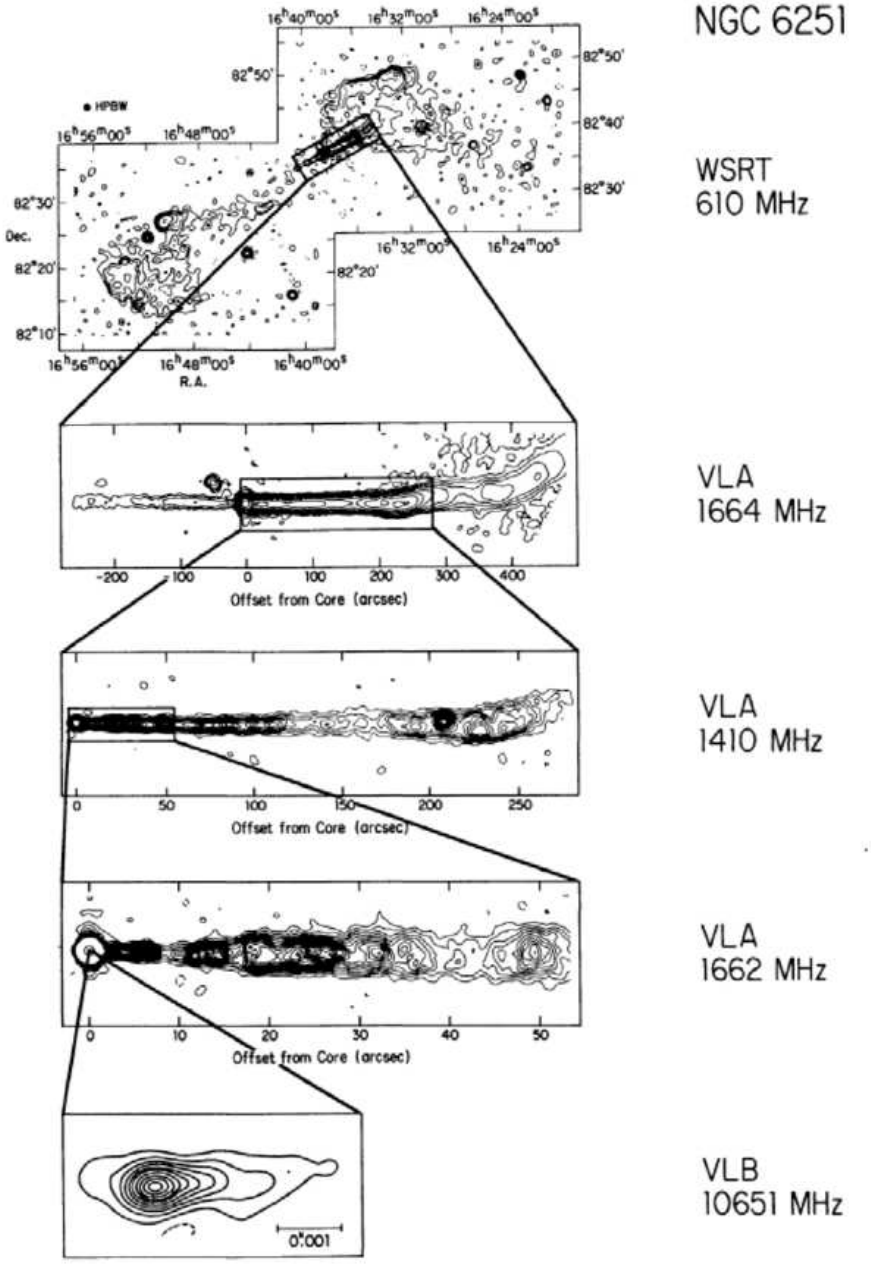

Figure 1.4: The top image shows an extended ($\sim$ 50 arcmin) radio-loud AGN, NGC 6251, observed at 610 MHz using the WSRT. The following images are observations of the brightest jet at progressively higher resolutions using different facilities. Located at a distance of 103 Mpc, the physical scale is given by 0.476 kpc/arcsec. Image from Bridle & Perley (1984).

1.2.3 Compton-thick AGN and the cosmic X-ray background

Given by the extreme conditions surrounding the central super-massive black hole, AGN have also been found to be ubiquitous emitters in the X-rays. It is believed the X-ray emission comes from the innermost region, the so-called "corona", where photons from the accretion disk can be scattered by either mildly-relativistic thermal electrons or highly-relativistic non-thermal electrons via Compton inverse scattering (Svensson 1996). X-rays, however, typically suffer absorption along the line of sight, thus limiting the detection of highly obscured AGN. In fact, if the Hydrogen column density is higher than $N_{\rm H} = 10^{24}\,{\rm cm}^{-2}$, then the media becomes "Compton thick" (at 10 keV)[5].

Antonucci (1993) proposed a "unification model" for Seyfert galaxies. He proposed that AGN are surrounded by a thick, dusty torus which dramatically changes the observed spectral properties of the sources. Basically, the emission from the inner corona (X-rays), accretion disk (optical/UV continuum) and BLR (broad emission lines) are expected to be absorbed if our line of sight towards the nucleus is intercepted by the torus (edge-on; see sketch in Appendix A, Fig. A.1). Under this simple geometrical assumption – in the X-ray domain – AGN are classified as Type 1 or Type 2 (following the same nomenclature as Seyfert galaxies) depending on a the column density along the line of sight lower or higher than $N_{\rm H} = 10^{22}\,{\rm cm}^{-2}$, respectively.

Deep $\sim$ Msec X-ray observations (Giacconi et al. 2002; Alexander et al. 2003) have provided the most efficient method of detecting AGN in the Universe (Mushotzky 2004). Using population synthesis models, Ueda et al. (2003) showed that the contribution from highly-absorbed AGN is essential to the cosmic X-ray background (CXRB – Wilman & Fabian 1999). Indeed, it is expected that a fraction of 20–30 per cent of the CXRB is composed by "Compton thick" sources – sources missed even in the deepest X-ray surveys undertaken with the present high-sensitivity space telescopes, *Chandra* and *XMM/Newton*.

Simpson et al. (2006) proposed these objects could be detected using deep radio surveys. They suggested tentatively that 20 per cent (or more) of the radio counts at $100 \leq S_{1.4{\rm GHz}} < 300\,\mu$Jy are radio-quiet AGN (see 1.1.2), thereby proposing a possible way forward for observing the missing highly-obscured AGN fraction, the so-called Type-2 quasars.

1.3 Star-forming galaxies

1.3.1 The Radio Emission From Star-Forming Galaxies

The physical mechanism responsible for the radio emission from star-forming galaxies is believed to be closely related to the high end of the initial mass function (IMF) – the massive stars. It is worth noting that in these galaxies the radio emission accounts for less than 10^{-4} of their bolometric luminosity.

[5] $1\,{\rm keV} = 1.6022 \times 10^{-16}\,{\rm J}$

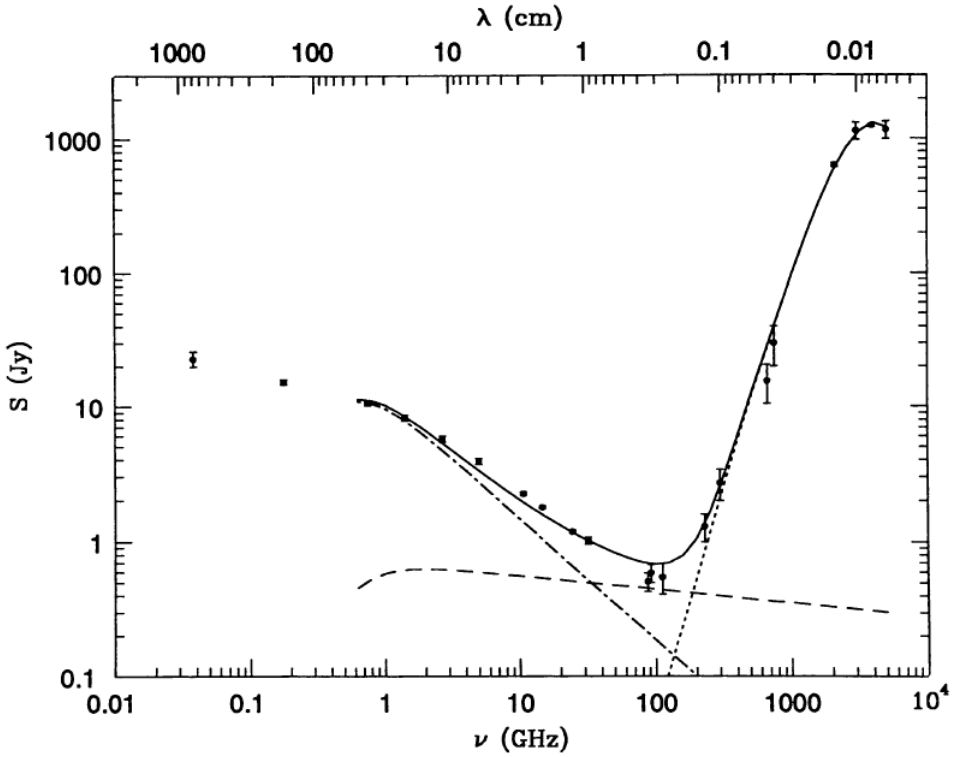

Figure 1.5: The observed radio to far-infrared spectrum of M82 (Klein et al. 1984; Carlstrom & Kronberg 1991) parameterised (solid line) by the sum of three components: synchrotron emission (dot-dash line), free-free from H II regions (dashed line) and a thermal component generated by reprocessed ionising photons absorbed by dust particles (dotted line). Image from Condon (1992).

There are two different mechanisms for radio emission from star-forming galaxies: (1) thermal emission (also called free-free or bremsstrahlung – breaking radiation) from H II regions ionised by short-lived ($\tau \leq 3 \times 10^7$ yr) massive stars ($> 8\,M_\odot$); and (2) synchrotron emission from electrons accelerated by supernova remnants (from massive stellar parents; SN Type II or Type Ib) which interact with the large-scale magnetic field of the galaxy. The former process dominates at $\gtrsim 30$ GHz and is characterised by a hard spectral shape ($\alpha \approx -0.1$). Approximately 10 per cent of the total radio power is due to this mechanism. The non-thermal process dominates the lower frequency range ($\lesssim 30$ GHz) and has a much steeper spectrum, typically $\alpha \approx -0.75$ (Condon 1992).

Most of the observed synchrotron emission arises from relatively old ($\gtrsim 10^7$ yr) relativistic electrons that have propagated for distances larger than 1 kpc from their short-lived ($\gtrsim 10^5$ yr) and now deceased parent supernovae – smoothed beyond recognition. The basic cycle of the radiation process begins with a massive ($> 8\,M_\odot$) supernova explosion. The huge amount of energy ($\sim 10^{44}$ Joules) liberated in a very short period of time produces a supersonic expansion ($\sim 10^4\,\mathrm{km\,s^{-1}}$) in the outer layers of the imploding star, thereby generating shock waves in

the ISM. It is believed that charged particles can be accelerated up to relativistic velocities by their passing, back and forth, across shock waves, via the so-called Fermi process (Fermi 1949). These relativistic charged particles (cosmic rays) propagate through the ISM to interact with the large-scale magnetic field of the galaxy, finally producing the observed synchrotron radiation. A final process, and a crucial part of the cycle, is the loss of energy and the eventual escape into intergalactic space of the cosmic rays. The details of this stage are uncertain since a wide variety of mechanisms may play a role in the energy loss – processes such as inverse Compton scattering, bremsstrahlung, ionisation and adiabatic expansion. From models it is expected that relativistic charged particles have probable lifetimes of $\lesssim 10^8$ yr (Condon 1992).

Based on this model the synchrotron radio emission traces the high end of the IMF of the galaxy, and provides a definitive measurement of recent star formation. For a constant IMF, it is expected that the strength of the radiation is proportional to the number of supernova explosions per unit time and thus the total star-formation rate of a galaxy. Condon (1992) shows that

$$\left(\frac{L_{\rm syn}}{\rm W\,Hz^{-1}}\right) \approx 5.3 \times 10^{21} \left(\frac{\nu}{\rm GHz}\right)^{-\alpha} \left[\frac{SFR\,(M \geq 5\,{\rm M}_\odot)}{\rm M_\odot\,yr^{-1}}\right] \tag{1.2}$$

where $L_{\rm syn}$ is the synchrotron (non-thermal) radio luminosity, α is the radio spectral index (~ -0.7 for star-forming galaxies) and SFR the star-formation rate, given by stars with masses higher than $5\,{\rm M}_\odot$, in units of ${\rm M}_\odot\,{\rm yr}^{-1}$.

It must remembered that the entire process responsible for the observed synchrotron emission is poorly understood and what can be learned from radio observations is limited in terms of quantitative interpretation. There is, however, an almost miraculously well-behaved relation at the low-energy end of the electromagnetic spectrum – the famous far-infrared (FIR)/radio correlation (van der Kruit 1971; Helou et al. 1985; Condon et al. 1991).

1.3.2 The FIR/radio correlation

The apparent conspiracy between FIR and radio power was first discovered by van der Kruit (1971, 1973) for a sample of Seyfert and spiral galaxies, making use of the WSRT at 1.4 GHz in combination with 10-μm mid-infrared data (Kleinmann & Low 1970). This insight was then confirmed (see Fig. 1.6) by the arrival of the *Infrared Astronomy Satellite (IRAS)*, which put this correlation on the podium as one of the most important in astronomy (Helou et al. 1985; Condon et al. 1991).

The correlation holds for a large variety of star-forming galaxies, covering six orders of magnitude in luminosity, and describes a commonality between the synchrotron power and the thermal FIR emission (between 8 and 1000 μm, approximately). The origin of the FIR emission is the same massive stellar parents of the synchrotron radiation (Harwit & Pacini 1975): H II regions and massive stars produce a vast amount of optical and UV radiation which is absorbed by cold dust present in star-forming regions. The dust is mainly composed by

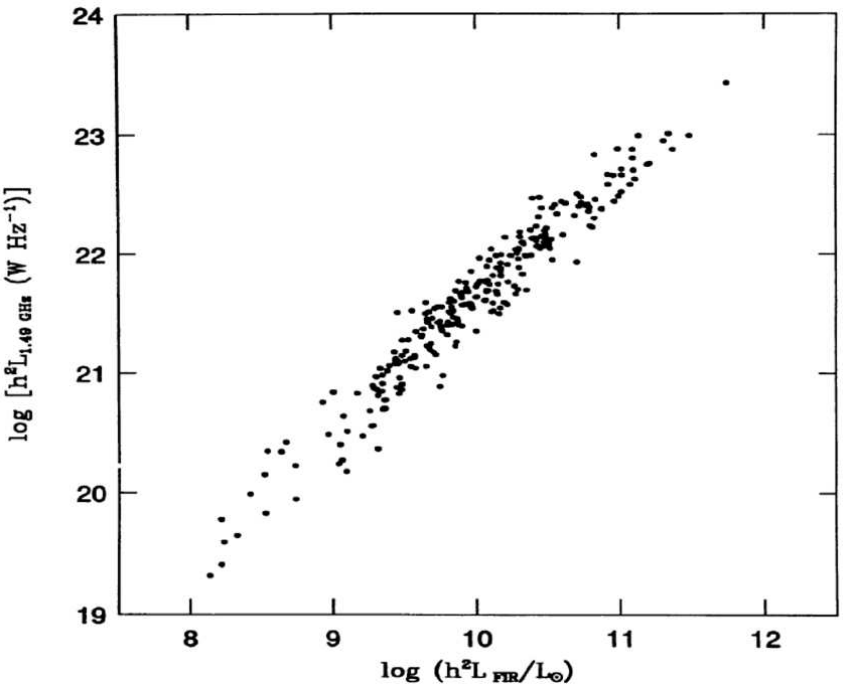

Figure 1.6: The FIR/radio correlation, based on a subsample of the Bright Galaxy Sample (BGS) undertaken by *IRAS* (Soifer et al. 1987). Sources have strong 60-μm emission and unknown AGN activity. Image from Condon (1992).

fine carbon and silicate grains, with typical grain-sizes of approximately 1 μm which interact strongly with (absorb) the optical and UV radiation. The dust is heated to temperatures of 20–200 K and re-emits a modified blackbody spectrum in the FIR. The peak of the FIR emission is at approximately 100 μm (see Fig. 1.5).

Given the origin of the FIR emission, it also provides an estimate of the star-formation rate of a galaxy (Condon 1992):

$$\left(\frac{L_{\mathrm{FIR}}}{\mathrm{L}_\odot}\right) \approx 1.1 \times 10^{10} \left[\frac{SFR\,(M \geq 5\,\mathrm{M}_\odot)}{\mathrm{M}_\odot \mathrm{yr}^{-1}}\right] \tag{1.3}$$

where L_{FIR} is the FIR luminosity in units of solar power ($\mathrm{L}_\odot$)[6]. Both L_{syn} and L_{FIR} are proportional to the star-formation rate, which explains the linearity of the FIR/radio correlation.

Condon (1992) showed that FIR and radio observations yield indistinguishable luminosity functions, i.e. they detect similar star-forming galaxy populations. These results imply that if the FIR/radio correlation holds up to high redshift, radio observations must provide a powerful extinction-free tool for the study of the cosmic star-formation history.

The linearity of the FIR/radio correlation was unexpected over such a large range of luminosities. In fact, models struggle with the interpretation since they require a fine-tuning of all

[6] $1\,\mathrm{L}_\odot = 3.84 \times 10^{26}\,\mathrm{W}$

the physical mechanisms responsible for the FIR and radio emission. See Xu et al. (1994), Bell (2003) or Thompson et al. (2006) for more details.

1.4 Submillimetre galaxies

Submillimetre-selected galaxies (SMGs) were first discovered using the Submillimetre Common-User Bolometer Array (SCUBA – Holland et al. 1999) on the 15-m James Clerk Maxwell Telescope (JCMT) in the late 1990s (Smail et al. 1997; Hughes et al. 1998; Barger et al. 1998; Eales et al. 1999). These observations revealed a new, very luminous and dust-enshrouded galaxy population, peaking at $z \approx 2-3$ (Smail et al. 2002; Chapman et al. 2005) with typical star-formation rates (SFRs) of $10^3\,\mathrm{M_\odot yr^{-1}}$ (Pope et al. 2006).

The intense star formation in these galaxies implies that they are able to produce a massive elliptical galaxy ($> 3\,\mathrm{L^*}$) within $\sim 1\,\mathrm{Gyr}$ and is one of the reasons why SMGs are believed to be the most likely progenitors of massive, passive ellipticals seen locally (Lilly et al. 1999; Blain et al. 1999). SMGs are closely related to the creation of galactic bulges during the period in which the Universe suffered much higher star-formation activity (Daddi et al. 2005; Lagache et al. 2005). These galaxies therefore play a key role in our comprehension of how galaxies formed and evolved as a function of cosmic time.

Before the discovery of SMGs, the *IRAS* telescope discovered some dusty and very luminous local ($z < 0.3$) galaxies. These objects were classified depending on their bolometric FIR emission as luminous, ultraluminous and hyperluminous IR galaxies (LIRGS, ULIRGs – e.g. Arp 220 – and HLIRGs) for $L_{8-1000\mu\mathrm{m}} = 10^{11-12}\,\mathrm{L_\odot}$, $L_{8-1000\mu\mathrm{m}} = 10^{12-13}\,\mathrm{L_\odot}$ and $L_{8-1000\mu\mathrm{m}} > 10^{13}\,\mathrm{L_\odot}$, respectively. These FIR emitters have special importance because they have luminosities approaching those of the SMGs at high redshift (Kovács et al. 2006; Coppin et al. 2008). Detailed observations of ULIRGs show that galaxy interactions and mergers are almost always apparent (Sanders & Mirabel 1996). This demonstrates that galaxy disruptions can produce extreme emission and that the FIR waveband carries critical information about galaxy evolution (Genzel et al. 2000). Bright ULIRGs have well-studied spectral energy distributions and are usually assumed to be adequate templates for their more distant SMG counterparts.

Submm radiation is usually assumed to be dominated by thermal emission from dust grains heated by a UV/optical radiation field, but it is impossible to discriminate between a star- and an accretion-related origin using only submm data. The arrival of highly sensitive submm-wave spectrometers, such in the Atacama Large Millimeter Array (ALMA; Wilson 2008), will make it possible to discriminate between different ionising fields. The rich zoo of spectral lines, e.g. the carbon monoxide (CO) rotational transitions, spaced every 115 GHz, are sensitive to physical conditions in the ISM.

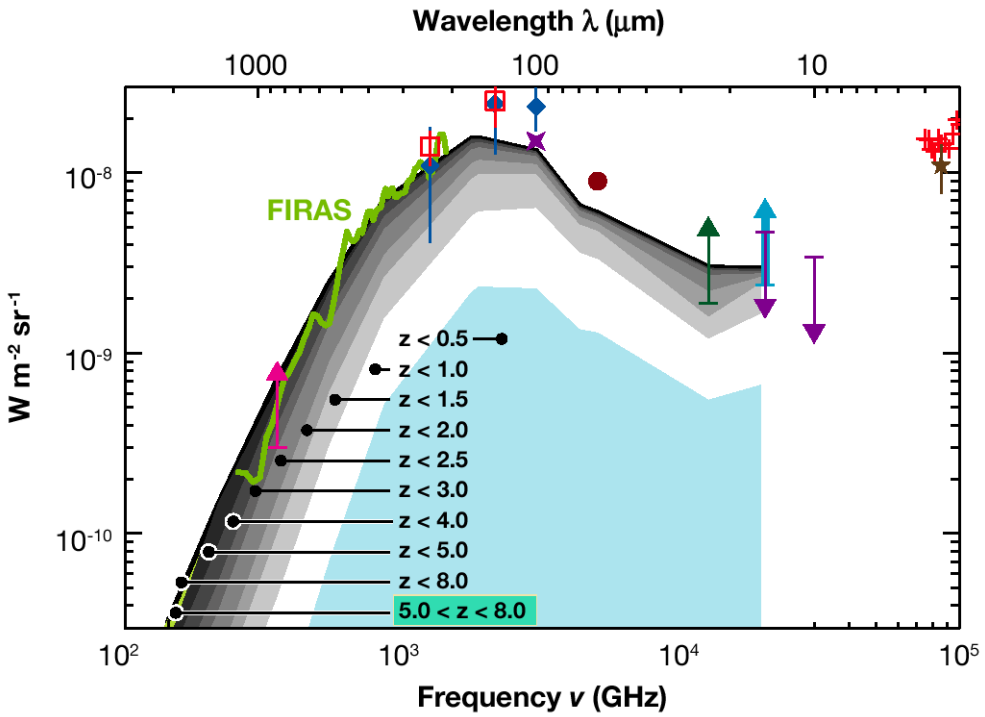

Figure 1.7: The cumulative contribution to the CIRB given by dusty galaxies at various redshifts (from 0.5 to 8), based on a model presented by Lagache et al. (2005). The different contributions are plotted on top of the extragalactic background observed over three decades in frequency, from the UV to submm wavelengths. Image from Lagache et al. (2005).

1.4.1 Cosmic infrared background

LIRGs and ULIRGs, i.e. galaxies emitting more than ∼90 per cent of their light above 5 μm, are considered to be the main contributors to the cosmic infrared background (CIRB). The contribution from low-redshift *IRAS* galaxies is just ∼2 per cent of the total background, which is mainly powered by their high-redshift counterparts (e.g. Dole et al. 2006).

Early studies using *IRAS* suggested that the number density of these dusty galaxies must evolve rapidly with redshift, at least up to $z \sim 0.2$ (Kim & Sanders 1998). This rapid evolution was confirmed by the *Infrared Space Observatory (ISO)* at 15 and 170 μm (Elbaz 2005), for $z \sim 2$ sourqces using SCUBA at 850 μm (Chapman et al. 2005) and at intermediate redshifts by *Spitzer* at 24 μm (e.g. Le Floc'h et al. 2005).

SMGs release a significant fraction of the energy generated by all galaxies over the history of the Universe. It is estimated they are responsible for approximately 20–50 per cent (Eales et al. 2000; Blain et al. 2002) of the CIRB.

At present, the study of these dusty-enshrouded galaxies is a major field of research. As may be expected, one of the main obstacles to detailed study is the strong obscuration suffered at optical wavelengths. In many cases this does not allow us to obtain a reliable spectroscopic

redshift or even to identify a counterpart. The number of stars born during the burst, the burst duration, and even the basic physical processes responsible for the intense activity of these galaxies are not yet fully understood.

1.4.2 Submillimetre observations

In the electromagnetic spectrum, the submillimetre range is defined to be between 200 μm and 1 mm, surrounded by the FIR and radio wavebands at shorter and longer wavelengths, respectively. For ground-based submm observations, the atmosphere (oxygen and water vapour absorption bands) absorb much of the radiation and restrict the observing wavebands to small atmospheric windows (e.g. 850 μm and 450 μm) where the opacity is low (Holland et al. 1999). Submm images can be highly disturbed by atmospheric variations. Even under ideal observing conditions, the expected opacity at the zenith is around 0.1 at 850 μm. This limitation ensures that telescopes are located in very dry regions, at high altitude.

The earliest mapping observations in the submm/mm range were made by ISOPHOT at 210 μm on board *ISO*. These data had very poor sensitivity and resolution (FWHM$\sim$ 2 arcmin). It was not until the late 1990s that a variety of submm/mm instruments with higher sensitivity and angular resolution began to appear, e.g. SCUBA (Holland et al. 1999) at the 15-m JCMT, the Max Planck Millimetre-wave Bolometer Array (MAMBO – Kreysa et al. 1999) at the Institut de Radio Astronomie Millimétrique's (IRAM's) 30-m Millimetre Radio Telescope (MRT), the Large Apex Bolometer Camera (LABOCA – Kreysa et al. 2003) at the 12-m Atacama Pathfinder Experiment (APEX), the Submillimeter High Angular Resolution Camera (SHARC – Voellmer et al. 2003) at the 12-m Caltech Submillimeter Observatory (CSO) and the Astronomical Thermal Emission Camera (AzTEC – Wilson 2008), which found temporary homes at JCMT and several other telescopes.

For submm observations the FWHM obtained from single-dish telescopes is commonly poorer than 12 arcsec, a radical issue which implies that the galaxy identification process has to be based on statistical analysis, taking into account the possibility of random associations (Downes et al. 1986). The poor resolution also leads to confusion (overlapped signals from faint, unresolved galaxies) in the deepest images. For example, SCUBA reached the classical confusion limit (one source for every $\sim$30 beams) in only a few tens of hours of integration at JCMT (Blain et al. 1998).

1.4.3 Radio-identified SMGs

The use of submm samples without secure counterparts is restricted to number counts and 2-dimensional (2-D) clustering properties, i.e. important but basic science. Deep radio observations were found to be the most efficient approach for identifying SMGs (Ivison et al. 1998, 2000). At least 65 per cent of SMGs brighter than $S_{850\mu\mathrm{m}} > 5$ mJy have been robustly identified using deep radio imaging (Ivison et al. 2002; Chapman et al. 2003; Greve et al. 2004). Ivi-

son et al. (2007b) showed that approximately 3/4 of SMGs can be identified in the Submm HAlf-Degree Extragalactic Survey (SHADES) fields using both deep radio maps (down to $5-10\,\mu\mathrm{Jy\,beam}^{-1}$) and deep *Spitzer* 24-$\mu$m images.

Given the low surface density of radio sources (see Eq. 1.1), a radio counterpart provides a very reliable (in a statistical sense) identification for an SMG. If the FIR/radio correlation – valid for local star-forming galaxies (Helou et al. 1985) – holds at the redshifts at which SMGs reside (Garrett 2002; Appleton et al. 2004 – see Chapter 4 of this thesis) then the radio and submm (rest-frame FIR) emission share a common origin, making the association very reliable.

Another useful property of interferometric radio observations is that high-resolution imaging can provide the accurate astrometry necessary to target a SMG spectroscopically, or to perform a reliable photometric analysis. Most of what is known about the properties of SMGs has relied on radio identifications. I should stress, however, that radio observations are able to observe only the $z \lesssim 3$ ULIRG-like SMGs (see Fig. 1.8) and therefore samples of radio-identified SMGs are biased in redshift (e.g. Eales et al. 2003).

1.4.4 Spectral energy distributions and selection biases

For ULIRGs – the local cousins of SMGs – mid-IR spectroscopic observations have suggested that the majority of the FIR emission is reprocessed starlight. Some of these studies are supported by the strength of polycyclic aromatic hydrocarbon (PAH) emission lines, benzene-like molecules that emit in the mid-IR and are sensitive to the physical conditions of the ISM (Genzel et al. 1998; Dale et al. 2006). However, in ULIRGs the dust emission is on sub-kpc scales (Downes & Solomon 1998; Sakamoto et al. 1999) which suggests some radiation may originate in nuclear activity instead. The nature of ULIRGs is still controversial and difficult to describe, even in these local objects.

Given the paucity of available FIR wavebands, it is important to keep the spectral energy distribution (SED) as simple as possible so as to avoid over-parameterising the description and then over-interpreting the results. The standard model uses three main parameters: the dust temperature, T_d, from the coolest dust grains, the emissivity function, $\epsilon \propto \nu^\beta$ (typically $\beta \approx 1-2$; Calzetti et al. 2000), and a spectral index, α, to describe the mid-IR regime, where $S_\nu \propto \nu^\alpha$ (see Dunne et al. 2000; Dunne & Eales 2001).

In the Rayleigh-Jeans regime, the observed flux density takes the following form:

$$S_\nu \propto \epsilon_\nu\, B_\nu \quad \text{where,} \quad B_\nu = \frac{2\,k_b\,T_\mathrm{d}\,\nu^2}{c} \tag{1.4}$$

where B_ν is the Planck function. The peak of the emission turns over at roughly $\lambda_\mathrm{max} \approx (2900\,K/T_\mathrm{d})\,\mu$m. The high-frequency end of the spectrum is due to the contribution of dust grains at different temperatures, limited to the temperature at which graphite evaporates (sublimation at $\sim 1500\,\mathrm{K}$), thus the spectrum always falls off at $\lambda \sim 2\,\mu$m with an exponential

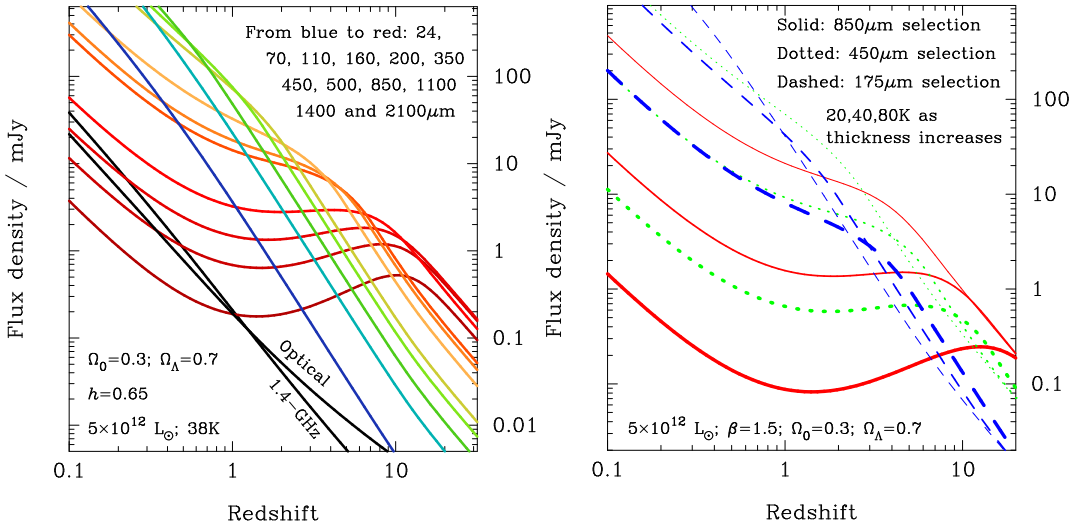

Figure 1.8: The flux density expected as a function of redshift for a dusty galaxy with an intrinsic FIR luminosity of $5 \times 10^{12}\,\mathrm{L}_{\odot}$. *Left:* considering a galaxy model of a SMG with a dust temperature $T_{\mathrm{d}} = 38\,\mathrm{K}$, the predictions reflect how the negative k-corrections at wavebands larger than 250 μm yield a flux density almost independent of redshift. *Right:* doubling T_{d} implies an order of magnitude change in flux density (e.g. Eales et al. 2000). Figures from Blain et al. (2002).

Wein tail (Robson 1996). For example, for the *IRAS* Bright Galaxy Sample (BGS – Soifer et al. 1987) in combination with 850-μm SCUBA data, typical parameters are $\beta = 1.3 \pm 0.2$ and $T_{\mathrm{d}} = 35.6 \pm 4.9\,\mathrm{K}$ (Dunne et al. 2000).

The steep and strong dependency in frequency, $S_{\nu} \propto \nu^{\beta+2}$, in the Rayleigh-Jeans portion of the spectrum, implies that SMGs should be relatively easy to detect up to $z \lesssim 10 - 20$ (see Fig. 1.8) . Indeed, the strong negative k-correction balances the dimming of a source due to its cosmological distance, providing a powerful tool to explore the high-redshift Universe almost independently of distance (Blain et al. 2002).

Fig. 1.8 shows the expected flux density for a ULIRG-like source with a fixed FIR luminosity ($5 \times 10^{12}\,\mathrm{L}_{\odot}$) as a function of redshift. These predictions clearly reveal the limitations of radio observations in detecting SMG sources at $z \gtrsim 3$, something that should always be remembered when interpreting radio-identified submm samples. The plot on the right-hand side of Fig. 1.8 shows a clear dependency on the dust temperature (T_{d}) which suggests that submm samples, based on flux density thresholds, are biased against the detection of hotter galaxies (Eales et al. 1999; Chapman et al. 2004a). This can be easily understood since the FIR spectrum moves to higher frequencies, the emission at the Rayleigh-Jeans regime decreases.

One final bias we should bear in mind is the possibility of extreme metallicities in these SMGs. The higher the metallicity, the more efficient the re-emission, so submm samples will be biased in favour of galaxies with high metallicities.

1.5 Aims and outline of the thesis

In this thesis, I use deep radio observations to study the properties of high redsihft galaxies using panchromatic analyses. I make use of interferometric radio telescopes – the Giant Metrewave Radio Telescope (GMRT) and the Very Large Array (VLA) – to image wide fields ($\sim 1\,\mathrm{deg}^2$) with existing deep coverage over the entire electromagnetic spectrum: the Lockman Hole and the Subaru *XMM/Newton* Deep Field. The origin of synchrotron radio emission and the techniques for its detection are described in Chapter 2. I describe how deep radio observations are able to define the properties of distant dusty-enshrouded galaxies. Particular interest is taken in the study of SMGs.

In Chapter 3, I explore radio spectral index as a probe of the physical mechanisms in distant galaxies – star formation or accretion-related activity. I explore the validity of the FIR/radio correlation at high redshift in Chapter 4. The results provide a better understanding of the faint and relatively unknown sub-mJy radio population.

As part of a preliminary analysis, in Chapter 5 I present strong constraints on the previously unknown radio SED (spectral index) of SMGs, using a conservative but robust sample of SCUBA and AzTEC sources in the Lockman Hole. These measurements will be complemented by existing *Spitzer* data and future *Herschel* PACS/SPIRE (Poglitsch et al. 2006) and SCUBA-2 (Holland et al. 2006) observations to provide a better understanding of these massive star-forming galaxies in the years ahead.

The summary and conclusions for all the findings in this thesis are presented in Chapter 6.

I also attach, as Appendix A, a study centred at the other end of the spectrum, using X-ray observations. Adopting the unification model, and other previously referenced models for AGN (Antonucci 1993), I present a simple approach that describes the average properties of the thick obscuring medium (the so-called "torus").

Finally, as complementary material, I include in Appendix B a brief recipe for the reduction of radio data using the Astronomical Image Processing System ($\mathcal{AIPS}$). I show how the radio images used in this work were created and include some useful tips.

CHAPTER 2

The origin of synchrotron radiation and its detection

"Me pregunto qué debo preguntarme para luego ser capaz de responder."
Cristóbal Espinoza.

2.1 Synchrotron radiation

Synchrotron emission is produced when a relativistic charged particle is accelerated by the presence of a magnetic field. Detailed electrodynamic analyses for accelerated charged particles can be found, for example, in astrophysical textbooks such as Rybicki & Lightman (1979), Longair (1994) or Jackson (1999). I focus here on the physics that describes the radiation emitted from an ensemble of charged particles interacting with a magnetic field in order to understand and to analyse the radio emission from distant galaxies.

2.1.1 The radiation field

It is well known that accelerated particles radiate energy. A formal treatment shows that Liénard-Weichert potentials describe the potential energy for the motion of accelerated charged particles. Placing these potentials into Maxwell's equations (in vacuum) it is possible to obtain the electromagnetic fields (Eq. 2.1) that naturally divide in two components.

The first is the electrostatic field, proportional to R^{-2} (where R is a distance parameter); the second is the radiative field, proportional to R^{-1}. Since the second term diverges to infinity, it implies it can propagate throughout space. In particular, emission from charged particles interacting with magnetic fields in distant galaxies can, therefore, be detected on Earth. The fields are usually referred to as the "velocity field" (left-hand side of Eq. 2.1) and the "acceleration field" (right-hand side of Eq. 2.1) due to their proportionality to the velocity ($\vec{\beta} = \vec{v}/c$) and acceleration ($\dot{\vec{\beta}}$), respectively.

$$\begin{aligned} \vec{E}(\vec{x},t) &= e\left[\frac{\hat{n}-\vec{\beta}}{\gamma^2\left(1-\vec{\beta}\cdot\hat{n}\right)^3 R^2}\right]_{\text{ret}} + \frac{e}{c}\left[\frac{\hat{n}\times\left\{\left(\hat{n}-\vec{\beta}\right)\times\dot{\vec{\beta}}\right\}}{\left(1-\vec{\beta}\cdot\hat{n}\right)^3 R}\right]_{\text{ret}} \\ \vec{B} &= \left[\hat{n}\times\vec{E}\right]_{\text{ret}} \end{aligned} \tag{2.1}$$

In Eq. (2.1), e is the particle's charge, $\hat{n}$ a unit vector in the direction of the propagation, and subscript "ret" means expressions are evaluated in a retarded charge's own time t', determined by $ct' = ct - R(t')$.

The power coming from an electromagnetic field is given by the radial component of the Poynting vector $\vec{S} = \frac{c}{4\pi}|\vec{E}|^2\hat{n}$. Considering that the electrostatic field will vanish at astronomical distances, I only take into account the propagating field to calculate the detected power per unit area, $\vec{S}\cdot\hat{n} = \frac{dP}{dA}$. Replacing the area factor by a solid angle, it is possible to show the generalised equation for the angular radiation pattern emitted by a distant, accelerated, charged particle:

$$\frac{dP(t')}{d\Omega} = \frac{e^2}{4\pi c}\frac{\left|\hat{n}\times\left\{(\hat{n}-\vec{\beta})\times\dot{\vec{\beta}}\right\}\right|^2}{(1-\vec{\beta}\cdot\hat{n})^5}. \tag{2.2}$$

In the case of interest, the charged particle is in circular motion, i.e. its acceleration, $\dot{\vec{\beta}}$, is perpendicular to its velocity, $\vec{\beta}$, therefore the radiation pattern can be expressed in spherical coordinates ($x = r\cos\phi\sin\theta$, $y = r\sin\phi\sin\theta$ and $z = r\cos\theta$) by the following equation,

$$\frac{dP(t')}{d\Omega} = \frac{e^2}{4\pi c}\frac{|\dot{\vec{\beta}}|^2}{(1-\beta\cos\theta)^3}\left[1-\frac{\sin^2\theta\cos^2\phi}{\gamma^2(1-\beta\cos\theta)^2}\right] \tag{2.3}$$

where I have considered instantaneously $\vec{\beta}$ and $\dot{\vec{\beta}}$ in the z and x directions, respectively. The equation shows two main results: the radiation pattern is highly beamed in the velocity direction when $\beta \to 1$ ($\langle\theta^2\rangle^{1/2} \propto 1/\gamma$) and the radiation is dominated in amplitude by high-velocity charged particles.

2.1.2 The emission pattern as a function of frequency

I have derived the emission pattern from a circularly accelerated charged particle. I now focus on a frequency treatment in order to understand the radio spectra coming from extragalactic

radio sources. This can be done using Fourier transform arguments. The general form for the energy radiated by an accelerated charged particle per unit of frequency and per unit of solid angle is given by:

$$\frac{dW}{d\omega d\Omega} = \frac{e^2}{4\pi^2 c}\left|\int_{-\infty}^{\infty} e^{i\omega(t-\hat{n}\cdot\vec{r}(t)/c)}\ \left[\hat{n}\times(\hat{n}\times\vec{\beta})\right]\ dt\right|^2 \tag{2.4}$$

where W is the energy (time-integrated power) and $\vec{r}$ is a vector which defines the dynamic for the charge relative to a local system of reference. The previous expression assumes the direction of the Poynting vector does not change in time, which is basically a small-angle approximation based on very distant objects (see Jackson 1999 for more details).

To find the energy distribution for a charged particle in circular motion it is necessary to solve the integral in Eq. (2.4).

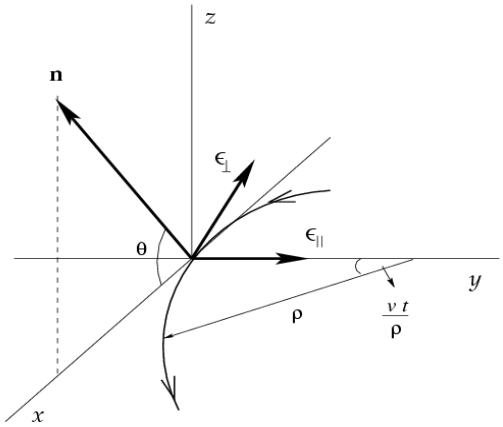

Figure 2.1: Useful coordinate system to describe the radiation pattern of a relativistic charged particle in an accelerated circular motion.

To tackle this problem, I define the coordinate system shown in Fig. 2.1. This new orthonormal system of reference $(\hat{n}, \hat{\epsilon}_\parallel, \hat{\epsilon}_\perp)$ is very useful because it naturally indicates the polarisation of the emission. The charge moves through the curved path with an angular velocity v/ρ defining a velocity $\vec{\beta} = \beta(\sin(vt/\rho)\hat{\epsilon}_\parallel - \sin\theta\cos(vt/\rho)\hat{\epsilon}_\perp)$.

Based on Eq. (2.3) and considering the relativistic regime, $\beta \to 1$ ($t \propto \gamma^{-1}$, $\theta \propto \gamma^{-1}$ and $\beta \approx 1-\gamma^{-2}$), I can assume all the emission is concentrated into a narrow cone whose opening angle is inversely proportional to the factor γ in the velocity direction. The radiation pattern is, therefore, composed of short bursts of emission, $\Delta t = \frac{\rho}{2\gamma v}$, occurring at snapshots determined by the period of rotation $T = \frac{2\pi\rho}{v}$.

The energy radiated per unit of frequency and per unit of solid angle can be expressed as

$$\begin{aligned}\frac{dW}{d\omega d\Omega} =& \frac{dW_{\parallel}}{d\omega d\Omega} + \frac{dW_{\perp}}{d\omega d\Omega} \\ =& \frac{e^2}{3\pi^2 c}\left(\frac{\omega\rho}{c}\right)^2\left(\frac{1}{\gamma^2}+\theta^2\right)^2\left[K_{2/3}^2(\xi) + \frac{\theta^2}{1/\gamma^2+\theta^2}K_{1/3}^2(\xi)\right]\end{aligned} \tag{2.5}$$

where

$$\begin{aligned}K_{2/3}(\xi) =& \sqrt{3}\int_0^{\infty} x\sin\left(\frac{3}{2}\xi\left(x+\frac{x^3}{3}\right)\right)dx \\ K_{1/3}(\xi) =& \sqrt{3}\int_0^{\infty} \cos\left(\frac{3}{2}\xi\left(x+\frac{x^3}{3}\right)\right)dx \\ \xi =& \frac{\omega\rho}{3c}\left(\frac{1}{\gamma^2}+\theta^2\right)^{3/2}.\end{aligned} \tag{2.6}$$

The first term from Eq. (2.5) corresponds to radiation polarised in the plane of the orbit $\left(\frac{dW_{\parallel}}{d\omega d\Omega}\right)$, while the second is the polarisation perpendicular to that plane $\left(\frac{dW_{\perp}}{d\omega d\Omega}\right)$.

2.1.3 An electron rotating around a magnetic field

I have not explicitly discussed the origin of the circular motion. This acceleration is given by the Lorentz Force, where parameter ρ (the gyro-magnetic radius) hides the dependency on the magnetic field.

I assume the coordinate system from Fig. 2.1, but also allow a linear velocity in the z direction, which introduces a new parameter, the pitch angle, α, defined by the direction of the magnetic field and the z-velocity of the particle. Since the emission pattern is highly beamed in the velocity direction (Eq. 2.3), I assume most of the emission, in one cycle of the particle, is confined to the cone created by the pitch angle rotated by 2π. Therefore, the energy per unit of frequency emitted over one cycle around the magnetic field is given by

$$\frac{dW}{d\omega} = \int_{-\infty}^{\infty}\left(\frac{dW_{\parallel}}{d\omega d\Omega} + \frac{dW_{\perp}}{d\omega d\Omega}\right)2\pi\sin\alpha d\theta \tag{2.7}$$

where the infinite integration limits are permissible and convenient, because the integrand is confined to small values of θ about α (of the order of $1/\gamma$). Integrating the previous equation, I find

$$\begin{aligned}\frac{dW_{\parallel}}{d\omega} &= \frac{\sqrt{3}e^2\gamma\sin\alpha}{2c}\left[F(x)+G(x)\right] \\ \frac{dW_{\perp}}{d\omega} &= \frac{\sqrt{3}e^2\gamma\sin\alpha}{2c}\left[F(x)-G(x)\right], \\ \Rightarrow \quad \frac{dW}{d\omega} &= \frac{\sqrt{3}e^2\gamma\sin\alpha}{c}F(x)\end{aligned} \tag{2.8}$$

where

$$
\begin{aligned}
F(x) &= x \int_x^{\infty} K_{5/3}(z) dz \\
G(x) &= x K_{2/3}(x) \\
\text{and} \quad x &= \frac{\omega}{\omega_c} = \frac{2\omega\rho}{3c\gamma^3}.
\end{aligned}
\tag{2.9}
$$

The integration has been carried out over only one cycle of the orbiting particle, therefore the emitted power per unit frequency is obtained dividing Eq. (2.8) by the orbital period. I use the Lorentz force to define $T = 2\pi/\omega_B = 2\pi\frac{\gamma m_e c}{eB}$, and thus the power per unit of frequency is given by

$$
\frac{dP}{d\omega} = \frac{1}{T}\frac{dW}{d\omega} = \frac{\sqrt{3}e^3 B \sin\alpha}{2\pi m_e c^2} F(x). \tag{2.10}
$$

Remember that $x = \frac{\omega}{\omega_c}$, and it takes the form $x \approx \frac{2\omega m_e c}{3eB\gamma^2 \sin\alpha}$ in the relativistic case ($v \approx c$). It is worth noting that this is the theoretical prediction for the synchrotron radiation coming from one single charged particle (see Fig. 2.2).

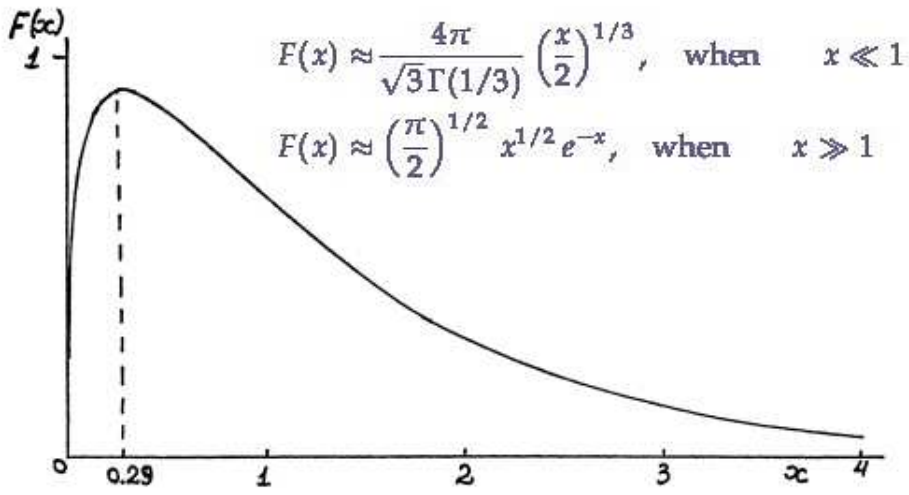

Figure 2.2: The function, $F(x)$, describing the radiated spectrum of synchrotron emission. Figure from Ginzburg & Syrovatskii (1965).

If I integrate over frequency, considering $dx = d\omega/\omega_c$, I obtain the total power radiated by the particle

$$
\begin{aligned}
-\frac{dE}{dt} &= \int_0^\infty \frac{dP}{d\omega} d\omega = \frac{\sqrt{3} e^3 B \sin\alpha\, \omega_c}{2\pi m_e c^2} \int_0^\infty F(x) dx \\
&= \left(\frac{B^2}{8\pi}\right) \left(\frac{8\pi e^4}{3 m_e^2 c^4}\right) c\gamma^2 \sin^2\alpha \left(\frac{9\sqrt{3}}{4\pi}\right) \int_0^\infty F(x) dx \\
&= 2\, \sigma_T\, c\, U_{\mathrm{mag}} \gamma^2 \sin^2\alpha
\end{aligned}
\tag{2.11}
$$

where σ_T is the Thompson scattering cross-section and U_{mag} is the total energy of the magnetic field.

2.1.4 Emission from an electron energy distribution

I am interested in extrapolating these results to an ensemble of electrons. It has been found that an electron power-law energy distribution is in accordance with observations. The origin of this electron energy distribution is controversial. Bell (1978) showed that shock waves can be responsible for this distribution of highly energetic electrons, based on sufficiently energetic electrons bouncing back and forth several times in shock wave discontinuities. This process is called Fermi acceleration (Fermi 1949) and could explain an electron power law energy distribution. On the other hand, Ramadurai & Biswas (1972) show that there are difficulties in reproducing a straight-forward power-law energy distribution in the mildly-relativistic case.

Nevertheless, let us assume

$$
N(E) dE = C E^{-p} dE \tag{2.12}
$$

where $N(E)dE$ is defined as the number of electrons per unit volume in the energy interval E to $E + dE$. Inserting a distribution of electrons in Eq. (2.10), considering $E = \left(\frac{2\omega m_e^3 c^5}{3eBx \sin\alpha}\right)^{1/2}$ (i.e. $E = \gamma m_e c^2$), then integrating over α assuming a randomly orientated pitch angle with respect to the magnetic field, yields

$$
\frac{dP}{d\omega} = \frac{\sqrt{3} e^3 C B}{2\sqrt{\pi} m_e c^2 (p+1)} \left(\frac{\omega m_e^3 c^5}{3eB}\right)^{-\frac{1}{2}(p-1)} \frac{\Gamma\left(\frac{p}{4} + \frac{19}{12}\right) \Gamma\left(\frac{p}{4} - \frac{1}{12}\right) \Gamma\left(\frac{p}{4} + \frac{5}{4}\right)}{\Gamma\left(\frac{p}{4} + \frac{7}{4}\right)}. \tag{2.13}
$$

This means that the synchrotron emission from an isotropic distribution of relativistic electrons is proportional to $B^{\frac{1}{2}(p+1)} \omega^{-\frac{1}{2}(p-1)}$, where p is the power index for the electron energy distribution. In multi-frequency radio observations, the radio spectral index is commonly defined as $\alpha = (1-p)/2$, which provides a parameterisation for the observed flux density: $S_\nu \propto \nu^\alpha$ (see Fig. 2.6).

2.1.5 Synchrotron self-absorption

According to the principle of detailed balance, for every emission process there is a corresponding absorption process. In the case of synchrotron radiation, this process is known as

synchrotron self-absorption. It can be demonstrated (see Rybicki & Lightman 1979 or Longair 1994 for more details) that the absorption coefficient can be defined by

$$\alpha_\nu = \frac{h\nu}{4\pi} \sum_{E_1} \sum_{E_2} \left[n(E_1) B_{12} - n(E_2) B_{21} \right] \phi_{21}(\nu) \tag{2.14}$$

where n is the particle density, B_{12} and B_{21} are the Einstein coefficients for absorption and induced emission, respectively, and $\phi_{21}(\nu) = \delta(E_2 - E_1 = h\nu)$, a delta function for the energy transition. The process is assumed to be isotropic. In the relativistic case ($E = pc$), the number of electrons per unit of volume is given by $n(E) = \frac{4\pi}{c^3} \frac{N(E)}{E^2}$ (based on $n(p) 4\pi p^2 dp = N(E) dE$), therefore

$$\alpha_\nu = \frac{c^2}{8\pi\nu^3 h} \int E^2 \left[\frac{N(E - h\nu)}{(E - h\nu)^2} - \frac{N(E)}{E^2} \right] P(\nu, E) dE \tag{2.15}$$

where energy is a continuous variable now. Since I have assumed relativistic motions ($E >> h\nu$), I can expand the last equation to first order to obtain

$$\alpha_\nu = -\frac{c^2}{8\pi\nu^2} \int E^2 \frac{d}{dE} \left(\frac{N(E)}{E^2} \right) P(\nu, E) dE. \tag{2.16}$$

Inserting Eq. (2.12), I define the absorption coefficient as a function of energy for a spatially isotropic electron energy distribution

$$\alpha_\nu = -\frac{c^2 (p+2)}{8\pi\nu^2} \int \frac{N(E)}{E} P(\nu, E) dE. \tag{2.17}$$

Integrating Eq. (2.17) over energy, and considering $P(\nu, E) = \frac{\sqrt{3} e^3 B \sin\alpha}{mc^2} F(\nu/\omega_c)$ – note that $F(\omega/\omega_c) = 2\pi F(\nu/\omega_c)$ – the absorption coefficient is given by

$$\alpha_\nu = \frac{\sqrt{3} e^3 C}{16\sqrt{\pi} m_e} \left(\frac{3e}{2\pi m_e^3 c^5} \right)^{p/2} \frac{\Gamma\left(\frac{p}{4} + \frac{11}{6}\right) \Gamma\left(\frac{p}{4} + \frac{1}{6}\right) \Gamma\left(\frac{p}{4} + \frac{3}{2}\right)}{\Gamma\left(\frac{p}{4} + 2\right)} \cdot \\ \times (B \sin\alpha)^{\frac{1}{2}(p+2)} \nu^{-\frac{1}{2}(p+4)} \tag{2.18}$$

This implies that the source function as a function of frequency is given by

$$S_\nu = \frac{P(\nu)}{4\pi\alpha_\nu} \propto \nu^{\frac{1}{2}(p+4)} \nu^{\frac{1}{2}(p-1)} \propto \nu^{5/2}. \tag{2.19}$$

In the synchrotron self-absorption process, the spectral energy distribution (SED) does not depend on the power index, p, so observational information about the mechanism for cosmic ray production is scarce.

2.1.6 Ageing effects in radio emission

Observations of powerful active galactic nuclei (AGN) with extended radio lobes (e.g. see Fig. 1.1) have found flatter radio spectra in hotspots than in the diffuse, faint emission around

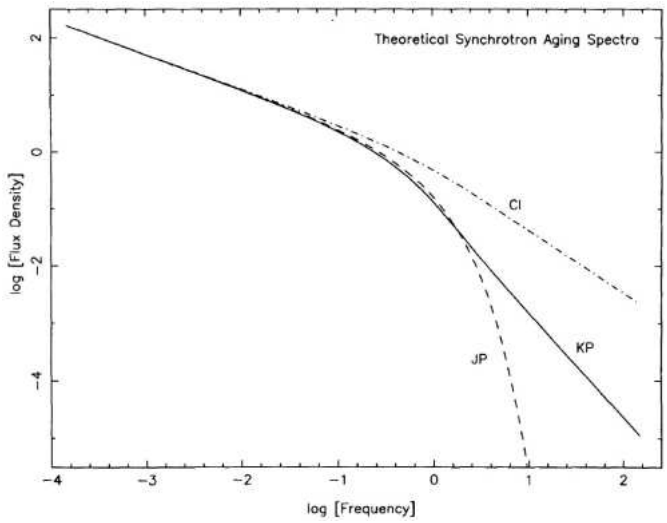

Figure 2.3: Examples for three radio SED models: continuous injection model (dot-dashed line – Carilli et al. 1991), the Jaffe & Perola (1973) model (dashed line) and the Kardashev-Pacholczyk model (solid line – Kardashev 1962 and Pacholczyk 1970). Image from Carilli et al. (1991).

them – the spectra become progressively steeper as we move away from the hotspots (e.g. Burch 1979; Alexander & Leahy 1987; Liu et al. 1992).

A basic jet model for radio sources explains this effect as being due to relativistic electrons moving away from a central AGN. Hotspots are evidence for a recent interaction of the relativistic jets with the surrounding media, and the diffuse emission can be considered as the residue of this interaction. In this process, highly energetic particles lose their energy (e.g. Eq. 2.11) faster than the low-energy particles (Carilli et al. 1991), producing a spectral break where the spectrum becomes steeper than the injected power law (see Fig. 2.3).

Many observations have supported the basic jet model for extended radio sources (Burch 1979; Alexander 1985; Alexander & Leahy 1987; Stephens 1987). Typical velocities for the radiating fluid in radio lobes measured by synchrotron ageing models range from 0.02 to 0.2 times the speed of light. For example, observations of the famous local radio source, Cygnus A, yield a source age of 6 Myr with a jet velocity in the radio lobes of $0.03\,c$ (Winter et al. 1980).

The connection between radio spectrum and age allows a study of the growth and evolution of the lobes by careful measurement of the spectrum throughout the length and width of the source. Assuming a particle distribution that is initially power-law in energy, and isotropic in pitch angle, and resides in an isotropic magnetic field (at resolution scales), the age of the radio emission can be estimated using (from Carilli et al. 1991):

$$t_s \approx 1610\, B^{-3/2}\, \nu_B^{-1/2}\ \mathrm{Myr} \tag{2.20}$$

where t_s is the "synchrotron age" of the distribution since the spectrum was a power law, B the magnetic field strength in μG and ν_B the break frequency in GHz. In general, different

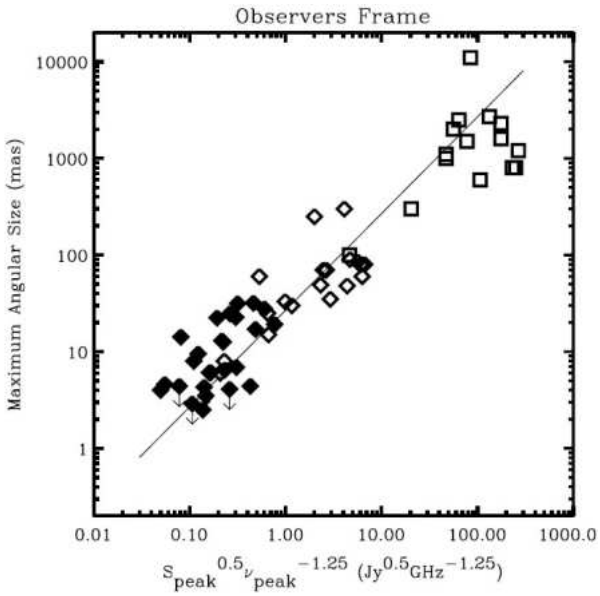

Figure 2.4: Correlation between the spectral turnover and the overall size in samples of GHz-peaked and compact, steep-spectrum sources (GPS and CSS – Snellen et al. 2000). Squares represent CSS sources and open and filled diamonds indicate bright and faint GPS sources. The line indicates a linear correlation between the two parameters. Image from Snellen et al. (2000).

approaches for modelling synchrotron ageing effects (Jaffe & Perola 1973; Pacholczyk 1970; Carilli et al. 1991) yield different frequency cut-offs, depending on a number of physical processes in the evolution of the particle distribution. The strongest dependency comes from the assumed injection mechanism for the electron power-law energy distribution.

The break frequency of the power law has been observed in bright galaxies. These are called ultra-steep-spectrum (USS) sources and are good tracers of high-redshift ($z > 2$) galaxies (Rottgering et al. 1994; Chambers et al. 1996; Jarvis et al. 2001). The principal difficulty with the study of synchrotron ageing in radio galaxies is that the high-frequency steepness occurs over a very broad range in frequency. Hence, proper analysis of the radio spectrum of extended extragalactic radio sources requires sensitive observations to be made over a broad range of frequencies. Another difficulty is that the spectrum varies with position, therefore observations at all frequencies must be spatially resolved and with well-matched spatial resolutions.

2.1.7 Size predictions

In accordance with the synchrotron absorption process and depending on the surrounding medium, it is possible to estimate the size of a radio source by measuring the peak frequency, ν_p, where the optically thick to thin transition occurs in the SED (see Figure 2.6). Based on

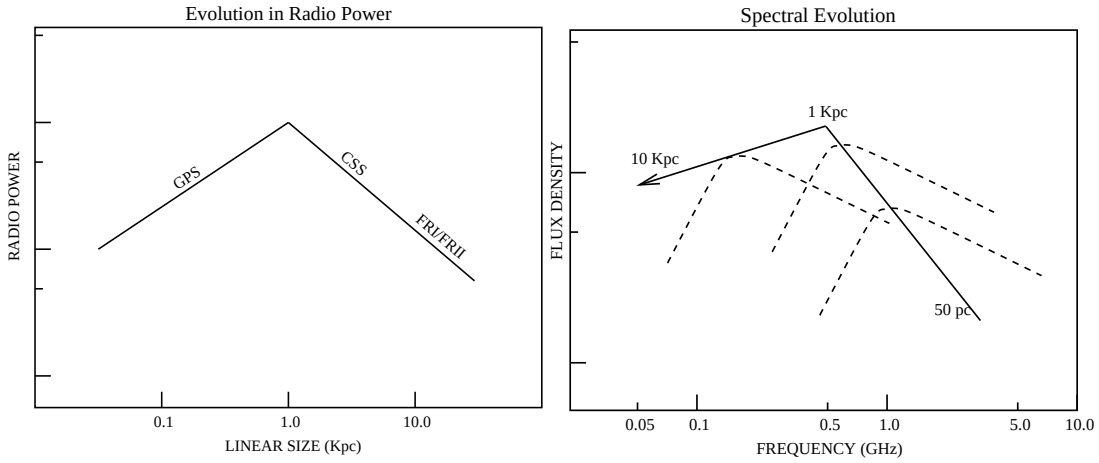

Figure 2.5: The evolution in radio power (*left*) and the SED (*right*) as a function of linear size assuming self-similar evolution for the sources and a surrounding medium given by a King profile (Trinchieri et al. 1986). Images from Snellen et al. (2000).

the self-absorption theory described in § 2.1.5 it is expected that the angular size, θ, of a radio source is proportional to (Kellermann & Pauliny-Toth 1981; Snellen et al. 2000):

$$\theta \propto B^{1/4} S_p^{1/2} (1+z)^{1/4} \nu_p^{-5/4} \tag{2.21}$$

where B is the magnetic field strength, S_p is the peak flux density (at which the optical depth, $\tau \approx 1$) and z is the redshift. Note that θ is weakly dependent on both B and z. This simple prediction is in agreement with the observed linear correlation (Fig. 2.4) between the maximum angular size and $S_p^{1/2} \nu_p^{-5/4}$ presented by Snellen et al. (2000). The maximum angular size refers to the furthest distance between the source components – sidelobes for AGN.

Based on high-resolution radio observations, Snellen et al. (2000) analysed a sample of so-called GHz-peaked sources (GPS) and compact, steep-spectrum sources (CSS; O'Dea 1998), and suggested these are young, expanding radio sources, with dynamical ages of $\sim 10^3 - 10^5$ yr. It was proposed that all GPS galaxies evolve into large-scale (FR II) radio galaxies and, thus, all large-scale radio galaxies were GPS in the past (Snellen et al. 2000). The surrounding medium (the interstellar density profile) is an important parameter in estimating the luminosities of these sources while they expand in linear size. A sketch of the expected jet-like radio power in interaction with a King density profile (Trinchieri et al. 1986) – a profile based on X-ray observations of the interstellar media in local elliptical galaxies – is shown in Fig. 2.5. The model predicts that the synchrotron emission is expected to be observed with self-absorption signatures at $\sim$ GHz if the source has a scale smaller than ~ 1 kpc (GPS).

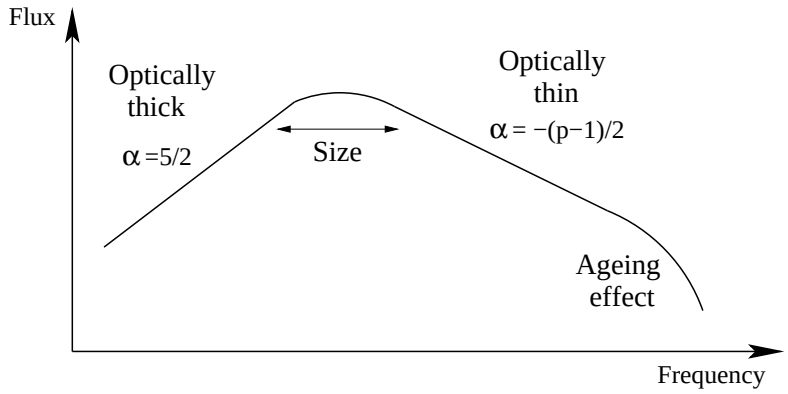

Figure 2.6: Schematic SED for optically thick and thin Synchrotron emission processes. At low and high frequencies the spectral flux distribution follows $S_\nu \propto \nu^{5/2}$ and $\propto \nu^{-(p-1)/2}$ respectively.

2.1.8 The synchrotron spectrum

The astrophysical synchrotron process is the one that dominates the very low-frequency end of the electromagnetic spectrum ($\lesssim 30\,\mathrm{GHz}$). Previously, I have described the emission coming from an ensemble of relativistic electrons with a power-law energy distribution in a randomly oriented magnetic field as a function of frequency, in both the optically thin and optically thick cases. Fig. 2.6 shows a simple sketch of the expected theoretical SED at radio wavelengths.

I have also shown how other parameters such as life-time dependencies or environmental properties may change the SED of the synchrotron radiation.

There are two major extragalactic radio populations that produce synchrotron radiation: star-forming galaxies and AGN. Condon (1992) has shown that star-forming galaxies have a very tight distribution in radio spectral index, $\alpha \approx -0.7$, implying a common nature for the origin of the electron energy distribution in these galaxies. This may support the Fermi acceleration as an universal mechanism of cosmic ray production. Synchrotron radio emission in star-forming galaxies is, therefore, evidence of relativistic charged particles accelerated by supernovae remnants and trapped in magnetic fields. Based on studies of local radio galaxies it is possible to identify two main galactic synchrotron components, one associated directly with supernovae and the second with extended emission where cosmic rays have diffused across the galaxy. It is worth noting that in star-forming galaxies the other important radio emission mechanism is bremsstrahlung (thermal, free-free or braking radiation), characterised by a spectral index, $\alpha \approx -0.1$, when optically thin. However, this thermal emission is overwhelmed by synchrotron radiation at frequencies below $\sim 30\,\mathrm{GHz}$ (Condon 1992).

On the other hand, the magnificent radio jets observed in AGN are evidence of highly collimated flows of charged particles interacting with a trapped and twisted magnetic field. The material is expelled as a jet from the nuclear region of an active galaxy (see Fig. 1.1).

2.2 Interferometric synthesis imaging

Interferometry is a technique to diagnose properties from multiple waves using the pattern of interference created by their superposition. Early development of interferometry were done by radio astronomers, mostly after World War II. Historically, radio astronomy was initiated by Karl Guthe Jansky (Jansky 1933) who proposed for first time the extraterrestrial origin of radio emission.

The main property of radio wavelengths for creating interference is the frequency bandwidth, which is relatively long ($\sim 10^6$ Hz) compared with other spectral ranges (e.g. $\sim 10^{12}$ Hz in the optical). In other words, it provides a coherence length sufficiently long to be able to obtain interference from distant signals connected by wires. In the simple case of two antennae, signals can be easily transported, preserving voltage and phase information, then combined in a correlator to produce diffraction patterns.

In the following sections I introduce the basic concepts and the commonly considered assumptions for the imaging of distant, astrophysical radio sources using radio interferometry. I outline a simplified theoretical treatment in order to describe the physical parameters which can be obtained from radio observations.

2.2.1 Radio interferometry

The propagating fields coming from relativistic electrons rotating around magnetic fields can be observed using antennae and analysed after electronic calibration (see Taylor et al. 1999 for more details). In the following treatment, I make two main assumptions: receptors take time-averaged signals over relatively long integration times to be able to neglect the short-time variability of the incoming radiation fields, and polarisation effects are not taken into account since the response can be made arbitrarily close to monochromatic by inserting filters after the reception of the signals.

A well-known problem in radio astronomy is that it is impossible to obtain information in the depth-distance dimension. In fact, all we can measure from radio sources is their "surface brightness", which is the integrated emission along the line of sight. Without any loss of generality I define a "celestial sphere", a very large sphere of radius $|\vec{R}|$, to define the spatial distribution for the electric field in this two-dimensional sphere, $\vec{\xi}_\nu(\vec{R})$. I define $\vec{R}$ as the distance to the astrophysical source, and $\vec{r}$ as the position of the observer. The interaction of the electromagnetic field $E_\nu(\vec{R})$ at the observer's antenna is given by:

$$E_\nu(\vec{r}) = \int \frac{e^{2\pi i \nu |\vec{R}-\vec{r}|/c}}{\left|\vec{R}-\vec{r}\right|} \vec{\xi}_\nu(\vec{R})\, dS, \tag{2.22}$$

where

$$\vec{\xi}_\nu(\vec{R}) = \int E(\vec{R}) dz, \tag{2.23}$$

and dS is the element of surface area on the "celestial sphere".

These electromagnetic fields can be measured at different locations ($\vec{r_1}$ and $\vec{r_2}$) and then correlated. This is where all radio interferometry starts.

The expected value of a correlation, assuming the radiation is not spatially coherent, is given by:

$$\begin{aligned} V_\nu(\vec{r_1},\vec{r_2}) &= \langle E_\nu(\vec{r_1}) E_\nu^*(\vec{r_2}) \rangle \\ &= \int \left\langle \left| \vec{\xi}_\nu(\vec{R}) \right|^2 \right\rangle \left| \vec{R} \right|^2 \frac{e^{2\pi i \nu \left| \vec{R}-\vec{r_1} \right| / c}}{\left| \vec{R}-\vec{r_1} \right|} \frac{e^{-2\pi i \nu \left| \vec{R}-\vec{r_2} \right| / c}}{\left| \vec{R}-\vec{r_2} \right|} \, dS \end{aligned} \tag{2.24}$$

where the brackets represent the expected value.

I write $\vec{s} \equiv \vec{R}/|\vec{R}|$ (see Fig. 2.7) and calculate the "observed intensity" as $\left\langle |\vec{\xi}_\nu(\vec{R})|^2 \right\rangle |\vec{R}|^2$. It is common to introduce a normalisation factor, A_ν, which takes into account that interferometers are not ideal receptors, and indeed they have a finite size and efficiency for detecting radiation as a function of frequency and direction. I replace the surface element dS by $|\vec{R}|^2 d\Omega$, and I take an approximation at first order in $\vec{r}/\,|R|$ for the exponential part of Eq. (2.24), i.e. $|\vec{R}-\vec{r_1}| - |\vec{R}-\vec{r_2}| \approx \vec{s}\cdot(\vec{r_2}-\vec{r_1}) \equiv \vec{s}\cdot\vec{b}$. It yields:

$$V_\nu(\vec{b}) \approx \int \mathcal{A}_\nu(\vec{s}) I_\nu(\vec{s}) \, e^{-2\pi i \nu \vec{s}\cdot\vec{b}/c} d\Omega, \tag{2.25}$$

where $\vec{b}$ represent the baseline vector, $\mathcal{A}_\nu(\vec{s}) = A_\nu(\vec{s})/A_{\nu 0}$ is the "normalised reception pattern" with respect to the centre of the beam, and $V_\nu(\vec{b})$ is called the "spatial coherence function" or the "spatial autocorrelation function" of the field, $E_\nu(\vec{r})$.

An interferometer is a device for measuring this spatial coherence function.

In general, the interferometers in which I am interested are composed of antennae which can track sources, and so the privileged coordinate system is centred in the track position as shown in Fig. 2.7. In the figure, $\vec{s_0}$ is the so-called "nominal source position".

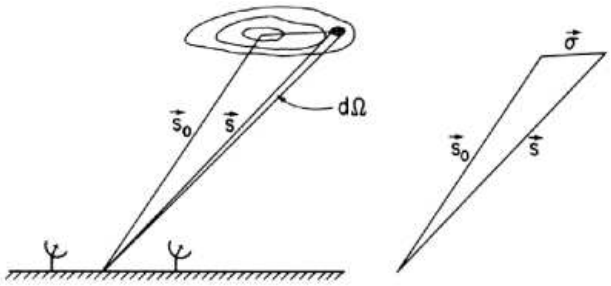

Figure 2.7: Schematic definition for the vectors used for deriving the radio-frequency response. Figure from Taylor et al. (1999).

Let us take into account a small field of view, $|\vec{\sigma}| \ll 1$, and define the vectors $\vec{s} = \vec{s_0} + \vec{\sigma} =$

$(l, m, 1)$, where $\vec{\sigma}$ is perpendicular to $\vec{s_0}$ and sufficiently small to approximate $|\vec{s}| \approx 1$. I express the baseline vector in wavelength units $\vec{b} = \lambda(u, v, w)$ to obtain,

$$V_\nu(\vec{b}) = e^{-2\pi i w} \int \mathcal{A}_\nu(l, m) I_\nu(l, m)\, e^{-2\pi i(ul+vm)} dl dm \tag{2.26}$$

It is common to define $V_\nu^T(u, v) = V_\nu(\vec{b}) e^{2\pi i \nu\, \vec{s_0}\cdot\vec{b}/c} = V_\nu(u, v, w) e^{2\pi i w}$ as the "complex visibility" relative to the chosen phase tracking centre,

$$V_\nu^T(u, v) = \int \mathcal{A}_\nu(l, m) I_\nu(l, m)\, e^{-2\pi i(ul+vm)} dl dm. \tag{2.27}$$

Note, this equation takes the simple form of a 2-dimensional Fourier transform, which allows us to obtain the observed surface brightness after simply inverting Eq. (2.27):

$$\mathcal{A}_\nu(l, m) I_\nu(l, m) = \int V_\nu^T(u, v)\, e^{2\pi i(ul+vm)} du dv. \tag{2.28}$$

This simple result is the basis for all interferometric synthesis imaging. Later, I discuss some observational issues arising from this simple Fourier inversion relating to non-monochromatic radiation, large fields of view, integration times and antennae responses.

2.2.2 An interferometer

It is necessary to introduce some technical details. Let us define the geometrical time delay (τ_g) produced by the arrival of a wavefront to two different antennae at different times,

$$\tau_g = \vec{s} \cdot \vec{b}\ / c, \tag{2.29}$$

where $\vec{s}$ and $\vec{b}$ are the same vectors defined before. This time delay is a function of the baseline and the rotation of the Earth, and provides a direct measurement of the interference fringes.

In a simple view of the electronic system – an antenna – used to detect radio signals, it is composed of an amplifier, with a well-defined bandwidth, $\Delta\nu$, and a filter for the polarisation of interest. These signals are combined in a "correlator", which is a multiplier followed by a time-averaging (integrating) electronic system. If I define $V_1(t)$ and $V_2(t)$ as the input signals to the correlator, it yields an output proportional to $\langle V_1(t) V_2(t) \rangle$, where the brackets represent the combined signal averaged in time. The received signals, after converted to voltage responses, can be treated using Fourier components of the form $V_1(t) = v_1 \cos\left(2\pi\nu\ (t - \tau_g)\right)$ and $V_2 = v_2 \cos(2\pi\nu t)$. In general, there are two independent signals, a cosine and a sine component, but in this case I just show one of them for simplicity. The output from the correlator is then defined by

$$r(\tau_g) = \frac{2}{1/\nu} \int_0^{1/\nu} V_1(t) V_2(t) dt = v_1 v_2 \cos(2\pi\nu\tau_g). \tag{2.30}$$

Slow variations in τ_g will be given by the Earth's rotation, and a fringe pattern will be produced by the cosine factor. These patterns are controlled by all radio interferometers.

Let us define the radio surface brightness integrated over the sky as a function of the frequency and direction, $I_\nu(\vec{s})$. An identical and ideal response for a pair of antennas yields the received power per bandwidth from a source element $d\Omega$ given by $A_\nu(\vec{s})I_\nu(\vec{s})\Delta\nu d\Omega$, where $A_\nu(\vec{s})$ is the antenna pattern response along the line of sight. In terms of baseline and source position vectors I define

$$r = \Delta\nu \int A_\nu(\vec{s}) I_\nu(\vec{s}) \cos(2\pi\nu\, \vec{s}\cdot\vec{b}/c) d\Omega. \tag{2.31}$$

The angular distribution is over 4π, although in practice the integration is over a small angular section where the source is defined. I assume that $\Delta\nu$ is sufficiently small to consider negligible variations in A and I as a function of ν – monochromatic radiation. Since the source is sufficiently far away, we can consider plane wavefronts (note this is not completely true for Solar observations). I also assume that the intrinsic radiation from the source is spatially incoherent, which means two points in the sky should not be correlated anyhow. I replace $\vec{s} = \vec{s_0} + \vec{\sigma}$ in Eq. (2.31):

$$\begin{aligned} r = {} & \Delta\nu \cos(2\pi\nu\, \vec{s_0}\cdot\vec{b}/c) \int A_\nu(\vec{\sigma}) I_\nu(\vec{\sigma}) \cos(2\pi\nu\, \vec{\sigma}\cdot\vec{b}/c)\, d\Omega \\ & - \Delta\nu \sin(2\pi\nu\, \vec{s_0}\cdot\vec{b}/c) \int A_\nu(\vec{\sigma}) I_\nu(\vec{\sigma}) \sin(2\pi\nu\, \vec{\sigma}\cdot\vec{b}/c)\, d\Omega \end{aligned} \tag{2.32}$$

and identify terms between Eqs. (2.27) and (2.32), to obtain:

$$\begin{aligned} r &= A_{\nu 0}\Delta\nu \left|V_\nu^T\right| \cos\left(\frac{2\pi\nu\, \vec{s_0}\cdot\vec{b}}{c} - \phi_V\right) \\ &= A_{\nu 0}\Delta\nu \left|V_\nu^T\right| \cos\left(2\pi w - \phi_V\right). \end{aligned} \tag{2.33}$$

where I define $V_\nu^T = \left|V_\nu^T\right| e^{i\phi_V}$. When interpreting interferometric measurements, the usual procedure is to measure the amplitude and phase of the fringe pattern as represented by the cosine term in Eq. (2.33), and then derive the amplitude and phase of V_ν^T by appropriate calibration. The brightness distribution of the source is obtained from the visibility data by a Fourier transform inversion of Eq. (2.27).

Finally we can consider a simple example. Let us assume a non-ideal receiving system with a frequency passband, $f(\nu)$. Consider an infinitesimal bandwidth, $d\nu$, and replacing it in Eq. (2.33), I obtain

$$r = A_{\nu 0} \left|V_\nu^T\right| \int_{\nu_0-\Delta\nu/2}^{\nu_0+\Delta\nu/2} f(\nu) \cos\left(2\pi\nu\tau_g - \phi_V\right) d\nu. \tag{2.34}$$

If I consider a square bandpass response such as

$$f(\nu) = \begin{cases} 1 & \text{if} \quad \nu_0 - \Delta\nu/2 < \nu < \nu_0 + \Delta\nu/2 \\ 0 & \text{elsewhere} \end{cases}, \tag{2.35}$$

I obtain

$$r = A_{\nu 0} \left| V_\nu^T \right| \Delta\nu \frac{\sin(\pi\Delta\nu\tau_g)}{\pi\Delta\nu\tau_g} \cos\left(2\pi\nu_0\tau_g - \phi_V\right), \tag{2.36}$$

where the solution is finally weighted by a *sinc* function.

2.2.3 Interferometric radio arrays

The treatment shown here has been based on the simplest case – two correlated antennae. However in the real world the interferometers of interest (Fig. 2.11) have approximately 30 independent antennae, implying a large number of ($\gtrsim 400$) different baselines. The National Radio Astronomy Observatory (NRAO) has developed software to manipulate the information from many baselines (e.g. flagging, calibration, imaging, source extraction), named the Astronomical Image Processing System, $\mathcal{AIPS}$ (see Appendix B for more details about the use of this software).

In practice, all baselines use the rotation of the Earth to generate a larger coverage of u and v data in the so-called uv plane. The more coverage in the uv plane, the better the deconvolution and the better the image. The resulting deconvolved image has an angular coverage of $\theta_{\text{primary}} \sim \lambda/D$ (the "primary beam"), where D is the diameter of the antennae. The maximum resolution is given by $\theta_{\text{syn}} \sim \lambda/B$, where B is the largest baseline from the array.

Ideally, all baselines provide unbiased data, but at low frequencies ($\lesssim 1\,\text{GHz}$) the shortest baselines ($\lesssim 0.8\,\text{k}\lambda$) are often affected by man-made interference and must often the discarded.

In the following sections, I present some of the common issues found in the 2-D Fourier deconvolution of the uv plane.

2.2.4 Instrumental effects

In previous sections I have shown the theories that make it possible to detect extragalactic radio signals using interferometry. Note, however, a large number of assumptions have been made in this treatment. Since interferometric telescopes are not ideal receptors, I discuss some issues that often arise.

There are four main instrumental effects that must be taken into account when analysing low-frequency radio observations covering wide fields of view.

Bandwidth smearing

This smearing effect is the result of channels with finite bandwidth being used in a 2-D Fourier transform inversion which assumes monochromatic radiation (see Eq. 2.36).

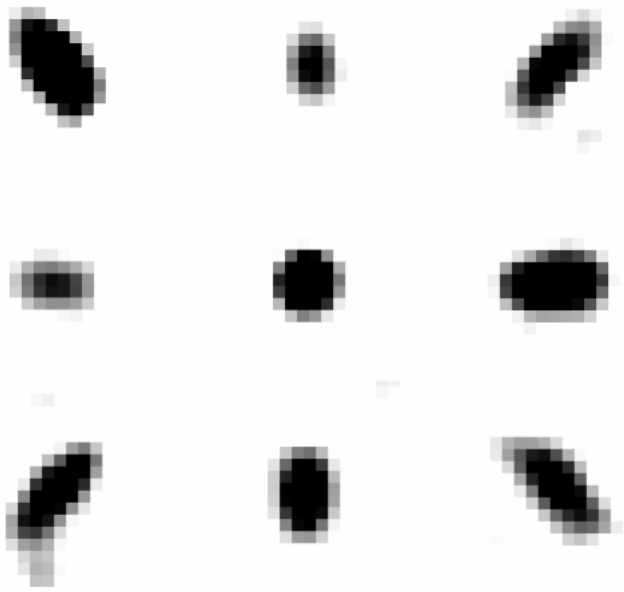

Figure 2.8: The effect of bandwidth smearing as a function of location with respect to the pointing centre. These images are based on point-like sources ($1.7 \times 1.6\,\mathrm{arcsec}^2$ FWHM) detected in the GOODS-North field using the VLA in its "A" configuration at 1.4 GHz (Morrison et al. 2008, *in preparation*). Sources are separated from the pointing centre (the central source) by ~ 20 arcmin. The greyscale ranges from 0 to 1 mJy.

Different approaches to estimate this bias can be seen in Taylor et al. (1999). I summarise a few approaches for bandwidth smearing parameterised by the factor,

$$\beta = \frac{\Delta\nu}{\nu_0}\frac{\theta_0}{\theta_{\mathrm{syn}}}$$

where $\Delta\nu$ is the channel bandwidth before imaging, ν_0 the central bandwidth frequency, θ_0 the distance of the source from the pointing centre and θ_{syn} the synthesised bandwidth (point source full width half maximum). This smearing affects the shape of the source, stretching it in the direction to the pointing centre (Fig. 2.8).

In the following equations, I and I_0 are the observed and intrinsic surface brightness for point sources, respectively.

- Assuming a Gaussian bandpass and circular tapering in the uv plane:

$$\frac{I}{I_0} = \frac{1}{\sqrt{1+\beta^2}} \tag{2.37}$$

- Assuming a squared bandpass and circular Gaussian tapering:

$$\frac{I}{I_0} = \frac{\sqrt{\pi}}{\gamma\,\beta}\,\mathrm{erf}\frac{\gamma\,\beta}{2} \tag{2.38}$$

where $\gamma = 2\sqrt{\ln 2}$

- Assuming a square bandpass and square uv coverage:

$$\frac{I}{I_0} = \frac{2}{\eta\,\beta}\,\mathrm{Si}\frac{\eta\,\beta}{2} \tag{2.39}$$

where $\eta = 3.79$ and $\mathrm{Si} = \int_0^\infty (\sin\,\mathrm{t}/\mathrm{t})\mathrm{dt}$.

The smearing-related losses predicted by all of these estimates differ by less than 10 per cent as a function of β. Based on an observation in the *Hubble* Deep Field North using the Very Large Array (VLA) at 1.4 GHz, Richards (2000) showed that a parameterisation given by a Gaussian bandpass and circular Gaussian tapering provides the best fit to the bandwidth smearing effect. He measured the bandwidth smearing bias by introducing sources in the uv plane, then extracting those sources, then fitting input/output gains in peak flux. Note that this parameterisation predicts the largest reduction in peak response for point sources when $\beta \lesssim 2$.

3-D smearing

As I have shown, the general response equation for a two-element interferometer is usually approximated to a 2-D Fourier transform due to the simplicity of the inversion problem. Nevertheless, this is only valid for co-planar baselines (where the w axis lies in the direction of the celestial pole) and for sufficiently small fields of view (Taylor et al., 1999).

At low frequencies, the primary beam is large, and so the approximation from Eq. (2.27) becomes inefficient and a formal 3-D Fourier transform is required. A smearing effect is expected from the rotation of the tangential plane with respect to the celestial sphere when the separation between these two is large.

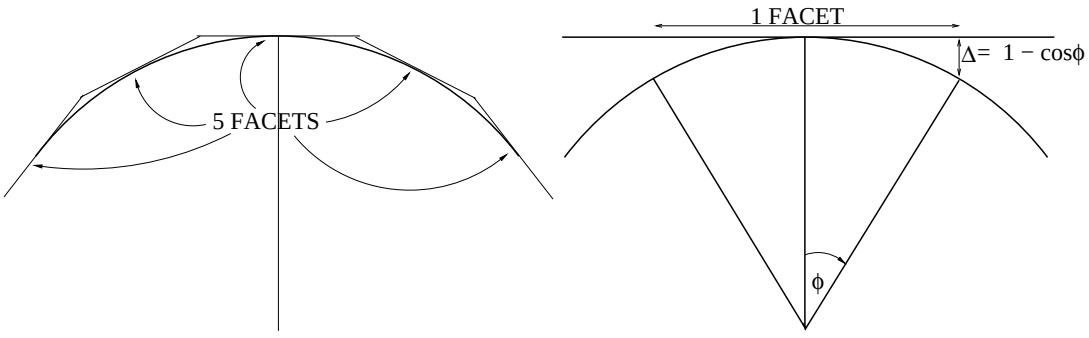

Figure 2.9: *Left:* The image shows the Polyhedron imaging approach to cover the primary beam using small patches where the inverse 2D-Fourier transform is still valid. *Right:* the separation between one facet and the celestial sphere (with an exaggerated curvature).

A solution to this problem is the so-called Polyhedron imaging approach (Taylor et al., 1999) which employs small patches to sub-divide the primary beam (a small-field approximation) so that the 2-D Fourier transform is still valid. In the analyses presented in this thesis, I have divided the primary beam into many facets in order to ensure this 3-D smearing bias is negligible; basically, $\Delta \ll \theta_{\rm syn}$, where Δ is defined in Fig. 2.9.

Time-delay smearing

This smearing effect is due to the rotation of the Earth (and therefore celestial sources too) with respect to the phase tracking centre during an integration (τ_a) – longer sampling times lead to more blurred images.

Based on theoretical assumptions from Taylor et al. (1999), the loss in peak intensity (maximal at the edge of the field of view) can be estimated by using

$$\overline{\langle R_\tau \rangle} \approx 1 - \frac{\alpha \pi^2}{12} \omega_e^2 \tau_a^2 \left(\frac{\theta}{\theta_{\rm syn}} \right)^2 \tag{2.40}$$

where $\overline{\langle R_\tau \rangle}$ is defined as the 12-hour average fractional reduction in amplitude for a source near the South or North Celestial Pole, α is a parameter determined by the baseline distribution and by weighting functions applied to the data (usually ranging from 0.24 to 0.28), θ is the distance between the source and the pointing centre, and $\theta_{\rm syn}$ is the FWHM of the synthesised beam.

The effect of time-delay smearing should be always minimised at the time that observations are made by shortening the integration, if possible.

Primary beam attenuation

The primary beam is the beam pattern associated with the collecting area (effective area) of the telescope. It is basically the Fourier transform of a circular aperture of diameter D, given by the size of the antenna, and provides the loss in gain as a function of distance from the pointing centre (see Fig. 2.10).

In general, instead of assuming an Airy-like profile, the antenna response is based on experimental measurements in order to include all possible instrumental issues that may affect the sensitivity. Near the primary beam centre, the gain is usually fitted with a polynomial function. For example, the response of the VLA at 1.4 GHz can be fitted with a tenth-order polynomial (see $\mathcal{AIPS}$ FLATN for more details), that first four terms of which are,

$$\mathrm{G}^{\rm VLA}_{\rm 1.4GHz} = 1 - 1.343\,10^{-3}\,\xi + 6.579\,10^{-7}\,\xi^2 - 1.186\,10^{-10}\,\xi^3 \tag{2.41}$$

where G is the loss in gain with respect to the pointing centre and $\sqrt{\xi}$ is the product of the distance from the pointing position in arcminutes and the frequency in GHz, i.e. $\xi = (\theta\,\nu)^2$. This polynomial fitting technique is also applied for the Giant Metrewave Radio Telescope

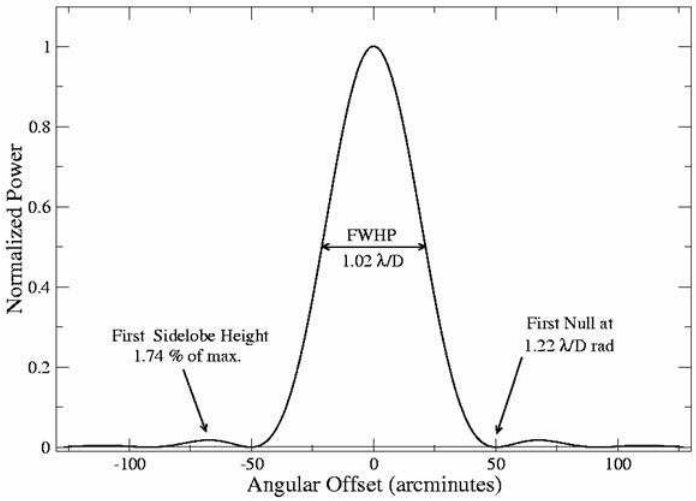

Figure 2.10: Theoretical pattern response for a 25-m-diameter antenna at 1 GHz.

(GMRT) response, although using an eighth-order polynomial fit[1] (Kantharia & Rao 2001). Using the GMRT at 610 MHz, the first five terms of primary beam response are given by

$$G^{\rm GMRT}_{\rm 610MHz} = 1 - 3.486\,10^{-3}\,\xi + 47.749\,10^{-7}\,\xi^2 - 35.203\,10^{-10}\,\xi^3 + 10.399\,10^{-13}\,\xi^4 \qquad (2.42)$$

I briefly describe two interferometric arrays, the VLA and GMRT, in the following sections.

2.2.5 The Giant Metrewave Radio Telescope

The GMRT (see top panel in Fig. 2.11) is one of the world's largest radio interferometers, located 80 km north of Pune, India. The telescope is operated by the National Centre for Radio Astrophysics (NCRA), a part of the Tata Institute of Fundamental Research, Mumbai.

An innovative technology was introduced by Indian engineers to build the GMRT. The parabolic antennae do not have a solid surface but are made of wire "ropes" – the SMART (Stretch Mesh Attached to Rope Trusses) concept. This makes the telescope relatively light, cheap and more stable to high winds. GMRT is a relatively new telescope (first light was in 1995) and has attracted the interest of radio astronomers due to its excellent low-frequency sensitivity and large primary beam. GMRT began to operate well in around 2005 and a large number of publications related to extragalactic radio sources have appeared since 2007 (e.g. Bondi et al. 2007; Moss et al. 2007; Tasse et al. 2007; Garn et al. 2007, 2008a,b).

The telescope is composed of 30 independent phase-tracking antennae arranged in a "Y" shape (16 antennae) plus a short-baseline, square core (14 antennae). The large number of antennae yields 435 baselines. Each antenna has a 45-m diameter with a maximum interfero-

[1] http://www.ncra.tifr.res.in/∼ngk/primarybeam/beam.html

metric baseline of 25 km. GMRT works at long wavelengths – from 6 m up to 0.2 m, where the wire mesh becomes transparent.

In this work, GMRT has been used specifically at 0.5 m (610 MHz), which provides optimal sensitivity and resolution for studies in combination with 1.4-GHz VLA observations.

At 610 MHz, data from GMRT is taken in two sidebands (intermediate frequency bands – IFs) centred at 602 MHz and 618 MHz. These IFs are divided into 128 channels, each 125 kHz wide, in both right and left polarisations – a total effective bandwidth of $\Delta\nu = 32$ MHz. A simple estimate ($\sim \lambda/B$, where B in the maximum baseline) predicts a maximum resolution of ~ 4 arcsec FWHM. However, typical synthesised beams are usually around 6 arcsec, depending on the location of the field and the number of long-baseline antennas that fail during the observing run.

The primary beam ($\sim \lambda/D$, where D the antenna diameter) at 610 MHz is large, $\sim$ 44 arcmin. During the final stages of data reduction, when creating images, we normally ignore information beyond the point at which the primary beam response falls below 30 per cent (~ 30 arcmin).

2.2.6 The Very Large Array

The VLA (see bottom Fig. 2.11) is a radio interferometer located 80 km west of Socorro, New Mexico, USA. It is part of NRAO and it is one of the most sophisticated radio telescopes in the world. The VLA was formally inaugurated in 1980 and since then it has been used as a multi-purpose instrument covering a wide range of scientific radio research projects.

The telescope is composed of 28 independent phase-tracking 25-m antennas, arranged in a "Y" shape, with at least one always set aside for refurbishment. Antennas are able to move along the Y-shaped arms, providing four different configurations: A, B, C and D. Antennas are relocated in a cycle of 16 months, spending three or four months in each configuration. The maximum baseline is 27 km in "A" configuration and 1 km in "D" configuration.

The VLA can operate in the frequency range from 74 to 50,000 MHz. In this thesis, I use the 1.4-GHz band (the so-called "L" band at 21 cm) with data taken in A and B configurations – with synthesised beams of ~ 1.5 and ~ 4 arcsec FWHM, respectively. The B-configuration data are well matched to the GMRT images at 610 MHz.

At 1.4 GHz, data from VLA is recorded using two IF pairs (each pair consists of right-circular and left-circular polarisation data) centred at 1,364.9 MHz and 1,435.1 MHz. These are divided into seven channels, each 3.125 MHz wide, providing a total effective bandwidth of 43.75 MHz. The primary beam has an angular coverage of 30 arcmin (to the half-power point) and the antenna response drops to 30 per cent around ~ 20 arcmin from the pointing centre.

Figure 2.11: The GMRT (*top*) and VLA (*bottom*) telescopes.

CHAPTER 3

Deep multi-frequency radio imaging using the GMRT and VLA

"History and philosophy hold the same lessons but one of them is taught by example."
Benedict Clark

3.1 Introduction

In early studies, radio astronomy was limited to bright sources associated with rare ($L_{1.4\mathrm{GHz}} \approx 10^{25-29}\,\mathrm{W\,Hz^{-1}}$) luminous radio galaxies and quasars (QSOs). Galaxies with nuclear activity are usually characterised by powerful radio lobes, which are evidence of interactions between highly collimated relativistic flows – coming from the nuclear activity – and the interstellar/intergalactic medium. These magnificent radio-loud structures were classified by Fanaroff & Riley (1974) depending on their shape (FR I and II). Optical identifications showed that these active galactic nuclei (AGN) are usually hosted by massive elliptical galaxies (Matthews et al., 1964). It was not until the 1980s that radio source counts at the sub-mJy level revealed a new radio population (Windhorst et al., 1985; Mitchell & Condon, 1985). These faint radio sources dominate the number counts and literally "light up" the radio sky (Garrett 2005) in the sub-mJy regime, as summarised in the review by Condon (2007). Various studies (e.g. Simpson et al., 2006; Seymour et al., 2008; Smolčić et al., 2008) have identified this population with star-forming galaxies (starbursts, spirals or irregulars) and radio-quiet AGN (faint FR I, Seyfert

galaxies).

The fractions of AGN and star-forming galaxies that contribute to the sub-mJy radio regime is still hotly debated. Many different approaches have been taken to disentangle these two populations: using far-infrared (far-IR)/radio flux ratios (Donley et al., 2005; Ibar et al., 2008); tackling their radio brightness temperatures and luminosities (Wrobel et al., 2005; Garrett et al., 2005); resolving their radio morphologies (Muxlow et al., 2005; Biggs & Ivison, 2008); identifying optical host galaxies via morphology (Padovani et al., 2007), or spectroscopy (Gruppioni et al., 1999; Barger et al., 2007), or their locus in colour-colour diagrams (Ciliegi et al., 2005); via X-ray identifications (Simpson et al., 2006); or using their radio spectral indices (Richards, 2000; Clemens et al., 2008). These approaches tend to yield substantially different results.

In terms of spectral indices, star-forming galaxies are usually considered to have $-0.8 \lesssim \langle\alpha\rangle \lesssim -0.7$ (where $S \propto \nu^{\alpha}$), with a relatively small dispersion, $\Delta\alpha = 0.24$ (Condon, 1992). A sample of $z < 0.5$ FR I & II sources have also been found to have similar spectral indexes (between 178 MHz and 750 MHz), with mean and scatter of $\alpha = 0.74 \pm 0.19$ and $\alpha = 0.79 \pm 0.14$, respectively (Laing et al. 1983). This implies that studies based on the radio spectral index find large difficulties to disentangle star-forming from steep-spectrum FR-AGN populations. Nevertheless, the radio spectral index is sensible to core-dominated radio-quiet AGN (Blundell & Kuncic 2007), GHz-peaked sources (GPS; Gopal-Krishna et al. 1983; O'Dea 1998; Snellen et al. 2000) and the ultra-steep spectrum sources (USS; Rottgering et al. 1994; Chambers et al. 1996; Jarvis et al. 2001) usually found at high redshift.

Recent studies, combining 610-MHz and 1.4-GHz data, have found evidence for flatter spectral indices (Bondi et al., 2007; Garn et al., 2008a) and larger dispersions at sub-mJy radio fluxes (e.g. Magliocchetti et al., 2008), suggesting that core-dominated radio-quiet AGN are playing a key role in the sub-mJy radio population.

In this paper, we present two very deep radio images centred on the Lockman Hole (LH): the deepest to date at 610 MHz ($\sigma \sim 15\,\mu$Jy beam^{-1}) obtained using the Giant Metrewave Radio Telescope (GMRT), and a deep 1.4-GHz image ($\sigma \sim 6\,\mu$Jy beam^{-1}) obtained using the Very Large Array (VLA). At these long wavelengths the dominant powering process comes from synchrotron radiation. We merge both datasets to characterise the spectral index of the μJy radio population as a function of flux density, thereby probing the physical mechanisms that dominate in this enigmatic radio population: optically thin (steep spectrum) or self-absorbed (hard spectrum) synchrotron emission. Our deep, well-matched observations – about three times deeper than previous data – mitigate the well-known bias towards the detection of steeper spectra at longer wavelengths, or flatter spectra at shorter wavelengths. This work provides a parameterisation of the radio spectral energy distribution (SED) that can be used to estimate more precise *k*-corrections for the observed radio emitters.

Throughout this chapter we assume a Universe with $\Omega_{\rm m} = 0.27$, $\Omega_{\Lambda} = 0.73$ and $H_0 = 71\,{\rm km\,s^{-1}\,Mpc^{-1}}$.

3.2 Radio observations

3.2.1 GMRT*

During six 12-hr sessions in 2006 February and July we obtained data for three pointings in the Lockman Hole (see Table 3.1), separated by 11 arcmin (LOCKMAN-E, LOCK-3, LHEX4), typically with 28 of the 30 antennas that comprise the GMRT,[1] near Pune, India. The total integration time in each field, after overheads, was 16 hr. A frequency of 610 MHz was chosen, recording 128 channels every 16 s in the lower and upper sidebands (602 and 618 MHz, respectively) in each of two polarisations. Integrations of 40-min duration were interspersed with

*Initially, both SHADES fields were expected to be part of this study, but the GMRT 610-MHz observations of the SXDF (reduced personally by me) were not as successful as those in the Lockman Hole (reduced by Rob Ivison). The reasons for the differences are not well understood – some of the possible issues are discussed in what follows. The GMRT observations of the SXDF were made in two observing runs: 2006 February 2–5 and 2006 December 4–9. The region was covered by three pointings, forming an equilateral triangle with 22-arcmin sides, covering an area of $\sim$0.5 deg^2. The total integration time per pointing was 11.4 hr. We used 3C 147 or 3C 48 as the primary flux calibrators. These were observed for 20 m at the beginning and end of each session. 0116−208 or 0240−231 were observed for 7 m every 45 m and used as phase calibrators. The full available bandwidth, 32 MHz, was split into two intermediate frequencies (IFs) of 128 channels each, and reduced independently. For the data reduction we used $\mathcal{AIPS}$ (see Appendix B for more details). Standard tasks (e.g. QUACK, TVFLG, UVFLG, SPFLG) were used to flag bad baselines, antennas, initial/final integrations and channels that suffered from narrow-band interference. A rough calibration using only one or two channels was performed with CALIB and CLCAL. These data were then flagged using noise-based criteria with the automated flagging algorithm, FLGIT. These semi-clean data were calibrated again, this time using all channels, and used to calculate accurate flux densities for the phase calibrators and target fields using GETJY. The channels in each IF were averaged into chunks of seven channels (to ensure bandwidth smearing was not a problem) leaving 15 averaged channels for imaging. Each pointing was broken into 37 facets, in order to minimise 3-D smearing, and imaged using IMAGR. The GMRT has a large number of antennas in the central region and these antennas dominate the *uv* coverage, resulting in a non-Gaussian beam shape. Baselines shorter than 1.5 kλ were omitted from the imaging. To generate the final images, we utilised one self-calibration in phase ('P!A') and two in phase and amplitude ('A&P'), normalising the gain to unity in the first pass with 'A&P'. The resulting images were combined using FLATN, after convolving them to a common beam size. The final radio image reaches an r.m.s. of $\sim$60 μJy beam^{-1} near the centre of the field, with a synthesised beam of 6.8×5.4 arcsec^2 at a position angle of 30°. The south-west field, centred at (RA, Dec) = ($2^{\rm h}18^{\rm m}44^{\rm s}.0, -5°7'20''$ J2000) had a considerably larger r.m.s., $\sim$100 μJy beam^{-1}, than the other two fields. The r.m.s. in the final image increases near bright sources, where it can be as high as $\sim$300 μJy beam^{-1}, limiting the detection of nearby sources. These data are approximately an order of magnitude shallower than those in the Lockman Hole, despite their similar integration times. It has not been possible to find a straightforward explanation for the discrepancies between the SXDF and Lockman Hole images. We point out four possible reasons: (1) the amount of RFI was considerably higher and was extremely difficult to identify in the data. Pune, which lies south of GMRT, probably contributed to the RFI, especially during daytime observations (the first dataset); (2) the imaging of equatorial fields, such as the SXDF, is known to be difficult. The problem may be due partly to poor *uv* coverage in low elevation fields, in combination with high winds during the observations; (3) some of the baselines could have suffered correlator problems which were difficult to identify and to flag, preventing deeper imaging; (4) finally, it is well known that low-frequency observations can be affected by instabilities in the ionosphere and such instabilities may have been present during our observations of the SXDF. Given the shallower imaging, we decided not to utilise these data to estimate spectral indices in this chapter. Nevertheless, these data has been used in studies by Vardoulaki et al. (2008) and Dunne et al. (2008).

[1]GMRT is run by the National Centre for Radio Astrophysics of the Tata Institute of Fundamental Research.

5-min scans of the nearby calibrator, 1035+564 ($S_{610\mathrm{MHz}} \approx 2$ Jy), with scans of 3C 48, 3C 147 and 3C 286 ($S_{610\mathrm{MHz}} = 29.4$, 38.3 and 21.1 Jy, respectively) for flux and bandpass calibration.

Calibration initially followed standard recipes within $\mathcal{AIPS}$, using FITLD, INDXR and SETJY. However, because of concerns that some baselines were picking up signal from local power lines and that 1035+564 might be too weak to act as a reliable secondary flux calibration source, a raft of new measures were introduced to avoid detrimental effects on the resultant images.

For each session, the bright source least affected by radio-frequency interference (RFI) and with the fewest malfunctioning antennas was chosen to be the primary flux density and bandpass calibrator. After intensive manual flagging of RFI using SPFLG and TVFLG, these data were SPLIT and calibrated in phase. Antenna-based bandpass solutions were determined, copied to the full dataset and used to determine new gain solutions for the primary calibrator. The gain and bandpass solutions were then applied to the entire dataset with no time-dependent corrections. The secondary calibrator was employed to identify problems with the antennas rather than to track changes in gain, although a more conventional approach was used to generate images with good positional information for use in initial phase self-calibration.

Next, calibrated data were processed with the FLGIT RFI-rejection algorithm. Each 128-channel integration was split into a series of seven 15-channel pieces, minus the first 10 and last 13 channels, and points deviating from linear fits to each piece by more than 5σ were rejected. Data brighter than $1.5\times$ the brightest calibrator were also rejected, leaving around 70 to 95 per cent of the original data intact, depending on the severity of the RFI.

The resulting data, now somewhat cleaner, were averaged down to yield 15 channels in each polarisation for each session, pointing and sideband: a total of 12 dual-polarisation, single-sideband, single-source datasets.

Before imaging, a specially modified version of UVAVG (now standard) was employed to determine and subtract the average value for each baseline and channel throughout the entire session (hence the need for time-independent calibration in the preceding steps).

Imaging each of these datasets entailed the creation of a mosaic of 37 facets, each 512^2 pixels (1.25^2-arcsec^2 per pixel), to cover the primary beam. A further 6–12 bright sources outside these central regions, identified in heavily tapered maps, were also imaged. Our aim was to obtain the best possible model of the sky. CLEAN boxes were placed tightly around all radio sources for use in self-calibration, first in phase alone (SOLMODE = 'P'), then in amplitude and phase (SOLMODE = 'A&P'), with a solution interval of 2 min, staggered by 1 min. The *uv* data were weighted using ROBUST = -0.5, UVRANGE = 0.8, 100 kλ and UVTAPER = 28, 28 kλ with UVBOX = 5.

After CLEAN components were subtracted from the *uv* data, more manual flagging was applied, as well as another pass through the UVAVG task and a clip at the 350-mJy level using UVFLG (now CLIP). CLEAN components were re-introduced (UVSUB, FACTOR=-1), then data with common sidebands from February and July were combined using DBCON to reduce the

GMRT pointings			
Field	R.A. (hr:min:sec)	Dec. (deg:min:sec)	r.m.s. (μJy beam^{-1})
LHEX-4	10:52:56.0	+57:29:06.0	33.7 (USB)
			29.6 (LSB)
LOCKMAN-E	10:51:59.0	+57:21:28.2	26.2 (USB)
			26.0 (LSB)
LOCK-3	10:51:02.0	+57:13:50.4	24.5 (USB)
			23.7 (LSB)
VLA pointings			
Field	R.A. (hr:min:sec)	Dec. (deg:min:sec)	r.m.s. (μJy beam^{-1})
LHEX-4	10:52:56.0	+57:29:06.0	7.2
LOCKMAN-E	10:52:08.8	+57:21:33.8	7.6
LOCK-3	10:51:02.0	+57:13:50.4	11.0

Table 3.1: The GMRT and VLA pointings used in this work. USB and LSB correspond to the upper and lower side band, respectively.

variation in beam size and shape amongst the datasets.

The final six mosaics (see Table 3.1), two for each pointing (upper and lower sidebands), were then convolved to a common beam size (7.1 arcsec $\times$ 6.5 arcsec, with the major axis at position angle 70°), then knitted together using FLATN. An appropriate correction was made for the shape of the primary beam with data rejected at radii beyond where the gain drops to 30 per cent. Data for each pointing and sideband were weighted according to individual noise levels (24–34 μJy beam^{-1}) and introduced in task FLATN to generate the final image. This final image has a noise level in the central $\sim$100 arcmin^2 of 14.7 μJy beam^{-1}, the deepest map so far reported at 610 MHz, despite the modest integration time (16 hr on sky for each pointing).

3.2.2 VLA

New and archival data were obtained in the same three positions using the National Radio Astronomy Observatory's (NRAO[2]) VLA, largely in its B configuration. At 1400 MHz this yielded images well matched to the resolution of GMRT. We tapered our A- and B-configuration data in the LOCKMAN-E field (Ivison et al., 2002) to yield images with a near-circular 4.0-arcsec synthesised beam. Using the same techniques outlined earlier, we then combined this central field with images made using pure B-configuration data in the two other pointings: the designated LOCK-3, 11 arcmin to the south west, for which we obtained 17 hr of data in 2005 March (Ivison et al., 2007b); plus archival data for LHEX4 which comprises 31 hr of integration, 11 arcmin to the north east of LOCKMAN-E (see Table 3.1). The final mosaic-image has an r.m.s. in the central 100 arcmin^2 of 6 μJy.

[2]NRAO is operated by Associated Universities Inc., under a cooperative agreement with the National Science Foundation.

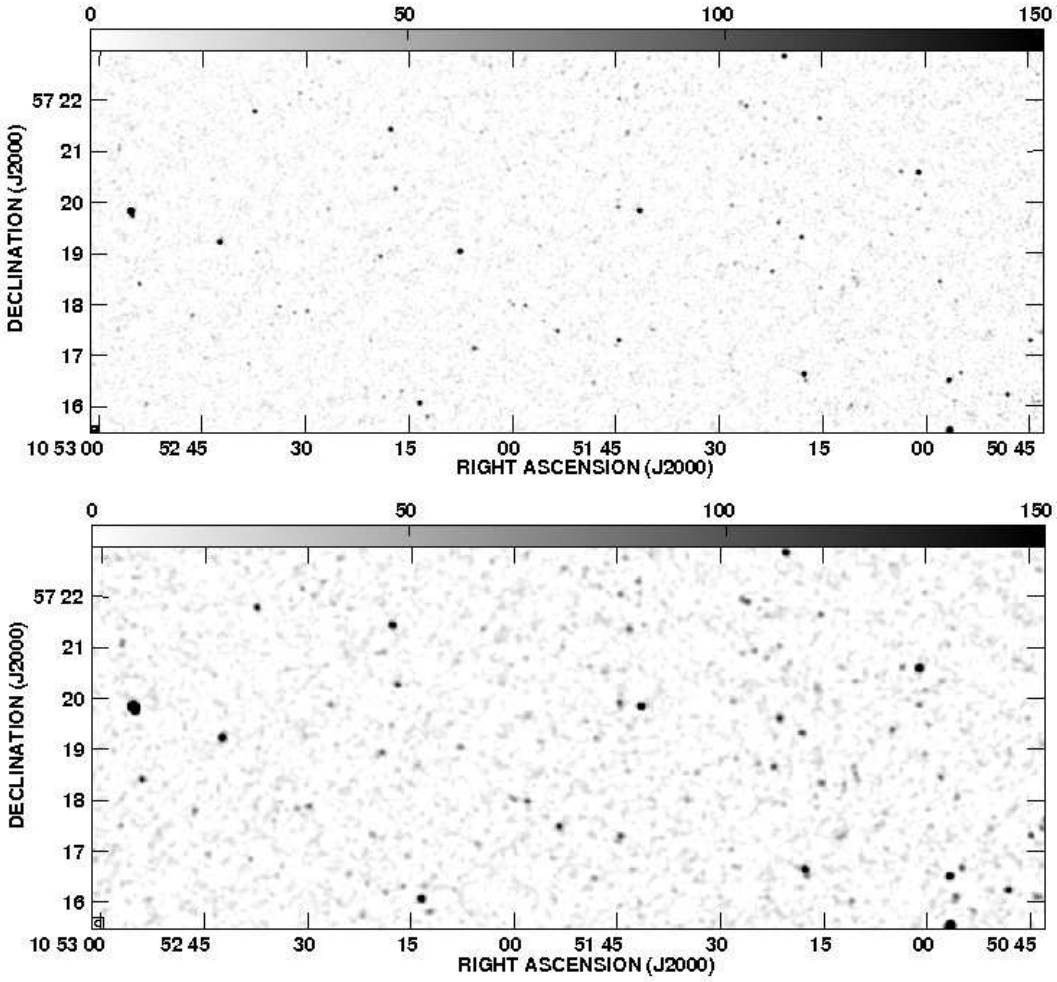

Figure 3.1: Top: A small region (18.7×7.5 arcmin^2) near the centre of the 1.4-GHz mosaic. The linear greyscale runs from 0–150 μJy beam^{-1}. The synthesised beam is 4.3 × 4.2 arcsec^2 (FWHM) with a position angle of 77°. Bottom: The deepest 610-MHz image obtained to date covering the same region and linear greyscale of the VLA image on top. This map has been scaled by a factor $\times 0.56 = (1400/610)^{\alpha}$ (where $\alpha = -0.7$) in order to visually compare it with the 1.4-GHz map. The restoring beam measures 7.1 × 6.5 arcsec^2 (FWHM) with a position angle of 70°.

3.3 Catalogues

3.3.1 Initial source extraction

Sources were extracted from the final FLATNed mosaics (signal images), down to a 3-σ (thereafter σ refers to the local noise) peak level, using the $\mathcal{AIPS}$ routine, SAD (CPARM = 500, 100, 50, 10, 6, 4, 3, 2.5; DPARM(1)=3; DPARM(2)= [15 μJy for GMRT; 7 μJy for VLA]; ICUT = 0.1; GAIN = 1). To provide a reliable signal-to-noise ratio (SNR) extraction criterion, a noise map was generated from the signal image using RMSD (IMSIZE=71,-1; OPTYPE='HIST'). This noise map is introduced as a secondary image for SAD (DPARM(9)$\geq$ 2) which ensured reliable source extraction around bright sources and near the map edges. The final sources were extracted with peak-to-noise ratios (the aforementioned PNRs) higher than $\sim$ 5, to avoid outliers.

The initial SAD catalogue was filtered excluding all those sources with peak values below 4$\times$ the local noise. This process results in a catalogue similar to that produced by SAD using DPARM(1)=4, but was easier to deal with during subsequent analysis. The last CPARM parameter is lower than the first DPARM parameter because some sources may have peak flux densities (in Jy beam^{-1}) that exceed their measured integrated flux densities (in Jy) – a reflection of the increasing uncertainties in the source fits at low SNRs. We use a threshold in peak flux density instead of a threshold in integrated flux because peak flux density is a linearly independent variable in the SAD fitting procedure (actually, in JMFIT) and therefore independent of the size of the source, whereas integrated flux density is a product of peak flux and area. This translates into cleaner and more complete selection criteria.

3.3.2 Instrumental effects

Four important instrumental effects must be taken into consideration (see § 2.2.4 for more details).

Bandwidth smearing

Bandwidth smearing is an inevitable when using channels with finite bandwidth in a two-dimensional (2-D) Fourier transform inversion which assumes monochromatic radiation. We have estimated this bias through knowledge of the distance between each source and the different pointing centres and use a theoretical correction given by:

$$\frac{I}{I_0} = \frac{1}{\sqrt{1+\beta^2}} \quad \text{where} \quad \beta = \frac{\Delta\nu}{\nu}\frac{\theta}{\theta_{\rm syn}} \tag{3.1}$$

which assumes a Gaussian bandpass and circular tapering in the uv plane (Taylor et al., 1999). I and I_0 are the observed and intrinsic peak brightness, $\Delta\nu$ is the channel bandwidth, ν is the frequency of the bandpass centre, $\theta_{\rm syn}$ is the synthesised beamwidth and θ is the distance between the source and the pointing centre.

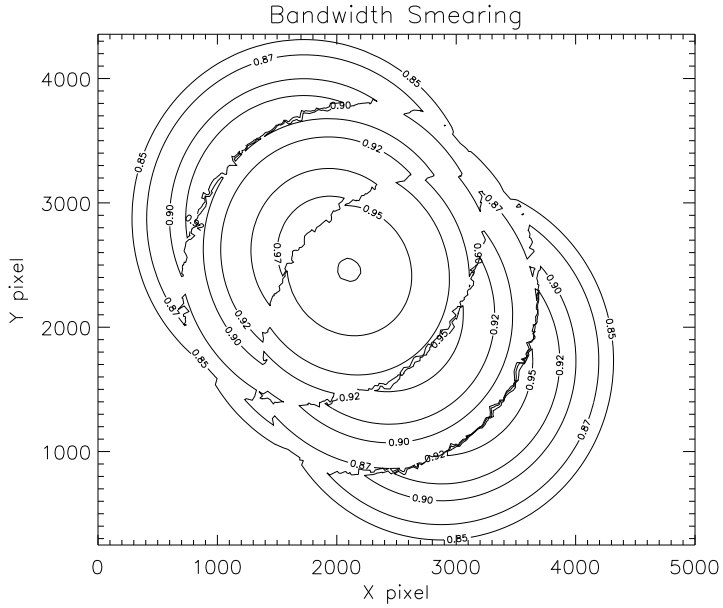

Figure 3.2: Mean bandwidth-smearing correction applied to the 1.4-GHz mosaic. Contours are plotted at: 0.85, 0.87, 0.90, 0.92, 0.95 and 0.97. Note that the smallest corrections do not occur exclusively at the image centre.

In overlapping regions we have averaged the correction by using a minimum variance weighting scheme (see Fig. 3.2),

$$\left\langle \frac{I}{I_0} \right\rangle = \frac{\sum_i \frac{I_i/I_0}{\mathrm{r.m.s.}_i^2}}{\sum_i \frac{1}{\mathrm{r.m.s.}_i^2}}, \tag{3.2}$$

which takes into account the central noise for each pointing. All sources, at both frequencies, were corrected for bandwidth smearing. This bias has been found to be important in the VLA image and not necessarily negligible for the GMRT data. The maximum correction factor is $I/I_0 \approx 0.84$ and $I/I_0 \approx 0.94$ for the VLA and GMRT mosaics, respectively. For example, VLA sources were modified using the values shown in Fig. 3.2. Note this bias modifies the tabulated peaks in the final catalogues, although the selection criterion remain unaffected since it is based on the observed peak values (uncorrected surface brightness in Jy beam^{-1}).

3-D smearing

The general response equation for a two-element interferometer is usually approximated to a 2-D Fourier transform due to the simplicity of the inversion problem. Nevertheless, this is only valid for co-planar baselines (where the w axis lies in the direction of the celestial pole) and for sufficiently small fields of view (Taylor et al., 1999). At low frequencies, the primary beam is large so this approximation becomes inefficient and a formal 3-D Fourier transform is

required. A smearing effect is expected from the rotation of the tangential plane with respect to the celestial sphere when the separation between these two is large.

Based on Fig. 2.9, we can theoretically estimate the effect of 3-D smearing in our images. For each VLA and GMRT image, we have diameters of $\sim$45 and $\sim$57 arcmin, respectively, spanned by seven facets. The maximum separation between the tangent plane and the celestial sphere is given by $\Delta = 1 - \cos\phi$, where ϕ is half the subtended angle of each facet ($\sim$6.4 and $\sim$8.1 arcmin, respectively). Therefore, this implies that in our images, the maximum separation between each tangent facet and the celestial sphere is given by $\sim$0.09 arcsec at 1.4 GHz and $\sim$0.14 arcsec and 610 MHz. In both cases, this separation is equivalent to approximately 2 per cent of the synthesised beamwidth. We consider this bias negligible, and no correction to the observed data was made to correct for 3-D smearing.

Time-delay smearing

This smearing effect is due to the rotation of celestial sources with respect to the phase tracking centre during the integration time, i.e. longer sampling times lead to more blurred images.

In our observations, we have used 16- and 5-sec integration times to collect data from the GMRT and VLA, respectively. Considering theoretical assumptions (again, see Taylor et al. 1999), we find that the maximum loss in peak intensity (expected at the edge of the field of view) is < 2 per cent for GMRT and < 0.3 per cent for the VLA. Consequently, we do not implement any correction to the data for time-delay smearing.

Primary beam attenuation

Primary beam attenuation is the intrinsic loss in gain as a function of distance from the pointing centre. VLA images were corrected using the default 10th order fit to the beam response at 1.4 GHz, described in $\mathcal{AIPS}$ (EXPLAIN PBPARM). For the GMRT images we used the 8th order polynomial fit reported by N. G. Kantharia[3].

Based on a GMRT mosaic composed of 7 pointings, Garn et al. (2007) reported the primary beam centre may be affected by an offset with respect to the nominal pointing (phase) centre. They revealed a systematic difference between the apparent brightness of sources observed by adjacent pointings, and solved this problem by using a common pointing offset of $\sim$ 2.5 arcmin for the primary beam corrections.

To investigate this thorny issue we have defined, in overlapping regions, the angle ϕ as the spherical angle formed by the source, the middle distance between two pointings and the northerly direction. This parameter is sensitive to pointing variations in source predictions as a function of position in the image. Actually, ϕ can be used to prove if there is a real offset for the primary beam correction.

First, we explore if the images created by the upper and lower sidebands (IFs – U and L),

[3] www.ncra.tifr.res.in/$\sim$ngk/primarybeam/beam.html

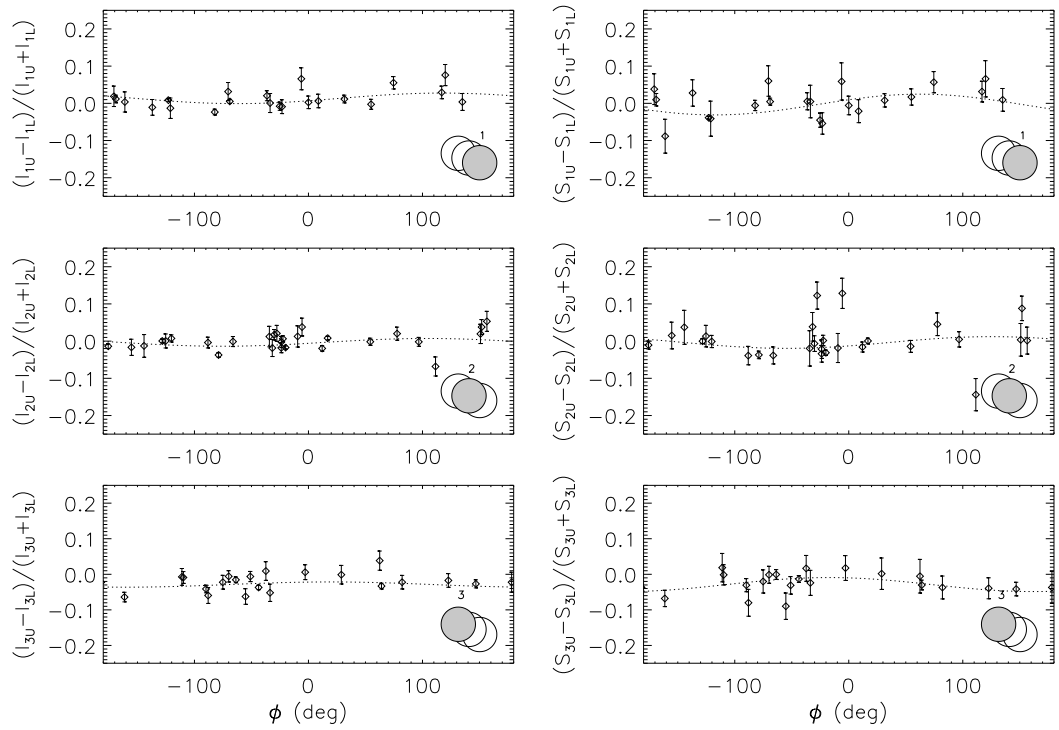

Figure 3.3: These figures compare source estimates from the two IFs of each pointing (subindex U and L are the upper sideband and lower sideband). The angle ϕ is defined in spherical coordinates by the source position, the pointing centre and the northerly direction. The *y*-axis shows the variation in peak brightness corrected by bandwidth smearing (*I – left*) and integrated flux densities (*S – right*), for all sources detected with peak-to-noise$>$ 25. The dashed lines are sinusoidal χ^2 fits that may provide the direction-angle and magnitude-amplitude in case of a primary beam offset with respect to the nominal phase centre.

from each of our three pointings, are being affected by independent pointing offsets (in these cases, ϕ is defined from the same pointing centre). In Fig. 3.3 we plot the parameter ϕ as a function of the gain factors $(I_{(1)} - I_{(2)})/(I_{(1)} + I_{(2)})$ and $(S_{(1)} - S_{(2)})/(S_{(1)} + S_{(2)})$, where I is the peak intensity value corrected by bandwidth smearing and S is the integrated flux density (the subindexes $_{(1)}$ and $_{(2)}$ show the images being compared). This estimation is based on single sources detected above a PNR $>$ 25, and shows no clear evidence for a primary beam offset but a typical difference in flux calibration of $\lesssim 5$ per cent. In the images, the dashed lines show a useful sinusoidal χ^2 fit that provide the *direction* of the offset via the phase of the fit and the amplitudes yield the *magnitude* of the offset. Note that in case of an offset, we expect a clear trend with a sinusoidal signal in these diagrams.

Based on the lack of evidence for a pointing offset in Fig. 3.3, the IFs were combined in order to test if different pointings show any variation in source properties (see Fig. 3.4). We find the use of peak values instead of integrated flux densities can result in an *apparent* pointing offset,

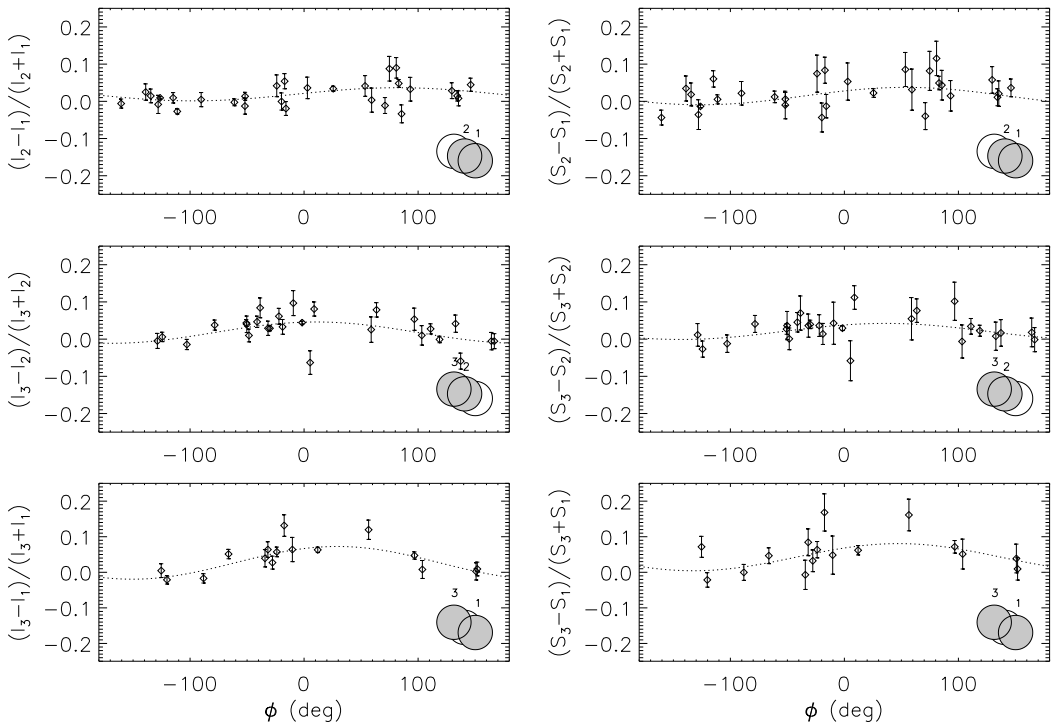

Figure 3.4: These figures are the same as those from Fig. 3.3 but based on estimates coming from different pointings. In these cases, ϕ is defined in spherical coordinates by the source position, the middle distance between the two pointings and the northerly direction. The plotted data corresponds to sources observed in overlapping regions with peak-to-noise$>$ 25.

mostly because of the fits obtained for the furthest (3–1) pointings (bottom in Fig. 3.4). It is worth to note that smearing effects may simulate the behaviour expected for a primary beam offset when I values are used. Since we have accounted for bandwidth smearing, these fits (if robust) suggest smearing is more prevalent than expected, with an unknown origin. Since integrated flux densities (S) do not show a clear pattern in ϕ and are not affected by smearing effects, these plots suggest there is no compelling evidence for a primary beam offset.

In order to test the reality of the apparent shifts seen in the fits, we ran simulations, applying the primary beam corrections in the directions indicated by the fits. The idea is to minimise the amplitude of the observed shifts. We find the offsets required to remove the pointing offsets are $\lesssim$ 1 arcmin, in different directions for all the pointings. This contradicts the single offset of $\sim$ 2.5 arcmin, in a common direction, used by Garn et al. (2007).

Due to the lack of evidence for a pointing shift, we decided not to apply any primary beam offset to our data.

Class	Description
S	Single Gaussian source without close neighbours
SD	Single Gaussian source with one close neighbour
ST	Single Gaussian source with two close neighbours
SE	Single Gaussian source with multiple close neighbours
D	Double Gaussian source without close neighbours
DT	Double Gaussian source with one close neighbour
T	Triple Gaussian source without close neighbours
M	Extended source composed of more than three Gaussians

Table 3.2: Source classification for the radio catalogues presented in Tables 3.3 and 3.4. By "neighbours" we mean sources extracted by SAD with PNR $> 4\sigma$.

3.3.3 Multiple sources

The definition and identification of multiple systems is a common problem in radio astronomy, i.e. how many radio sources are related to a single galaxy? This is especially difficult for deep radio observations where extremely deep optical imaging is required to identify the host galaxy. We can use intuition to find obvious double-sided jets from bright, extended radio galaxies (FR II), but this becomes more difficult at faint flux levels for all angular scales, for obvious reasons.

The classification of multiple systems is also highly resolution-dependent. A source adequately described by a single Gaussian at 610 MHz may require more than one component at 1.4 GHz, confusing catalogues, number counts, and the study of spectral indices. Later, we explicitly refer to 610-MHz- or 1.4-GHz-selected samples to avoid confusion.

In order to identify and classify the sources, we have extracted all those sources having close neighbours (PNR $>$ 4), based on a simple criterion: if the distance between two sources is lower than 1.2$\times$ the sum of their measured FWHMs – the "friendly distance" – then these sources are separated from the so-called "single-source" sample. We have thus applied a "friend-of-a-friend" technique, using an elliptical (direction-dependent) search region – an efficient classification method. All these sources have been treated independently in order to check the reliability of the detections. A minority of them have been considered as single emitters with more than one Gaussian component. In Table 3.2 we describe the final classifications. This identification is not restricted in SNR (e.g. Ciliegi et al., 1999; Seymour et al., 2004; Biggs & Ivison, 2006) because some sources display diffuse emission, or have much fainter components superimposed. Classifications are presented in column 9 of Tables 3.3 and 3.4 and are useful when cross-matching catalogues at different wavelengths.

TVSTAT has been used to determine the flux densities of extended sources (usually sources with more than three Gaussian components – see Table 3.2). This gives a more accurate estimate for complex systems than adding the various Gaussians together. A final inspection by eye checked the reliability of the components in extended sources (including distant radio

lobes in some cases), sources showing side-lobe patterns and sources with diffuse emission not included by the Gaussian fits. For all extended sources, errors in peak and flux density are assumed to be 5 per cent of the value reported by TVSTAT.

Two other important source parameters are the angular size and the orientation of the sources. We have measured the angular size as follows. For multiple systems, it corresponds to the separation of the furthest components, plus their FWHM in both directions, defined by the angle they form on the sky (the "phase angle"). For single sources, it is equivalent to twice the maximum FWHM. The angular size parameter and the phase angle are presented in columns 6 and 7 of Tables 3.3 and 3.4.

3.3.4 Source catalogues

Various clean-up processes were applied to the initial catalogues produced by SAD (see §3.3.1). First, we eliminated those sources lying closer than 30 pixels (24 and 37.5 arcsec at 1.4 GHz and 610 MHz) from the image border, where the noise is considerably higher, and removed sources forming part of multiple structures that have been considered as single emitters. The final catalogues comprise sources with PNR $> 5\sigma$ (uncorrected by bandwidth smearing) and integrated fluxes in excess of $3\times$ the local r.m.s. (to avoid sources with unphysically small sizes).

Lastly, we ran both source extractions again using $2\times$FWHM-convolved images to include extended emission missed by the first selection process. We find 15 and 16 new sources in the GMRT and VLA mosaics, respectively.

Final catalogues are presented in Tables 3.3 and 3.4. We have identified a total of 1,586 and 1,425 sources with PNR $\geq 5\sigma$ and integrated fluxes in excess of 3σ (the local r.m.s.) at 610 MHz and 1.4 GHz, respectively. Tables show: the standard IAU name, Right Ascension (R.A.) and Declination (Dec.), the corrected PNR, flux density (μJy), the maximum angular size and phase angle (as defined in §3.3.3), the multiplicity classification, and the spectral index (see §3.6), including flags in special cases.

3.4 Statistical analyses

3.4.1 Fraction of false-positive detections

In this section we explore the characteristics of our 5-σ catalogues. To assess the number of false-positive detections that may arise in our images, we re-ran the detection algorithm on the negative fluctuations of the map. The vast majority of these bright (>5-σ) negative sources are located near the brightest positive emitters and can thus be explained by deconvolution artifacts; at fainter fluxes, the negative sources clearly follow the noise levels in the image. In Fig. 3.5 we show the ratio of negative to positive sources (selected following exactly the same

Table 3.3: A small sample of the sources found in the Lockman Hole field at 610 MHz using the GMRT. Source extraction is based on peak brightness $> 5\times$ the local r.m.s. and integrated flux density $> 3\times$ the local r.m.s. criteria. column 1: Standard source name; column 2: Right ascension; column 3: Declination. For double and triple systems the position is given by the brightest component. For extended sources it is given by the most central component; column 4: Peak to noise ratio corrected by bandwidth smearing (§ 3.3.2); column 5: Integrated flux density; column 6: Maximum angular size (§ 3.3.3). For single sources it corresponds to twice the maximum FWHM. For multiple sources, it is given by the distance between the furthest components plus the FWHM in the direction defined by them. column 7: The orientation angle of the source with respect to the north direction. column 8: Classification of the source. S = single, D = double (d1 & d2 as components), T = triple (t1, t2 & t3 as components) and M = extended. The upper index $^{(\times 2)}$ indicates sources extracted from the $2\times$ FWHM convolved image (see § 3.3.3 for more details); column 9: The radio spectral index between 610 MHz and 1.4 GHz. '–' = outside cross-matching region, '!' = unreliable spectral index (e.g. based on sources that were split, missing fainter components, or large offsets in the cross-match). A complete version of this table can be found in Ibar et al. (2009) (*in preparation).*

IAU Name	Position at 610MHz (J2000.0)		SNR^{BWSC}_{peak}	Flux	Max. Size	Phase angle	Class	$\alpha^{610MHz}_{1.4GHz}$
	hr:min:sec	deg:min:sec		(μJy)	(arcsec)	(deg)		
(1)	(2)	(3)	(4)	(5)	(6)	(7)	(8)	(9)
GMRTLHJ105141.7+572204	10:51:41.71	+57:22:04.5	5	55± 20	14.8	4	SD	< -0.67
GMRTLHJ105141.9+572218	10:51:41.92	+57:22:18.7	12	129± 20	13.6	170	SD	-0.43
GMRTLHJ105142.0+573603	10:51:41.99	+57:36:03.0	212	8737± 436	32.1	173	M	-0.69 !
GMRTLHJ105142.0+575105	10:51:42.01	+57:51:06.0	6	766± 164	25.9	127	S	–
GMRTLHJ105142.0+574443	10:51:42.01	+57:44:43.2	5	115± 39	13.8	118	S	< -0.06
GMRTLHJ105142.1+571501	10:51:42.06	+57:15:01.5	25	392± 26	14.8	18	S	-0.80
GMRTLHJ105142.1+573447	10:51:42.09	+57:34:47.4	19	483± 43	14.6	65	S	0.98
GMRTLHJ105142.5+570925	10:51:42.51	+57:09:25.8	11	241± 35	15.0	115	S	-0.96
GMRTLHJ105142.6+573714	10:51:42.59	+57:37:14.4	13	319± 42	14.7	65	S	-1.11
GMRTLHJ105142.8+571638	10:51:42.76	+57:16:38.8	6	78± 23	16.8	101	S	-1.14
GMRTLHJ105143.0+564722	10:51:43.04	+56:47:22.2	5	205± 74	12.6	21	S	–
GMRTLHJ105143.2+572122	10:51:43.24	+57:21:22.4	13	236± 27	17.1	20	S	-1.00
GMRTLHJ105143.4+571835	10:51:43.40	+57:18:35.1	5	64± 24	13.8	81	S	-0.95
GMRTLHJ105143.7+573858	10:51:43.74	+57:38:58.1	9	246± 45	15.0	145	S	-0.93
GMRTLHJ105143.8+572246	10:51:43.78	+57:22:46.2	6	87± 24	14.0	69	S	-1.33
GMRTLHJ105143.8+572936	10:51:43.80	+57:29:36.4	29	891± 43	20.7	163	S	-0.87
GMRTLHJ105143.9+565945	10:51:43.90	+56:59:45.5	10	202± 31	17.5	116	S	< -0.48
GMRTLHJ105144.5+572203	10:51:44.49	+57:22:03.4	11	134± 20	13.0	79	S	-1.11
GMRTLHJ105144.6+571717	10:51:44.57	+57:17:17.8	13	294± 31	18.3	147	S	-0.52
GMRTLHJ105144.6+571955	10:51:44.61	+57:19:55.1	14	231± 26	16.8	15	S	-1.09
GMRTLHJ105145.6+570510	10:51:45.65	+57:05:10.6	5	129± 36	17.9	112	S	< -0.63
GMRTLHJ105145.9+565957	10:51:45.86	+56:59:57.1	11	249± 36	16.8	81	S	< -0.64
GMRTLHJ105146.0+573359	10:51:46.00	+57:33:59.6	6	187± 58	13.1	43	S	-0.58
GMRTLHJ105146.7+575210	10:51:46.74	+57:52:10.3	12	667± 91	15.9	131	S	–
GMRTLHJ105146.8+572032	10:51:46.76	+57:20:32.6	6	155± 35	19.2	97	ST	-1.48
GMRTLHJ105147.0+573844	10:51:47.02	+57:38:44.8	6	142± 37	15.8	129	S	< -1.02
GMRTLHJ105147.1+570757	10:51:47.07	+57:07:57.2	6	68± 20	12.3	61	S	< -0.32
GMRTLHJ105147.1+564735	10:51:47.14	+56:47:35.5	128	8806± 170	25.6	162	D	–
	10:51:47.14	+56:47:35.5	128	8255± 114	14.8	24	d1	
	10:51:47.54	+56:47:25.0	6	551± 126	21.5	114	d2	
GMRTLHJ105147.3+571441	10:51:47.34	+57:14:41.1	14	189± 23	14.3	103	S	-0.54
GMRTLHJ105147.8+570831	10:51:47.81	+57:08:31.5	5	178± 46	23.2	161	ST	< -1.08

Table 3.4: The 1.4 GHz catalogue. See Table 3.3 for details.

IAU Name	Position at 1.4GHz (J2000.0)		SNR^{BWSC}_{peak}	Flux	Max. Size	Phase angle	Class	$\alpha^{610MHz}_{1.4GHz}$
	hr:min:sec	deg:min:sec		(μJy)	(arcsec)	(deg)		
(1)	(2)	(3)	(4)	(5)	(6)	(7)	(8)	(9)
VLALHJ105211.5+573953	10:52:11.48	+57:39:53.2	21	193± 17	9.2	46	S	0.11
VLALHJ105211.8+573510	10:52:11.82	+57:35:10.2	12	53± 8	7.1	37	SD	−1.55
VLALHJ105211.9+570540	10:52:11.86	+57:05:40.5	7	58± 16	9.9	161	S	−0.22
VLALHJ105212.0+572321	10:52:12.04	+57:23:21.6	6	24± 7	7.4	146	S	−1.48
VLALHJ105212.1+573454	10:52:12.08	+57:34:54.6	9	46± 10	8.0	161	S	> -0.98
VLALHJ105212.1+572621	10:52:12.11	+57:26:21.4	10	64± 10	10.2	136	S	−0.38
VLALHJ105212.2+571525	10:52:12.16	+57:15:25.4	9	68± 12	10.4	73	S	−1.00
VLALHJ105212.3+571549	10:52:12.27	+57:15:49.5	19	84± 8	8.0	90	SD	−0.53!
VLALHJ105212.5+572453	10:52:12.49	+57:24:53.1	48	278± 10	9.2	97	S	−0.62
VLALHJ105212.6+570641	10:52:12.63	+57:06:41.3	6	56± 17	10.2	32	S	−1.61
VLALHJ105213.3+572650	10:52:13.29	+57:26:50.6	12	71± 9	9.3	156	S	> -0.30
VLALHJ105213.4+571605	10:52:13.38	+57:16:05.3	52	301± 10	8.8	59	S	−0.77
VLALHJ105213.4+572600	10:52:13.44	+57:26:00.2	10	45± 8	7.8	161	S	−0.43
VLALHJ105213.6+574436	10:52:13.64	+57:44:36.0	6	64± 21	7.8	166	S	> -0.93
VLALHJ105213.8+571338	10:52:13.76	+57:13:38.9	13	89± 11	9.2	5	SD	−0.82!
VLALHJ105213.9+573935	10:52:13.89	+57:39:35.9	9	54± 12	7.4	124	S	> -0.95
VLALHJ105214.0+571841	10:52:14.04	+57:18:42.0	6	44± 11	11.9	107	S	−1.32
VLALHJ105214.2+573140	10:52:14.18	+57:31:40.9	7	91± 17	14.1	38	S	> -0.62
VLALHJ105214.2+573328	10:52:14.21	+57:33:28.2	7	85± 17	11.9	35	S	−0.91
VLALHJ105214.6+571335	10:52:14.60	+57:13:35.9	5	24± 8	7.9	62	SD	−0.82!
VLALHJ105214.7+565827	10:52:14.68	+56:58:27.7	6	94± 36	7.7	52	S	> -0.18
VLALHJ105214.8+573644	10:52:14.80	+57:36:44.0	5	49± 16	13.3	109	S	> -1.20
VLALHJ105215.0+572635	10:52:15.00	+57:26:35.1	16	161± 14	11.1	115	S	−0.74
VLALHJ105215.2+571319	10:52:15.25	+57:13:19.5	16	107± 12	10.1	16	S	> 0.27
VLALHJ105215.4+571655	10:52:15.36	+57:16:55.1	5	21± 7	8.0	134	S	−1.55
VLALHJ105215.4+571105	10:52:15.44	+57:11:05.8	17	99± 10	9.7	96	S	−0.72
VLALHJ105215.6+572503	10:52:15.64	+57:25:03.6	14	66± 8	9.2	159	S	−0.48
VLALHJ105215.7+572942	10:52:15.67	+57:29:42.1	13	84± 11	8.8	44	S	−0.20
VLALHJ105216.0+571619	10:52:16.00	+57:16:19.5	11	62± 10	9.5	139	S	−0.45
VLALHJ105216.0+573224	10:52:16.01	+57:32:24.4	6	42± 12	8.3	36	S	> -1.09

criteria) as a function of flux density. In the figure we have not taken into account those sources clearly related to sidelobe patterns around bright sources.

This demonstrates that the contamination given by spurious noise-shaped sources is always minimal at all flux densities in the catalogues. Based on Fig. 3.5, we expect 15 sources to be spurious in the GMRT catalogue and 27 in the VLA catalogue. In particular, inspection (by eye) of the negative sources extracted in the VLA mosaic shows that they are often located in the south-east pointing, where the noise in higher and shares the same scale as real sources.

3.4.2 Mock source extraction

We consider the residual image (without bright $> 5\,\sigma$ sources) as the best estimate of the non-Gaussian noise structure at all scales in the mosaics. The following simulations are based on identical extractions using both the normal ("positive" map) and inverted images (negative map) as background noise reference. The use of these two images minimises the effect that some real fainter $\lesssim 5\,\sigma$ sources may be boosting the noise.

We recognise three main properties of the noise. The first is intrinsic to the primary beam shape and depends on the distance from the pointing centre. The second is due to ripples produced by interference that was not caught whilst editing the uv data. The third is isolated to the regions around bright sources, where the local noise increases due to sidelobes or

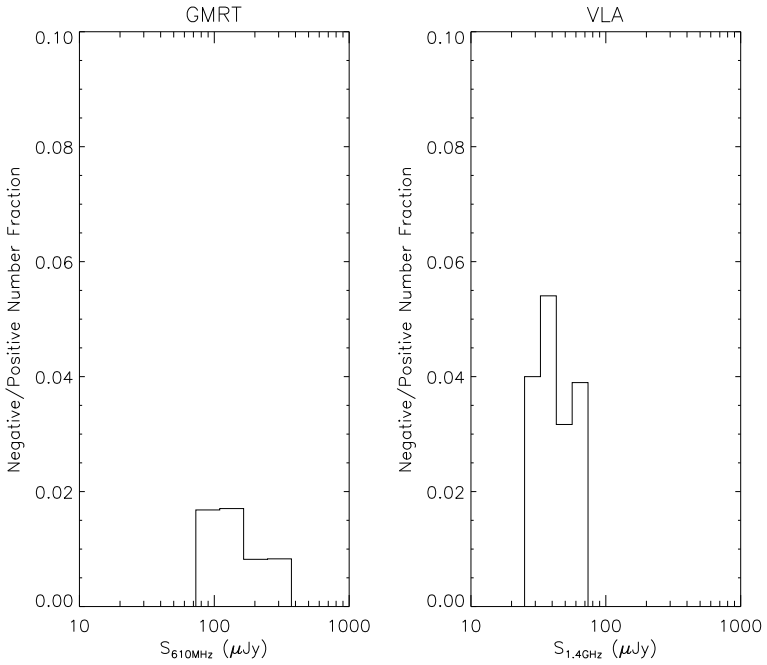

Figure 3.5: Fraction of negative sources (from the inverted map) over positive (catalogued) sources, detected using the same PNR $> 5\sigma$ criteria, as a function of flux density. The *left* and *right* panels are based on 610-MHz and 1.4-GHz detections, respectively. Error bars are assumed to be Poissonian.

deconvolution artifacts, hindering the detection of faint sources.

We have modelled 25,000 point sources (smeared by bandwidth, depending on their location – see §3.3.2) using the task IMMOD, with peaks from $1\times$ to $500\times$ the central r.m.s. noise in the mosaic ($\sim$15 μJy beam^{-1} at 610 MHz, and $\sim$6 μJy beam^{-1} at 1.4 GHz). Each simulation introduces 500 mock sources into the normal and inverted residual images, and then extracts a catalogue using criteria identical to those in §3.3. This process was repeated 50 times.

Mock sources were introduced with random phase angles, located >30 pixels form the image border, and none of them overlap. To avoid the bright residuals around powerful radio sources, regions in the vicinity of the brightest 20 sources were avoided. A total of $\sim$16,000 sources ($\sim$60 per cent in each simulation) are recovered at the same position by the 5-σ-peak extraction, a number which allows a detailed estimation of possible biases in the sample. Results are presented in Fig. 3.6 & 3.7.

3.4.3 SAD bias

Seymour et al. (2004) referred to "SAD bias" as an over-estimate of flux densities for low SNR sources due to fluctuations at the edges of the area used for fitting. They show this effect by plotting the average gain in flux densities (the ratio of the extracted and input flux densities) as a function of input peak flux. We have found, however, that this gain is only seen to be a

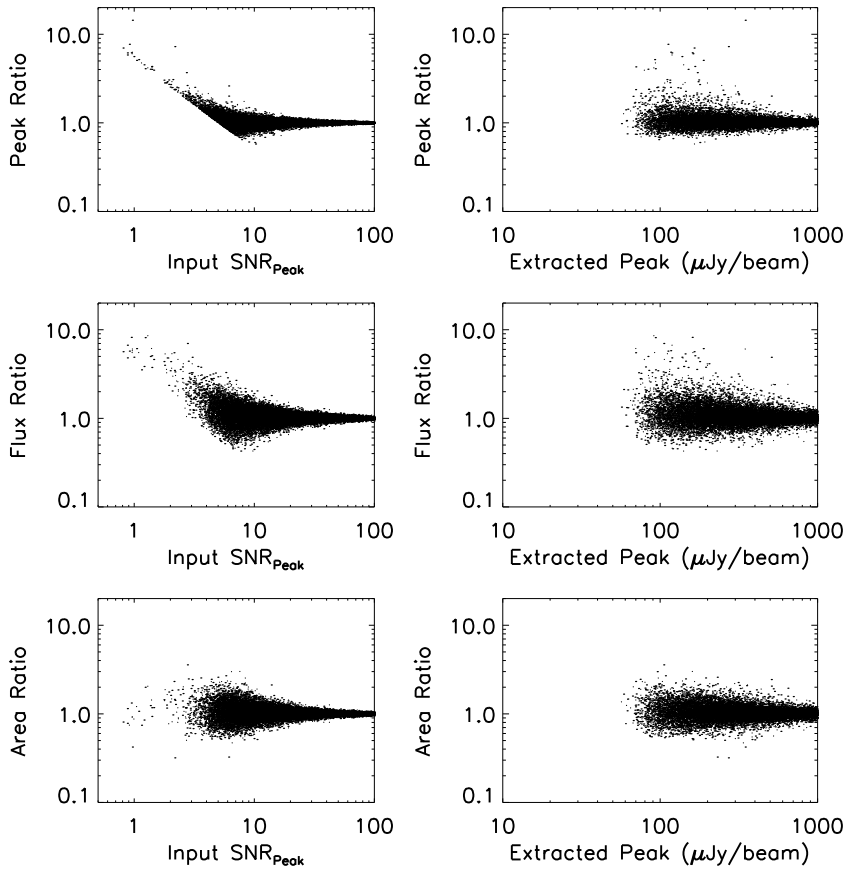

Figure 3.6: Simulations of extracted/mock ratios as a function of input peak-to-noise values (*left*; SNR_{Peak} is the same PNR) and extracted peak brightness (*right*; in μJy beam^{-1}). Simulations are based on the GMRT mosaic. Dots represent mock sources extracted with peaks PNR > 5. From top to bottom, we plot gain in peak, flux and area, respectively (see §3.4.3 for more details about the simulations).

function of input peak flux because of incompleteness: faint sources are preferentially detected if they are boosted by the noise and the uncertainties in the source extraction. In other words, there is a non-negligible fraction of undetected faint sources that compensate for this gain. To be able to relate IMMOD/SAD simulations to the observed catalogues, extracted parameters should be used instead of input values. We find this bias mostly disappears if gains are plotted as a function of extracted peak fluxes.

Figs. 3.6 and 3.7 (for the GMRT and VLA sources, respectively) show the extracted/mock ratios for peak brightness, integrated fluxes and areas, as a function of input peak-to-noise ratio (SNR_{peak}) and extracted peak brightness in μJy beam^{-1}. These figures are based on all mock sources detected above the 5-σ-peak criteria, including the bandwidth smearing effect.

Simulations show that the so-called SAD bias (Seymour et al., 2004) – similar to the input SNR_{peak} versus flux ratio – is due to incompleteness produced by the peak threshold criteria. Flux densities from faint sources should not be corrected; instead, a probability related to its

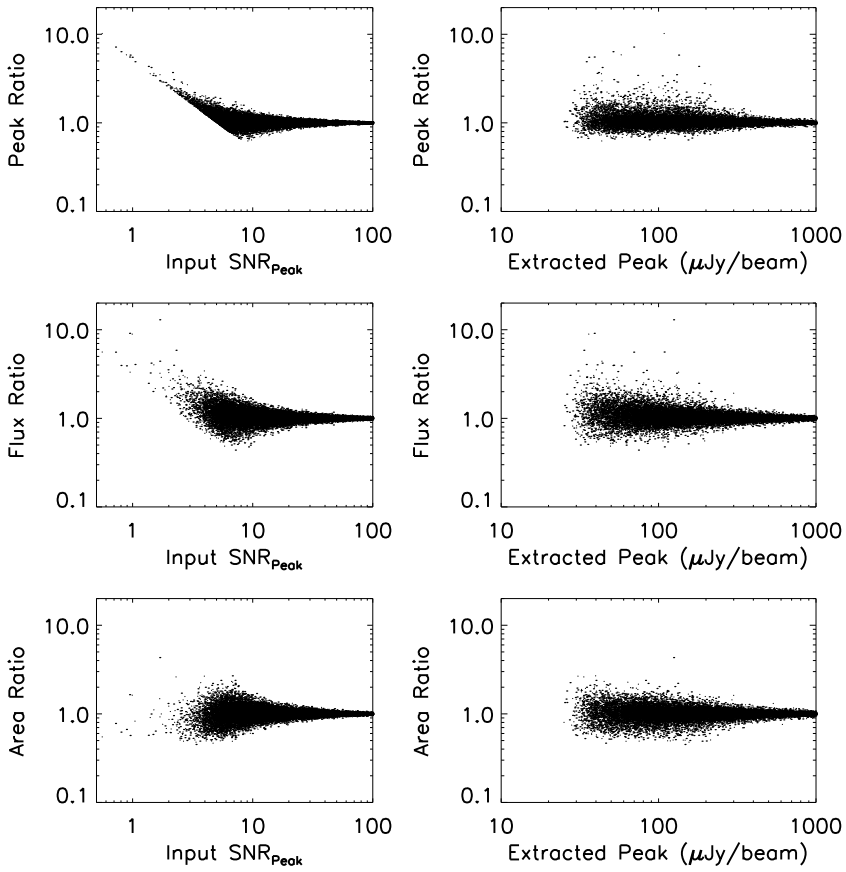

Figure 3.7: The same as Fig. 3.6 but simulations based on the VLA mosaic.

reliability should be assigned to each source.

It is interesting to note the non-zero detections of very faint sources (<2-σ) extracted with considerably higher fluxes $\sim$100 μJy. We have used the normal (positive) residual background image to introduce mock sources, thus leaving open the possibility for some of them to be located at positions where real $\lesssim 5\,\sigma$ sources were before – these are indeed detected in the "positive" extractions. Nevertheless, since we also use the inverted residual image, these boosted sources are just a small minority that should be looked at in an statistical sense only. It would be impossible to distinguish between a boost from a real source or due to source-shaped noise (the arcsec-scale of the noise). Residual large-scale ($\sim$arcmin) sidelobes from bright sources may also help to boost mock sources to higher signal-to-noise ratios.

It can be clearly seen in Figs. 3.6 and 3.7 that sources below $5\,\sigma$ (in the Input SNR$_{\rm peak}$ versus peak ratio panels) show the input excess above the clear background threshold. As we said before, these sources are boosted by the uncertainties from the SAD fits and by the small-scale source-shaped noise. A formal treatment considering the noise power spectrum should be carried out in order to understand its significance for faint source extraction. This study,

however, is beyond of the scope of this work.

Figs. 3.6 and 3.7 clearly shows the increasing uncertainties in the SAD fitting procedure as we go to lower SNR (the so-called "trumpet-like" shape). For example, at a 5-σ level, errors as high as a factor $2\times$ are expected in peak flux values, and as high as $3\times$ in area and integrated flux density. Later in the text (§ 3.6), we see how important these uncertainties are for estimating the radio spectral index of the sources.

We find that the distribution of area ratios is not drastically affected by the selection criteria. Although, a clear tendency to extract sources smaller than the beam-sized input sources is seen in the area ratios at 1.4 GHz. These sources come predominantly from the "positive" extractions rather than from the negative ones.

3.5 Number counts

We have derived number counts in the Lockman Hole using the final catalogues shown in Tables 3.3 and 3.4. The differential number counts, dN/dS, were calculated using the observed number of sources per bin of flux density, N, divided by the bin width (ΔS in Jy) and by the effective area ($A_{\rm eff}$ in steradians) available for detection.

$$\frac{dN}{dS} = \frac{N}{A_{\rm eff}\Delta S} \tag{3.3}$$

3.5.1 Effective area

In our catalogues, the selection criteria for a radio emitter is determined by the local noise at the position of the source. The noise across the image has a complicated structure and is correlated on several different scales. We consider the effective area as the solid angle in which it is possible to extract a source as a function of flux density. This can be obtained by using the previous simulations from § 3.4.2. Since mock sources were introduced randomly in the image, we can assume that the completeness function – the fraction of extracted over input sources as a function of flux density – normalised to the area of the field, provides the effective area, $A_{\rm eff}(S)$, which includes all possible biases from the SAD extraction or by the noise structure of the map.

Fig. 3.8 shows the solid angle versus point-source flux limit used in Eq. (3.3) to estimate the differential number counts at 610 MHz and 1.4 GHz.

3.5.2 Resolution bias

The angular size distribution of the sub-mJy radio population is not well known. In this work, most of the sources lie in the sub-mJy regime with resolutions poorer than $\gtrsim 4$ arcsec. Therefore we are unable to obtain a detailed and self-consistent angular size distribution.

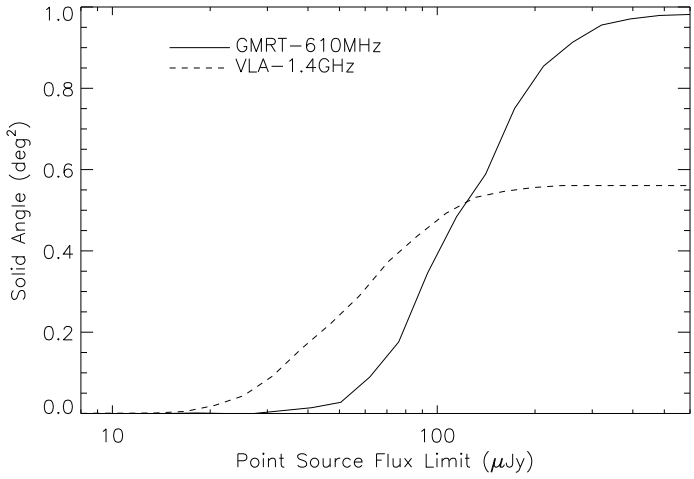

Figure 3.8: Solid angle versus point-source flux limit. *Solid* and *dashed* lines are based on GMRT and VLA mosaics, covering a total of 3,534 and 2,019 arcmin^2, respectively.

Source catalogues based on a threshold criterion are biased against extended sources as a function of flux densities, so in order to estimate the fraction of sources being missed by our threshold criterion, we applied the following treatment.

Area threshold

Number counts are calculated as a function of integrated flux density, while our catalogues are mainly based on a PNR threshold criterion. This restricts the detection of faint radio sources to those with small angular sizes. The resolution bias can be simply summarised by the following equation:

$$\frac{\mathrm{Flux}_{[\mathrm{SAD}]}}{\mathrm{Peak}_{[\mathrm{SAD}]}} = \left(\frac{\pi}{4\,\ln 2}\right)\ \frac{\mathrm{Bmaj}_{[\mathrm{SAD}]}\ \mathrm{Bmin}_{[\mathrm{SAD}]}}{A_{\mathrm{beam}[\mathrm{SAD}]}} \tag{3.4}$$

where the [SAD] index implies values from the SAD output; integrated "Flux" is given in Jy, "Peak" flux in Jy beam^{-1}, Bmaj and Bmin are the major and minor FWHMs in arcsec, and the $\mathcal{AIPS}$-defined synthesised beam area, $A_{\mathrm{beam}} = 1.1331\,\mathrm{Bmaj}^{\mathrm{beam}}\,\mathrm{Bmin}^{\mathrm{beam}}\,\mathrm{arcsec}^2$. The factor 1.1331 comes from the relation between standard deviation and FWHM: $2\pi\,\sigma_{\mathrm{maj}}\,\sigma_{\mathrm{min}} = 2\pi/(2\sqrt{2\ln 2})^2\,\mathrm{Bmaj}\,\mathrm{Bmin}$, which is defined in all $\mathcal{AIPS}$ routines as an area (e.g. number of pixels in the output of TVSTAT).

Eq. (3.4) implies that for a PNR threshold, the area of a source as a function of flux density is restricted to:

$$A_{\mathrm{source}} \leq \frac{A_{\mathrm{beam}}}{5 \times \mathrm{r.m.s.}}\mathrm{Flux} \tag{3.5}$$

In particular, our threshold limit implies the faintest sources are restricted to be point-like, or a little smaller, due to the to uncertainties in area fitting.

Angular size distribution

Previous studies have shown a decrement for the angular size of the radio sources towards faint flux densities. An early study by Windhorst et al. (1990) parameterised the cumulative angular size distribution with the following equation

$$h(\theta) = \exp[-\ln(2) \times (\theta/\theta_{\rm med})^{0.62}] \tag{3.6}$$

where θ is the maximum FWHM of a source and $\theta_{\rm med} = 2 \times S^{0.3}_{1.4\rm GHz}$ arcsec is the median angular size as a function of flux density in mJy. This estimate predicts small variations in $\theta_{\rm med}$ as a function of radio flux density. Bondi et al. (2003), however, found that the Windhorst et al. distribution yields a considerably higher number of sources with large angular sizes – by almost a factor of two (with $\theta > 4$ arcsec) in the sub-mJy regime. This translates into an overestimate of the sources expected to be missed in our observations. Bondi et al. (2003) found that the cumulative angular size distribution of sources with $0.4 \leq S_{1.4\rm GHz} < 1$ mJy (expected to be unbiased for $\theta \lesssim 15$-arcsec sources) is well described by,

$$h(\theta) = \begin{cases} (1.6^{\theta})^{-1} & \text{for} \quad \theta \leq 4'' \\ \theta^{-1.3} - 0.01 & \text{for} \quad \theta > 4''. \end{cases} \tag{3.7}$$

High-resolution radio observations (Muxlow et al. 2005), using data from both the Multi-Element Radio-Linked Interferometer Network (MERLIN) and the VLA, gave the angular size distribution for the sources in the $40\,\mu{\rm Jy} < S_{1.4\rm GHz} \lesssim 1$ mJy regime. Almost all the sources are resolved with angular sizes below 4 arcsec, which implies that our observations might be unaffected by resolution bias at μJy flux densities. Nevertheless, they estimate their sample is 10 per cent incomplete based on previous observations with the Westerbork Synthesis Radio Telescope (WSRT; with a synthesised beamsize of 15 arcsec, FWHM) in the same field, which we use as an upper limit for μJy detections.

We have adopted an angular size distribution given by Eq. (3.6) for bright (>1 mJy) sources, and the average of Eqs (3.6) and (3.7) for fainter sources.

Correction factors

In order to relate Eq. (3.5) to the assumed cumulative angular size distribution, we have considered $\theta = \sqrt{A_{\rm source}/1.1331/\eta}$, where η is the median ratio between the major and minor FWHM of the observed sources. Although this is a strong assumption, changing this parameter does not significantly modify our results.

In Fig. 3.9 we plot the expected missed fractions as a function of flux density for both observing frequencies. Note, we have assumed a threshold of 10 per cent incompleteness for

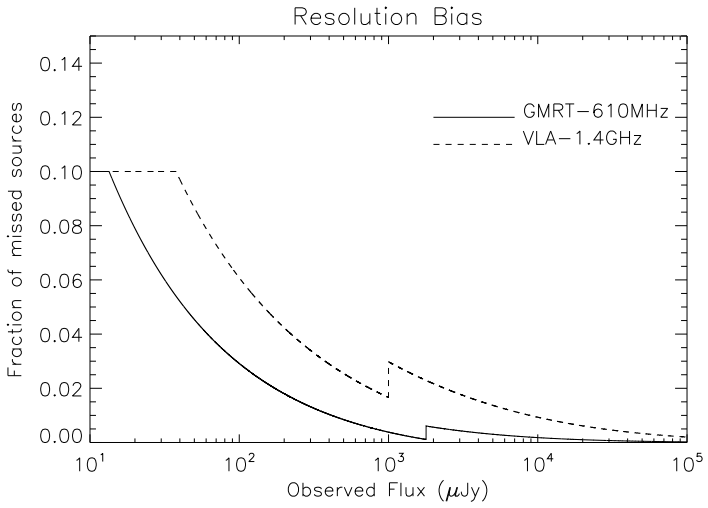

Figure 3.9: Estimated missed fraction of extended sources as a function of flux density. *Solid* and *dashed* lines are the estimates for the VLA and GMRT detections, respectively. Estimates are based on Eq. (3.5) and an averaged cumulative size distribution based on Eq. (3.6) and (3.7) – see the text. We have assumed a spectral index of $\alpha = -0.7$ for the GMRT predictions.

our faintest radio flux levels, based on Muxlow et al. (2005).

Since the angular size distribution of the 610-MHz sources is more uncertain than that of the 1.4-GHz sources, we have assumed a radio spectral slope of $\alpha = -0.7$ to calculate the missed fraction at 610 MHz.

These correction factors are small due to the resolution of our observations. Indeed, this bias is minimised when we include extended sources extracted from the convolved images. At 100 μJy we predict that 3 per cent of GMRT sources and 6 per cent of VLA sources are not selected in our catalogues.

3.5.3 Differential number counts

The differential number counts from Eq. (3.3), normalised for an Euclidean Universe, are plotted in Fig. 3.10. At both frequencies we have used the effective area shown in Fig. 3.8 and the correction for resolution bias plotted in Fig. 3.9. The flux density used to multiply the differential number counts is given by the bin centre (in log-space), and errors are Poissonian for uncorrected counts, for both the observed and mock sources. Tables 3.5 and 3.6 present the counts.

We observe a flattening in the Euclidean differential number counts towards sub-mJy flux densities at both 610 MHz and 1.4 GHz (Fig. 3.10). We find evidence for a second peak in number counts at $\sim$80 μJy and $\sim$200 μJy for the VLA and GMRT counts, respectively. These provide strong constraints on the contribution of *IRAS*-like sources to the sub-mJy radio fluxes,

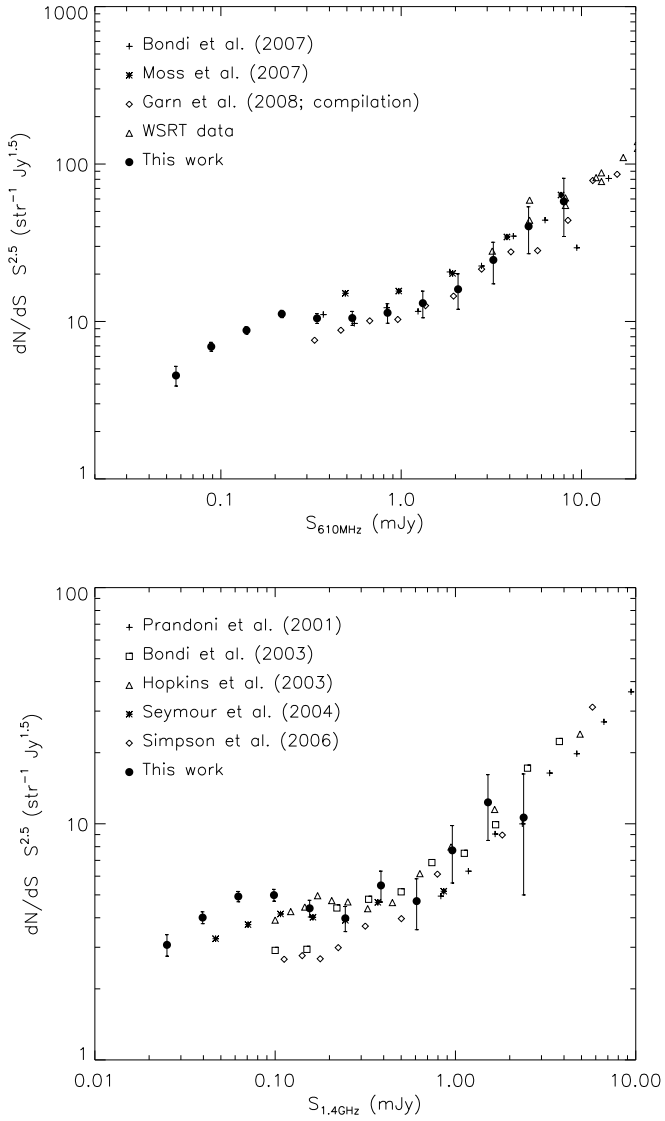

Figure 3.10: Differential source counts as a function of flux density in the Lockman Hole at 610 MHz (*top*) and 1.4 GHz (*bottom*), normalised by the value expected in a static Euclidean Universe. Errors are assumed to be Poissonian (Gehrels, 1986) and are combined in quadrature for the observed number of sources in the bin and the mock source simulations described in §3.4.2. At 610 MHz, we plot data from previous studies: the VLA-VIRMOS Deep Field (Bondi et al., 2007), the 1^h *XMM-Newton/Chandra* Survey (Moss et al., 2007), a compilation from Garn et al. (2008b) which includes data from the ELAIS N1, Lockman Hole and *SIRTF* First-Look Survey fields and counts obtained using the WSRT (Valentijn et al., 1977; Katgert, 1979; Valentijn, 1980; Katgert-Merkelijn et al., 1985). We also show previous 1.4-GHz counts, based on studies using the VLA in its B configuration and using the Australia Telescope Compact Array: the Australia Telescope ESO Slice Project (Prandoni et al., 2001), the Phoenix Deep Survey (Hopkins et al., 2003), VLA-VIRMOS Deep Field (Bondi et al., 2003), the 13^h *XMM-Newton/ROSAT* Deep X-ray Survey (Seymour et al., 2004) and the Subaru/*XMM-Newton* Deep Field (Simpson et al., 2006).

Table 3.5: The 610 MHz radio source counts.

S bin (mJy)	S (mJy)	N	$N/\Delta S/A_{\rm eff}$ ($\rm str^{-1}Jy^{-1}$)	$dN/dS \times S^{2.5}$ ($\rm str^{-1}Jy^{1.5}$)
0.045 - 0.071	0.056	58	$(1.90 \pm 0.27) \times 10^{11}$	4.54 ± 0.65
0.071 - 0.111	0.088	253	$(9.41 \pm 0.61) \times 10^{10}$	6.92 ± 0.45
0.111 - 0.174	0.139	379	$(3.88 \pm 0.20) \times 10^{10}$	8.79 ± 0.46
0.174 - 0.273	0.218	383	$(1.60 \pm 0.08) \times 10^{10}$	11.17 ± 0.59
0.273 - 0.428	0.341	214	$(4.86 \pm 0.35) \times 10^{9}$	10.47 ± 0.76
0.428 - 0.671	0.536	114	$(1.58 \pm 0.16) \times 10^{9}$	10.52 ± 1.07
0.671 - 1.052	0.840	63	$(5.55 \pm 0.79) \times 10^{8}$	11.36 ± 1.61
1.052 - 1.651	1.318	37	$(2.07 \pm 0.40) \times 10^{8}$	13.07 ± 2.52
1.651 - 2.590	2.068	23	$(8.24 \pm 2.09) \times 10^{7}$	16.02 ± 4.07
2.590 - 4.063	3.244	18	$(4.10 \pm 1.21) \times 10^{7}$	24.60 ± 7.25
4.063 - 6.374	5.089	15	$(2.18 \pm 0.72) \times 10^{7}$	40.23 ± 13.29
6.374 - 10.000	7.984	11	$(1.02 \pm 0.41) \times 10^{7}$	57.92 ± 23.26

based on population synthesis models (Hopkins et al. 2000). The appearance of these features at sub-mJy radio fluxes is traditionally explained as a transition from a dominant bright radio-loud AGN population to a star-forming and radio-quiet AGN populations (Windhorst et al., 1985; Simpson et al., 2006; Condon, 2007).

In this work we extend the number counts down to very faint 610-MHz flux densities in complete agreement with previous studies at higher flux levels. The 1.4-GHz counts are a little higher than the majority of previous estimates in the $< 100\mu$Jy regime.

The origin of the wide scatter in reported 1.4-GHz number counts was controversial until Condon (2007) estimated a count fluctuation of only $\sigma = (1.07 \pm 0.26)\, N^{1/2}$ based on 17 non-overlapping fields in the *Spitzer* First-Look Survey (FLS – Condon et al., 2003) region (where N is the statistical fluctuation expected without clustering). Based on this, Condon (2007) states that most of the observed variance is 'mundane, not cosmic', thereby concluding that years of debate have been devoted to differences induced by different instruments and analysis techniques and possibly – in more candid terms – human error. Biggs & Ivison (2006) came to a similar conclusion, finding around double the source count in the *Hubble* Deep Field North as had been measured by Richards (2000) and tracking the problem to a simple arithmetical error rather than any fundamental problem with the data or their reduction.

One possible origin for some of the reported scatter may be the use of different VLA configurations for deep survey work, either through problems setting the absolute flux scale, or via inadequate correction for bandwidth smearing. We have separated the A- and B-configuration data centred on our LOCKMAN-E VLA pointing to test if this introduces notable differences in flux. We find a flux density ratio of $S_{\rm A}/S_{\rm B} = 1.03 \pm 0.21$ for those sources detected in both configurations with peak-to-noise ratios greater than 10. We conclude that use of different configurations does not significantly bias estimates of flux densities in our catalogues. The scatter must originate elsewhere, assuming that data have been calibrated carefully, using appropriate *uv* restrictions or calibrator models.

We have tested the possibility that spurious sources contaminate the samples by follow-

Table 3.6: The 1.4 GHz radio source counts.

S bin (mJy)	S (mJy)	N	$N/\Delta S/A_{\rm eff}$ ($\rm str^{-1}Jy^{-1}$)	$dN/dS \times S^{2.5}$ ($\rm str^{-1}Jy^{1.5}$)
0.020 - 0.032	0.025	91	$(9.71 \pm 1.02) \times 10^{11}$	3.07 ± 0.32
0.032 - 0.050	0.040	275	$(4.06 \pm 0.23) \times 10^{11}$	4.01 ± 0.23
0.050 - 0.078	0.062	373	$(1.60 \pm 0.08) \times 10^{11}$	4.92 ± 0.25
0.078 - 0.124	0.098	299	$(5.18 \pm 0.30) \times 10^{10}$	4.99 ± 0.29
0.124 - 0.195	0.155	161	$(1.46 \pm 0.12) \times 10^{10}$	4.39 ± 0.36
0.195 - 0.308	0.245	78	$(4.24 \pm 0.52) \times 10^{9}$	3.98 ± 0.48
0.308 - 0.485	0.386	55	$(1.87 \pm 0.28) \times 10^{9}$	5.48 ± 0.82
0.485 - 0.765	0.609	24	$(5.14 \pm 1.25) \times 10^{8}$	4.70 ± 1.14
0.765 - 1.206	0.961	20	$(2.70 \pm 0.74) \times 10^{8}$	7.72 ± 2.11
1.206 - 1.902	1.515	16	$(1.38 \pm 0.43) \times 10^{8}$	12.33 ± 3.83
1.902 - 3.000	2.389	7	$(3.81 \pm 2.02) \times 10^{7}$	10.63 ± 5.63

ing an identical source extraction procedure, but using the inverted (negative) signal map. In theory, noise can contaminate the number counts through the inclusion of spurious sources and by boosting intrinsically faint sources to higher flux densities. We predict, however, that the contamination by spurious sources is always less than 5 per cent for every flux density bin (see Fig. 3.5). Nevertheless, besides the large scatter seen in previous published number counts, our results are in good agreement with previous observations using the VLA's B configuration (Bondi et al., 2003; Seymour et al., 2004) and the Australia Telescope Compact Array (Prandoni et al., 2001; Hopkins et al., 2003).

3.6 Spectral indices

We have cross-matched (within 7 arcsec) the GMRT and VLA radio catalogues in order to estimate the spectral index of the radio emitters. This measurement yields evidence for the synchrotron mechanism which dominates the observed radiation from the sub-mJy radio population.

3.6.1 Astrometric precision

We plot in Fig. 3.11 the offsets of the VLA sources with respect to the GMRT positions, using only single sources (§3.3.3). The offset distribution is approximately Gaussian with ΔR.A. $= -0.60 \pm 0.71$ and ΔDec. $= 0.40 \pm 0.65$ arcsec (the mean and standard deviation in R.A. and Dec., respectively). These mean offsets of $\sim$0.5 arcsec are observed at all flux levels, and its origin is unknown. Garn et al. (2007) found an incorrect time stamp in the GMRT data, resulting in a rotation of the positions near the edge of each pointing. This problem was corrected during the reduction of our data and is not responsible for the observed offsets, which may instead relate to VLA correlator issues which have only recently come to light (Morrison et al. 2008, in preparation).

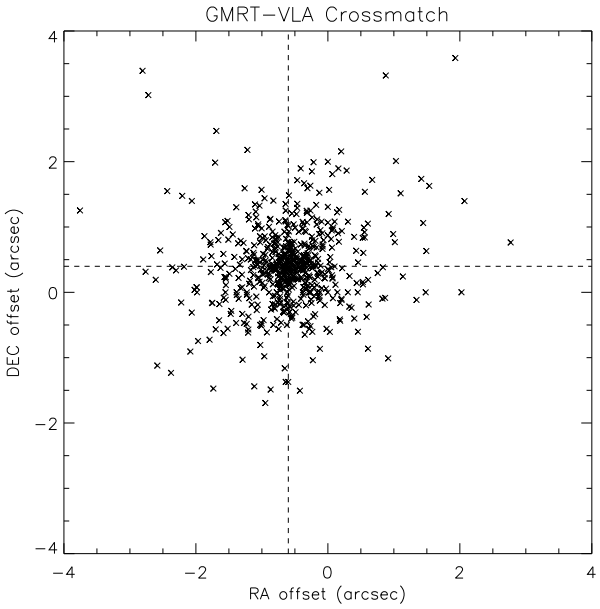

Figure 3.11: Relative offsets between single sources found at 1.4 GHz with respect to the 610 MHz GMRT positions. Offsets are approximately normally distributed. In R.A. and Dec. we find offsets of -0.60 ± 0.71 and 0.40 ± 0.65 arcsec, respectively. *Dashed lines* show the mean offset values.

An external reference is used to test the 610-MHz astrometry – recent work by Garn et al. (2008b) which includes a 610-MHz observation in the Lockman Hole. We find 89 common sources (see §3.8.1 for details) with a median offset of $\Delta\mathrm{RA} = -0.54 \pm 0.05$ and $\Delta\mathrm{DEC} = 0.00 \pm 0.04$. These offsets may help to explain the R.A. offset found in Fig. 3.11, but not that in Dec.

We have been unable to find a straightforward reason for the observed offsets between the VLA 1.4-GHz and GMRT 610-MHz sources. We have not implemented a positional shift in our catalogues, although we highlight this issue in the table captions.

3.6.2 Spectral indices

In Fig. 3.12 we show the radio spectral index between 610 MHz and 1.4 GHz as a function of flux density. We analyse the spectral indices based independently on GMRT- and VLA-selected samples, where a 610-MHz-selected catalogue naturally tends to prefer the detection of steep-spectrum sources while selection at 1.4 GHz favours flatter spectra.

Since the VLA and GMRT images have different resolutions, special care has to be taken when we analyse the results based on different frequency-selected samples. The 610-MHz catalogue, from a lower-resolution image, tends to have more counterparts per source than the 1.4-GHz catalogue. This issue confuses the statistical studies of spectral indexes since more unrelated galaxies are summed up or split depending on the sample criterion.

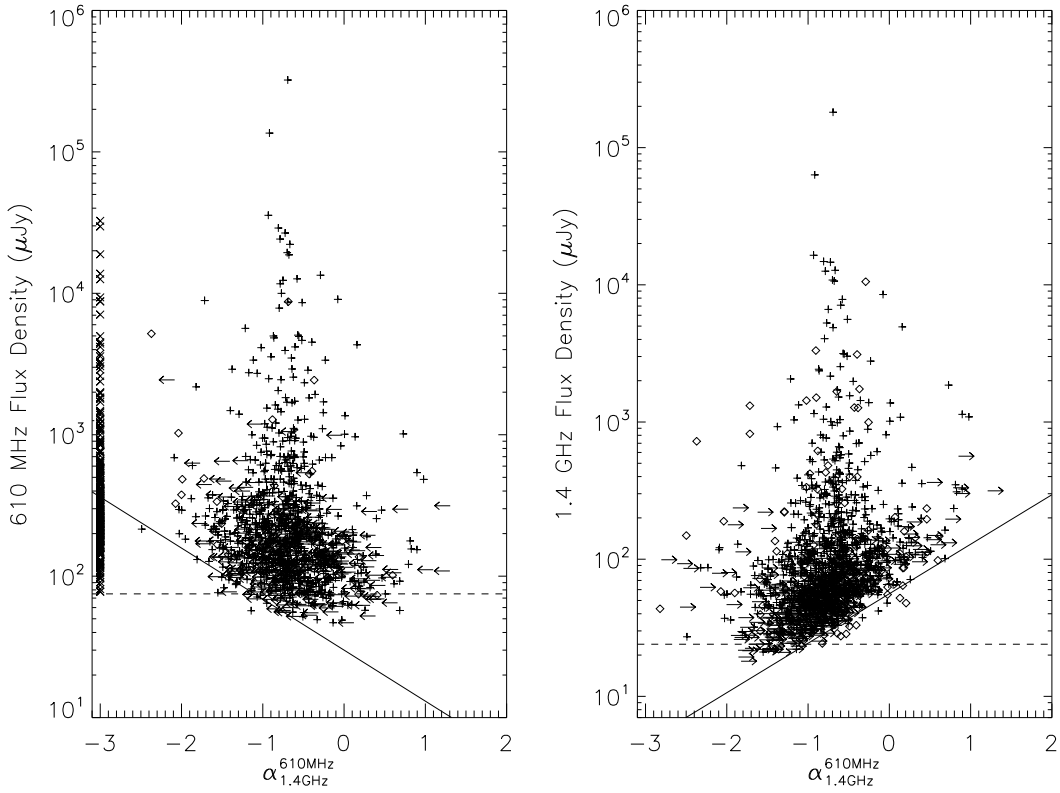

Figure 3.12: Spectral index, $\alpha^{610\mathrm{MHz}}_{1.4\mathrm{GHz}} = -2.77 \times \log(S_{610\mathrm{MHz}}/S_{1.4\mathrm{GHz}})$, as a function of flux density, based on a 610-MHz-selected sample (*top*) and a 1.4-GHz-selected sample (*bottom*). *Dashed* and *solid* lines correspond to the primary and secondary point-source flux limit for each survey. *Plus* symbols represent detections. *Arrows* represent upper limits. *Diamonds* represent unreliable upper limits. The *crosses* at $\alpha = -3$ are sources outside the overlapping region.

For example, given our selection criteria and the resolution difference between the observing frequencies, it is possible that a single source at 610 MHz is related to two single detections at 1.4 GHz. In this case, the spectral index of the GMRT source is calculated using the sum of the flux densities from both VLA sources. For the VLA-selected sources we have divided the flux density at 610 MHz based on the relative contribution from each VLA source (spectral indexes based on split sources are flagged as such). Where there is no clear close counterpart (within 7 arcsec), 5-σ upper limits are calculated using the local r.m.s. (§3.3.1), weighting by an area factor to compensate for the difference in resolution.

Fig. 3.12 shows the spectral indices for GMRT-selected (left) and VLA-selected (right) samples. Both distributions show a large scatter, casting doubt on previous studies which assume a clean star-forming galaxy population with a single spectral index in the sub-mJy radio regime.

Upper limits dominate at the faintest fluxes, partly due to the difficulty in obtaining counterparts so close to the detection threshold, where the catalogues are incomplete, and partly

due to the tendency to detect steeper-spectrum sources at 610 MHz or flatter-spectrum sources at 1.4 GHz. In our work, this bias does not allow the study of spectral index for sources with $S_{1.4\mathrm{GHz}} \lesssim 100\,\mu$Jy. The larger number of upper limits at 1.4 GHz reflects the extra depth of the VLA imaging.

In Table 3.7 we show the observed statistical results for spectral indices as a function of flux density (parenthesis show mock values – see below). In order to avoid a large fraction of upper limits in these statistical calculations, we have used only $\geq$10-σ (PNR) detections for each of the catalogue-based samples, but down to $5-\sigma$ for the counterpart. We find no trend in the distribution of spectral indexes toward fainter flux densities in either the GMRT- or the VLA-selected catalogues. Since these two different selection criteria tend to select spectra with different spectral indexes, numerical differences of $\sim$0.2 in the mean and $\sim$ 0.1 in the median α are seen in the frequency-based estimates for similar flux density bins. These results rule out the suggested flattening in spectral index at sub-mJy radio flux densities quoted in previous studies (Bondi et al., 2007; Garn et al., 2008a).

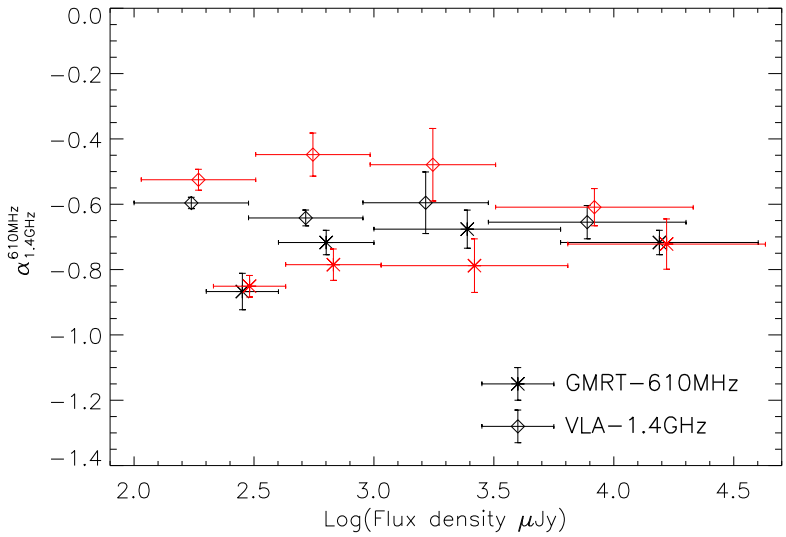

Figure 3.13: The median-bootstrap (*in black*) and the Kaplan-Meier (Feigelson & Nelson 1985) mean (*in red*) spectral indices as a function of flux density. Data are based on 610-MHz- and 1.4-GHz-selected samples and shown in Table 3.7. In the image, mean values are slightly shifted in flux density (just for clarity).

The constant mean and median values of α in the sub-mJy regime (certainly between $0.1-1$ mJy) is a robust result, and suggests the sub-mJy radio population is dominated by optically-thin synchrotron emission from star-forming galaxies and/or from steep-spectrum lobe-dominated FR AGN. We show the trend for the mean and median spectral index as a function of flux density in Fig. 3.13. The mean estimate (in red) includes upper limits using Kaplan-Meier product-limit estimator (ASURV – Feigelson & Nelson, 1985), and the median

Based on the 610-MHz GMRT catalogue				
610-MHz flux bin (mJy)	$\langle\alpha_{1.4\mathrm{GHz}}^{610\mathrm{MHz}}\rangle_{\mathrm{ASURV}}^{\mathrm{K-M}}$	$(\langle\alpha\rangle \pm \sigma_\alpha)_{\mathrm{normal}}$	$(\langle\alpha\rangle \pm \sigma_\alpha)_{\mathrm{biweight}}$	$\langle\langle\alpha_{1.4\mathrm{GHz}}^{610\mathrm{MHz}}\rangle\rangle_{\mathrm{bootstrap}}$
$6.00 - 40.00$	-0.72 ± 0.08	-0.72 ± 0.33 (-0.70 ± 0.02)	-0.73 ± 0.12 (-0.70 ± 0.01)	-0.72 ± 0.04 (-0.70 ± 0.00)
$1.00 - 6.00$	-0.79 ± 0.08	-0.69 ± 0.41 (-0.70 ± 0.05)	-0.71 ± 0.36 (-0.70 ± 0.04)	-0.68 ± 0.06 (-0.70 ± 0.00)
$0.40 - 1.00$	-0.79 ± 0.05	-0.71 ± 0.40 (-0.73 ± 0.16)	-0.74 ± 0.28 (-0.72 ± 0.15)	-0.71 ± 0.04 (-0.72 ± 0.00)
$0.20 - 0.40$	-0.85 ± 0.03	-0.81 ± 0.41 (-0.73 ± 0.28)	-0.80 ± 0.39 (-0.72 ± 0.28)	-0.78 ± 0.05 (-0.72 ± 0.00)
Based on the 1.4-GHz VLA catalogue				
1.4-GHz flux bin (mJy)	$\langle\alpha_{1.4\mathrm{GHz}}^{610\mathrm{MHz}}\rangle_{\mathrm{ASURV}}^{\mathrm{K-M}}$	$(\langle\alpha\rangle \pm \sigma_\alpha)_{\mathrm{normal}}$	$(\langle\alpha\rangle \pm \sigma_\alpha)_{\mathrm{biweight}}$	$\langle\langle\alpha_{1.4\mathrm{GHz}}^{610\mathrm{MHz}}\rangle\rangle_{\mathrm{bootstrap}}$
$3.00 - 20.00$	-0.61 ± 0.06	-0.61 ± 0.26 (-0.68 ± 0.02)	-0.68 ± 0.15 (-0.68 ± 0.02)	-0.65 ± 0.05 (-0.68 ± 0.00)
$0.90 - 3.00$	-0.48 ± 0.11	-0.48 ± 0.60 (-0.70 ± 0.04)	-0.65 ± 0.52 (-0.70 ± 0.04)	-0.60 ± 0.09 (-0.70 ± 0.00)
$0.30 - 0.90$	-0.45 ± 0.07	-0.55 ± 0.43 (-0.68 ± 0.18)	-0.66 ± 0.29 (-0.69 ± 0.17)	-0.63 ± 0.02 (-0.69 ± 0.00)
$0.10 - 0.30$	-0.52 ± 0.03	-0.57 ± 0.41 (-0.61 ± 0.44)	-0.61 ± 0.39 (-0.67 ± 0.39)	-0.60 ± 0.02 (-0.67 ± 0.00)

Table 3.7: Statistical properties of the distribution of spectral indexes as a function of flux density. For both the 610-MHz- and 1.4-GHz-selected samples we use only $\geq$10-σ detections to minimise the uncertainties from upper limits. *Columns:* (1) The flux density bin; (2) the mean value given by the Kaplan-Meier product-limit estimator (ASURV – Feigelson & Nelson, 1985) which includes possible upper limits in the bin; (3) the mean and standard deviation of the spectral index distribution based on detections only; (4) the central location (mean) and scale parameter (sigma) based on the biweight estimator which is resistant to outliers and non-Gaussian distributions (Beers et al. 1990); (5) the median value for the distribution based on a bootstrap approach. The parentheses shown in some of the columns are the statistical estimates based on a single $\alpha = -0.7$ population with input/extracted flux ratios from the mock sources described in §3.4.2. These constitute a useful check on the reliability of the results, e.g. whether the observed scatter is intrinsic or dominated by errors.

(in black) is obtained from detections using a bootstrapping approach. The small variations in these estimates reflect the non-Gaussianity and large scatter of the distribution, especially for the faintest detections.

The scatter of the whole $\alpha_{1.4\mathrm{GHz}}^{610\mathrm{MHz}}$ distribution is about $\sigma_\alpha \approx 0.4$ in the sub-mJy regime, which suggests the detection of a large variety of populations – probably a substantial number of synchrotron self-absorbed AGN cores (Blundell & Kuncic 2007; Snellen et al. 2000) and high-z ultra steep-spectrum sources (Jarvis et al. 2001).

Taking into account the point-source simulations from §3.4.2, we have estimated the distribution of spectral indices based on variations between input/extracted flux densities. Assuming a radio population with $\alpha = -0.7$, and taking into account the uncertainties in source extraction, we predict that the spectral index distribution should broaden towards faint fluxes, reaching a scatter similar to that observed in our faintest flux density bins (see Table 3.7). These simulations are presented in parenthesis next to the observed results, and imply that the broad distribution of spectral indices is intrinsic above $S \gtrsim 200\,\mu$Jy but dominated by the fitting (trumpet-like) uncertainties at fainter flux densities.

Based on all sources, 6 per cent (<13 per cent) and 6 per cent (<10 per cent) have $\alpha > 0$ in the GMRT- and VLA-selected catalogues, respectively (the fractions in parenthesis include upper limits). Inspection by eye to these flat-spectrum sources reveals a compact nature at both wavelengths, brighter in the VLA image than in the GMRT image, probably due to synchrotron self-absorption from compact ($\lesssim$1 kpc) GHz-peaked sources (Snellen et al. 2000), which are believed to be young FR II sources.

3.7 X-ray identifications

Deep, hard X-ray observations (in the 2–10 keV band) provide the most efficient method of identifying AGN in the Universe (Mushotzky 2004), at least with column densities $N_\mathrm{H} < 10^{24}\,\mathrm{cm}^{-2}$ (Compton thin). Heavily absorbed AGN are common (Maiolino et al. 1998) and are expected to be responsible for the bulk of the cosmic X-ray background (CXRB; Ueda et al. 2003; Hasinger 2004). Indeed, a large ($\sim 20-30$ per cent) fraction is believed to be Compton thick ($N_\mathrm{H} > 10^{24}\,\mathrm{cm}^{-2}$), a population missed even in the deepest X-ray observations. Given that radio observations are unaffected by obscuration, Simpson et al. (2006) have suggested that deep radio surveys may provide a method to find this missed population – the so-called QSO-2s.

X-ray observations can probe the nature of the faint sub-mJy radio population, and we can estimate the fraction of X-ray sources that are detected as a function of radio flux density.

As a preliminary study, we have cross-matched our VLA 1.4-GHz catalogue (Table 3.4) with one of the deepest ($\sim$1 Msec) X-ray surveys undertaken with *XMM/Newton* in the Lockman Hole (Mat Page, *private communication*). Inside the region covered by our VLA mosaic, the X-ray catalogue contains 678 sources with $S_{2-10\mathrm{keV}} > 10^{-16}\,\mathrm{erg\,sec}^{-1}\,\mathrm{cm}^{-2}$ (the flux in the

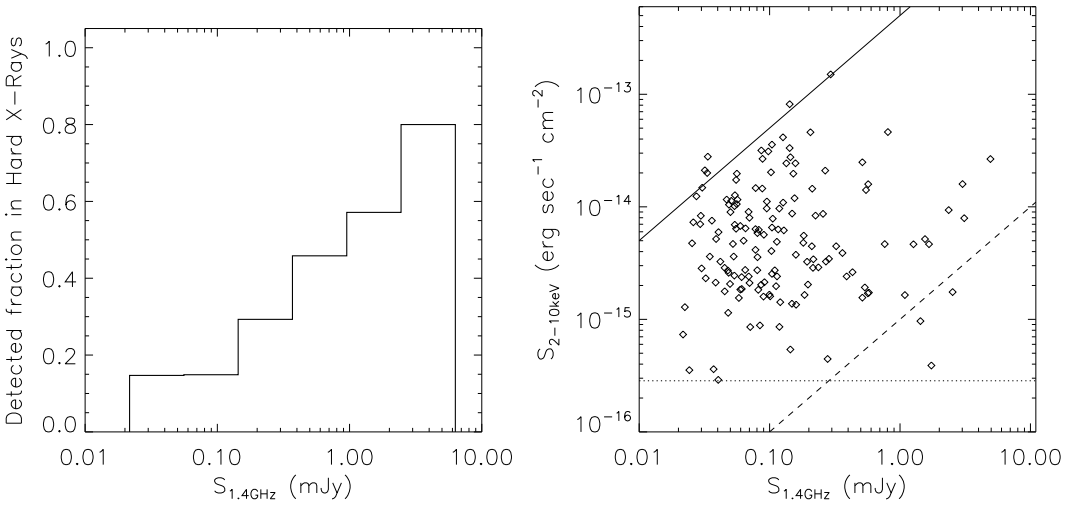

Figure 3.14: *Left:* The fraction number of radio sources (at 1.4 GHz) detected by *XMM/Newton* in the hard X-ray band ($S_{2-10\mathrm{keV}} \geq 10^{-16}\,\mathrm{erg\,sec^{-1}\,cm^{-2}}$). *Right:* The flux densities in the radio vs. X-ray for all cross-matched sources. The solid and dashed lines correspond to the expected correlation for radio-quiet AGN (Condon 1992; Ranalli et al. 2003) and star-forming galaxies (Brinkmann et al. 2000) introduced by Simpson et al. (2006), respectively. The dotted line represent the flux densitylimit of the X-ray catalogue.

hard X-ray band). We find 152 X-ray sources (22 per cent of the X-ray sample) with a $> 5\sigma$ (PNR) detection at 1.4 GHz, within 5 arcsec.

In Fig. 3.14 (*left*) we show the fraction of radio sources detected in the hard X-ray band as a function of radio flux density. We observe a clear decline of counterparts from 50 per cent at ~ 1 mJy to 15 per cent at $\lesssim 100\,\mu$Jy. In Fig. 3.14 (*right*), we see that a large number of radio sources are detected in X-rays at faint, $S_{1.4\mathrm{GHz}} < 300\,\mu$Jy, flux densities, as previously noted by Simpson et al. (2006). However, in terms of the relative *fraction* of radio sources with X-ray counterparts, they remain to be a minority. Fig. 3.14 (*right*) shows the expected correlations described by Simpson et al. (2006) between radio and X-ray fluxes for starbursts (Condon 1992; Ranalli et al. 2003) and radio-quiet AGN (Brinkmann et al. 2000) as dashed and solid lines, respectively. Deviations from these correlations can be produced by photoelectric absorption (lower X-ray fluxes) or by jets oriented close to our line of sight (larger radio fluxes). X-ray-absorbed sources are common (Ueda et al. 2003) and the scatter below the solid line probably indicates a large number of X-ray-obscured radio-quiet sources.

We note that our use of a much deeper X-ray observation than Ueda et al. (2008) ($S^{\mathrm{limit}}_{2-10\mathrm{keV}} = 3 \times 10^{-15}\,\mathrm{erg\,sec^{-1}\,cm^{-2}}$ used by Simpson et al.) does not show any clear evidence for a considerable increase of faint X-ray sources detected at radio wavelengths. We find that between $S_{2-10\mathrm{keV}} = 10^{-15} - 10^{-13}\,\mathrm{erg\,sec^{-1}\,cm^{-2}}$, the fraction of X-ray sources detected in the radio is relatively constant, $\sim$25 per cent. For the few sources identified below

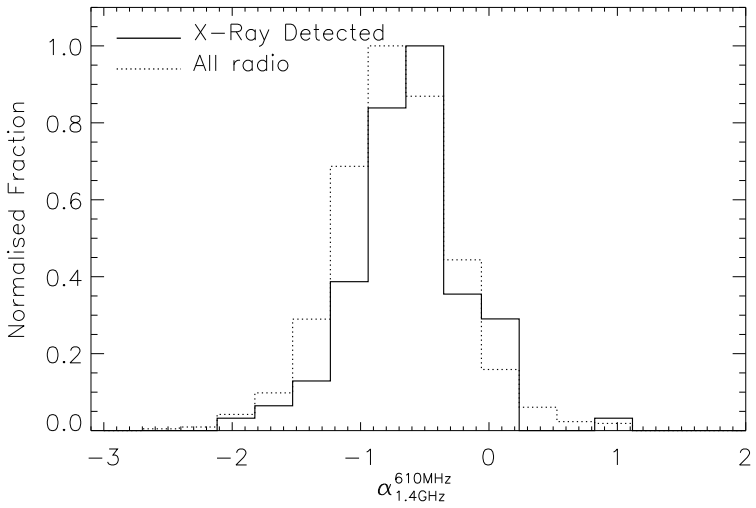

Figure 3.15: The radio spectral index between 610 MHz and 1.4 GHz for the sample of radio sources detected in the hard X-ray band.

10^{-15} erg sec^{-1} cm^{-2}, less than 15 per cent are detected in the radio.

Following the criteria of Simpson et al. for radio-quiet AGN – i.e. those sources lying closer to the solid than the dashed line in Fig. 3.14 (*right*) – our ability to probe even fainter X-ray fluxes has shown that the faint radio sources are mostly star-forming galaxies, or heavily absorbed sources.

If we assume the X-ray catalogue contains almost all the Compton-thin AGN in the redshift range of the radio sources (peak at $z \approx 0.8$) and that 25 per cent are Compton-thick AGN (undetected, obviously), we estimate that radio-quiet AGN comprise approximately 20 per cent of the radio population at $\lesssim 100\,\mu$Jy.

These results provide evidence for a transition at $S_{1.4\mathrm{GHz}} \approx 1$ mJy from bright and powerful AGN to a dominant star-forming galaxy population, contaminated at the $\sim$ 20-per-cent level by radio-quiet AGN (see § 4.4.1 for more details).

Of the 152 X-ray sources detected at 1.4 GHz, 97 have a reliable radio spectral index (PNR $>$ 5 in both 610 MHz and 1.4 GHz images). We plot, in Fig. 3.15, the radio spectral index of the X-ray sources alongside those of the entire VLA sample. A Kolmogorov-Smirnov test gives a probability of 11 per cent that both populations come from the same parent distribution. This low probability is also supported by the large number (55) of upper limits – X-ray sources detected at 1.4 GHz but undetected at 610 MHz – which suggests a flatter radio spectrum than the the bulk of the radio sample.

We conclude that radio-quiet AGN are no more numerous than star-forming galaxies at faint flux densities and tend to have flatter radio spectral indexes. The fraction of radio sources harbouring an AGN decreases towards faint flux densities, in disagreement with the tentative

suggestion of a dominant radio-quiet AGN population by Simpson et al. (2006).

3.8 Discussion

3.8.1 Comparison with a previous 610-MHz survey

Garn et al. (2008b) published a 6-σ 610-MHz catalogue covering 5 deg^2 in the Lockman Hole using GMRT. This allows a direct comparison with our detections at 610 MHz. The Garn et al. mosaic ($\sigma_{610\mathrm{MHz}} \sim 60\,\mu$Jy beam^{-1}) covers the north-west portion of our GMRT mosaic, with $\sim$0.6 deg^2 in common. Cross-matching their catalogue with ours reveals good agreement in flux densities for the brightest detections, suggesting our calibration has been adequate. However, we find a very large number of spurious, faint sources in their catalogue. In Fig. 3.16 (top) we show the fraction of Garn et al. sources which are recovered (within 7 arcsec) in our 4$\times$ deeper image, as a function of their radio flux densities. Given the depth of our image, we expect all Garn et al. sources should have a counterpart in our catalogue, but no hints of emission in the image (Fig. 3.16 – bottom) are found for the vast majority of their $\lesssim$ 3 mJy sources. We conclude that Garn et al. (2008b) have not provided a reliable 6-σ catalogue. It is interesting to note, however, that the number counts presented in Fig. 3.10 are in agreement with ours, probably because they base their number counts using the cleanest regions in their maps.

Looking at the full Garn et al. Lockman Hole image, their sources lie mainly near the edge of their mosaic, where the noise levels are greatest. The cleanest areas of their image contain very few sources, suggesting that their source extraction did not utilise knowledge of the local noise level. The distribution of 610-MHz sources in the *Spitzer* FLS (Garn et al. 2007, as used by Magliocchetti et al. 2008) appears similar, with a dearth of sources in the deepest portion of the mosaic (see figure 1 of Magliocchetti et al. 2008). This suggests that some of the faint steep-spectrum emitters seen by Magliocchetti et al. are spurious (by random association), and that their spectral index distribution is likely broadened at faint flux densities.

3.8.2 Comparison with a previous 1.4-GHz catalogue

Biggs & Ivison (2006) used some of the VLA data utilised in this paper. They present a high-resolution (A-configuration) map with a $\sim$1.3-arcsec beam (FWHM), and a different method of source detection. We find our work yields slightly higher flux densities. For the flux density ratios, we find a mean and standard deviation given by $S^{\mathrm{ours}}_{1.4\mathrm{GHz}}/S^{\mathrm{Biggs}}_{1.4\mathrm{GHz}} = 1.16 \pm 0.15$ for cross-matched sources with peak-to-noise ratio higher than 15. We have demonstrated in §3.5.3 that this difference is not produced by calibration problems from adding A- and B-configuration data. The origin of the normalisation difference is unknown. For example, reducing all our 1.4-GHz fluxes by a factor 1.16$\times$ would decrease the observed spectral indices (numerically)

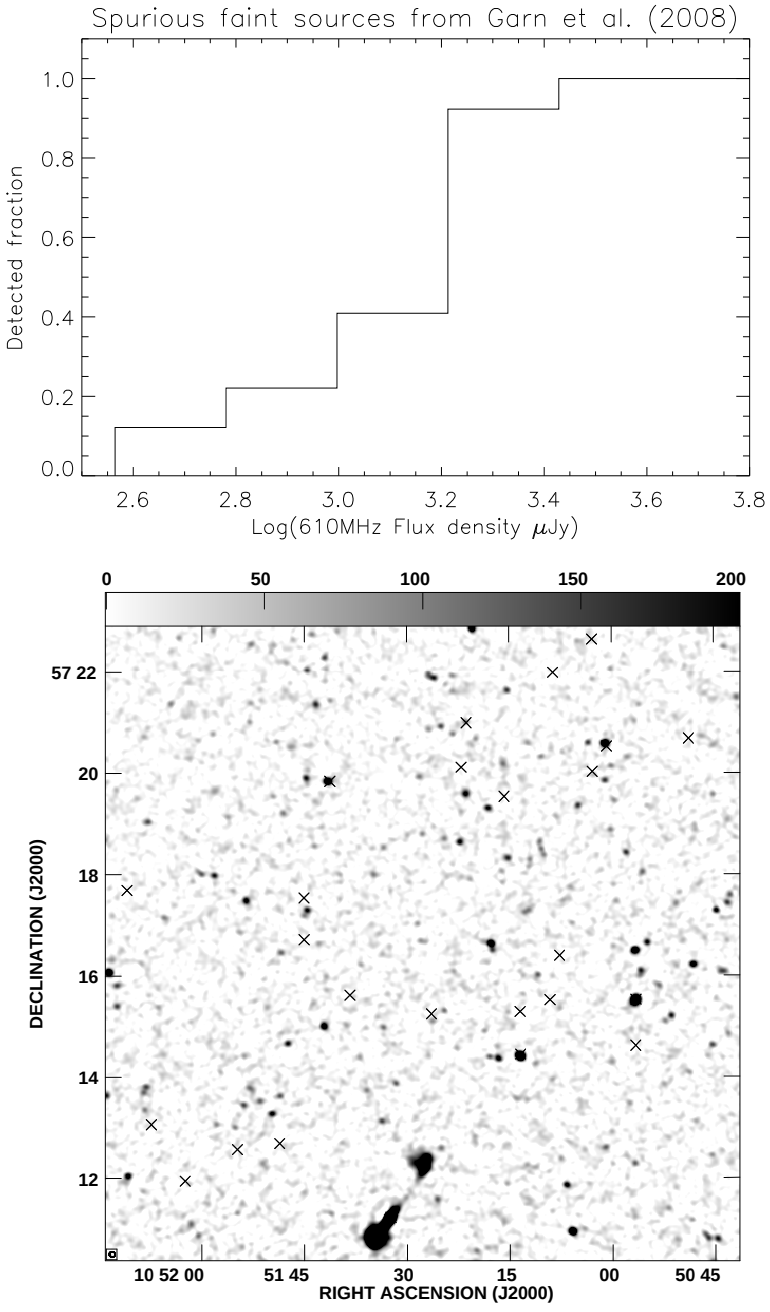

Figure 3.16: *Top:* Fraction of Garn et al. (2008b) sources recovered in our image as a function of their 610-MHz flux density. *Bottom:* An area of $12 \times 12\,\mathrm{arcmin}^2$ from our 610-MHz mosaic shown in greyscale with a linear stretch from 0–200 μJy beam^{-1}. Crosses show source positions catalogued by Garn et al. (2008b). We expect detections of all their sources since they have $S^{\mathrm{Garn}}_{610\mathrm{MHz}} > 300\,\mu$Jy.

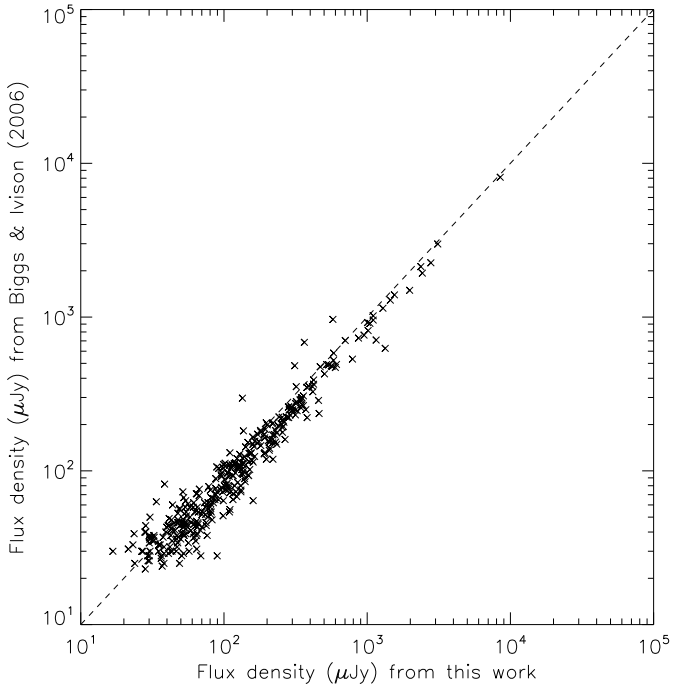

Figure 3.17: Integrated flux densities for the sources detected in the Lockman Hole at 1.4 GHz in comparison with a previous work by Biggs & Ivison (2006). Sources have been cross-matched using a search radius of 4.2 arcsec.

by 0.18 (i.e. the spectra become steeper), but we stress that this would not affect the absence of a trend in the spectral index distribution towards faint flux densities, nor the width of the observed α distribution.

3.8.3 Previous spectral index studies

The radio spectral index observed between 610 MHz and 1.4 GHz has been controversial since the earliest studies. Using the WSRT, Katgert & Spinrad (1974) found – from a small sample of sources with $S_{610\mathrm{MHz}} \gtrsim 10$ mJy – a spectral index distribution, $\alpha_{1.4\mathrm{GHz}}^{610\mathrm{MHz}} = -0.52 \pm 0.39$, an unusual result with a broad distribution with respect to higher frequency surveys. A much larger sample gave a similar result: $\alpha_{1.4\mathrm{GHz}}^{610\mathrm{MHz}} = -0.68 \pm 0.31$ (Katgert, 1979), statistically in agreement with the previous work, but showing clear evidence for a complex radio SED. Our survey covers only $\sim$1 deg^2 and therefore contains only a small number of sources in the $S_{610\mathrm{MHz}} \gtrsim 10$ mJy range. For these sources, we find a mean $\langle\alpha\rangle \approx -0.72$ and standard deviation of $\sigma_\alpha \approx 0.16$, in agreement with early results but with a considerably tighter distribution. Since these sources are mostly powerful steep-spectrum radio-loud AGN (Hopkins et al. 2000), we have also compared these spectral indexes with a sample of $z < 0.5$ FR II

Flux range	$\langle\langle\alpha_{1.4\mathrm{GHz}}^{610\mathrm{MHz}}\rangle\rangle^{\mathrm{Ref}}$	$\langle\langle\alpha_{1.4\mathrm{GHz}}^{610\mathrm{MHz}}\rangle\rangle^{\mathrm{Ours}}$
$0.5 < S_{1.4\mathrm{GHz}}$ (mJy)	$-0.67 \pm 0.05^{(1)}$	-0.63 ± 0.03
$0.15 < S_{1.4\mathrm{GHz}}$ (mJy) < 0.5	$-0.46 \pm 0.03^{(1)}$	-0.63 ± 0.02
$0.1 < S_{1.4\mathrm{GHz}}$ (mJy) < 0.15	$-0.61 \pm 0.04^{(1)}$	-0.59 ± 0.02
$1.0 < S_{610\mathrm{MHz}}$ (mJy)	$-0.56 \pm 0.04^{(2)}$	-0.71 ± 0.04
$0.5 < S_{610\mathrm{MHz}}$ (mJy) < 1.0	$-0.36 \pm 0.12^{(2)}$	-0.71 ± 0.04
$30 < S_{610\mathrm{MHz}}$ (mJy)	$-0.76^{(3)}$	-0.81 ± 0.11

Table 3.8: A direct comparison of our results with previous work on the spectral index between 610 MHz and 1.4 GHz: (1) Bondi et al. (2007); (2) Garn et al. (2008a); (3) Tasse et al. (2007). The double parentheses enclose median values, where we estimate our errors using a bootstrapping analysis.

sources ($\alpha_{750MHz}^{178MHz} = 0.79 \pm 0.14$, mean and scatter), finding good agreements as well (Laing et al. 1983).

With the advent of the GMRT, a variety of spectral index results have appeared in the literature. They cover different flux density ranges, so we present in Table 3.8 a comparison using the same flux ranges. We find good agreement – within the errors – with the estimates of Bondi et al. (2007) and Tasse et al. (2007), although not with Garn et al. (2008a), probably because of faint spurious associations (discussed in §3.8.1) or simply by incompleteness.

3.8.4 The nature of the sub-mJy radio emitters

There is little agreement in the literature concerning the optical properties of sub-mJy radio sources. Some studies support the idea that faint radio emitters are primarily star-forming galaxies. The spectroscopic classification of $S_{1.4\mathrm{GHz}} \gtrsim$ 40-μJy sources by Barger et al. (2007) shows that the dominant population has strong Balmer lines and no broad or high-ionisation lines. Likewise, Bondi et al. (2007) find that late-type starbursts dominate the $S_{1.4\mathrm{GHz}} \lesssim 100\,\mu$Jy regime based on analysis of an optical colour-colour plot (Ciliegi et al., 2005). Work based on a morphological classification in the optical (Padovani et al., 2007) shows that star-forming galaxies comprise only about a third of the sub-mJy population. More radically, based on another optical colour-colour study, Simpson et al. (2006) presented evidence for no change in the composition of the radio source population towards faint flux densities, arguing for a dominant passively-evolving massive elliptical galaxy population at all flux levels, $S_{1.4\mathrm{GHz}} \geq 100\,\mu$Jy. On the other hand, at $\sim$100 μJy, bright sub-millimetre-selected galaxies – which are clearly dominated by star formation – make up a significant number of the optically faint radio emitters (Ivison et al., 2002, 2007b; Chapman et al., 2004a; Pope et al., 2006).

The approaches taken by all these studies reflect the difficulty of disentangling star-forming galaxies from nuclear AGN activity.

We note that the large scatter ($\sigma_\alpha \approx 0.4$) seen in Fig. 3.12 for the spectral indices suggests a more complicated scenario than a simple star-forming galaxy population. We have found that radio spectral index as an estimator for the nature of the host galaxy is highly degenerate:

supernovae and nuclear activity are closely related (Gebhardt et al. 2000); redshift effects may be combined with synchrotron losses, steepening the spectra (Jarvis et al. 2001) and given the poor resolution of our images, spectral indices cannot be obtained for resolved components. Therefore, the galaxy nature is difficult to disentangle using the radio spectral index only. Nevertheless, we find a dominant optically thin population, with approximately 15–50 per cent of the faint sub-Jy radio population composed of radio-quiet AGN – based on hard X-ray detections (§ 3.14).

3.9 Concluding remarks

We have observed the Lockman Hole field using the GMRT at 610 MHz and the VLA at 1.4 GHz (in A and B configuration), obtaining two extremely deep radio images, with noise levels of 15 and 6 μJy, respectively. The data reveal a flattening followed by a second peak in the Euclidean-normalised number counts in the sub-mJy radio regime – evidence that star-forming galaxies may dominate at these flux densities.

We discuss the reliability of the 610-MHz catalogue presented by Garn et al. (2008b) in the Lockman Hole, finding that their catalogue is highly contaminated by spurious sources, with similar problems apparent in their previous *Spitzer* FLS catalogue (Garn et al. 2007). This may have influenced the detection of steep-spectrum radio emitters reported by Magliocchetti et al. (2008).

We study the spectral index of the radio emitters by combining the GMRT and the VLA measurements. The GMRT data are 4$\times$ times deeper than previous imaging, allowing for clean results and avoiding the well-known bias for steeper- or flatter-spectrum sources at longer or shorter wavelengths, respectively.

Our results, based on $\geq$10-σ selection criterion, show that the mean and median spectral index does not evolve as a function of radio flux density, certainly between 200 μJy and 10 mJy. We find $\alpha_{1.4\mathrm{GHz}}^{610\mathrm{MHz}} \approx -0.6$ to -0.7, which suggests optically-thin synchrotron radiation is the dominant radio-mechanism in the sub-mJy population. The two most probable contributors are star-forming galaxies and Fanaroff & Riley sources, ruling out a possible dominant flat-spectrum population (AGN-cores; GPS) at these faint flux densities (Bondi et al. 2007; Garn et al. 2008a).

We find the distribution of spectral indices has, however, a significant scatter ($\sigma_\alpha \approx 0.4$), which suggests a more complicated scenario where different populations mix together. The presence of inverted-spectrum ($\alpha > 0$) sources is just 6 per cent ($\lesssim$11 including upper limits) of the total sample.

Based on X-ray identifications, we estimate that only 15 per cent of the sample is made up of radio-quiet AGN at $S_{1.4\mathrm{GHz}} \lesssim 100\,\mu$Jy, rising to $\sim$50 per cent at $\sim$ 1 mJy. These results suggest a transition from a dominant AGN population to star-forming galaxies and radio-quiet AGN at sub-mJy radio fluxes, but disagree with the idea that radio-quiet AGN dominate the sub-mJy radio population, as proposed by Simpson et al. (2006).

CHAPTER 4

Exploring the infrared/radio correlation at high redshift*

"La evolución es la asimilación del aprendizaje en el tiempo, y para que exista la posibilidad de aprendizaje tiene que existir conocimiento que pueda ser aprendido, ahí es donde radica la importancia de la generación de conocimiento. Los científicos son personas que estudian la naturaleza desde distintos puntos de vista para aprender su funcionamiento y traspasar ese aprendizaje al resto de la sociedad. En definitiva, los científicos son importantes en la medida que sea positivo evolucionar, pero ¿realmente lo es?."

Christopher Thraves.

4.1 Introduction

The far-infrared/radio (FIR/radio) relation is one of the tightest correlations known in astronomy. Established over three decades ago (e.g. van der Kruit 1971; Helou et al. 1985), it covers about five orders of magnitude in luminosity (Condon 1992; Garrett 2002). The correlation is tightest for local star-forming galaxies and relates the integrated thermal emission from the dust present in star-forming regions with the non-thermal synchrotron emission produced by relativistic particles (cosmic rays) accelerated by supernova remnants (Harwit & Pacini 1975).

*This work has been published in Ibar et al. (2008).

A complete explanation of the origin of this remarkable correlation is essential for our understanding of how galaxies formed and evolved, particularly if the correlation extends from primeval galaxies to the fully mature galaxies observed locally, as recent studies have hinted (Kovács et al. 2006).

Being relatively direct probes of recent star formation, FIR and radio data are amongst the most powerful tools available to test whether primordial galaxies shared the same properties as galaxies present today. Low-frequency radio data have been used to estimate redshifts using radio-to-submm flux density ratios (e.g. Carilli & Yun 2000), and to determine the cosmic star formation history (e.g. Haarsma et al. 2000; Ivison et al. 2007a; Dunne et al. 2008; Smolčić et al. 2008), facilitating the investigation of the cosmic IR background (CIRB). If the relation between flux densities observed in the FIR and radio wavebands holds at high redshift, then we can exploit deep high-resolution radio imaging to resolve the CIRB and to explore the properties of luminous distant galaxies – for example, studies of submm (or "SCUBA") galaxies (Smail et al. 1997; Hughes et al. 1998) which are encumbered by the confusion encountered in the submm (rest-frame FIR) waveband, and studies of active galactic nuclei (AGN; Beelen et al. 2006) that are subject to selection biases caused by obscuration at shorter wavelengths.

While the combination of *Spitzer* observations at 24 and 70 μm and radio observations at 1.4 GHz support the universality of the FIR/radio correlation up to a redshift of approximately unity (Appleton et al. 2004), extending this correlation to higher redshifts requires extremely deep and complementary observations at radio and IR wavelengths, as well as reliable estimates of redshift. The work presented here is based on a deep multi-wavelength study in the Subaru-*XMM/Newton* Deep Field (SXDF). We have exploited 1.4-GHz images from the Very Large Array (VLA), reaching a 5σ flux density threshold of $\sim 35\,\mu$Jy and covering an area of approximately 1 deg^2. The region has also been observed to impressive depths at optical (SuprimeCAM; Furusawa et al. 2008), near-IR (UKIDSS-UDS; Lawrence et al. 2007) and mid-IR (*Spitzer* Wide-area IR Extragalactic Survey – SWIRE; Lonsdale et al. 2003) wavelengths.

Starburst galaxies, radio-quiet and radio-loud AGN are the three main populations which can be observed to high redshifts with the data employed in this work. It is known that radio-quiet AGN (i.e. Seyfert galaxies) follow the FIR/radio correlation (Roy et al. 1998), but on the other hand, radio-loud AGN may vary considerably in radio luminosities due to their extra core and jet radio emission, thus weakening and biasing the correlation. In theory, it is possible to identify these radio-loud AGN via their deviation from the expected relation and therefore to determine the fraction of these so-called "radio-excess" sources as a function of radio flux density. This would then allow us to constrain the predictions of synthesis population models for the transition at sub-mJy radio fluxes from radio-loud AGN to starburst galaxies/radio-quiet AGN (Dunlop & Peacock 1990; Jarvis & Rawlings 2004).

The aim of this work is to explore and discuss the correlation between the monochromatic fluxes at 24 μm and 1.4 GHz across a broad range of redshifts and test the capabilities of the relation for selecting radio-loud AGN (Donley et al. 2004).

Throughout this chapter we have used $\Omega_m = 0.3$, $\Omega_\Lambda = 0.7$ and $H_0 = 70\,\mathrm{km\,s^{-1}\,Mpc^{-1}}$ (Spergel et al. 2007).

4.2 Multi-wavelength observations in the SXDF

4.2.1 Radio observations at 1.4 GHz

Radio observations of the SXDF were carried out by Ivison et al. (2007b) during July 2003 using the VLA at 1.4 GHz. The total integration time was approximately 60 hours, reaching an r.m.s. depth of $7\,\mu\mathrm{Jy\,beam^{-1}}$ near the centre of the field. The radio map is centred at R.A. 2h 18m, Dec. $-5^\circ\ 0'$, with a synthesised beam (FWHM) of 1.86 arcsec $\times$ 1.61 arcsec at position angle 15°. The source detection was carried out using a $5\,\sigma$ threshold, sufficient to avoid significant contamination by spurious sources, obtaining a total number of 563 radio sources in an area of $\sim$0.45 deg^2.

In order to exploit the larger area covered by previous multi-wavelength observations in the SXDF, we have also used the 1.4-GHz catalogue presented by Simpson et al. (2006). Their observations comprised thirteen VLA pointings reaching a mosaic r.m.s. noise of $\sim$12–$20\,\mu\mathrm{Jy\,beam^{-1}}$. The Simpson et al. catalogue contains 505 sources and covers 0.8 deg^2 to a flux density limit of $100\,\mu$Jy.

By combining both radio samples, we obtained a total sample of 828 radio sources. Extended sources and obvious doubles, identified by eye, were considered as single emitters. The distribution of radio flux densities peaks at about $100\,\mu$Jy and reaches flux densities as faint as $35\,\mu\mathrm{Jy}$ ($5\,\sigma$) and as bright as 80 mJy.

4.2.2 Spitzer observations

The SXDF was observed by *Spitzer* as part of the SWIRE Legacy programme (Lonsdale et al., 2003). The SXDF lies inside one of the seven high-latitude SWIRE fields: the *XMM*-LSS field, which has a total area of 9.1 deg^2. Observations were obtained at 3.6, 4.5, 5.8 and $8.0\,\mu$m with IRAC and at 24, 70 and $160\,\mu$m with MIPS (Surace et al. 2004). In order to explore the FIR/radio correlation, we have used only the detections at $24\,\mu$m. It is known that use of the monochromatic 24-μm flux densities yields a larger scatter than the 70-μm data (Appleton et al. 2004); however, we are limited by the relatively shallow coverage at $70\,\mu$m and the more severe confusion at that wavelength.

To explore the FIR/radio relation as a function of redshift, we use the combined radio source catalogue described in §4.2.1 and cross-match it with the conservative ($10\,\sigma$) SWIRE source catalogue retrieved from the *Spitzer* Science Centre archive. We obtained 370 counterparts with fluxes $S_{24\mu\mathrm{m}} \gtrsim 0.4$ mJy using a 12.5-arcsec-diameter aperture for the photometry.

We then extended the catalogue to fainter 24-μm flux densities by measuring the observed

flux density on the 24-μm map, using the same diameter aperture centred at the radio positions. This allowed the inclusion of 125 sources with 24-μm flux densities of $S_{24\mu\mathrm{m}} \gtrsim 200\,\mu$Jy ($\sim 4\,\sigma$; Shupe et al. 2008). In this work, for all the remaining radio sources we used upper limits at $S_{24\mu\mathrm{m}} = 200\,\mu$Jy.

4.2.3 Subaru and UKIRT observations

The SXDF is home to the very deep optical survey undertaken by Subaru/SuprimeCAM (Miyazaki et al. 2002). This comprises five overlapping pointings, providing broad-band photometry in the $BVRi'z'$ filters to typical 5-σ (AB magnitude) depths of $B = 27.5$, $V = 26.7$, $R = 27.0$, $i' = 26.8$ and $z' = 25.9$, respectively (2-arcsec-diameter apertures). The seeing in the composite images is $\sim$0.8 arcsec (Sekiguki et al. 2005).

The central region of the SXDF is also being observed at near-IR wavelengths with the Wide-Field Camera (WFCAM) on the 3.8-m United Kingdom Infrared Telescope (UKIRT). As the deepest tier of the UKIRT Infrared Deep Sky Survey (UKIDSS, Lawrence et al. 2007), the Ultra Deep Survey (UDS) aims to cover 0.8 deg^2 to $K_{\mathrm{AB}} = 25$. In this work, we use the UKIDSS First Data Release (DR1; Warren et al. 2007) where the 5-σ point source depths (in AB magnitudes) at J and K are 23.61 and 23.55, with seeing of 0.86 and 0.76 arcsec, respectively.

We have used the K-band as the reference to cross-match with all other near-IR and optical images. Unfortunately, the UDS map misses part of the radio coverage of the SXDF, limiting the radio sample to an area with 726 radio sources, out of which 639 (88 per cent) have clear counterparts in the UDS K data within a search radius of 1.5 arcsec.

4.2.4 Photometric redshifts

We obtained reliable photometric redshifts for 586 of the radio sources detected at near-IR wavebands. The estimation was carried out using all available detections[1] from the B, V, R, i', z', J, K, 3.6-μm and 4.5-μm photometric bands and considering a conservative criteria: not including those sources with poor χ^2 fitting nor those contaminated by halos from nearby stars.

The spectral energy distribution (SED) fitting procedure provides a photometric estimation consistent within $\Delta z/(1+z) = 0.05 \pm 0.04$ for the UDS galaxies in general (see Cirasuolo et al. 2007 for details), and spectroscopic redshifts available for 63 of the 586 radio sources (Yamada et al. 2005, Simpson et al. 2006 and the NASA Extragalactic Database) indicate that the photometric redshifts of the radio sources are also accurate at this level. The precision of this estimation is good enough to allow an adequate k-correction to the data (see Fig. 4.1). The resulting redshift distribution of the radio sources peaks at about $z \sim 0.7$ and includes galaxies up to $z \approx 3.5$.

[1] In this work, the photometric redshifts and the cross-matching of all photometric broad bands with the radio catalogue were provided by Michele Cirasuolo.

4.3 The FIR/radio relation

Based on the analysis presented in § 4.2, 369 sources (out of potentially 726 due to the missed UDS area) have both a 24-μm detection with flux density $S_{24\mu\mathrm{m}} > 200\,\mu$Jy and a reliable redshift (49 of which are spectroscopic).

We present in Fig. 4.1 the FIR/radio relation in terms of the basic observable parameter, q_{24} – the ratio between the monochromatic fluxes at 24 μm and 1.4 GHz, $\log(S_{24\mu\mathrm{m}}/S_{1.4\mathrm{GHz}})$ – as a function of redshift. Ideally, the correlation should be calculated using the bolometric FIR flux, however the paucity of long-wavelength data makes this quantity difficult to estimate prior to the future arrival of SCUBA-2 (Holland et al. 2006) and/or the *Herschel Space Observatory* (Poglitsch et al. 2006) – see Fig. 4.2.

4.3.1 Un-k-corrected data

Fig. 4.1 shows that the vast majority of the sources detected at 24 μm follow a tight correlation between q_{24} and redshift, up to $z \approx 3.5$. Upper limits have been included using $S_{24\mu\mathrm{m}} = 200\,\mu$Jy and show probable evidence for a large number of radio-excess sources (i.e. radio-loud AGN) at the observed radio flux density regime.

K-corrections to the data have been tested assuming standard starburst galaxy templates for the 24-μm detections and a simple power law for the radio flux densities. The expected variations of q_{24} as a function of redshift are overplotted in Fig. 4.1 and are used to study and characterise the behaviour of the star-formation-dominated source distribution. Nevertheless, the presence of radio-loud AGN sources in the sample introduces outliers in the correlation that may cover a wide range of q_{24} values due to radio excess emission coming from core and jet structures; for example, the radio-loud AGN such as Cygnus A (a powerful double-lobed radio galaxy) and Centaurus A (one of the closest known radio galaxies) have $q_{24} = -3.2$ and -1.1 values, respectively, far away from the main data trend from Fig. 4.1. In particular, our data show that the population with $S_{1.4\mathrm{GHz}} > 3.2$ mJy ($10^{-2.5}$ Jy; large squares in Fig. 4.1), characterised to be AGN-dominated by Condon (1992), have $q_{24} \lesssim -1$, well below the bulk of the data points and similar to the estimation obtained from the composite radio-loud AGN template. Since we expect and want a correlation valid for star-forming systems, sources with $S_{1.4\mathrm{GHz}} > 3.2$ mJy are excluded from our analysis of the FIR/radio correlation, basically because these sources are predominantly radio-loud AGN that introduce biases in the statistics.

Using the biweight estimator[2] (Beers et al. 1990) to characterise the data, we find a central location (mean) and scale parameter (sigma; all q_{24} values quoted in this chapter will similarly be given in this way) given by $q_{24} = 0.66 \pm 0.39$ (based on all detections at 24 μm including sources without estimated redshifts). The sub-sample of sources with $0 < z < 1$ gives

[2] In order to statistically describe the data, we used the biweight estimator which is resistant to outliers and is also robust for a broad range of non-Gaussian distributions. This is essential to remove remaining AGN from the statistics of the sample.

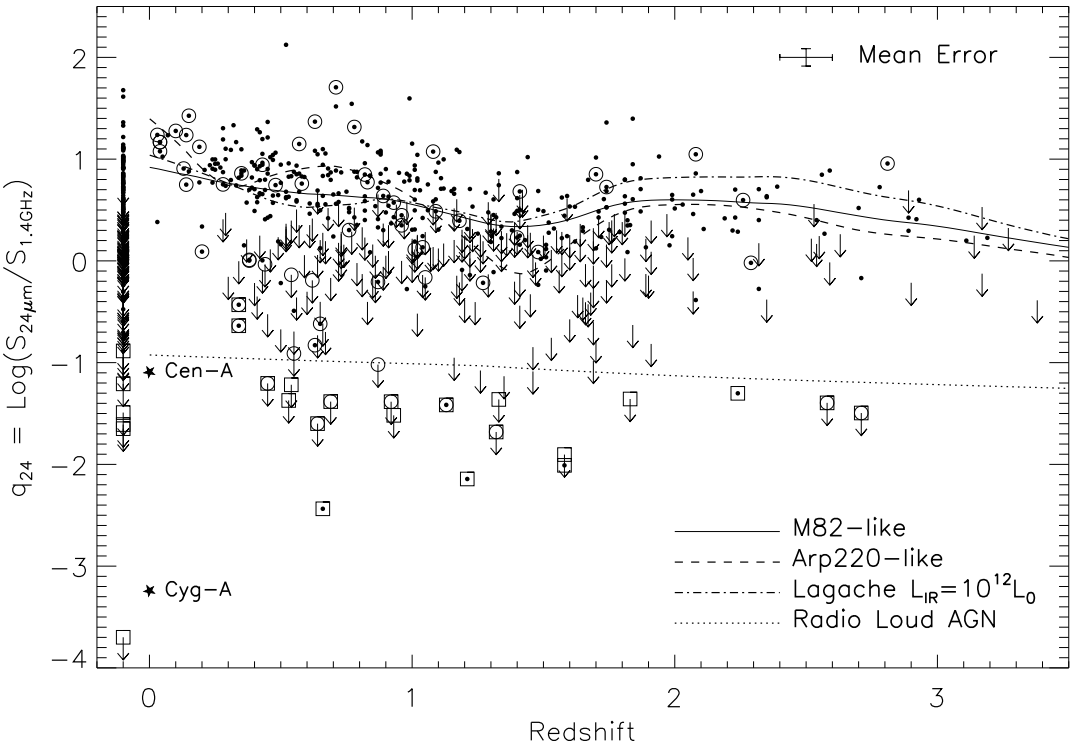

Figure 4.1: *Black dots:* ratio between the observed monochromatic fluxes at 1.4 GHz and 24 μm, $q_{24} = \log(S_{24\mu\mathrm{m}}/S_{1.4\mathrm{GHz}})$, as a function of redshift. Note that these data have not been *k*-corrected. *Downward arrows:* upper limits considering a mid-IR flux threshold given by 200 μJy. Sources without photo-z's are plotted at $z = -0.1$. *Large circles:* sources with spectroscopic redshifts. *Large squares:* sources with radio flux densities $S_{1.4\mathrm{GHz}} > 3.2$ mJy. Uncertainties in the observed flux densities give an average q_{24} mean error of ~ 0.1 dex, and error bars in redshift are approximately $\sigma_z \approx 0.1$ (Cirasuolo et al. 2007). Overplotted lines show different *k*-corrections for the observed q_{24} values as a function of redshift. The assumed mid-IR templates were convolved with the 24-μm filter from *Spitzer*/MIPS and are used to show the expected variation of the q_{24} values as a function of redshift. Three of these mid-IR templates are based on star-forming galaxies: two local standard massive starburst galaxies, M82 and Arp 220, and a SED model for an ULIRG galaxy with $L_{\mathrm{IR}} = 10^{12}\,\mathrm{L}_{\odot}$, as described by Lagache et al. (2004). All these three templates are assumed to have a simple spectral index $\alpha = -0.7$ for the radio emission, where $S_\nu \propto \nu^\alpha$, and normalised to the best fit to the data detections. Finally, a composite spectrum for radio-loud AGN given by Elvis et al. (1994) is also included, although as indicated by the locations of Cen A and Cygnus A, radio-loud AGN may be distributed over a wide range of q_{24} values. In particular, this template is not normalised to the best fit but uses values from the actual composite spectrum at both wavelengths.

an observed $q_{24} = 0.80 \pm 0.33$, in agreement with the results of Appleton et al. (2004), i.e. $q_{24} = 0.84 \pm 0.28$. The data also suggest a decreasing trend of q_{24} as a function of redshift. A

simple linear regression to the detected sources with estimated redshift gives a dependency $q_{24}(z) = (0.85 \pm 0.01) + (-0.20 \pm 0.01)\, z$. Nevertheless, this trend is probably seen because data have not been *k*-corrected (Hogg et al. 2002) as we describe later. It is worth noticing that the available 49 sources with spectroscopic redshifts support the validity of the photometric estimation at high redshift (large circles in Fig. 4.1).

4.3.2 *k*-corrected data

IR spectroscopic studies of local starburst galaxies have shown three main components in the mid-IR range (5–38 μm): silicate bands around 10 and 18 μm, a large number of PAH emission features, and a slope of the spectral continuum, where an AGN may be present (Brandl et al. 2006). In order to model the *k*-correction to the mid-IR emission from the bulk of the star-forming sources, we have convolved the SED of M82 (a local standard starburst galaxy with a distribution obtained from a fit to the observed photometry presented by Silva et al. 1998 – see Fig. 4.2), Arp 220 (obtained from photometry listed in the NASA/IPAC Extragalactic Database and compiled by Pope et al. 2006) and a model of an ultraluminous IR galaxy (ULIRG; $L_{\rm IR} = 10^{12}\,{\rm L}_{\odot}$) given by Lagache et al. (2004), with the 24-μm filter profile from *Spitzer*/MIPS. The radio emission is assumed to be well represented by a power law with a spectral index $\alpha = -0.7$, based on an average faint radio source (Condon 1992; see also Chapter 3). Note that the assumption of these *k*-corrections may largely change the q_{24} values at high redshift, mainly due to the 10-μm silicate feature redshifted to $z \approx 1.5$, where variations of up to an order of magnitude in *k*-correction are seen. The overplotted lines, in Fig. 4.1, show the expected change in the observed q_{24} parameter as a function of redshift based on the different adopted templates. Apart from the composite radio-loud spectra, the *k*-corrections have been normalised to the best fit to the data.

A descending trend in q_{24} as a function of redshift is expected from all three starburst-like *k*-corrections, in agreement with the observed slope. The *k*-corrected relation based on sources with mid-IR detections ($> 200\,\mu$Jy) and estimated redshifts, changes to $q_{24} = 0.99 \pm 0.32,\ 1.45 \pm 0.38,$ and 1.08 ± 0.37 (biweight estimator) using the M82-like, Arp 220-like and the Lagache et al. model, respectively. The M82-like *k*-corrected q_{24} values are presented in the upper panel of Fig. 4.3, to demonstrate the improvement in the correlation as a function of redshift. Fig. 4.4 shows a redshift-binned version of this plot (for the 24μm-detected sources), demonstrating that both the mean and scatter of the M82-like *k*-corrected q_{24} value remain constant out to $z \sim 3.5$; it also demonstrates that *k*-correcting with an Arp 220-like spectrum leads to large variations in the relation with redshift. Based upon this behaviour of the distribution, we argue that an M82-like *k*-correction gives the nicest description for the bulk of the star-forming sources.

The M82-like *k*-correction to all radio sources with detections at 24μm in the range $0 < z < 1$ gives $q_{24} = 1.03 \pm 0.31$, in agreement with the previous Appleton et al. (2004) estimate ($q_{24} = 1.00 \pm 0.27$). A simple linear regression to the M82-like *k*-corrected data is given by

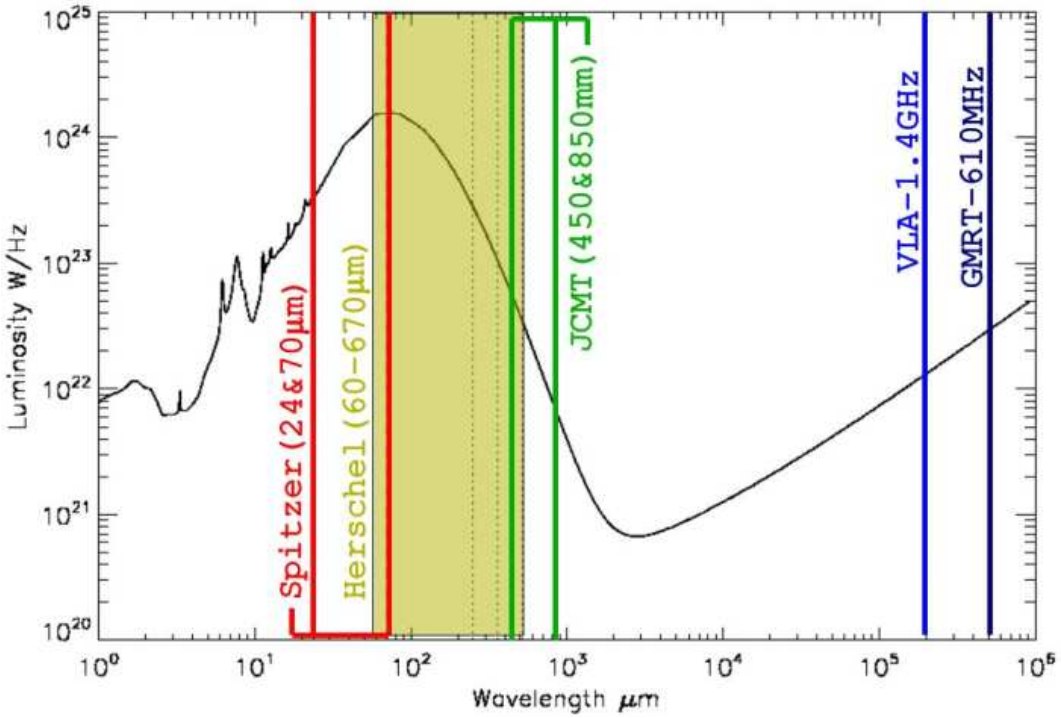

Figure 4.2: The M82 template used in this work (Silva et al. 1998). The *Spitzer*-24 μm band clearly shows the *k*-correction issues we expect to have for observing high redshift galaxies, specially by the silicate absorption band at 10 μm. We also show the *Spitzer*-MIPS, *Herschel*-PACS/SPIRE, JCMT-SCUBA2, VLA-1.4 GHz and GMRT-610 MHz bands for comparison.

$q_{24}(z) = (0.94 \pm 0.01) + (-0.01 \pm 0.01)\, z$, suggesting a constant dependency (at 1σ level) for the q_{24} fraction with redshift. This result assumes that all galaxies in the sample can be fitted with a single M82-like template, although the fact that the correlation naturally appears to have the same mean and scatter as a function of redshift, up to $z \sim 3.5$, is highly suggestive that the FIR/radio correlation holds all the way back to primordial times.

4.3.3 The correlation based on a complete radio sample

The mean and scatter values quoted for the correlations described above may be being biased by incompleteness at 24 μm for sources with faint radio fluxes: a large number of star-forming dominated radio sources with $S_{1.4\mathrm{GHz}} \lesssim 300\,\mu$Jy are not expected to have been detected at 24 μm (see for example Orienti et al. 2004). To demonstrate this problem, we plot in Fig. 4.5 the mean q_{24} as a function of a cut-off in the 1.4-GHz flux density. It clearly shows a decreasing trend for the mean q_{24} from fainter radio fluxes up to $S_{1.4\mathrm{GHz}} \approx 300\,\mu$Jy, where a flattening starts to appear. This means that considering a high enough radio cut-off, the correlation becomes independent of the radio sample. Given by these results, we have decided to analyse the correlation based on those radio sources which have got a flux density, $S_{1.4\mathrm{GHz}} > 300\,\mu$Jy.

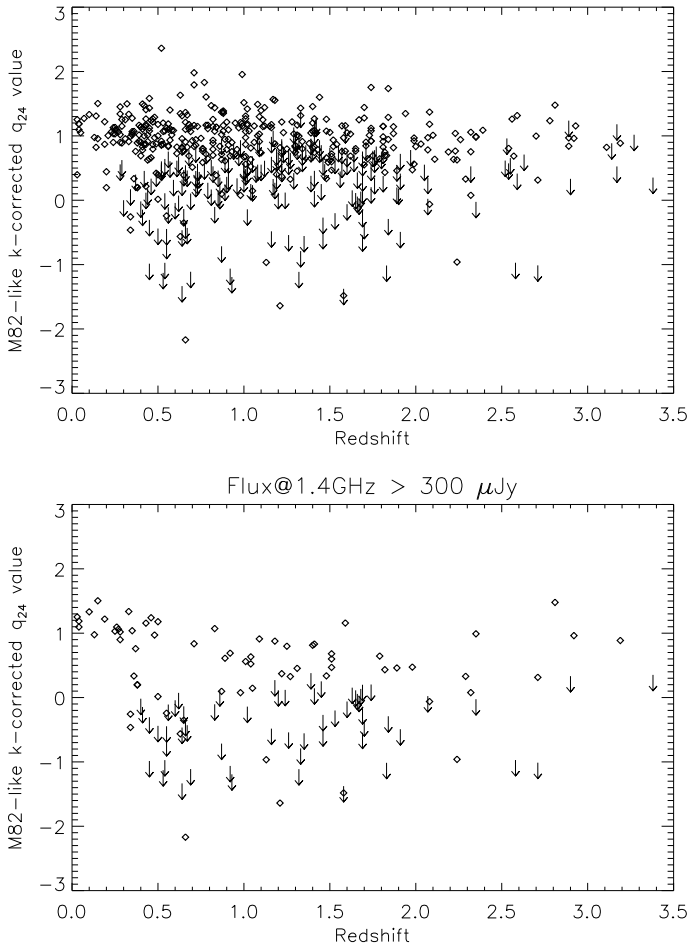

Figure 4.3: *K*-corrected q_{24} values as a function of redshift, using a M82-like template (Silva et al. 1998) for the mid-IR and a spectral slope $\alpha = -0.7$ for the radio emission. *Top:* Full radio sample. *Bottom:* Radio sources with 1.4-GHz flux densities above 300 μJy. Upper limits are considered at $S_{24\mu\mathrm{m}} = 200\,\mu$Jy.

This radio sample is essentially complete at 24 μm for star-forming galaxies, and all residual 24-μm non-detections are associated with radio-loud AGN activity (see below).

Using the biweight estimator, we find that for the radio population with $S_{1.4\mathrm{GHz}} > 300\,\mu$Jy and mid-IR detections ($S_{24\mu\mathrm{m}} > 200\,\mu$Jy), the observed q_{24} values has significantly lower mean and larger scatter for the (non-*k*-corrected) correlation $q_{24} = 0.30 \pm 0.56$ (it changes to $q_{24} = 0.70 \pm 0.63$ for the sub-sample of sources at $0 < z < 1$).

A histogram of q_{24} for the sources with $S_{1.4\mathrm{GHz}} > 300\,\mu$Jy is shown in Fig. 4.6. It shows that the bulk of the undetected sources are found below $q_{24} = -0.18$ due to the 200-μJy threshold adopted for the mid-IR image. This value of q_{24} implies sources three times brighter in radio luminosity than those from our observed mean value $\langle q_{24} \rangle = 0.30$, and ~ 10.5 times brighter than the observed mean value found by Appleton et al. (2004), $\langle q_{24} \rangle = 0.84$. Yun et al. (2001)

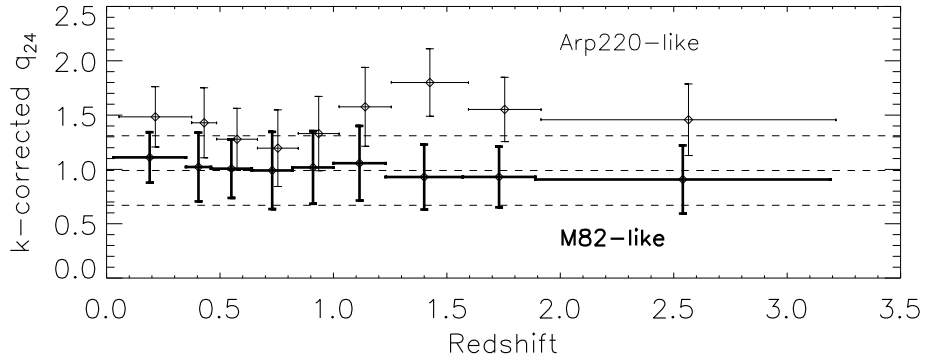

Figure 4.4: Binned mean and scatter of the M82-like *k*-corrected 24μm/1.4 GHz correlation (thick black data) as a function of redshift, based on the full radio sample. The overplotted lines correspond to the mean and 1σ limits, for the all-redshift distribution. Also shown (in thin black data) are the equivalent values for an Arp 220-like *k*-correction (shifted by an small factor in order to improve the visualisation only), which results in considerably more residual redshift variation. Note that the significantly higher q_{24} values for the Arp 220-like *k*-correction results from the upturn in the Arp 220-like correction at $z < 0.3$ and due to the particularly extreme silicate absorption features (cf. Fig. 4.1).

have defined radio-excess sources as those whose radio luminosity is $\geq$ 5 times the value predicted from the FIR/radio correlation. In this sense, radio-loud AGN based on 24-μm detections are sensitive to the assumed mean value for the FIR/radio correlation (Appleton et al. 2004, Donley et al. 2005, Boyle et al. 2007). We find that 62 per cent of the radio sources (24 detections and 82 upper limits) plotted in Fig. 4.6 have $q_{24} < -0.18$. These values clearly suggest that there are a large number of radio-loud AGN in this radio flux regime.

It is worth noting that the incompleteness produced by sources without photometric redshifts (compare thick continuum and dashed lines in Fig. 4.6) does not introduce significant changes in the mean and scatter of the q_{24} distribution.

The *k*-corrected mean and scatter values (biweight estimator) for the distribution of sources with $S_{1.4\mathrm{GHz}} > 300\,\mu$Jy, mid-IR detections ($> 200\,\mu$Jy) and estimated redshifts, changes to $q_{24} = 0.71 \pm 0.47$, 1.25 ± 0.47, and 0.77 ± 0.48 after using the M82-like, Arp 220-like and Lagache et al. model, respectively. The bottom panel in Fig. 4.3 shows the M82-like *k*-corrected q_{24} values as a function of redshift for this sub-sample. It suggests a slight descending trend, from $z < 0.5$ to higher redshifts, probably associated with the presence of steeper mid-IR spectra for brighter radio sources, although it is not possible to statistically discriminate a better representative SED between the tested templates.

A simple linear regression to the M82-like *k*-corrected q_{24} distribution, based on radio sources brighter than 300μJy and detected at 24μm, is given by $q_{24}(z) = (0.71 \pm 0.04) + (-0.03 \pm 0.03)\, z$. For this complete radio sample, we also find a flat distribution at 1σ level, suggesting the validity of the FIR/radio correlation up to $z \approx 3.5$. Note, however that even at these bright radio flux densities, at $z \gtrsim 1$ the upper limits may overlap with the mean

	Radio sample	q_{24} correlation mean & scatter	Linear regression	M82-like k-corrected q_{24} mean & scatter	Linear regression for the M82-like k-corrected q_{24}'s
(1)	$S_{24\mu\mathrm{m}} > 200\mu\mathrm{Jy}$	0.66 ± 0.39	$q_{24} = (0.85 \pm 0.01) - (0.20 \pm 0.01)\, z$	0.99 ± 0.32	$q_{24} = (0.94 \pm 0.01) - (0.01 \pm 0.01)\, z$
(2)	$S_{24\mu\mathrm{m}} > 200\mu\mathrm{Jy}$ & $0 < z < 1$	0.80 ± 0.28		1.03 ± 0.31	
(3)	$S_{1.4\mathrm{GHz}} > 300\mu\mathrm{Jy}$ & $S_{24\mu\mathrm{m}} > 200\mathrm{Jy}$	0.30 ± 0.56	$q_{24} = (0.66 \pm 0.04) - (0.28 \pm 0.03)\, z$	0.71 ± 0.47	$q_{24} = (0.71 \pm 0.04) - (0.03 \pm 0.03)\, z$
(4)	$S_{1.4\mathrm{GHz}} > 300\mu\mathrm{Jy}$ & $S_{24\mu\mathrm{m}} > 200\mu\mathrm{Jy}$ & $0 < z < 1$	0.70 ± 0.63		0.95 ± 0.56	

Table 4.1: Summary of the results presented in § 4.3. The linear regressions are based on the detected sources at 1.4 GHz and 24 μm, using intrinsic error bars from the source extraction processes.

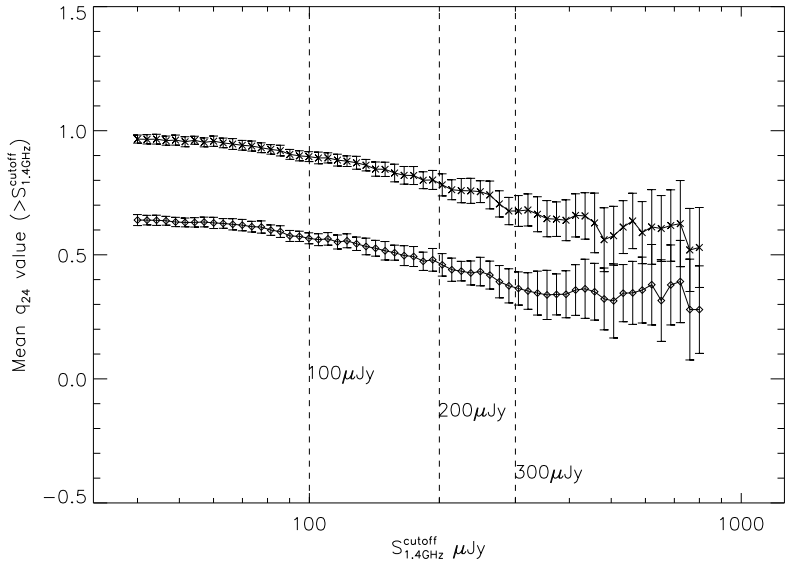

Figure 4.5: Mean q_{24} value as a function of cut-off in radio flux density. Diamonds and crosses are based on the observed and M82-like *k*-corrected data, respectively, both showing similar dependencies with the cut-off in radio. The error bars represent the uncertainty on the mean value estimated using boot-strap re-sample technique. The vertical dashed lines are at 100 μJy, 200 μJy and 300 μJy. Since sources with $S_{1.4\mathrm{GHz}} > 3.2$mJy ($10^{-2.5} Jy$) are essentially all radio-loud AGN (Condon 1984), these were not included in the estimation for the mean value.

value found for the correlation, suggesting the possibility of confusion at higher redshifts between radio-loud AGN and those affected by mid-IR features in the SEDs. Future studies with submm/FIR facilities, such as SCUBA-2 and the *Herschel Space Observatory*, will help to better estimate the total bolometric FIR luminosity, and therefore discriminate between those sources affected by SED features or due to powerful radio AGN activity.

4.4 Radio-loud AGN activity

4.4.1 The transition from radio-loud AGN to star-forming-dominated galaxies

Making use of the M82-like *k*-corrected data presented in the last section, we have worked out a method of selecting radio-loud AGN from our radio sample, based on different q_{24} thresholds.

It is well known that most powerful radio sources (> 1 mJy) are radio-loud AGN (Condon 1992), but the number counts obtained from deep radio surveys have suggested the appearance of a new, dominant population at fainter radio flux densities. This faint radio popula-

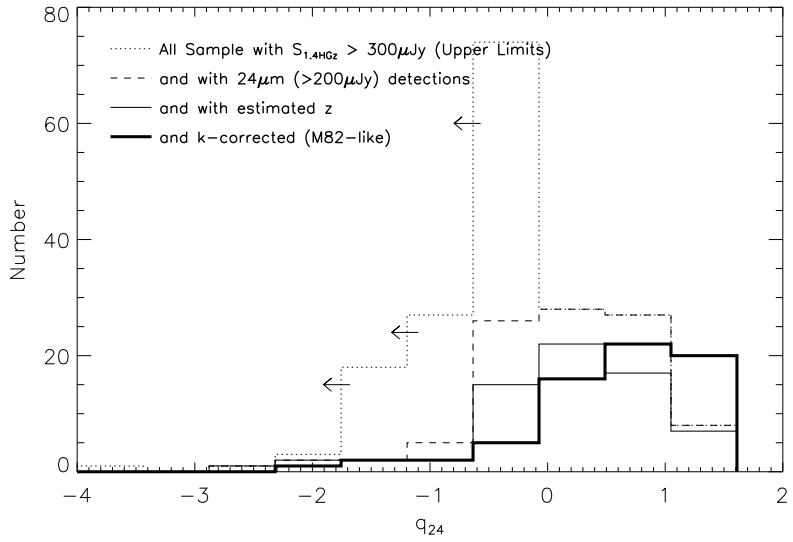

Figure 4.6: Histogram of the q_{24} values for the radio sources with radio flux densities brighter than $300\,\mu$Jy using different selection criteria. Upper limits are assumed considering $S_{24\mu\mathrm{m}} = 200\,\mu$Jy. The distribution for the k-corrected data using a M82-like template is plotted by a thick black line.

tion may be composed of star-forming galaxies (Condon 1984) and radio-quiet AGN (Jarvis & Rawlings 2004). However, the transition from radio-loud AGN to star-forming galaxies is still not well defined.

To look at the relative fractions of these populations as a function of radio flux density, we use the previous M82-like k-corrected data to identify radio-loud AGN based on different q_{24} cut-off thresholds (Donley et al. 2005). The main assumptions for the following results are the mean and scatter of the $24\,\mu$m$/1.4\,$GHz correlation (§4.3.3), and the flux thresholds from the radio and mid-IR maps.

Fig. 4.7 shows three different diagrams for the expected fraction of starburst/radio-quiet AGN ("star-forming-dominated" systems[3]) and radio-loud AGN as a function of the 1.4-GHz flux density. A value of $q_{24} = \langle q_{24} \rangle - 2\sigma_{q_{24}}$ (i.e. $2\,\sigma$ below the mean value) is adopted as the cut-off value of q_{24} used to separate and distinguish "star-forming dominated" sources from radio-loud AGN. In particular, the cut-off used in the main panel of Fig. 4.7 is at $q_{24} = -0.23$, which in terms of luminosity means that radio-loud AGN are selected by having a radio power $\gtrsim 9$ times than that predicted by the mean value. All radio sources with measured 24-μm flux densities and q_{24} values above the threshold are indicated in Fig. 4.7 as "star-forming dominated". The so-called "radio-excess" fraction corresponds to all those sources detected at

[3]We call these objects "star-forming-dominated" sources simply because they follow the FIR/radio correlation. We note that radio-quiet AGN (luminous Seyferts) can also lie on the correlation, with radio emission in the form of jets, suffering the same orientation-dependent beaming as radio-loud AGN, such that their emission is definitely AGN-related.

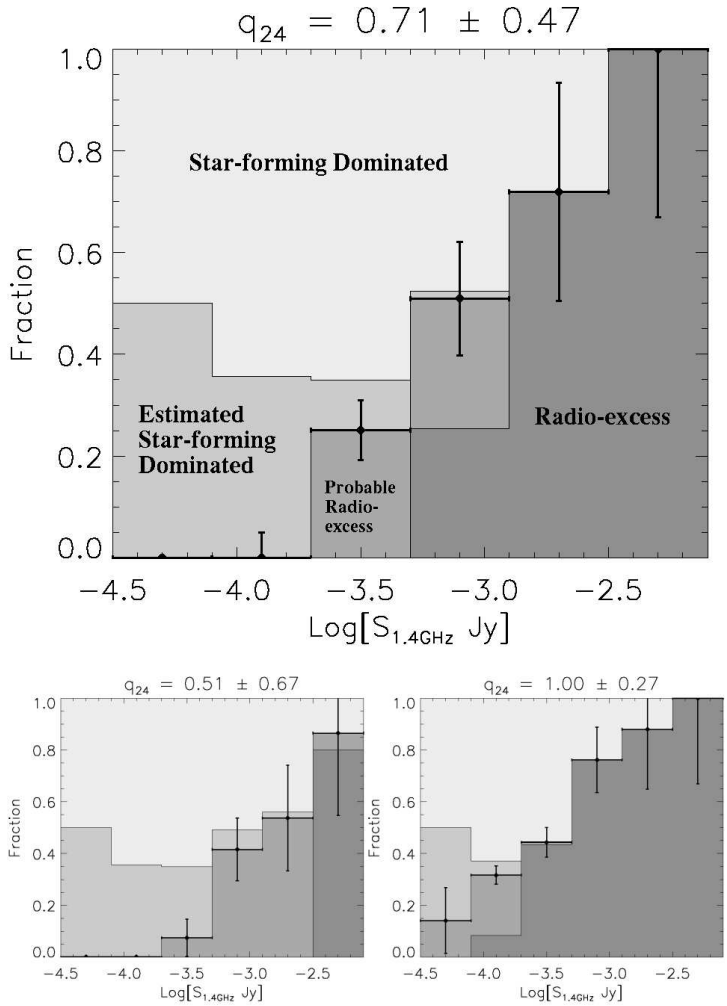

Figure 4.7: The transition from radio-excess to starburst-dominated sources based on different q_{24} thresholds using the M82-like k-corrected data. Sources without redshift have been included using a mean M82-like k-correction (+0.33), not varying considerably the results but improving the error bars. The "radio-excess" fraction is composed of those sources detected at 24 μm, or with upper limits, with q_{24} less than $2\,\sigma$ from the mean value of the correlation. The "star-forming dominated" fraction is, therefore, that with q_{24} above the $2\,\sigma$ threshold for radio-excess selection. The "probable star-forming dominated" fraction is based on an estimation which corrects for the incompleteness at 24 μm of the "star-forming dominated" sources (see text for details). Hence, all the rest of the sources are very unlikely to follow the 24 μm/1.4 GHz correlation and are called the "probable radio-excess" fraction. Error bars, based on the number counts, are 1-σ confidence limits given by Gehrels (1986). The main upper panel shows our best estimate of the different populations, based on the results from §3.3. The small panels at the bottom consider the same grey-colour criteria. On the left-hand side we modify the q_{24} mean and scatter based on the higher end of the correlation ($\langle q_{24} \rangle + \sigma_{q_{24}} \approx 1.2$), and on the right-hand side we use the previous Appleton et al. (2004) results.

24 μm with q_{24} below the cut-off value, or undetected but with upper limits below the threshold. The remaining population of sources will be those that are undetected at 24μm but have upper limits in q_{24} that lie above the q_{24} threshold for AGN selection. Those will be a mixture of starburst/radio-quiet systems and radio-loud AGN.

We have already said in § 4.3 that the faint radio population ($\lesssim 300\,\mu$Jy) is affected by incompleteness at 24 μm. In fact, for sources that follow the FIR/radio correlation then, using the threshold for detection in the SWIRE data, we can predict the expected fraction of detections at 24 μm as a function of radio flux density. We can then use this to correct the observed fraction of star-forming sources for incompleteness. In order to do so, we ran Monte-Carlo simulations for each radio flux density bin (from Fig. 4.7), using the mean and scatter of the 24 μm/1.4 GHz correlation, to obtain the probability of detection based on the 24-μm image threshold at 200 μJy. The correction for incompleteness to the "Star-forming Dominated" population is called, in Fig. 4.7, the "estimated star-forming dominated" fraction, which is mainly introduced at faint radio fluxes. The reminder of the uncertain population is classified as the "probable radio-excess" fraction.

The main panel of Fig. 4.7 shows the prediction for the transition from radio-loud-AGN-dominated to a star-forming-dominated population at sub-mJy radio fluxes, using the mean and scatter of the M82-like k-corrected 24 μm/1.4 GHz correlation (from §3.3), both to define the q_{24} threshold value and as inputs to the Monte Carlo simulations. It is found that for star-forming sources with $S_{1.4\mathrm{GHz}}$ = 200–500 μJy ($10^{-3.7} - 10^{-3.3}$ Jy), or with higher radio fluxes, the expected fraction of counterparts at 24 μm starts to become complete. Actually, the Monte-Carlo estimation predicts that $\gtrsim$ 85 per cent of the sources should have counterparts at 24 μm in this bin (it changes to $\gtrsim$ 98 per cent considering the Appleton et al. 2004 q_{24} values). This confirms the previous estimation for the complete star-forming radio sample based on a cut-off at $S_{1.4\,\mathrm{GHz}} = 300\mu$Jy.

In order to show how the results change with uncertainties in the FIR/radio correlation, the two small panels at the bottom in Fig. 4.7 use an exaggerated scatter for the correlation, and the Appleton et al. (2004) results (left and right hand side, respectively), as indicated by the values above the panels, but in each case keeping almost the same fit to the high end of the q_{24} distribution ($\langle q_{24}\rangle + \sigma_{q_{24}} \approx 1.2$).

From our best fit we predict a significant (25 ± 5 per cent) fraction of radio-loud AGN at flux levels of $S_{1.4\mathrm{GHz}} \sim 300\,\mu$Jy. The number of radio-loud AGN clearly increases as a function of the radio flux density and above $S_{1.4\mathrm{GHz}} \gtrsim 3.2$ mJy ($10^{-2.5}$ Jy) essentially all radio sources are radio-loud AGN. At $\sim 50\mu$Jy flux density levels, the fraction of radio-loud AGN significantly decreases to zero ($\lesssim$20 per cent from the lower panel estimations), leaving the star-forming dominated systems as the only population at this faint radio flux regime.

These simple analyses suggest that a large number of radio-loud AGN could be selected using deep mid-IR and radio surveys based on a simple radio-excess selection criteria. In terms of the AGN population, we note that our predictions for the "radio-excess" fraction is

just part of the total number of AGN, because many radio-quiet AGN may be included in the "star-forming-dominated" population.

One way to tackle the number of radio-quiet AGN is by looking at the radio sources which have got an X-ray detection in the hard $2-10\,\mathrm{keV}$ band. We have shown in Fig. 3.14 that the fraction of radio sources with X-ray counterparts decreases as a function of radio flux, following a similar trend as that found in Fig. 4.7. Based on the fraction of radio sources with X-ray detections, we suggest a 15 per cent remaining of radio-quiet AGN at flux levels of $\lesssim 100\,\mu$Jy in the called "star-forming-dominated" population.

4.4.2 Host galaxy properties

To explore the optical galaxy host properties of the different populations presented in §4.4.1, we have estimated the rest-frame $(U-B)$ colour (limited to sources with estimated redshifts) for each source. The colour histograms for the three populations, "star-forming dominated" sources, the "radio-excess" sources and "all others" (upper limits with $q_{24} > -0.23$) are plotted in Fig. 4.8.

Considering only the population with radio flux densities $S_{1.4\mathrm{GHz}} > 300\,\mu$Jy (left-hand panel), we find that both the "radio-excess" and "all others" populations present clearly redder distributions compared to the the "star-forming dominated" population. A Kolmogorov-Smirnov (KS) test rejects the hypotheses that either the "radio-excess" or "all others" sources are drawn from the same parent population as the "star-forming dominated" sources at >99.99 per cent significance in both cases, proving that they have a different nature. On the other hand, the colour distributions of the "radio-excess" and "all others" populations are statistically indistinguishable. This similarity is expected because, as argued in §4.3.3, at these radio flux densities the "all others" population ought to be composed entirely of "radio-excess" sources (see Fig. 4.7). At lower radio flux densities, the "all others" population should contain a mixture of starburst-dominated galaxies and radio-loud AGN, and the right-hand panel of Fig. 4.8 shows that indeed at these lower radio flux densities this population has a more pronounced tail towards bluer $(U-B)$ colours.

The red colours found for the radio-excess sources may come from the absence of star formation or due to dust obscuration in these sources. Since they do not have detections at $24\,\mu$m – due to a probable absence of re-emission – we suggest that this radio-loud AGN population is hosted in red galaxies with little or no star formation. This is potentially a very useful way to detect obscured AGN missed in deep X-ray surveys, which are responsible for a large fraction of the cosmic X-ray background (Ueda et al. 2003).

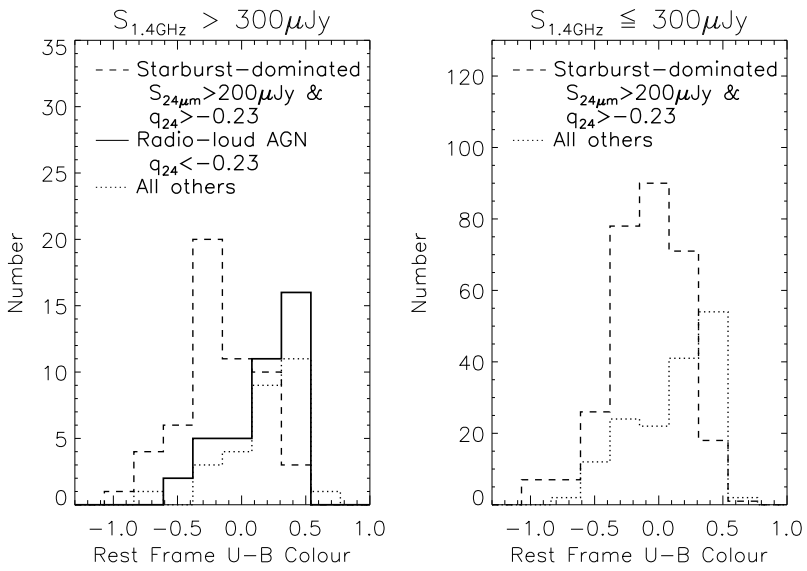

Figure 4.8: Histogram of rest-frame $(U - B)$ colours of all sources with estimated redshift in two bins of radio density flux. Dashed, continuum, and dotted lines show the distribution of the "star-forming dominated", "radio-excess" and "all others" ("estimated star-forming" plus "estimated radio-excess") fractions, respectively. These correspond to those plotted in the main panel of Fig. 4.7. It shows that the "radio-excess" population has a fundamentally different nature to the "star-forming dominated" sources, and also confirms that at bright radio flux densities ($> 300\,\mu$Jy) the "all others" population is comprised almost entirely of "radio-excess" objects.

4.5 Discussion

Previous studies of the universality of the FIR/radio correlation at high redshift have combined 1.4-GHz data with 15-μm data from the *Infrared Space Observatory* (Garrett 2002) and *Spitzer* 24- and 70-μm data (Appleton et al. 2004), both showing evidence of a correlation up to $z \sim 1$. More recently, Kovács et al. (2006) and Beelen et al. (2006) have shown evidence for the correlation at higher redshifts, for a sample of 15 submm galaxies (SMGs; $z \sim 0.5 - 3.5$) and for a handful of distant quasars ($z \sim 2 - 6$), respectively. In this work, despite the difficulty of measuring a reliable bolometric FIR emission, the monochromatic 24-μm flux densities show a tight correlation with the 1.4-GHz flux density up to $z \approx 3.5$. *k*-corrections based on an M82-like template indicate that both the mean and the scatter of the q_{24} values remain constant as a function of redshift (see Fig. 4.4). These findings suggest that the strength of the magnetic fields plays a minor role across the cosmic time, as recently observed by Bernet et al. (2008) in local and high-redshift galaxies.

The mean and scatter of the distribution of q_{24} values obtained after a M82-like *k*-correction for all radio sources detected at 24 μm is $q_{24} = 0.99 \pm 0.32$. This is in broad agreement with the results of Appleton et al. (2004), $q_{24} = 0.84 \pm 0.28$, based on a sample $z \lesssim 1$. However, if

our sample is restricted to brighter radio sources for which all star-forming sources would be expected to have been detected at 24 μm, then the mean relation becomes $q_{24} = 0.71 \pm 0.47$, with a scatter about twice that of Appleton et al. (2004). The median error value for q_{24} has been found to be about 0.1 dex, which suggests that this scatter is intrinsic for the correlation and does not come from observational errors. We can conceive of two possible explanations for this increased scatter at higher radio flux densities. First, it may be that, because of the smaller number of sources, some radio-excess objects may fail to be excluded by the biweight estimator, and therefore increase the scatter of the relation. Second, it may be that for these more powerful sources, the M82-like template (a relatively low luminosity source) is not an accurate representation of the mid-IR emission for all sources – a broader range of SED types might increase the scatter. Indeed, the presence of a handful of sources with higher q_{24} values at low redshifts $z < 0.5$ (bottom panel in see Fig. 4.3) would be more consistent with a steeper mid-IR spectra, such as that given by the Arp 220-like template.

Recently, Boyle et al. (2007) have found a significantly higher mean value, $q_{24} = 1.39 \pm 0.02$ ($2\,\sigma$ away from our estimation) whilst applying stacking techniques (Wals et al. 2005) to 1.4-GHz images from the Australia Telescope Compact Array using positions from *Spitzer* detections in the *Chandra* Deep Field South (CDFS) and European Large-area Infrared Survey (ELAIS) fields. Their work lacks redshift information, however, and therefore does not include *k*-corrections. We have shown the relevance of different mid-IR features for high-redshift sources in the flux regime of this work, suggesting a clear underestimation for the intrinsic 24 μm/1.4 GHz scatter in their work. Also, a stacking analysis for a mixture of star-forming galaxies and radio-loud AGN does not discriminate an exclusive correlation for star-forming galaxies. Since the flux thresholds from our work are similar to their ones, we suggest that selection effects based on different sample selection criteria (from radio or mid-IR detections) may also be affecting the scatter on the 24μm/1.4 GHz correlation.

A simple radio flux estimate ($S^{\rm limit}_{1.4{\rm GHz}} \approx 35\,\mu$Jy) shows that a starburst galaxy with a typical M82 luminosity can only be observed up to moderate redshifts, $z \sim 0.4$. In fact, it is expected that the observed high-redshift, high-luminosity Universe is composed mainly of ULIRGs and AGN. ULIRGs are usually related to interacting systems (Sanders et al. 1988) and are expected to suffer strong absorption, implying large *k*-corrections for the 24-μm emission. There are hints of steeper mid-IR SEDs at $S_{1.4{\rm GHz}} > 300\mu$Jy (bottom Fig. 4.3), but the lack of a clear excess scatter in the FIR/radio distribution at $z \approx 1-2$ (Fig. 4.1) suggests that the bulk of the ULIRG-like high-redshift sources from our sample do not suffer large selection effects due to silicate absorption. The correlation found in this work is therefore quite unexpected, but suggests that a M82-like mid-IR template, intrinsically coming from a lower luminosity source, is still a good representation for the mid-IR SED of high-redshift star-forming-dominated systems. The M82-like template is also supported by Lagache's ULIRG ($L_{IR} = 10^{12}{\rm M}_{\odot}$) model, leaving Arp 220 as an extreme case. These results are interesting since Kasliwal et al. (2005) estimate that about half of ULIRGs at $z \approx 1-1.8$ may be undetected at 24 μm due to silicate absorption

at 9.7 μm, a suggestion not supported by our data. The mid-IR SED of selected-SMGs is still under debate, but templates such as M82 (Menéndez-Delmestre et al. 2007) and Arp 220 (Pope et al. 2006) have both been found to provide good fits.

In § 4.4, we have shown the capabilities of deep mid-IR and radio imaging for the selection of radio-loud AGN ("radio-excess") based on different cut-offs in q_{24}. We have shown that at $S_{1.4\mathrm{GHz}} > 300\,\mu$Jy, selected radio-excess sources indicate nuclear activity. The radio-excess sources present a redder distribution of rest-frame $(U - B)$ colours than those identified as star-forming-dominated galaxies. This strongly suggests a different nature from the populations selected by a simple q_{24} threshold at -0.23. Previous population synthesis models (Jarvis & Rawlings 2004) have predicted that radio-excess sources at these flux densities are mainly FR I types (Fanaroff & Riley 1974). It is known that FR I sources do not fall into the standard unified scheme for AGN (Antonucci 1993) and show no bright AGN nucleus. Therefore their red colours indicate that these radio-loud sources do not present significant star-formation activity and/or are hosted in red massive galaxies.

Jarvis & Rawlings (2004) predict that approximately half of the sources with radio fluxes between $100\,\mu\mathrm{Jy} \leq S_{1.4\mathrm{GHz}} < 300\,\mu$Jy present radio-loud activity. We have predicted from our best fit a fraction of 25 $\pm$ 5 per cent in this flux regime, disagreeing by a factor of two with their estimate. Nevertheless, Fig. 4.7 shows that the Appleton et al. estimate may explain a 50 per cent fraction. On the other hand, Simpson et al. (2006) tentatively suggested a radio-quiet AGN fraction of 20 per cent in this flux regime, a result in complete agreement with our findings in Fig. 3.14. Note these radio-quiet sources have been found to follow the FIR/radio correlation (Roy et al. 1998), so they are not identifiable using a simple q_{24} threshold.

4.6 Summary

We have analysed the 24-μm properties of a radio-selected sample in order to explore the well-known FIR/radio correlation at high redshifts. We have shown evidence that 24-μm data do not give the best estimate of the total bolometric FIR emission, reflected in a considerably larger scatter on the correlation than previous work using longer wavelengths (*IRAS*/60 μm – Yun et al. (2001), *Spitzer*/70 μm – Appleton et al. 2004). Nevertheless, despite the large scatter, the IR-24 μm/radio-1.4 GHz correlation seems to extend up to redshift ~ 3.5 with roughly the same mean and scatter. The fact that we do not observe considerable variations in the correlation as a function of redshift, mainly seen on the well-defined upper end of the k-corrected q_{24} distribution (see top Fig. 4.3 and 4.4), suggests strongly its validity all the way back to primeval times. This is the first evidence for the extension of the correlation over this very wide range of redshifts.

Statistically, the correlation is described by the basic observable parameter, q_{24}, the ratio of the flux densities at 24 μm and 1.4 GHz, respectively. The q_{24} factor parameterises the link (in the local Universe at least) that star-forming galaxies have between their synchrotron emis-

sion (from cosmic rays accelerated by massive supernovae explosions, i.e. the high end of the stellar mass function in galaxies), with the reprocessed ultraviolet photons emitted by dust at FIR wavelengths. The presence of AGN may also modify the mid-IR spectra and the radio emission, increasing the scatter in a q_{24}-based correlation. We found a mean value (biweight estimator) of $q_{24} = 0.30 \pm 0.56$ for the observed and $q_{24} = 0.71 \pm 0.47$ for the k-corrected (M82-like) data based on an expected complete radio sample ($S_{1.4\mathrm{GHz}} > 300\,\mu$Jy) at 24 μm.

Three different k-corrections have been tested: two based on well-known local starbursts (M82 and Arp 220) and one on a ULIRG model (Lagache et al. 2004). The main difference introduced by using different templates is caused by the silicate absorption feature at $\sim$10 μm being redshifted into the observed 24-μm band at $z \approx 1 - 2$ (Fig. 4.1). We found no strong evidence for extreme silicate absorption in the bulk of our sample and, based on the smallest scatter found for q_{24} data, we suggest an acceptable k-correction is given by an M82-like mid-IR template. We do, however, find tentative evidence for a steeper mid-IR spectrum than M82 for brighter radio sources $> 300\mu$Jy, in order to explain the slight offset from the correlation for sources with $z < 0.5$.

We have found a clear dependency between the detected number of star-forming-dominated galaxies (starburst and radio-quiet AGN) and radio flux density. Making use of the derived 24 μm/1.4 GHz correlation, and the flux density threshold from the 24-μm image, we ran Monte-Carlo simulations to estimate the incompleteness at 24 μm, and therefore the intrinsic fraction of star-forming-dominated galaxies. This allowed us to estimate the probable number of radio-loud AGN and to describe the transition from AGN-dominated to star-forming-dominated galaxies at faint radio flux densities (< 1 mJy). Our best-fit estimate predicts a significant fraction (25 ± 5 per cent) of radio-loud AGN at $S_{1.4\mathrm{GHz}} \sim 300\,\mu$Jy, rising quickly to become a dominant AGN population at brighter radio flux densities (> 1 mJy), and falling towards zero (certainly $\lesssim 20$ per cent) at fainter fluxes. These results are in broad agreement with previous studies (e.g. Condon 1984).

We have also shown that the rest-frame ($U - B$) colours of the sources that are expected to be radio-loud AGN have a redder distribution than the starburst/radio-quiet AGN galaxies (Fig. 4.8), strongly suggesting a different nature for those sources selected by our simple $q_{24} = -0.23$ threshold. These radio-excess sources seem to be hosted by red galaxies with little or no star formation (implied by their non-detection at 24 μm). This is therefore an extremely promising way to select obscured Type-2 AGN (Comastri 2003) which are missed by deep X-ray observations, though spectroscopic follow-up of these sources and better sampling of the FIR emission is needed to fully test this method.

CHAPTER 5

The radio spectral index of sub-millimetre galaxies

"A la falta de respuestas, buenas son las estrellas,
de cazuela ¿pillaste tu estrella...?"

Arlette de la Maza.

5.1 Introduction

The revolution produced by the discovery of massive star-forming galaxies ($\sim 10^3 \mathrm{M}_\odot\,\mathrm{yr}^{-1}$) at high redshifts, each capable of creating a massive elliptical galaxy ($> 3\,L^*$) within 1 Gyr, has put powerful constraints on cosmological galaxy formation models. These sub-millimetre- (submm-) selected galaxies (SMGs) were discovered in the late 1990s (Smail et al. 1997; Hughes et al. 1998; Barger et al. 1998; Eales et al. 1999) using the Submm Common-User Bolometer Array (SCUBA – Holland et al. 1999) on the 15-m James Clerk Maxwell Telescope (JCMT). SCUBA was designed to exploit the so-called "negative *k*-correction" in the submm waveband (Blain & Longair 1993), allowing the detection of very distant, dusty galaxies. SMGs are believed to be the parent population of present-day elliptical galaxies and are responsible for up to half of the cosmic IR background (CIRB) at $z > 1$. Nevertheless, understanding the nature of these massive galaxies has been extremely challenging work, a situation influenced principally by four factors: (1) the poor resolution of submm images, which typically have a ∼14-arcsec beam

(FWHM), implies that identifying counterparts at other wavelengths can be difficult; (2) confusion becomes an issue at the noise levels required to detect significant numbers of SMGs; (3) SMGs typically reside at very high redshifts (mean $\langle z \rangle \approx 2.2$ – Chapman et al. 2005) therefore they require extremely deep imaging to be detected, even in broadband photometric imaging surveys and (4) their dusty nature obscures a large fraction of their light, be it from stars or AGN.

The obvious difficulty in obtaining spectroscopic redshifts implies photometric techniques are usually used to estimate the distance to these sources, sometimes using optical/IR data (e.g. Brodwin et al., 2006), sometimes using data at longer wavelengths (e.g. Wiklind, 2003). Techniques employing long-wavelength observations are currently inadequate for most requirements, with $\Delta z \sim 1$ (Chapman et al. 2005; Daddi et al. 2008). To provide the required level of precision we need good templates of relevant spectral energy distributions (SEDs) spanning the entire observable range. Radio data at 610 and 1,400 MHz, together with data at 450 and 850 μm (350 and 670 GHz) from SCUBA-2 (Holland et al. 2006), 60–210 and 250–500-μm data from PACS and SPIRE aboard the *Herschel Space Observatory* (Poglitsch et al. 2006), and near-/mid-IR data from cameras like WFCAM (Casali et al., 2007) on the 3.8-m UK IR Telescope (UKIRT) and IRAC and MIPS aboard the *Spitzer Space Telescope* (Werner et al., 2004), should yield $\Delta z \lesssim 0.1$.

Radio imaging has played an important role in characterising distant, massive star-forming galaxies and AGN, providing a high-resolution proxy for rest-frame FIR emission (Chapman et al., 2004b; Muxlow et al., 2005; Biggs & Ivison, 2008) via the FIR/radio correlation (Helou et al., 1985; Garrett, 2002; Appleton et al., 2004; Ibar et al., 2008). A crucial part of the template SED lies in the radio waveband: current photometric redshift templates adopt the standard $S_\nu \propto \nu^\alpha$ form for star-forming galaxies, with $\alpha = -0.7$ or -0.8 (Condon, 1992). Hunt & Maiolino (2005) questioned this assumption: using $\alpha = -0.7$ for SMGs is not based on any relevant observational evidence and flatter radio SEDs typical of blue compact dwarf (BCD) galaxies were preferred in Hunt & Maiolino's photometric redshift analyses of SMGs. Given the flatter observed spectrum of Arp 220 (e.g. Ivison et al., 2004) – a local ULIRG – and the expectation that the most powerful starbursts will suffer self-absorption, it would seem entirely possible that the observed radio SEDs of SMGs are flatter than $S_\nu \propto \nu^{-0.7}$. Indeed, Clemens et al. (2008) recently measured a mean spectral index of $\alpha = -0.5$ between 1.4 GHz and 4.8 GHz for a sample of ULIRGs, though this steepens to $\alpha = -0.7$ and -0.8 between 4.8–8.4 and 8.4–22.5 GHz, respectively, which corresponds to 1.5–2.6 and 2.6–7.0 GHz for an SMG at $z \sim 2.2$.

Kovács et al. (2006) employed 350-μm observations of 15 radio-pinpointed SMGs with known redshifts to constrain their characteristic temperatures with unprecedented precision. In doing so, they were able to demonstrate the first signs of a deviation from the FIR/radio correlation exhibited locally, $q \simeq 2.3$, the ubiquity of which has surprised astronomers for decades (Helou et al., 1985). Kovács et al. suggested that SMGs are over-luminous at radio

frequencies. They find a mean $q \approx 2.07 \pm 0.09$, assuming a dust temperature, $T_{\rm d} = 40\,{\rm K}$ and emissivity index, $\beta = 1.5$ (see their paper for a discussion of q). Kovács et al. noted, however, that a steepening of the radio spectral index from -0.8 to -1.1 would be sufficient to move SMGs back onto the FIR/radio correlation. We thus have two strong, independent motives for exploring the spectral indices of SMGs.

Here, I report deep, dual-frequency, matched-resolution radio observations that were designed to address this issue, targeting one of the two SCUBA Half Degree Extragalactic Survey (SHADES) fields (Mortier et al., 2005; Coppin et al., 2006) – the Lockman Hole (Lockman et al. 1986). This "hole" has the lowest Galactic column density along the line of sight ($\sim$5 $\times 10^{19}\,{\rm cm}^{-2}$) in the northern hemisphere and it has been the site of surveys with SCUBA, *Spitzer*, *GALEX* and *XMM/Newton* (Brunner et al., 2008; Hasinger et al., 2001; Scott et al., 2002; Mainieri et al., 2002; Lonsdale et al., 2003; Streblyanska et al., 2005; Mortier et al., 2005). The absence of bright radio sources in this region (and the excellent calibrator, 1035+564) have also made the Lockman Hole home to the deepest radio imaging (using the VLA and GMRT; see Chapter 3 for more details) so far obtained (Biggs & Ivison, 2006; Owen et al., 2008; Ibar et al., 2009), sensitive to star-forming galaxies and AGN of all known kinds: to SMGs, to similarly luminous (but hotter) starbursts (Blain et al., 2004), to radio-excess AGN (Drake et al., 2003; Donley et al., 2005) and to less luminous μJy-level AGN and starbursts (Seymour et al., 2004; Simpson et al., 2006).

5.2 Multi-wavelength observations in the Lockman Hole

5.2.1 SCUBA imaging

SCUBA (Holland et al. 1999) was designed and constructed at the Royal Observatory, Edinburgh, in collaboration with Queen Mary's College, University of London. Now retired, SCUBA was first mounted on the JCMT in 1996 and was one of the most successful ground-based instruments ever built. When operational, SCUBA had two arrays of bolometric receptors operating at 850 μm (37 pixels) and 450 μm (91 pixels), providing a beamsize of $\sim$14 and $\sim$7.5 arcsec FWHM, respectively.

As one half of a submm survey undertaken with SCUBA – SHADES (Dunlop 2005, Mortier et al. 2005, Coppin et al. 2006) – the Lockman Hole was observed at 450 and 850 μm. In this work, I use the catalogue provided by Coppin et al. (2006), comprising 60 sources detected with 850-μm signal-to-noise ratios (SNRs) above 3.0 (in more than one independent reduction of the data) and with a probability lower than 5 per cent that the true flux density is zero and has been boosted by the noise (i.e. that the source is spurious).

5.2.2 AzTEC imaging

The AzTEC camera was developed by the University of Massachusetts in collaboration with researchers at the California Institute of Technology, Cardiff University, Instituto Nacional de Astrofísica Óptica y Electrónica (INAOE) in México, Sejong University and Smith College. It is a 144-element bolometer array, configured to operate at one of two wavelengths: 1.1 mm (with a bandwidth $\Delta\nu \sim 49$ GHz) or 2.1 mm (Wilson 2008). Thus far, AzTEC has been only operated in its 1.1-mm wavelength configuration.

During 2005 November and 2006 February, the SHADES fields were observed by AzTEC on JCMT at 1.1 mm down to an r.m.s. depth of 1.1 mJy and 1.4 mJy for the Lockman Hole and the SXDF fields, respectively (Austermann et al. 2008, *in preparation.*). The FWHM beamsize was roughly 18 arcsec and the observations suffer the same spatial-resolution-related problems as SCUBA. In this work, I use a sample of 92 sources in the Lockman Hole detected with SNR > 3.5.

The SCUBA and AzTEC imaging of the SHADES fields comprise the largest set of continuous areas mapped at both 1.1 mm and 850 μm. A total of 138 SMGs (14 in common) have been cross-matched with the radio catalogues.

5.2.3 GMRT and VLA imaging

In Chapter 3, I presented the deep radio observations obtained in the Lockman Hole using the GMRT and VLA telescopes, operated at 610 MHz and 1.4 GHz, respectively. The two image mosaics have r.m.s. noise levels in the central regions of 15 and 6 μJy, respectively, and provide an unbiased estimate of radio spectral indices for the population with $S \gtrsim 200\,\mu$Jy.

In order to maximise the role of radio data in pinpointing SMGs, I have merged the VLA and GMRT image mosaics into a single "1-GHz" map, assuming an spectral index, $\alpha = -0.7$ (based on the results in Chapter 3). The new image has an r.m.s. of 7.6 μJy (at 1 GHz) and it has helped to increase the number of radio detections and SMG associations. This new image has provided $> 5\,\sigma$ radio counterparts for approximately 50 per cent of full SMG sample, within 8 arcsec.

5.2.4 Submm/radio identifications

Due to the large beamsize of the submm images, identifications of radio counterparts via a cross-matching process must be based on probabilistic arguments. Given the low surface density of radio sources (compared to deep optical images) and because of the far-IR/radio correlation (see Chapter 4), the probability of finding an unrelated radio source close to an SMG is very low. I make use of the method presented by Downes et al. (1986) to find the probability, P, that a radio identification is correct.

I have considered the subset of radio-identified SMGs – those with SNR > 5 radio counter-

parts within 8 arcsec detected in the 610-MHz, 1,400-MHz *and* 1-GHz maps – with $P < 0.05$. The selection criteria were not affected by the different depths of the original VLA and GMRT images. Indeed, an independent cross-matching exercise using the original radio maps results in the loss of a small fraction of the radio-identified sample: only 2–3 sources.

A total of 45 sources (out of 128, i.e. 35 per cent of the parent SMG sample) have been selected using these conservative criteria (roughly half the identification rate commonly achieved by dropping to a 3.5-σ radio detection threshold in similarly deep radio maps – see Ivison et al. 2002, 2007b; Pope et al. 2006).

5.3 The radio spectral index of SMGs

In Fig. 5.1 I plot the radio spectral index of radio-identified SMGs and compare with those of the full 610-MHz-selected sample (see Chapter 3 for details). I find no statistical difference between these distributions: a Kolmogorov-Smirnov test suggests that both datasets come from the same parent distribution, with 90-per-cent confidence. The median radio spectral index of the SMGs, $\alpha = -0.72 \pm 0.07$ (bootstrapping) is consistent with optically thin synchrotron dominating their emission. I can rule out flatter radio SEDs, such as those seen in BCD galaxies (Hunt & Maiolino 2005) or a dominant synchrotron self-absorbed AGN population (Ivison et al. 2004).

There is marginal evidence for an excess of steep-spectrum sources and a lack of flat-spectrum sources. This is probably due to the high redshifts of some SMGs (e.g. Eales et al. 2003; Younger et al. 2007; Wang et al. 2007; Daddi et al. 2008; Schinnerer et al. 2008) and synchrotron ageing effects. Nevertheless, statistically I cannot distinguish between the properties of the SMGs and those of the full radio sample.

The identification of SMGs in deep radio imaging made it possible to probe the detailed properties of dust-enshrouded galaxies out to $z \lesssim 3.5$, but the vast majority of those radio-identified SMGs were detected at a significance of $\lesssim 10\,\sigma$. I showed in Chapter 3 that the study of the radio spectral index for the faint radio-selected population is dominated by uncertainties in the flux density measurements. It is to be expected, therefore, that the large scatter found in the spectral index distribution of SMGs (mean and scatter, $\alpha = -0.73 \pm 0.46$) is also dominated by these uncertainties.

I have checked for a possible dependency of the radio spectral index on submm flux density by splitting the sample into SCUBA and AzTEC sources (Fig. 5.2, left-hand plot) but I do not find any dependency on submm flux density for either the mean or the scatter.

I also plot, in the right panel of Fig. 5.2, the radio spectral index as a function of the logarithmic ratio between the submm and radio flux densities (often called q). In early work, q was used as a rough estimate of redshift (Hughes et al. 1998; Carilli & Yun 1999; Smail et al. 2000; Dunne et al. 2000) having assumed that SMGs are dominated by star formation and that the far-IR/radio correlation is valid at high redshifts (Helou et al. 1985; Garrett 2002; Apple-

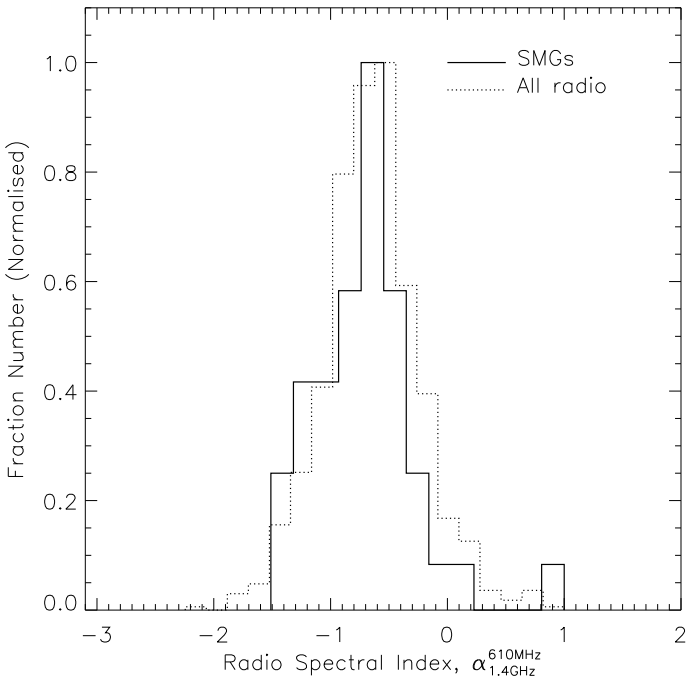

Figure 5.1: *Continuous line:* radio spectral index (between 610 MHz and 1.4 GHz) of a radio-identified sample of 45 SMGs. SMGs were selected in the Lockman Hole region using SCUBA at 850 μm and AzTEC at 1.1 mm. *Dashed line:* radio spectral index distribution for the full 610-MHz-selected sample presented in Chapter 3.

ton et al. 2004; Ibar et al. 2008). In Chapter 4, I showed strong evidence for the validity of this correlation back to primordial times, and the possibility of discriminating between star-forming galaxies and radio-loud AGN using a threshold in q. Nevertheless, in the case of SMGs, the negative K-correction ($S_\nu \propto \nu^{3-4}$ in the Rayleigh-Jeans regime) is strongly dependent on the dust temperature, which is particularly important for deriving luminosities and related properties (Eales et al. 1999; Blain 1999; Chapman et al. 2005). This results in a more difficult estimate than when using a *Spitzer* 24-μm sample with relatively secure photometric redshifts. I do not find any clear trend of radio spectral index as a function of $S_{\rm submm}/S_{\rm radio}$.

I do observe a few sources with unusually low values of q in the AzTEC sample. They may be associated with radio-loud AGN or low-redshift ULIRGs.

5.4 Summary

I have analysed the radio spectral index of a sample of SMGs in the Lockman Hole. These spectral index, $\alpha_{1.4GHz}^{610MHz}$, are based on observations taken using GMRT at 610 MHz and the VLA at 1,400 MHz. I have chosen one of the largest continuous areas mapped at both 1.1 mm

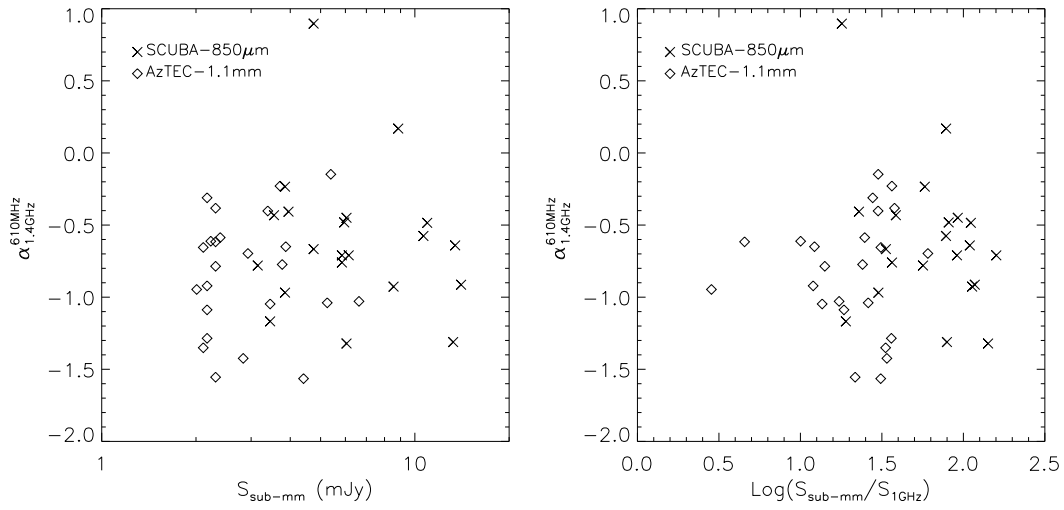

Figure 5.2: *Left:* radio spectral index (between 610 and 1,400 MHz) as a function of the submm flux density, at 850 μm (SCUBA) and 1.1 mm (AzTEC). *Right:* $\alpha_{1.4\mathrm{GHz}}^{610\mathrm{MHz}}$ as a function of q, defined as the logarithmic ratio between the flux density observed in the submm with respect to the merged "1-GHz" map.

and 850 μm, by AzTEC and SCUBA, respectively. Statistically, I analyse a sample of 45 SMGs (35 per cent of the full SMG sample) which have reliable estimates of radio spectral index based on a conservative $> 5\sigma$ radio detection criterion.

I find a median value of $\alpha = -0.72 \pm 0.07$ for the radio-identified SMGs (which is biased against galaxies at $z \gtrsim 3$). This suggests that the majority of SMGs emit optically thin synchrotron emission from star-forming regions. The distribution of spectral indices does not behave differently to that of the general, faint radio population. The large scatter in the $\alpha_{1.4\mathrm{GHz}}^{610\mathrm{MHz}}$ distribution, -0.73 ± 0.46, and the radio flux density range in which they are found, suggests the distribution as a whole is dominated by flux density measurement errors. I do not observe any dependency of the radio spectral index on observed submm flux density, or on the observed $S_{\mathrm{submm}}/S_{\mathrm{radio}}$ ratio.

These results have determined the radio SED of SMGs and they therefore enable a reliable *k*-correction for the observed flux densities. The additional SED constraint will alleviate the problems (degeneracies) faced by long-wavelength photometric redshift techniques, and strengthens our interpretation of SMG as being dominated by processes typical of dusty star-forming galaxies rather than those seen in active galactic nuclei.

5.5 Future work

A future revision of this work will take into account some important issues – the loss of faint 1.4-GHz radio identifications following convolution to a common FWHM in the merging of

VLA and GMRT images and the use of higher resolution images to provide more accurate positions when possible. I will also implement a robust statistical correction for flux boosting in the radio SEDs of SMGs, yielding the best possible submm/radio-based redshift distribution for SMGs. I also expect to use all detections down to $\sim 3\,\sigma$ at radio frequencies, and implement stacking techniques in the radio maps to obtain more statistically significant results.

Building on the existing analysis, I will introduce the known spectroscopic redshifts of some of the Lockman Hole SMGs in order to better understand the degeneracy in Fig. 5.2 produced by the *k*-correction.

Looking further into the future, I expect to use these radio and submm data in combination with data from SCUBA-2 and data from SPIRE and PACS aboard the *Herschel Space Observatory*. As shown in Fig. 4.2, merging all these observations will provide the well-sampled SEDs required to estimate the bolometric energy emitted in the far-IR and radio wavebands for a significant fraction of the galaxies in the Universe.

Chapter 6

Summary of results and conclusions

"Fuera/
frio y calor/ estrella, luz, viaje/ imagen
ojo, cerebro, corazón/ conciencia,
respiro,
ojo mas ojo/ boca, palabras,
preguntas, respuestas/ preguntas
respiro,
sonrisa, risa/calor y frio/
adentro."

Amaya Fuenzalida

In this thesis I have demonstrated the impressive capabilities of interferometric radio observations in describing the properties of distant galaxies. I have made use of the Giant Metrewave Radio Telescope (GMRT) and the Very Large Array (VLA) to observe the two fields that comprise the SCUBA Half Degree Extragalactic Survey (SHADES) – the Lockman Hole and the Subaru-*XMM/Newton* Deep Field. These observations have facilitated the description of the physical mechanism responsible for the synchrotron emission from dusty star-forming galaxies and active galactic nuclei (AGN) out to redshifts, $z \lesssim 3.5$.

Listing the results found in each chapter of the thesis:

- In the run up to routine observations with the forthcoming generation of radio facilities, the nature of sub-mJy radio population has been hotly debated. In Chapter 3, I describe

multi-frequency data designed to probe the emission mechanism that dominates in these faint radio sources. My analysis is based on observations of the Lockman Hole using the GMRT at 610 MHz and the VLA at 1.4 GHz – deep mosaics with noise levels of 15 and 6 μJy beam^{-1}, respectively. I present the deepest 610-MHz number counts to date and compare with the shallower catalogue of Garn et al. (2008b) in the same field. The GMRT and VLA data are combined to obtain spectral indices. Statistical analyses show no clear evolution for the median spectral index, which is found to be approximately $\alpha_{1.4\mathrm{GHz}}^{610\mathrm{MHz}} \approx -0.6$ to -0.7 (based on an almost unbiased 10-σ criterion), where $S_\nu \propto \nu^\alpha$, down to a flux level of $S_{1.4\mathrm{GHz}} \gtrsim 100\,\mu$Jy. The fraction of inverted spectrum sources ($\alpha_{1.4\mathrm{GHz}}^{610\mathrm{MHz}} > 0$) is less than 10 per cent. The results suggest that the most prevalent emission mechanism in the sub-mJy regime is optically-thin synchrotron, ruling out a dominant self-absorbed flat-spectrum or ultra-steep spectrum radio population. However, the spectral index distribution has a significant scatter, ($\Delta\alpha \approx 0.4 - 0.5$ in $S_{1.4\mathrm{GHz}} \gtrsim 40\,\mu$Jy), suggesting a mixture of radio AGN and star-forming galaxies at all flux levels. Based on hard X-ray detections to the radio sources, I find an AGN fraction of $\sim$15 and $\sim$50 per cent at flux levels of $S_{1.4\mathrm{GHz}} \lesssim 100\,\mu$Jy and ~ 1 mJy, respectively, in agreement with a transition from an AGN to a star-forming galaxy/radio-quiet AGN population at sub-mJy fluxes. Radio sources detected in the hard X-ray band have slightly flatter spectral index $\alpha_{1.4\mathrm{GHz}}^{610\mathrm{MHz}} = -0.64 \pm 0.03$ (median) and a large fraction ($\sim$35 per cent) are only detected at 1.4 GHz.

- In Chapter 4, I have analysed the 24-μm properties of a radio-selected sample in the SXDF in order to explore the behaviour of the far-infrared/radio relation at high redshifts. Statistically, the correlation is described by q_{24}, the ratio between the observed flux densities at 24 μm and 1.4 GHz, respectively. Using 24-μm data results in considerably more scatter in the correlation than previous work using data at 60–70 μm (Helou et al. 1985; Appleton et al. 2004). Nevertheless, I do observe a steady correlation as a function of redshift, up to $z \approx 3.5$, suggesting its validity back in primeval times. I find $q_{24} = 0.30 \pm 0.56$ for the observed and $q_{24} = 0.71 \pm 0.47$ for the k-corrected radio sample, based on sources with $S_{1.4\mathrm{GHz}} > 300\,\mu$Jy and 24 μm detections. I find no strong evidence for extreme silicate absorption in the bulk of our sample, suggesting a suitable k-correction given by a M82-like mid-IR template. Using thresholds in q_{24} to identify radio-excess sources, I have been able to characterise the transition from radio-loud AGN to star-forming galaxies and radio-quiet AGN at faint ($\lesssim 1$ mJy) radio flux densities. My results are in broad agreement with previous studies which showed a dominant radio-loud AGN population at > 1 mJy (Hopkins et al. 2000). The rest-frame $(U - B)$ colours of the expected radio-excess population have a redder distribution than those that follow the correlation. This is therefore a promising way to select obscured, radio-loud, type-2 AGN missed by deep X-ray observations. Spectroscopic follow-up of these sources is required to further test this method.

- In Chapter 5, I present a preliminary analysis of the broadband radio spectra of a sample

of sub-millimetre galaxies (SMGs) in the Lockman Hole, a natural extension of the study described in Chapter 3. The SMGs were found using the Sub-millimetre Common-User Bolometer Array (SCUBA) and the Astronomical Thermal Emission Camera (AzTEC) on the James Clerk Maxwell Telescope (JCMT). I describe the use of deep radio observations to identify counterparts to SMGs and the significance of these measurements for constraining their spectral energy distributions (SEDs). Based on conservative and robust counterpart selection criteria (which yields 45 radio counterparts in a sample of 128 sources), I have found that SMGs have radio spectral indices that are statistically indistinguishable from those of the faint radio population. A median value of $\alpha_{1.4\mathrm{GHz}}^{610\mathrm{MHz}} = -0.72 \pm 0.07$ suggests that radio emission from the majority of these sources is optically thin synchrotron, ruling out the possibilities of significant ultra-steep- or flat-spectrum populations (Hunt & Maiolino 2005).

I include, as Appendix A, research based on X-ray observations undertaken using the *Chandra* Space Telescope in the *Chandra* Deep Field South (CDF-S – Tozzi et al. 2006). I discuss the difficulties encountered when observing highly obscured AGN, a problem which connects with my studies of faint radio emitters.

- In unification models, AGN are believed to be surrounded by an axisymmetric structure of dust and gas which influences their observed properties according to the direction from which they are observed. In Appendix A, I show that it is possible to constrain the properties of this obscuring material using X-ray observations. The distribution of column densities observed by *Chandra* in the CDF-S is used to determine geometrical constraints for several well-known torus models. It is found that the best torus model involves a classic "donut" shape with an exponential angular dependency for the density profile (e.g. Granato & Danese 1994). The opening angle is strongly constrained by the observed column densities. Other torus models are clearly rejected by the X-ray observations (Pier & Krolik 1992).

APPENDIX A

Constraining torus models for AGN using X-ray observations*

"En torno a la buena mesa nos deleitaremos con manjares terrestres y caldos marinos, obteniendo exquisitos momentos familiares irreproducibles"

Pablo Ibar Plasser.

A.1 Introduction

A unified scheme to explain the variety of active galactic nuclei (AGN) was proposed by Antonucci (1993). This model is based on the differences observed in Seyfert galaxies, a class of local active galaxies. According to this "unification model", the active nucleus is surrounded by a toroidal structure composed of gas and dust, which determines dramatic spectral differences depending on our line of sight towards the central source. In the X-ray domain, if an AGN has a neutral hydrogen column density ($N_{\rm H}$) in the line of sight smaller (when viewed face-on) or larger (when viewed edge-on) than $10^{22}\,{\rm cm}^{-2}$, then the object is classified as Type 1 or Type 2, respectively (see sketch from Fig. A.1).

*This work is partly based on my MSc thesis submitted on July 2005 at the 'Universidad de Chile, Facultad de Ciencias Físicas y Matemáticas' in Santiago, Chile. During the first year of my PhD at the Institute for Astronomy, University of Edinburgh, this previous study was vastly improved and finally published in Ibar & Lira (2007).

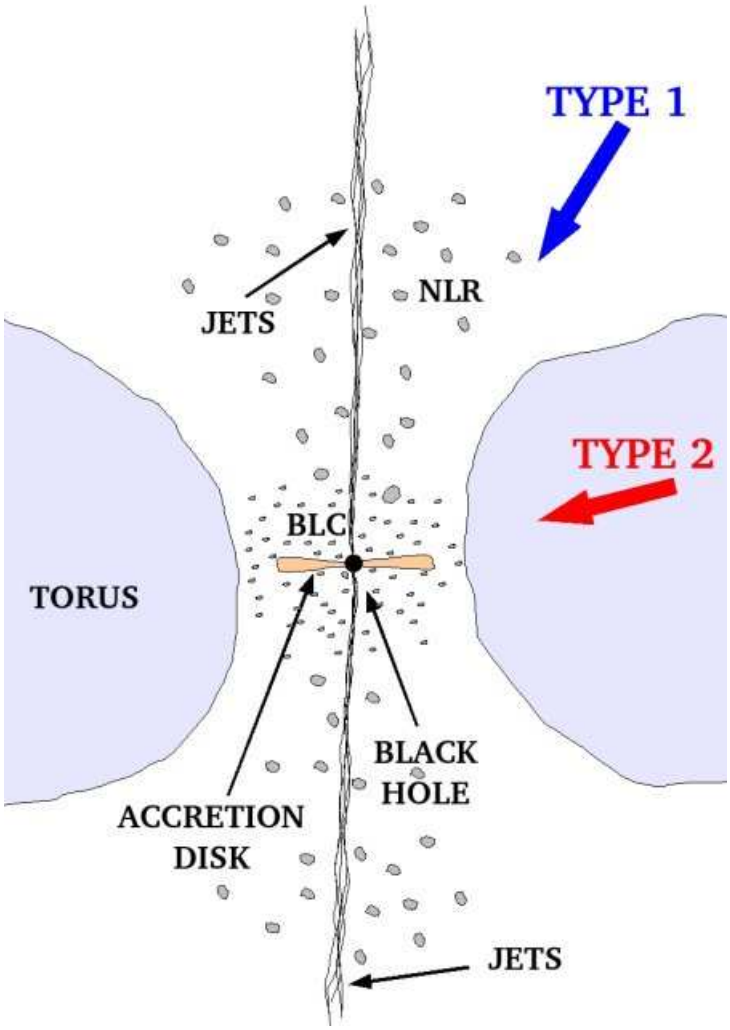

Figure A.1: The simple "unification model" for the central region of an active galaxy. Main components: a supermassive black hole, an accretion disk, the broad-line and narrow-line regions (BLG and NLR), the dusty torus and the two-sided jets.

The dusty toroidal structure that surrounds the central source absorbs the optical, ultraviolet and soft X-ray emission from the active nucleus. However, hard X-ray photons ($> 2\,\mathrm{keV}$) can partially escape from this cold material. Therefore, X-ray observations make it possible to measure the column density along the line of sight and to put tight constraints on the properties of the obscuring medium.

It is commonly believed this X-ray emission is produced in a "corona" near the supermassive black hole, where low-energy photons from the accretion disk are reprocessed by energetic electrons (either mildly relativistic thermal electrons or highly relativistic non-thermal electrons) via inverse Compton scattering. The main result of this process is an observed spectral energy distribution (SED) described by a power law ($S_\nu \propto \nu^{-\Gamma+1}$), with a typical slope $\Gamma \approx 1.8$ (Turner et al. 1997, Tozzi et al. 2006), and an exponential cutoff energy at $\approx 300\,\mathrm{keV}$

(Matt et al. 1999). The radiation can also be reflected and/or scattered depending on the distribution of circumnuclear material causing the overall spectral shape to become flatter, $\Gamma \approx 1.7$, with an apparent smaller energy cut-off (see Svensson 1996).

As hard (high-energy) X-ray photons can penetrate the surrounding material and eventually escape from the AGN host, they can be detected with the present generation of X-ray telescopes. But, if the hydrogen column density along the line of sight becomes larger than the inverse of the photoelectric cross-section $\sigma_{10\mathrm{keV}}^{-1} \approx 10^{24}$ cm^{-2} (see Matt 2002), then the medium becomes "Compton thick" ($\tau = N_{\mathrm{H}}\,\sigma \approx 1$). In this case, all the central radiation is absorbed and the only observable emission comes from photons scattered and/or reflected by the circumnuclear media (Wilman & Fabian 1999).

Since Compton-thin AGN (those with $N_{\mathrm{H}} < 10^{24}\,\mathrm{cm}^{-2}$) are ubiquitous emitters in the $2-10$-keV X-ray band, deep X-ray surveys have proven the best way to estimate the number density and evolution of active galaxies in the Universe (Mushotzky 2004). These X-ray surveys are always flux-limited, inevitably (nowadays $S_{2-10\,\mathrm{keV}}^{\mathrm{limit}} \approx 10^{-16}\,\mathrm{erg\,sec}^{-1}\,\mathrm{cm}^{-2}$), and are therefore biased against faint sources. In fact, the populations of high-redshift, low-luminosity and highly-obscured AGN are still not well determined. This problem translates into a poorly determined faint end of the luminosity function, implying uncertainties in the contribution of AGN to the cosmic X-ray background (CXRB), which is known to require of a sizable population of faint, obscured sources in order to explain its hard SED (Ueda et al. 2003).

The aim of the present work is to constrain previously proposed torus geometries based on the observed distribution of hydrogen column densities (N_{H}) in AGN observed by *Chandra* in the so-called *Chandra* Deep Field South (CDF-S).

A.2 Deep X-ray observations

A.2.1 AGN in the *Chandra* Deep Field-South

Several deep *Chandra* images of the extragalactic sky have been obtained, with the 2-Msec *Chandra* Deep Field-North (CDF-N; Alexander et al. 2003) and 1-Ms *Chandra* Deep Field-South (CDF-S; Giacconi et al. 2002) being the two deepest ($S_{2-10\,\mathrm{keV}}^{\mathrm{limit}} \approx 1.4 \times 10^{-16}\,\mathrm{erg\,sec}^{-1}\,\mathrm{cm}^{-2}$ for CDF-N and a factor $2\times$ shallower for the CDF-S). Zheng et al. (2004) presented accurate photometric redshifts for 342 sources in the CDF-S using the multi-colour dataset available for this field. This corresponds to $\sim$99 per cent of the sample and includes 173 sources with reliable spectroscopic redshifts from Szokoly et al. (2004).

Given the fraction of X-ray sources in the CDF-S with photometric redshifts ($\sim$99 per cent), this field is an ideal choice for our study of torus properties. Redshifts are essential to compute N_{H} (see below) and X-ray luminosity. In this work, we use the conservative sample (321 sources) described by Tozzi et al. (2006) in the CDF-S, which does not include sources with total X-ray lumionsities $L_X < 10^{41}\,\mathrm{erg\,sec}^{-1}$ – a range expected to be dominated by star-forming

galaxies.

A.2.2 Hydrogen column densities

The distribution of $N_{\rm H}$ values for the sources in the CDF-S were derived by Tozzi et al. (2006). They performed direct X-ray spectral fitting to the 82 brightest sources observed by *Chandra* (with redshift information) providing independent estimations for Γ and $N_{\rm H}$. Based on these sources, Tozzi et al. (2006) determined a weighted mean spectral index of $\Gamma \sim 1.75$. For the rest of the sources with poor X-ray spectroscopic information, they fix $\Gamma = 1.8$ to derive the redshifted column densities. The distribution was then corrected for incompleteness in the luminosity and redshift parameter space using the survey effective area and the luminosity function of Ueda et al. (2003). This luminosity function was determined using 247 AGN detected in the $2-10$ keV X-ray band from a compilation of $ASCA$, $HEAO-1$ and *Chandra* observations, and shows luminosity-dependent density evolution, in which the low-luminosity AGN population peaks at a lower redshift than the high-luminosity sources. This is consistent with optical observations of the quasar population which peaks at $z \sim 2$ (Boyle et al. 2000).

In the following analyses we constrain the torus obscuring media using the final corrected $N_{\rm H}$ distribution, seen in Fig. A.2 (from Tozzi et al. 2006).

A.3 General properties of the model

We first assume that X-ray emission from AGN comes from the region nearest to the super-massive black hole. This region has a typical spatial scale of $R_C \approx 10-100\ R_S$ (where $R_S = GM_{\rm BH}/c^2$ is the Schwarzschild radius), implying physical sizes of $R_C \approx 10^{-5}-10^{-3}$ pc for a typical super-massive black hole with $M_{\rm BH} \approx 10^7-10^8$ $M_\odot$. Recent mid-infrared (-IR) interferometric observations of NGC 1068 suggest the torus has a diameter of around 3.4 pc (Jaffe et al. 2004), while near-IR reverberation mapping of nearby Seyfert galaxies estimates an inner limit at $\sim 10^{-2}-10^{-1}$ pc (Suganuma et al. 2006). For practical purposes we approximate the X-ray source as a point-like emitting region, implying that a straightforward treatment of the X-ray radiation will provide the total column density along the line of sight.

A.3.1 Torus properties

We consider four different torus models (presented in § A.4) to obtain synthetic distributions of column densities which are then compared with the intrinsic distribution from Tozzi et al. (2006).

We model the obscuring region as a simple axisymmetrical matter distribution surrounding the accretion disk (see Fig. A.1). Given the symmetry of the problem, random lines of sight with polar angles between 0 and $\pi/2$ (weighted by the angle differential area), are used to

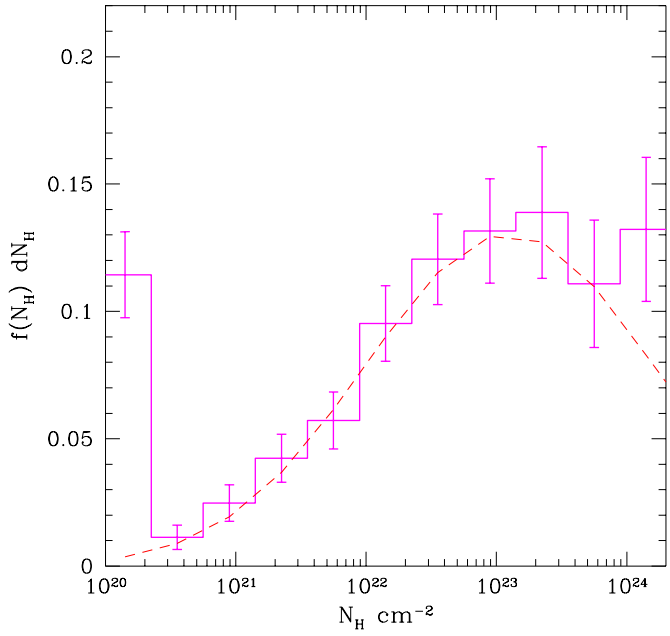

Figure A.2: The intrinsic $N_{\rm H}$ distribution for AGN found in the CDF-S by Tozzi et al. (2006) and used in this work. Incompleteness, sampling-volume effects and statistical errors from measurements are included in the histogram. Poissonian errors are assumed in each bin.

calculate the optical depth for each random direction, where the polar angle, ϕ, is defined as the angle subtended between the line of sight and the torus equatorial plane.

We assume a solar abundance for the torus, a photoelectric cross-section for absorption given by Morrison & McCammon (1983), a standard Galactic gas-to-dust ratio $N_{\rm H}/E(B-V) = 5.8 \times 10^{21}$ cm^{-2} given by Bohlin et al. (1978) and a solar neighbourhood value, $R_V = 3.1$ (Schultz & Wiemer 1975). These assumptions relate the hydrogen column density, $N_{\rm H}$, with the optical extinction, A_V, and the optical depth, τ_V ($A_V = 1.09\tau_V$),

$$\begin{aligned} N_{\rm H}(\phi) = \sigma^{-1}\tau &= \int \rho(r,\phi)dr \\ &= 5.8 \times 10^{21}\ E(B-V)\ \text{cm}^{-2} = 1.9 \times 10^{21} A_V\ \text{cm}^{-2} \\ &= 2.0 \times 10^{21} \tau_V\ \text{cm}^{-2} = 2.0 \times 10^{21}\ \tau_{Vi}\ N_T\ \text{cm}^{-2} \end{aligned} \tag{A.1}$$

where, if the medium is continuous, $\rho(r,\phi)$ is the matter density distribution and σ the effective absorption cross section. Otherwise, if the medium is clumpy, τ_{Vi} represents the optical depth for one cloud and N_T the average number of clouds along the line of sight. It is easy to show that if the density distribution, ρ, has no angular dependency (i.e., $\rho = \rho(r)$), then the radial dependency will be hidden by the assumed maximum column density, $N_{\rm Hmax}$, along

the line of sight. $N_{\rm Hmax}$ also constrains other model parameters, such as the inner radius, the outer radius, the density in the equatorial plane, and/or the cloud optical depth. In this work we fix the maximum value for the column density at $N_{\rm Hmax} = 10^{25}\,{\rm cm}^{-2}$, according to X-ray observations of Type 2 AGN in the $0.1 - 100\,{\rm keV}$ band using the *BeppoSAX* X-ray satellite (Maiolino et al. 1998). We have also assumed a minimum column density along the line of sight given by $N_{\rm Hmin} = 10^{20}\,{\rm cm}^{-2}$, according to the limit imposed by absorption by the Milky Way.

Due to the degeneracy of the model parameters, we use the minimum possible number of free parameters to describe the torus distribution. The chosen parameterisations do not give physical sizes of the distributions explicitly, but instead reduced parameters such as R_{int}/R_{out} (where R_{out} is the external radius and R_{int} is the inner radius for the torus) are used. R_{int} can be estimated by the "evaporation radius" for graphites (at $T \approx 1500\,{\rm K}$) defined by assuming thermal equilibrium between the incident ultraviolet (UV) radiation and the rate of re-emission from the dust. Assuming $a_{\rm gr} = 0.05\,\mu{\rm m}$ as a typical grain size, and following Barvainis (1987):

$$R_{int} \approx 0.4 L_{\rm UV,45}^{1/2}\ {\rm pc}, \tag{A.2}$$

where $L_{\rm UV,45}$ is the UV luminosity in units of $10^{45}\,{\rm erg\,sec}^{-1}$. Assuming this value as a lower limit for the distance, we can estimate the external radius, R_{out}, and other model parameters using our torus model results (see Table A.1).

A.4 Modelling the torus

The degeneracy of model parameters and the uncertainties given by the lack of faint sources in the $N_{\rm H}$ distribution determined by Tozzi et al. (2006), require us to keep the number of free parameters within our torus models to a minimum. As a result, we do not allow the parameters to change with luminosity or redshift.

Barger et al. (2005) presented a complete sample of local X-ray selected AGN ($z < 1.2$), in which a luminosity dependence for the fraction of Type 2 over Type 1 AGN is seen, as Ueda et al. (2003) proposed earlier. This implies a possible dependency of the covering factor of the dusty torus on luminosity, and therefore a change in the geometrical torus distribution. This implies our results can be understood as an average geometrical distribution for the entire AGN population, given by a simple axially symmetric geometry, with no dependency on luminosity or redshift. A discussion on the luminosity dependency can be found in § A.5.

To determine the torus parameters which best fit the observed column densities, we use a χ^2 test with uncertainties taken from Tozzi et al. (2006) (Fig. A.2). Our experience determining the intrinsic $N_{\rm H}$ distribution based on "hardness ratio", $(H-S)/(H+S)$, where H and S are the counts in the hard and soft X-ray bands, respectively, suggests that this method introduces uncertainties in the inferred $N_{\rm H}$ values that dominate over the Poissonian errors. The spectral

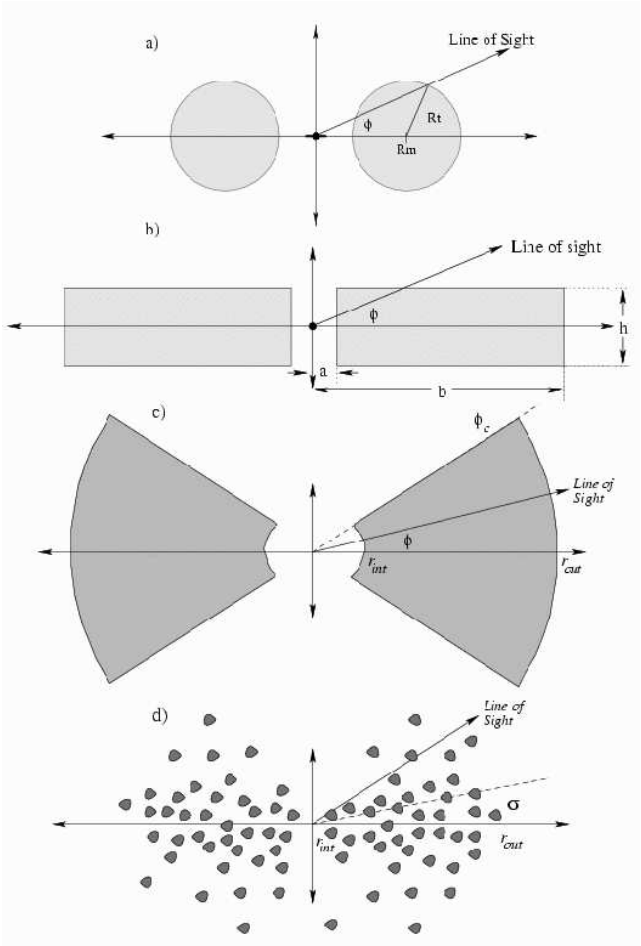

Figure A.3: Geometrical matter density distributions assumed for the torus models. Sketches labelled a), b) c) and d) are based on the previous work by Treister et al. (2004), Pier & Krolik (1992), Granato & Danese (1994) and Nenkova et al. (2002), respectively.

fitting treatment introduced by Tozzi et al. (2006) gives more reliable values for the intrinsic properties of the obscuring region in AGN.

Tozzi et al. (2006) found 14 sources showing reflection-dominated spectra. These Compton-thick sources were not used in our analysis because of the large uncertainty in the number counts of this population. Indeed, the last bin from the intrinsic column density distribution shown in Fig. A.2, which includes objects with $N_{\rm H} > 10^{24}\,{\rm cm}^{-2}$, represents only a lower limit.

The models presented in the remainder of this section were motivated by previous work that was carried out to explain a variety of observational properties of AGN (Treister et al. 2004; Pier & Krolik 1992, Pier & Krolik 1993; Granato & Danese 1994; Elitzur et al. 2004).

A.4.1 Model 1

Adopting the torus distribution proposed by Treister et al. (2004), we modelled the geometry sketched in Fig. A.3a to find different optical depths as a function of the line of sight, ϕ. In this case the matter density is not distributed as in an homogeneous medium, but has the following dependence with ϕ and r:

$$\rho(r,\phi) = \rho_{\rm eq} \left(\frac{r_{\rm int}}{r}\right)^{\beta} \; e^{-\gamma|\sin(\phi)|} \tag{A.3}$$

where $\rho_{\rm eq}$ is the inner density (at $r_{\rm int} = R_m - R_t$) in the equatorial plane. In this model, the free parameters are R_m/R_t (see Fig. A.3a), γ, and β. The analytical equations which describe the column density as a function of ϕ are given by:

$$\begin{aligned}
&\text{If} \quad 0 \leq \phi < \sin^{-1}(R_t/R_m) \quad \text{and} \quad \beta \neq 1 \quad \text{then,} \\
&N_{\rm H} = N_{\rm Hmax}\, e^{-\gamma|\sin(\phi)|} \times \\
&\quad \frac{\left[\left(\cos(\phi)+\sqrt{(R_t/R_m)^2-\sin(\phi)^2}\right)^{1-\beta} - \left(\cos(\phi)-\sqrt{(R_t/R_m)^2-\sin(\phi)^2}\right)^{1-\beta}\right]}{(1+R_t/R_m)^{1-\beta}-(1-R_t/R_m)^{1-\beta}} \\
&\text{If} \quad 0 \leq \phi < \sin^{-1}(R_t/R_m) \quad \text{and} \quad \beta = 1 \quad \text{then,} \\
&N_{\rm H} = N_{\rm Hmax}\, e^{-\gamma|\sin(\phi)|} \times \\
&\quad \frac{\ln\left(\left(\cos(\phi)+\sqrt{(R_t/R_m)^2-\sin(\phi)^2}\right)/\left(\cos(\phi)-\sqrt{(R_t/R_m)^2-\sin(\phi)^2}\right)\right)}{\ln((1+R_t/R_m)/(1-R_t/R_m))} \\
&\text{If} \quad \sin^{-1}(R_t/R_m) \leq \phi \leq \pi/2 \quad \text{then,} \quad N_{\rm H} = N_{\rm Hmin}
\end{aligned} \tag{A.4}$$

The maximum and minimum column density along the line of sight are through the equatorial plane and at the poles, respectively.

$$\begin{aligned}
&\text{If} \quad \beta \neq 1 \quad \text{then,} \\
&\quad N_{\rm Hmax} = \rho_{\rm eq}\, r_{\rm int}^{\beta} \frac{R_m^{1-\beta}}{1-\beta} \left[\left(1+\frac{R_t}{R_m}\right)^{1-\beta} - \left(1-\frac{R_t}{R_m}\right)^{1-\beta}\right] \\
&\text{If} \quad \beta = 1 \quad \text{then,} \quad N_{\rm Hmax} = \rho_{\rm eq}\, r_{\rm int} \ln\left(\frac{1+R_t/R_m}{1-R_t/R_m}\right)
\end{aligned} \tag{A.5}$$

This model gives a good fit to the data, with $\chi^2_{\nu,\rm min} = 1.30$. Results adopting $\beta = 0.0$ are presented in Fig. A.4 and show a well-constrained region of the $R_m/R_t - \gamma$ parameter space. The best fit values are spread between $1.07 \lesssim R_m/R_t \lesssim 1.15$ and $7.0 \lesssim \gamma \lesssim 9.0$ at 3 σ confidence levels. The same results are obtained when a value $\beta = 2.0$ is used. Adopting a radial density profile, where $\beta = 1.0$ and 3.0, results in a small decrease in the value of γ, but does not introduce further changes.

From the family of parameters found, we show in Fig. A.5 examples for synthetic $N_{\rm H}$ distributions compared with the intrinsic distribution determined by Tozzi et al. (2006). It is seen that the parameter R_m/R_t mostly affects the distribution of Type 1 sources (i.e., for $N_{\rm H} < 10^{22}\,{\rm cm}^{-2}$), while γ changes the Type 2/1 fraction.

Model	$\chi^2_{\nu,\min}$	Parameter 1	Parameter 2	Parameter 3	$R_{\rm out}$(pc)	$\rho_{\rm eq}$(cm^{-3})
1	1.30	$1.07 \lesssim R_m/R_t \lesssim 1.15$	$7.0 \lesssim \gamma \lesssim 9.0$	$0.0 \lesssim \beta \lesssim 3.0$ ‡	$5.7 - 12$	$2.8 - 6.0 \times 10^5$ †
2	8.13	$2.4 \lesssim h/a \lesssim 3.3$	$250 \lesssim b/a \lesssim 600$	–	$100 - 240$	$1.3 - 3.2 \times 10^4$
3	5.65	$1.0 \lesssim \phi_c$ (rad) $\lesssim 1.2$	$8.0 \lesssim \gamma \lesssim 10.0$	free	1.0 *	5.4×10^6 †
4	2.65	$0.38 \lesssim \sigma$ (rad) $\lesssim 0.44$	$\tau_{Vi} \lesssim 0.8$	–	free	–

Notes:

* fixed parameter;

† these parameters can be modified taking into account radial dependencies for the model, i.e. $\beta \neq 0$;

‡ obtained assuming $\gamma = 9.0$.

Table A.1: Summary of the estimated parameters for the models described in § A.4. Ranges are obtained from 3-σ confidence limits (see contour plots in the Fig. A.4). The last two columns are determined for a UV luminosity of 10^{45} erg sec^{-1} and Eq. (A.2). No radial dependency for the density distribution ($\beta = 0$) is assumed in the models. In model 3 we fix $R_{\rm out}$ to be 1 pc to estimate a density at the equatorial plane, although this is a free parameter. Model 4 is not shown in the last columns due to the different cloud treatment explained in § A.4.4.

A sketch of the torus geometrical distribution, choosing the best-fit parameters, is shown in Fig. A.6, where the "donut" structure for this model is seen. For these assumed parameters, this model predicts an intrinsic fraction of sources with column densities $> 10^{24}$ cm^{-2} of $\sim$27 per cent.

A.4.2 Model 2

This model is proposed here following the previous studies by Pier & Krolik (1992), Pier & Krolik (1993) based on the torus IR re-emission. We use their geometrical distribution (Fig. A.3b) to find the dependency of the column density on the line of sight.

This model assumes a homogeneous density with h/a and b/a as free parameters, where h, b, and a are as shown in Fig. A.3b. The dependency of the column density with the line of sight ($0 \leq \phi \leq \pi/2$) is given by:

$$\begin{aligned}
&\text{If} \quad 0 \leq \phi < \tan^{-1}\left(\tfrac{h}{2b}\right) \quad \text{then,} \quad N_{\rm H} = N_{\rm Hmax}\,\frac{\cos\left(\tan^{-1}(h/2b)\right)}{\cos(\phi)} \\
&\text{If} \quad \tan^{-1}\left(\tfrac{h}{2b}\right) \leq \phi < \tan^{-1}\left(\tfrac{h}{2a}\right) \quad \text{then,} \\
&\quad N_{\rm H} = N_{\rm Hmax}\,\frac{\cos\left(\tan^{-1}(h/2b)\right)}{b/a-1}\left(\tfrac{h}{2a}\sin(\phi)^{-1} - \cos(\phi)^{-1}\right) \\
&\text{If} \quad \tan^{-1}\left(\tfrac{h}{2a}\right) \leq \phi \leq \pi/2 \quad \text{then,} \quad N_{\rm H} = N_{\rm Hmin}
\end{aligned} \tag{A.6}$$

where the maximum column density is:

$$N_{\rm Hmax} = \rho_{\rm eq}\,\frac{b-a}{\cos\left(\tan^{-1}\left(\tfrac{h}{2b}\right)\right)} \tag{A.7}$$

Comparing the synthetic distributions of column densities with that observed, we find the results shown in Fig. A.4. The parameters are not well constrained and imply $2.4 \lesssim h/a \lesssim 3.3$ and $250 \lesssim b/a \lesssim 600$ at 3 σ confidence levels. The model also shows an extreme radial-to-vertical thickness ratio ($b/h \approx 75 - 250$).

Synthetic $N_{\rm H}$ histogram predictions are shown in Fig. A.5. It is seen that the change of parameter b/a systematically produce an overestimation of the number of sources at around $N_{\rm H} = 10^{22.5}\,{\rm cm}^{-2}$, while the change of h/a dramatically modifies the first bin of unobscured sources.

Clearly, this model is limited by its constant density distribution. This translates into a large b/a, needed to reproduce the wide range of observed column densities (since $N_{\rm H} \propto \Delta s$), and a very sensitive distribution in the innermost region of the torus (see Fig. A.6). Also, the model does not predict a large fraction of highly obscured sources, implying it could not explain the CXRB or the number of Compton-thick sources observed in the CDF-S ($\sim$10 per cent; Tozzi et al. 2006). The typical intrinsic fraction of Compton-thick sources predicted by the model is only $\sim$3 per cent. These are generated by a narrow angular section near the equatorial plane, able to produce large column densities (see Fig. A.6).

When we compare our analysis with the results from Pier & Krolik (1992) we find further disagreements. Their typical dimensions, as constrained by IR torus re-emission, are $\sim$1 pc; we, on the other hand, obtain tori with typical scales of $\sim$200 pc, assuming $L_{\rm UV} = 10^{45}\,{\rm erg\,sec}^{-1}$.

We conclude that this torus model can be rejected by our X-ray treatment for the numerous reasons already discussed, such as the large outer radius, which is not seen in local AGN (Jaffe et al. 2004; Prieto et al. 2004), the extreme geometrical distribution in the inner regions, and the small number of predicted Compton-thick sources.

A.4.3 Model 3

This model has the spatial density distribution shown in Fig. A.3c and is based on the work presented by Granato & Danese (1994). The density profile has an exponential dependency with the polar angle parameterised by a factor γ (when $\phi < \phi_c$), and a power-law dependency for the radius parameterised by the index, β:

$$\rho(r,\phi) = \rho_{\rm eq} \left(\frac{r_{\rm int}}{r}\right)^{\beta} e^{-\gamma|\sin(\phi)|} \tag{A.8}$$

where $\rho_{\rm eq}$ is the inner torus density at the equatorial plane. The free parameters of the model are γ, β and the opening angle, $\phi_{\rm c}$. The equation which describes the dependence of the column density and the line of sight is:

$$\begin{aligned} &\text{If} \quad 0 \leq \phi < \phi_{\rm c} \quad \text{then,} \quad N_{\rm H} = N_{\rm Hmax}\, e^{-\gamma|\sin(\phi)|} \\ &\text{If} \quad \phi_{\rm c} \leq \phi \leq \pi/2 \quad \text{then,} \quad N_{\rm H} = N_{\rm Hmin} \end{aligned} \tag{A.9}$$

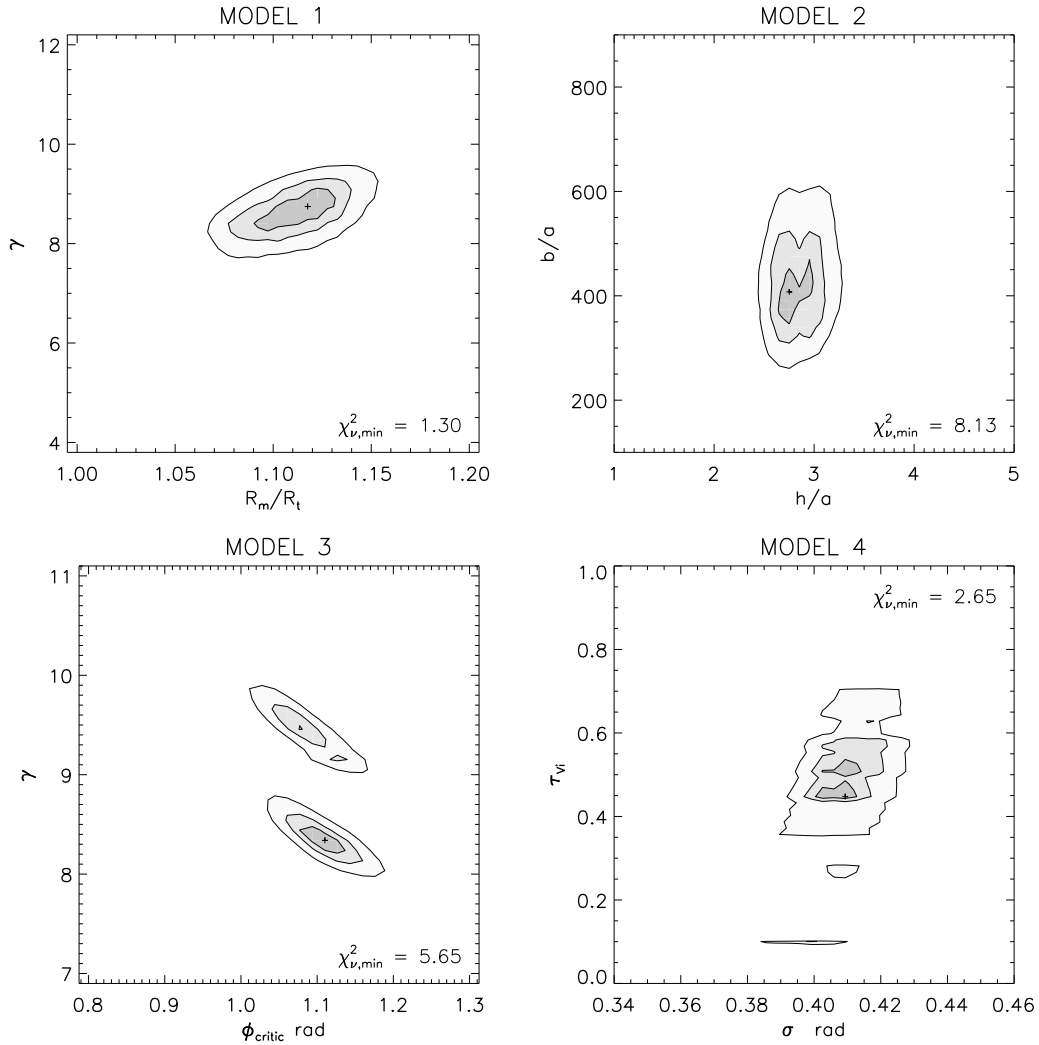

Figure A.4: Best-fit parameters found for each model following § A.4. Contours represent 1, 2 and 3 σ confidence limits. Note that for model 1, $\beta = 0.0$. The small plus sign shows the minimum χ^2.

where $N_{\rm Hmin}$ and $N_{\rm Hmax}$ are fixed at 10^{20} and $10^{25}\,{\rm cm}^{-2}$, respectively. The minimum value fixes $N_{\rm H}$ at the poles and the maximum value fixes $N_{\rm H}$ in the equatorial plane.

$$\begin{aligned} &\text{If} \quad \beta \neq 1 \quad \text{then,} \quad N_{\rm Hmax} = \rho_{\rm eq}\, r_{\rm int}^{\beta} \left(\frac{r_{\rm out}^{1-\beta} - r_{\rm int}^{1-\beta}}{1-\beta} \right) \\ &\text{If} \quad \beta = 1 \quad \text{then,} \quad N_{\rm Hmax} = \rho_{\rm eq}\, r_{\rm int} \ln \left(\frac{r_{\rm out}}{r_{\rm int}} \right) \end{aligned} \tag{A.10}$$

Searching for best-fit parameters using the χ^2 test, we obtain the results shown in Fig. A.4. This model gives a poor fit to the data ($\chi^2_{\nu,min} = 5.65$), and is not able to reproduce the observed $N_{\rm H}$ distribution between the first bin and those at $\lesssim 10^{22}\,{\rm cm}^{-2}$ (Fig. A.5). The sharp gap seen at $N_{\rm H} \lesssim 10^{21}\,{\rm cm}^{-2}$ in the synthetic distributions corresponds to the transition produced

when the line of sight no longer hits the torus ($\phi > \phi_c$). This dichotomy also affects the χ^2 distribution where multiple minima are seen. Parameters between $57^o \lesssim \phi_c \lesssim 69^o$ and $8.0 \lesssim \gamma \lesssim 10.0$ are found. Changes in the value of ϕ_c affect the distribution for Type 1 sources only (i.e. for $N_H < 10^{22}\,cm^{-2}$), while γ affects the number of sources at $N_H \approx 10^{21}\,cm^{-2}$ and changes the fraction of Type 2/1. The estimated intrinsic fraction of Compton-thick sources, using the best-fit parameters, is about 26 per cent.

When we compare our results with the work by Granato & Danese (1994) we find that our analysis can constrain ϕ_c (except for large γ values), while they found the SED for the re-emission does not depend strongly on this parameter. On the other hand, we cannot constrain the outer radius, since this scale parameter is contained in N_{Hmax} (Eq. A.10), and can reach a wide range of values (e.g. $> 100\,pc$, as found by Granato & Danese 1994).

A.4.4 Model 4

Many previous attempts to reproduce the IR re-emission from the obscuring torus were based on continuous density distributions (as those presented in models 1 to 3). Elitzur et al. (2004) and Nenkova et al. (2002) developed the formalism to handle dust clumpiness. Their results indicate that the inclusion of thick clouds may resolve the difficulties encountered by previous theoretical efforts that have tried to reproduce the observed IR SEDs of local AGN. They have shown that some problems are naturally resolved if a clumpy media with $\sim 5-10$ clouds along radial rays (each one with $\tau_{V_i} \gtrsim 40$) is considered. The fundamental difference between clumpy and continuous density distributions is that radiation can propagate freely between different regions of an optically thick medium when it is clumpy, but not otherwise.

Following Elitzur et al. (2004) we define the model sketched in Fig. A.3d, with a random spatial cloud distribution per unit length given by

$$n_T(r,\phi) = n_{eq}\left(\frac{r_{int}}{r}\right)^{\beta} e^{-\phi^2/\sigma^2} \tag{A.11}$$

where n_{eq} is the inner number of clouds by unit length in the equatorial plane, σ the half opening angle for the angular distribution, and β the power law index describing the radial dependency. Integrating the last equation along the line of sight, we obtain the average number of clouds, N_T as a function of the angle ϕ:

$$N_T(\phi) = N_{eq}\, e^{-\phi^2/\sigma^2} \tag{A.12}$$

where N_{eq} is the average number of clouds along the equatorial plane.

$$\begin{aligned} &\text{If} \quad \beta \neq 1 \quad \text{then,} \quad N_{eq} = n_{eq}\frac{r_{int}^{\beta}}{1-\beta}\left(r_{out}^{1-\beta} - r_{int}^{1-\beta}\right) \\ &\text{If} \quad \beta = 1 \quad \text{then,} \quad N_{eq} = n_{eq} r_{int} \ln\left(\frac{r_{out}}{r_{int}}\right) \end{aligned} \tag{A.13}$$

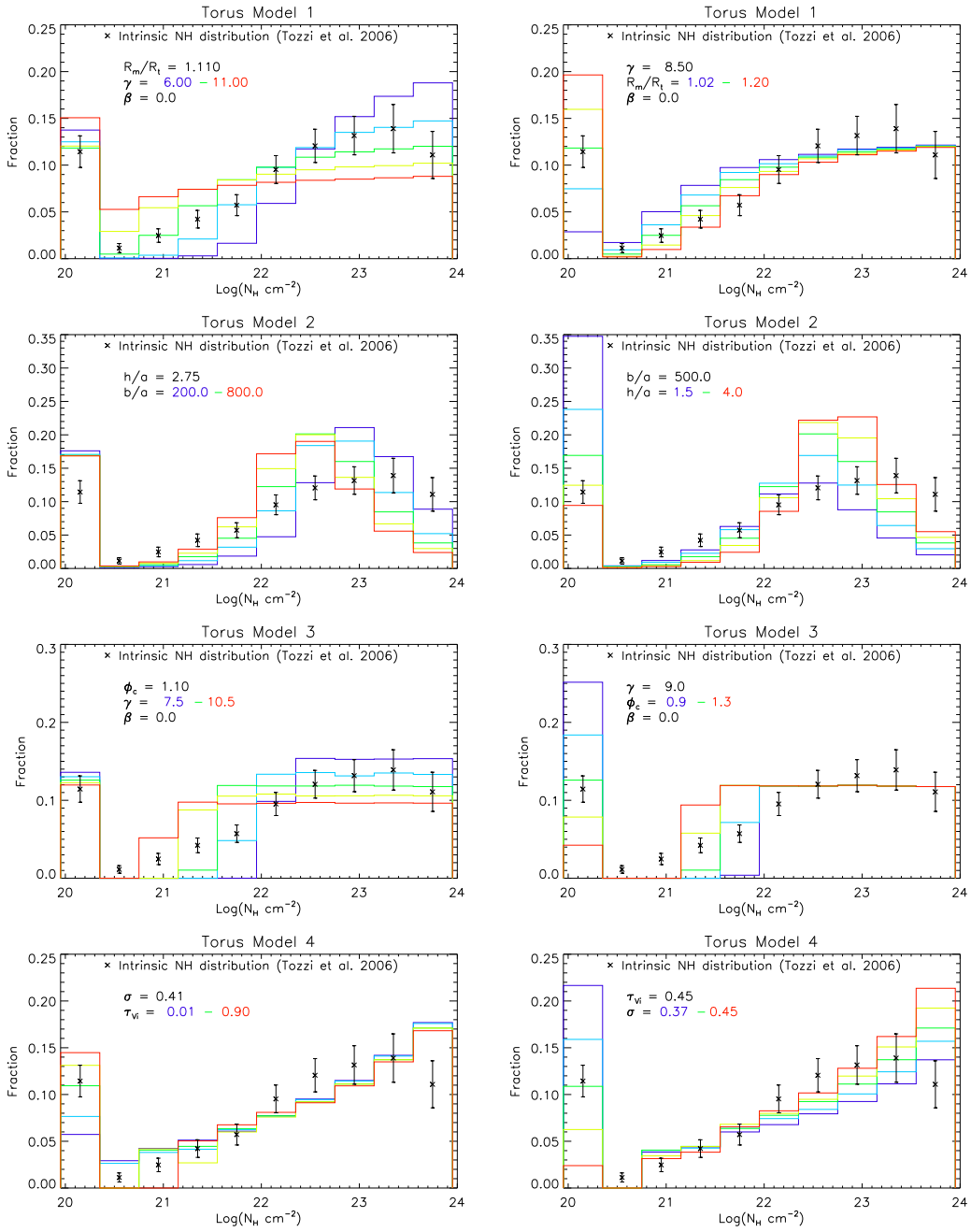

Figure A.5: Comparison of the intrinsic column densities of the observed *Chandra* sources in the CDF-S field (crosses; Tozzi et al. 2006) and the family of best-fit results obtained from our synthetic modelling. For each model, two histograms are presented, varying the range of interest of one parameter only.

Assuming $\tau_V = N_T \tau_{V_i}$, and considering Eq. (A.1), we can estimate the $N_{\rm H}$ dependency on the line of sight by

$$N_{\rm H}(\phi) = N_{\rm Hmax}\, e^{-\phi^2/\sigma^2} \tag{A.14}$$

The fixed parameter $N_{\rm Hmax}$ constrains the optical depth, the number of clouds along the line of sight at the equatorial plane, and the parameter β:

$$N_{\rm Hmax} = 2.0 \times 10^{21} N_{\rm eq} \tau_{Vi} \tag{A.15}$$

If a certain value τ_{Vi} is assumed for the clumps, the only remaining free parameter for this distribution is σ. However, restricting N_T to represent a discrete number of clouds and assuming a Poissonian probability for the number of clouds along the line of sight, it is also possible to constrain the optical depth per cloud, τ_{Vi}. In the case where the optical depth tends to zero but N_T tend to infinity, the continuous case is recovered, and column densities are allowed to have any value. Note that Nenkova et al. (2002) assumed $\tau_{V_i} = 40$ to reproduce the IR re-emission from the torus, implying a minimum column density of $8.0 \times 10^{22}\,{\rm cm}^{-2}$. Clearly, smaller optical depths per cloud are necessary to explain the observed distribution of $N_{\rm H}$. This difficulty may be explained by extra absorption from diffuse material in the torus, or in the local galaxy.

The best-fit values for σ and τ_{Vi} are shown in Fig. A.4. Multiple minima in the χ^2 distribution are found due to the quantised cloud number and the bin sizes in the $N_{\rm H}$ histogram. Values between $22^{\rm o} \lesssim \sigma \lesssim 25^{\rm o}$ and $\tau_{Vi} \lesssim 0.8$ are preferred. Parameter σ changes the number of objects at $N_{\rm H} = 10^{20}\,{\rm cm}^{-2}$ and at $N_{\rm H} = 10^{25}\,{\rm cm}^{-2}$, without significantly altering the intermediate values where an increasing slope in the synthetic distributions is seen. The optical depth per cloud creates a dichotomy between Type 2 and Type 1 objects, where the minimum value of $N_{\rm H}$ is given by the optical depth of a single cloud.

From Fig. A.6, it is clear that this model gives the largest number of Compton-thick sources produced by lines of sights near the equatorial plane (approximately a fraction of ~ 58 per cent using best fit parameters). If a lower $N_{\rm Hmax}$ of $10^{24}\,{\rm cm}^{-2}$ is adopted, the Gaussian angular dependency generates large discrepancies with the observed column densities.

Comparing our parameters with the results coming from the re-emission treatment given by Elitzur et al. (2004), we find that our typical Gaussian angular distributions are smaller. They find a valid range of $\sigma = 45^{\rm o} \pm 15^{\rm o}$. Also, their estimations for the number of clouds along the equatorial plane ($N_{\rm eq} \approx 5 - 10$) correspond to a maximum column density of $\sim 10^{24}\,{\rm cm}^{-2}$ (see Eq. A.1), one order of magnitude smaller than our assumptions. In our models, since $N_{\rm Hmax} = 10^{25}\,{\rm cm}^{-2}$, the value of $N_{\rm eq}$ depends on the assumed τ_{Vi}.

Note that since $N_{\rm H} \propto N_T$, this clumpy model requires a wide range for the number of clumps (at least ~ 3 orders of magnitude) to describe the wide range of observed $N_{\rm H}$.

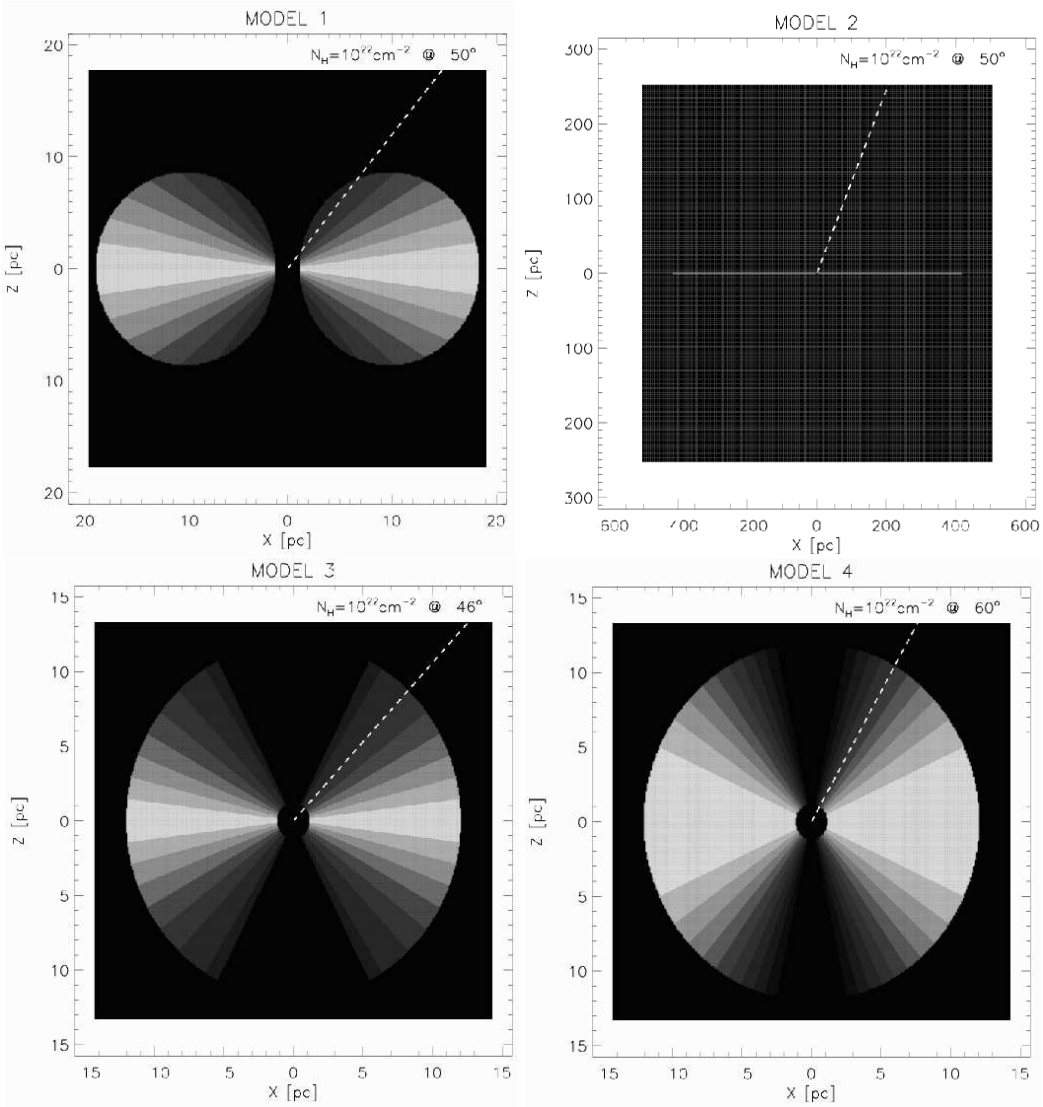

Figure A.6: Geometrical matter density distribution using best-fit parameters for each model. Model 1: $R_m/R_t = 1.14$, $\gamma = 9.0$ and $\beta = 0.0$; model 2: $h/a = 3.0$ and $b/a = 350$; model 3: $\phi_c = 1.1$ and $\gamma = 9.5$; model 4: $\sigma = 0.4$ and $\tau_{Vi} << 1$ (continuous case). The inner radius is set at 1.2 pc for all models, and an outer radius at 12 pc for models 3 and 4 (but adjustable by β for more compact structures). Different shades indicate increments of $\Delta \log(N_{\rm H}) = 0.5$, starting from $10^{25}\,{\rm cm}^{-2}$ in the equatorial plane. The dashed line represents the line of sight that divides the Type 1 and the Type 2 sources. Note that model 2 is shown at a different scale.

A.5 Discussion

A.5.1 Torus properties as a function of luminosity

The work of Barger et al. (2005), based on a complete AGN sample at $z < 1.2$, shows a dependency of the fraction of Type 2/1 AGN with luminosity. This observational evidence implies that our simple models, where the torus does not evolve with luminosity or redshift, might not be an accurate representation.

Treister & Urry (2005) found a simple explanation for Barger's results: a "modified unification model" where the percentage of obscured AGN varies linearly from 100 per cent at $L_X = 10^{42}\,\mathrm{erg\,sec^{-1}}$ to 0 per cent at $L_X = 3 \times 10^{46}\,\mathrm{erg\,sec^{-1}}$. We can explore how this luminosity evolution would change our results for the torus models. Using the luminosity dependency for the fraction of Type 2 AGN determined by La Franca et al. (2005), we find that in the case of model 1 (that with the best statistical results), parameter γ, which is mostly responsible for the variations observed in this fraction, changes to $\approx$ 7.0, 14 and 23 (fixing $R_m/R_t = 1.1$) for the X-ray luminosity bins 10^{42-43}, 10^{43-44} and $10^{44-45}\,\mathrm{erg\,sec^{-1}}$, respectively. These values take into account the observational incompleteness for the Type 2 population in La Franca's X-ray sample (one third of the sources is expected to be missed). Table 1 shows that our results give an estimate of $7.0 \lesssim \gamma \lesssim 9.0$, coinciding roughly with γ for the lowest and middle luminosity bins in La Franca's sample.

Unfortunately, the current statistics for the observed N_{H} distribution does not allow us to test such luminosity dependency. Nevertheless, the number density of the most luminous sources is much smaller than those of low and intermediate luminosity. Considering a L_X integration of the Ueda et al. (2003) luminosity function (from 10^{42} to $10^{45}\,\mathrm{erg\,sec^{-1}}$), we predict fractions of 63, 30, and 7 per cent for the 10^{42-43}, 10^{43-44} and $10^{44-45}\,\mathrm{erg\,sec^{-1}}$ luminosity bins, respectively. Therefore, the general N_{H} distribution is clearly dominated by the less powerful (Seyfert like) AGN, for which the derived torus properties might be a good representation.

A.5.2 Column densities uncertainties

Our analysis is based on the distribution of hydrogen column densities. From these measurements, it is not possible to determine how far from the central source the absorption is produced. This implies that over-densities of gas located closer than the graphite sublimation radius will not have the assumed gas-to-dust ratio. This possibility is consistent with the extreme variability of the column density observed in the Seyfert galaxy, NGC 1365 (Risaliti et al. 2005). Assuming higher metallicities gives harder photoelectric absorption, increasing the estimated number of Type 1 sources. Finally, a modification of the parameter R_V from 3.1 to 5.0 produces only small differences in our results.

A spectroscopic analysis such as the one conducted by Tozzi et al. (2006) is essential to estimate the intrinsic distribution of column densities. Broad-band estimates, using hardness

ratios, are not sufficiently precise and are highly affected by the template assumed for the X-ray source. These uncertainties affect the best-fit model parameters, and the errors for the $N_{\rm H}$ estimates. A direct fit to the spectral features is required to describe the obscuring properties of the AGN population.

A.5.3 Torus model results

Recent IR observations have revealed compact torus structures in nearby Seyfert 2 galaxies (Jaffe et al. 2004; Prieto et al. 2004, Prieto et al. 2005, Swain et al. 2003) in agreement with the sizes predicted from model 1, and for models 3 and 4 where this physical size can be freely adjusted.

It has been argued that a constant torus density distribution does not explain the re-emitted IR spectrum in AGN, but the inclusion of a clumpy medium solves this problem. Models 1 to 3 can be discretized using Eq. (A.1), although they should adopt small optical depths per cloud to allow predictions of Type 1 sources at $\lesssim 10^{21}\,{\rm cm}^{-2}$ and to avoid a large dichotomy between Type 2 and Type 1 objects (see model 4 for details).

Exponential angular dependencies of the density parameter, ρ (see Eq. A.1), allow smooth density decrements from the equatorial plane to the poles, so that a wide range of $N_{\rm H}$ can be obtained. This suggests model 1 and 3 are the most favorable obscuring structures. Radial dependencies for the models ($\beta > 0$) can shrink the effective torus radius, increasing the inner equatorial density, more in line with dynamical simulations of a thick clumpy torus (see Beckert & Duschl 2004).

A.5.4 Highly-absorbed sources

According to the X-ray analysis of Seyfert 2 galaxies presented by Maiolino et al. (1998), the Compton-thick sources make up a large fraction of the AGN population. In this work, the assumption of a maximum column density at $N_{\rm H} = 10^{25}\,{\rm cm}^{-2}$ allows us to estimate the Compton-thick fraction by simple geometrical assumptions (see Fig. A.6). We predict intrinsic fractions of 27, 3, 26 and 58 per cent for models 1, 2, 3 and 4, respectively. Tozzi et al. (2006) estimated a lower limit for the Compton-thick fraction of $\sim$10 per cent in the CDF-S, while Beckmann et al. (2006) found four Compton-thick sources from a total of 40 AGN observed with *Integral* in the 20–40-keV energy range at $z \sim 0$. These values are somewhat smaller – but still consistent with – predictions from models 1 and 3, given the uncertainties involved. In particular, model 4 predicts a substantially higher number of heavily-absorved sources.

A.6 Conclusions

1. Using the observed distribution of $N_{\rm H}$ columns for AGN in the CDF-S (Tozzi et al. 2006), we have constrained the geometry of the obscuring region present in AGN. Four different torus geometries, based on previously proposed models (see Fig. A.3), have been explored. No luminosity or redshift dependencies have been included in the torus modelling.

2. Best fits from our models are presented in Table A.1. These results can be used to estimate physical properties of the torus, such as the inner and outer radii, and the density at the equatorial plane, as a function of the AGN luminosity.

3. Detailed analysis shows that a matter density profile, $\rho(\phi)$, with an exponential dependency in ϕ, such as in models 1 and 3, gives the best representation of the wide range of observed column densities (from $\sim 10^{20}\,{\rm cm}^{-2}$ to $\sim 10^{25}\,{\rm cm}^{-2}$). A constant density distribution (model 2) requires very extended structures to recover the wide observed $N_{\rm H}$ range (since $N_{\rm H} \propto \Delta s$), not in accord with actual observations of local Seyfert galaxies where pc-scale torus-like structures have been detected. It also under-estimates the fraction of Type 2 sources. A Gaussian angular dependency (model 4), as in the clumpy model proposed by Nenkova et al. (2002), results in a substantial over-estimation of highly obscured sources. We also find that the optical depth for individual clumps, τ_{Vi}, has to be ~ 60 times smaller than the value adopted by Nenkova et al. to compute the torus IR re-emission (note $N_{\rm H} \propto N_T$). We note that the clumpy torus treatment could also be applied to the other model distributions using Eq. (A.1) and a suitable value for τ_{Vi}. Models 3 and 4 suffer multiple χ^2 minima caused by the dichotomy between Type 1 and Type 2 sources (given by the critical value of ϕ and the presence of at least one clump along the line of sight, respectively).

4. We therefore conclude that model 1, a classical "donut" structure gives the best parameterisation for the obscuring region around AGN. Since no luminosity dependency has been included in our modelling, the results can be regarded as a luminosity averaged parameterization of the torus, basically dominated by intermediate- and low-luminosity sources.

APPENDIX B

A short description of radio data reduction using $\mathcal{AIPS}$

"Antes dejaba que cualquiera entrara a mi pieza
y siempre me reclamaban de lo sucia que estaba
que en el suelo hay papeles, discos, calzoncillos por todas partes.
Ahora solo dejo entrar a los que desordenan."

Francisco 'Banana' Pérez.

The Astronomical Image Processing System ($\mathcal{AIPS}$) is a software package developed by the National Radio Astronomy Observatory (NRAO) for interactive calibration, editing and imaging of radio interferometric data, based on Fourier synthesis imaging methods (see Chapter 2 for details). In this Appendix, we describe the use of $\mathcal{AIPS}$ for calibration, display and analysis of GMRT and VLA data to generate astronomical images suitable for scientific research.

B.1 Radio observations

When we conducted the deep radio observations used in this thesis, observing sessions at both the GMRT and VLA telescopes usually comprised a series of ∼45-min scans centred on the field of interest – the Lockman Hole or the Subaru XMM-*Newton* Deep Field (SXDF) – split

into 16-sec (at GMRT) or 5-sec (at VLA) integrations, and sandwiched between short (2–5-min) scans of a calibrator. The calibrator is used to track the amplitude, phase, and – if sufficiently bright – to provide time-dependent antenna-based bandpass solutions. Ideally, the calibrator is nearby ($<$10 deg), bright ($>$1 Jy) and unresolved. The absolute flux calibration is based on snapshots to bright 3C 48, 3C 147 or 3C 286 sources ($\sim$ 30 mJy at 610 MHz), usually obtained at the beginning and at the end of each session. These very bright 3C sources often make it possible to ignore contamination by radio-frequency interference (RFI), which is particularly troublesome at $<$1 GHz.

Data from GMRT are collected in two sidebands, the upper sideband (USB; LTA files) and the lower sideband (LSB; LTB files). They each contain 128 frequency channels in both right- and left-handed circular polarisations (linear at 1.4 GHz). To convert these files into FITS format (Flexible Image Transport System) it is necessary to run 'listscan' and 'gvfits', which are maintained at the GMRT site[1].

B.2 Loading the data in $\mathcal{AIPS}$ and first steps

FITLD is used to load the raw FITS data into $\mathcal{AIPS}$. Use DOUVCOMP=$-$1 to avoid data compression (which would limit dynamic range) and to create weights for each integration on each baseline, based on the nominal sensitivity and integration time. This task creates a *uv* dataset (UC lists these) which can be called by GETN #, where # is the catalogue number. The header, which contains all the important information, can be shown via IMH.

The first step is to create an index of scans and initialise the calibration files, the NX and CL tables, using INDXR. This assigns a code to each source and records the time ranges over which each source is observed during the track. At this stage the data are not calibrated in any sense.

It is useful to print out the scans times and antenna names (and associated numbers and positions) for each session using LISTR (OPTYPE = 'SCAN') and PRTAN. This information is particularly useful for identifying the main calibrators and finding a good reference antenna.

Next, we record the flux densities of the sources to be used as calibrators (the 3C sources) in the SU table (to see the list of tables attached to a *uv* dataset or image, use IMH), adopting previously known values provided by the SETJY task (OPTYPE = 'CALC', APARM = 0).

B.3 Flagging

As described in Chapter 2, data consist of amplitudes and phases, for each channel, polarisation (right/left-handed), sideband (USB and LSB), and baseline (pair of antennas). Ideally these data will contain the sky signal only, but low-frequency observations suffer radio-frequency interference (RFI) from a large variety of electromagnetic devices (and occasionally

[1] `http://www.ncra.tifr.res.in/~aips/utilities/`

from extraterrestrial sources like the Sun). RFI is the main reason why telescopes are located far from man-made contamination. In $\mathcal{AIPS}$, many tools have been developed for flagging – which is best thought of as instructing $\mathcal{AIPS}$ to ignore data, rather than deleting data, via a FG table – and it is a crucial step in the data reduction process. It is good to remember that it is better to have a few clean visibilities than lots of contaminated visibilities. Images made from RFI-ridden data will contain strong patterns that only become visible during the final imaging, so it is vital to do a thorough job here.

We describe a simple and effective way of cleaning radio interferometric data. First, we average the frequency channels to produce a 'channel 0' continuum file (VLA nomenclature) using AVSPC. These continuum data is then displayed using TVFLG to plot the baselines as a function of time (see Fig. B.1). We identify bad antennas by the lack of relative signal, or strong RFI, that is seen as anomalously large and variable amplitudes. Since the outer channels of each sideband are relatively insensitive, we average only the central 75 per cent of the channels. VLA and GMRT data have 8 and 128 channels, respectively, for each sideband. In particular, for GMRT we use ICHANSEL = 11, 115, 1, 0 in AVSPC.

We use the TVFLG task to display and to interactively flag the data based on the set of commands using the cursor and the keyboard (A selects; B and C execute; D exits). Many actions can be executed using the table of commands displayed on the top-left of the screen. Some default parameters are usually changed each time we run this task: for example, both polarisations often fail simultaneously, so we can modify ENTER STOKES FLAG to '1111' (to flag both polarisations together), or LL/RR for left or right, respectively. It is also crucial that the ALL CHANNEL FLAG is turned on.

We start the flagging by displaying each source alone, starting with the brightest. Note that when we flag an antenna based on its characteristics whilst observing the brightest calibrator, that antenna (and bandpass tables – see below) will then be absent in future calibrations, therefore we have effectively flagged those channels and/or baselines for all the sources in the database. We flag all the very bright or faint baselines, since these are symptomatic of correlator problems. We commonly find bad values in the first and/or last integration on each source, so we use QUACK to delete them. We note all possible bad baselines and time ranges which contain strong RFI (see Fig. B.2). $\mathcal{AIPS}$ asks whether we like to save the flagging information in a new FG table eveytime we exit from the display interface. We (must) copy this FG table to the un-averaged *uv* dataset using TACOP (a lot of time has been lost when we forgot to copy the table).

Using SPFLG – another graphical interface – we check the time ranges and baselines noted earlier. SPFLG is similar to TVFLG but shows all spectral channels (not the averaged data) as a function of time for a single baseline. We use ENTER STOKES FLAG and SWITCH BASELINE FLAG to flag specific undesirable data. For example, to flag RFI, we display only the short baselines (e.g. ANTENNAS = 1, 2, 3, 4, 0; BASELINES = 5, 6, 7, 8, 0), flagging all antennas (BL = **–**) to avoid the tedious work of going through the baselines, one by one. If antenna 1

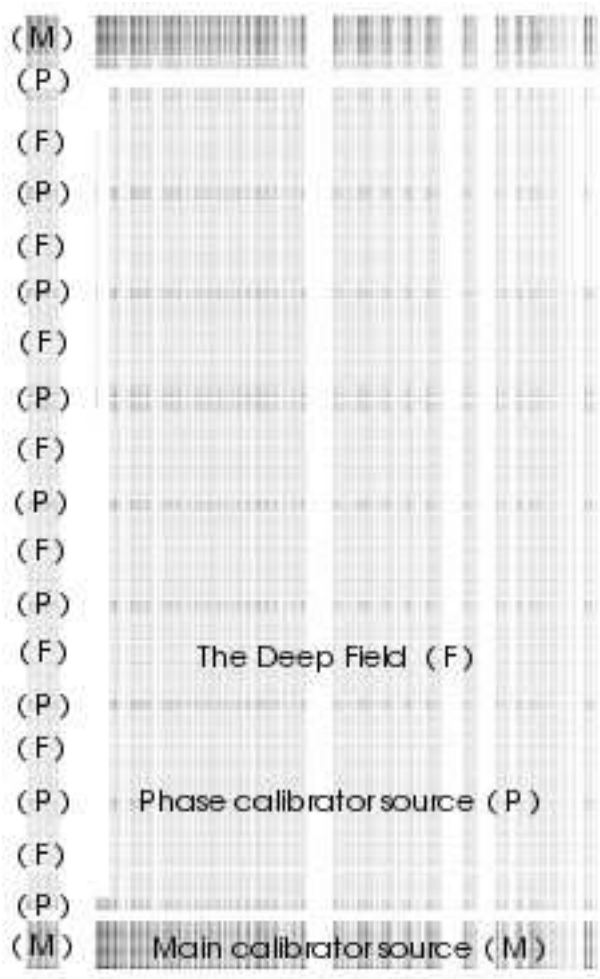

Figure B.1: TVFLG displaying baseline (x axis) versus time (y axis) for all observed sources, grouped by antenna such that baselines 1–2, 1–3, 1–4, etc., appear to the left. The darker times correspond to brighter sources. Bad baselines have been flagged.

contains strong RFI, we use BL = 01–**.

We display the phase calibrator and the target deep-field data together so that it is possible to flag bad channels that are visible in the faint field but saturated in the phase calibrator.

Again, it is better to have a small amount of good data than a large amount of bad data.

We take note of the baselines deleted in order to flag them for the main calibrator as well (to obtain a better bandpass calibration). We might also clip the data to eliminate extremely bright pixels. We keep track of the FG table using TACOP for every use of a flagging routine.

We re-run the averaging and flagging processes (many times) until a homogeneous dataset is obtained for the deep-field data, as viewed with both TVFLG and SPFLG.

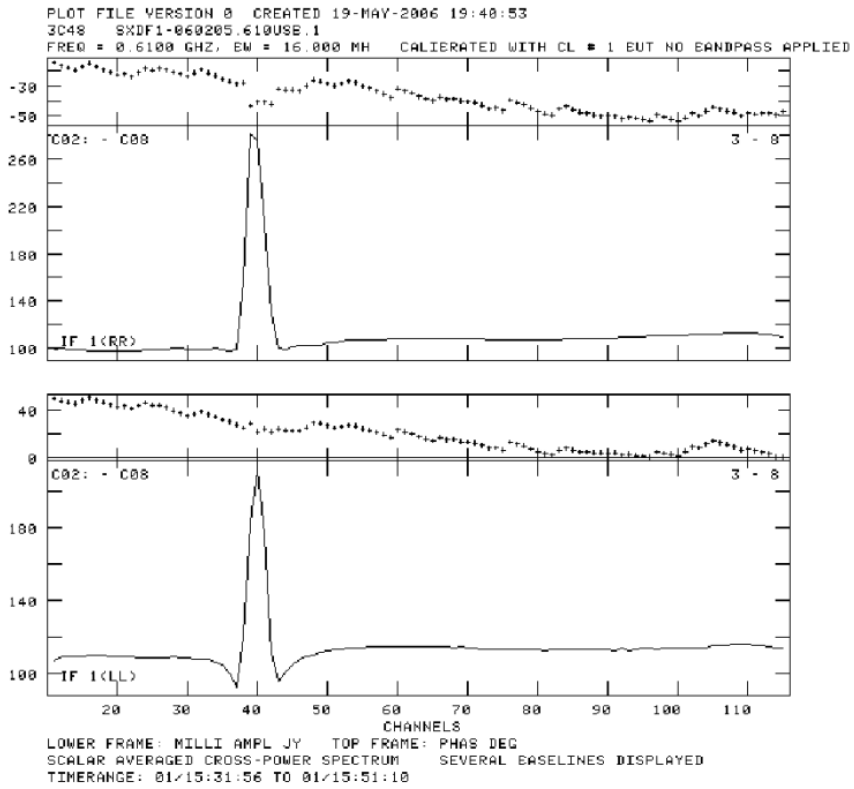

Figure B.2: Strong RFI seen on short GMRT baselines, plotted using POSSM.

B.4 Starting to calibrate the data

In the next step, we generate a bandpass (BP) table usually based on observations of the brightest calibrator (top and bottom sources in Fig. B.1). BPASS estimates the normalised (with respect to a channel reference) gain response of each antenna as a function of frequency channel, i.e. the set of corrections in amplitude and phase appropriate for each channel and baseline. We use POSSM to display the BP table using APARM(8) = 2 (e.g. as in Fig. B.4).

Since the data have not been calibrated yet, we should obtain the BP table using only 1–2 channels to avoid phase discontinuities (ICHANSEL = 63, 64, 1, 0). This 'division' operation (normalisation) is actually a subtraction of the average phase and a division by the average amplitude, and may thus result in rather a noisy bandpass. Nevertheless, we consider this as an approximate initial calibration, which at this stage is fine. We take care in BPASS with the SMOOTH parameter – if used once, it should be used in all subsequent tasks. We decide not using it. If we see strong RFI in the BP table, flag the bright calibrator again using SPFLG. We run BPASS until you obtain a smooth function for all antennas (e.g. see left in Fig. B.4).

Now that we have the flag (FG) and bandpass tables (BP), we proceed with the first calibration process. This simple calibration consists of applying the bandpass table (which can be thought of as focussing the telescope) then determining the antenna gains for the calibrators.

The resulting solutions are used to calibrate the target deep-field data later, interpolating the antenna responses as a function of time.

CALIB is the task we use to calculate the gain of each antenna as a function of time for the primary (main) and secondary (phase) calibrator (we do not include the target field as a calibrator), which are stored at first in an SN table.

We quote as mandatory to check the number of good solutions (>95 per cent expected) found by CALIB and to plot them using SNPLT. The SN table must show reasonable gains (close to unity, since they are normalised to an antenna reference) for all antennas at all times. We check for dead or faulty antennas which have telltale characteristics in these plots – e.g. very high normalisation factors. If this is the case, we go back and flag these time ranges, baselines or antennas.

We use GETJY to bootstrap flux information between calibrators (if the phase calibrator is sufficiently bright).

Now, using both the BP and SN tables, it is possible for us to interpolate the calibration to the deep-field data using CLCAL. This task creates a second CL table.

We check the quality of the 'cl' table using SNPLT (INEXT = 'CL', OPTYPE = 'PHAS' then 'AMP'). We expect to find a smooth distribution at around unity for the amplitude, and a similarly smooth distribution, perhaps wrapping once or twice, for phase. Another way to check the CL solutions is to display the spectrum of the main calibrator, using POSSM (SOURCES = '3C147' ", DOCALIB = 1, DOBAND = 1), where we expect to see a smooth spectrum normalised to the flux defined earlier by SETJY.

Due to the large amount of RFI present in low-frequency data, we use FLGIT – an automatic way of flagging data using noise and/or amplitude information. This task helps to flag RFI missed in the previous flagging processes. In general, we expect approximately 10–30 per cent of the visibilities to be flagged (we run it many times to fine-tune the parameters in APARM). The task estimates the noise using the channels defined in ICHANSEL. For GMRT data, we adopt 7 chunks of 15 channels, discarding the first 10 and last 13 channels, for each sideband. This generates a flagged and calibrated *uv* dataset with 105 frequency channels.

B.5 The careful calibration

We create new tables for the flagged and roughly calibrated *uv* dataset, aiming to more carefully calibrate the deep field data – a second iteration of the tasks we have already run, this time using all the available channels in the calibration tasks. We start by running INDXR, SETJY and BPASS. In this case, the bandpass solution has to be almost flat (check it using POSSM with APARM(8) = 2), as shown in Fig. B.4 (right).

We use two steps for calibrating the main calibrator, the first in phase only, the second in amplitude and phase together. The first stage is correcting for atmospheric shifts on timescales of seconds or minutes, so we use a short integration time (CALIB with BCHAN = 1; ECHAN =

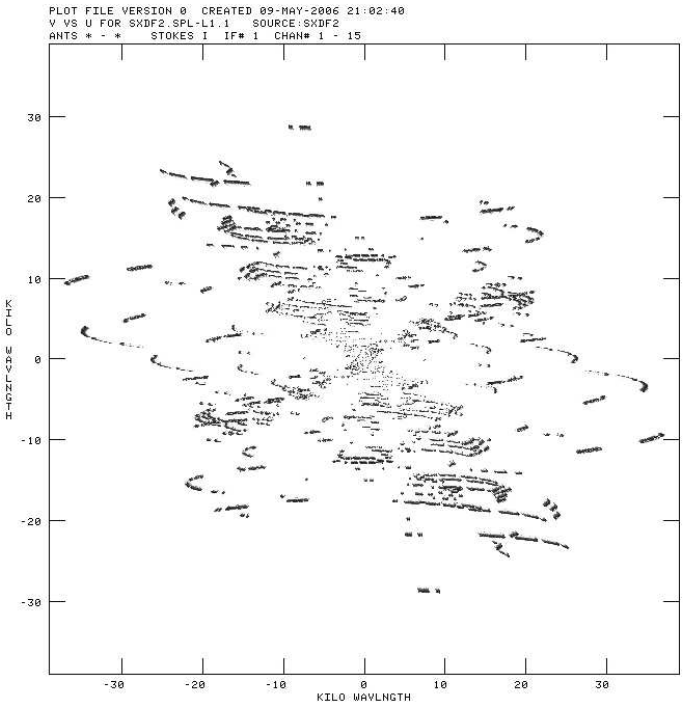

Figure B.3: The *uv* plane for GMRT data in the SXDF field, after rough calibration and extensive flagging.

115; SOLMODE = 'P'; SOLINT = 1). Then we apply this phase calibration using CLCAL prior to a subsequent calibration cycle with CALIB, this time with DOCALIB = 1, SOLINT = -1 (which averages over a scan) and SOLMODE = 'A&P'. With these new tables, we can bootstrap a flux density from the main calibrator to the phase calibrator using GETJY.

Finally, we use the CLCAL task (with the phase calibrator as CALSOUR) to calculate time-dependent gains for the entire time range using SNVER = 2, CALSOUR = 'phase calibrator name(s)', SOURCES = 'blank field name(s)'. We check the resulting CL table using SNPLT.

In the case of GMRT data, we then average the data in frequency using SPLAT. The number of channels per sideband is reduced to 15, with an effective bandwidth of 7×0.125 MHz. These are used later when imaging (IMAGR).

Some GMRT data – those taken in 2006 July and December – were affected by a correlator offset of unknown origin. For those, we employ a specially modified version of UVAVG (now standard) to determine and subtract the time-averaged values for each baseline and channel (after extensive flagging) throughout the session. For this to be effective, we required time-independent calibration in all steps. In this case, we did not bootstrapped the CL table from the main calibrator to the phase calibrator, but we applied it directly from the main calibrator, with no time dependence. An additional time-dependent calibration of phase was then necessary, for which we employed the previously created VLA 1.4-GHz image of each field as the model, solving only in phase, excluding amplitude information via SOLMODE = 'p!a'.

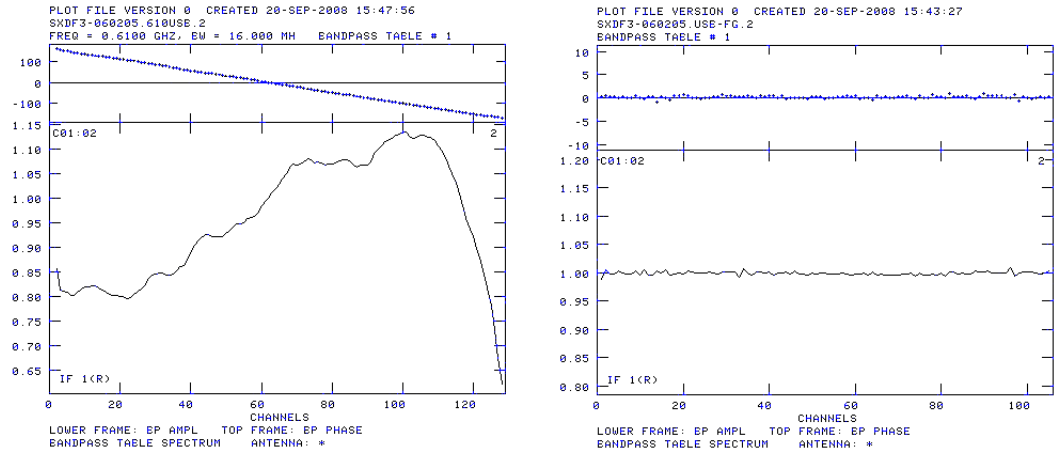

Figure B.4: Bandpass corrections, in amplitude and phase, for one GMRT baseline. *Left:* The bandpass solution based on the first rough calibration (128 channels). *Right:* The final bandpass solution (105 channels).

B.6 Imaging

First, we require knowledge of the primary beam size, and the expected synthesised beam size (spatial resolution), to make the best use of the data.

In order to minimise the 3-D smearing explained in §2.2.4, we use a polyhedron imaging technique to divide the primary beam into small slabs (facets). To create images covering the entire primary beam to the half-power point, for the GMRT and VLA data, we used 37 slabs, as shown in Fig. B.5.

Bright sources outside the primary beam can cause problems, contaminating the central images with un-deconvolved sidelobe patterns. To identify all these bright sources, we create a very large ($\sim$2 deg^2) dirty image (heavily tapered, i.e. weighting down the long spacings to allow the use of large pixels). We create new facets centred on the positions of any bright source found. We typically find $\sim$10 bright sources outside the primary beam area, i.e. we need to image around 47 slabs. The positions and sizes of these slabs are stipulated in the BOXFILE parameter of IMAGR (see EXPLAIN BOXFILE) with the following format:

```
F     1    512   512   0      0
F     2    512   512   487.5  0
⋮           ⋮             ⋮
F     37   512   512   487.5  -1462.5
C     38   256   256   02  02  02.02  -04  22  02.02
⋮
```

where the 'F rows' are the 37 central slabs and 'C rows' correspond to the positions of the

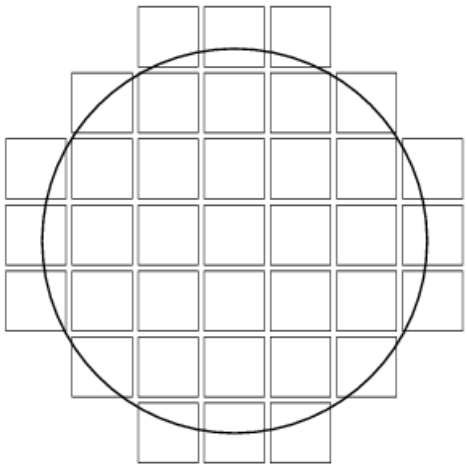

Figure B.5: Polyhedron imaging approach (Taylor et al. 1999) used to create the GMRT and VLA images covering the entire primary beam to the half-power point. Note, this is just an sketch of the imaging approach – there are no gaps between slabs in our treatment.

bright, outer sources.

Then we are ready to run IMAGR to produce the firstun-cleaned images. For GMRT, we used the following inputs:

>DO3D = 1 ('*each field is tangent to the celestial sphere*')

>NFIELD = 47 ('*the total number of slabs in BOXFILE*')

>NITER = 10000 ('*number of clean iterations*')

>CELL = 1.25 ('*pixel size, set to* $FWHM_{\rm GMRT}$ $\sim$*6 arcsec*')

>IMSI = 256 ('*minimum image dimension, mainly controlled by BOXFILE*')

>ROBUST = -0.5 ('*uv weighting function to arrive at a nice Gaussian beam, in conjunction with UVTAPER*')

>BOXFILE = 'HOME:BOXFILE' ('*HOME: is an environment variable pointing to the home directory*')

>NCHAV = 15 ('*number of channels*')

>UVRANGE = 0.8,100 ('*minimum and maximum baseline (in* $k\lambda$*) to exclude those <400-m baselines swamped by RFI*')

>UVTAPER = 28,28 ('*to arrive at a nice Gaussian beam, in conjunction with ROBUST*')

>UVBOX = 5 ('*average the weights slightly to avoid spurious data having an unduly large impact*')

IMAGR simultaneously produces the $\sim$47 dirty images, as defined by the boxfile, and it also calculates the shape of the dirty beam appropriate for each image (ICL and IBM classes, respectively).

Thus begins another iterative process. For the first IMAGR iteration, we allow the clean algorithm to run amok, finding a bright source, replacing 10 per cent of the flux with a delta function, all the way down to a few times the noise level, then convolving those delta functions

with a Gaussian approximation of the inner portion of the dirty beam to produce a so-called clean image.

Next, boxes are placed around each source in the cleaned image (these boxes are stored in the BOXFILE), and the clean algorithm is instructed to operate only within the boxes. We thus build an accurate model of the sky, human intervention allowing us to avoid building clean components from sidelobe structure.

```
>nfield=0; txinc=1; tyinc=1; pixrange=0,0.01
>for j=ICL001:ICL037+; getn j; tvlod; filename; end
```

where ICL037+ is the catalogue number of the last image. With this loop we display all fields, allowing us to select sources interactively using the cursor. We create small circles around the sources (C button, twice); the D button is used to continue with the next field; and A is used to move or to change the size of existing circles. We can now run IMAGR again.

We then use a model of the sky, built from the clean components created by IMAGR, to self-calibrate the data – i.e. to fine-tune the antenna-based phase and amplitude solutions as a function of time.

Self-calibration is accomplished using CALIB together with the clean components associated with the images we have made (CALSOUR = '', SOLMODE = 'P', NMAPS = 37+, and GET2N = the ICL001 image).

As noted earlier, we have developed a way of exploiting existing radio observations in a field, even if they were taken at a different frequency, so long as the primary beam sizes are roughly similar. This has been the case for the SXDF at 610 MHz, where VLA 1.4-GHz data were used as the model for self-calibration, to great effect.

We use SNPLT to check the SN table in phase (INEXT = 'SN', OPTY = 'PHAS', PIXRANGE = $-180, 180$). The solutions should resemble a smooth wriggling line – these are the atmospheric phase fluctuations being calibrated away.

We can subtract the clean components from the *uv* dataset to create source-free *uv* data, using UVSUB with FACTOR = 1. By looking to the distribution of amplitude as a function of baseline length, we can decide on a threshold to CLIP the data – at approximately 0.4 Jy for 610-MHz data in the SXDF – thereby eliminating RFI and bad data. The sources can be re-introduced using UVSUB with FACTOR = -1, and IMAGR can be used once more to create less noisy images.

Next, we self-calibrate the data in both phase and amplitude (SOLMODE = 'A&P'), normalising the amplitudes so that the average does not deviate from unity, to provide an additional constraint (CPARM(2) = 1). We run IMAGR again, using these penultimate images to self-calibrate the *uv* data one last time, this time without the constraint on average gain (CPARM = 0).

The final 37+ images are obtained by running IMAGR one the last time in the self-calibrated *uv*-data. Until here, the entire process was usually iterative, and took several months.

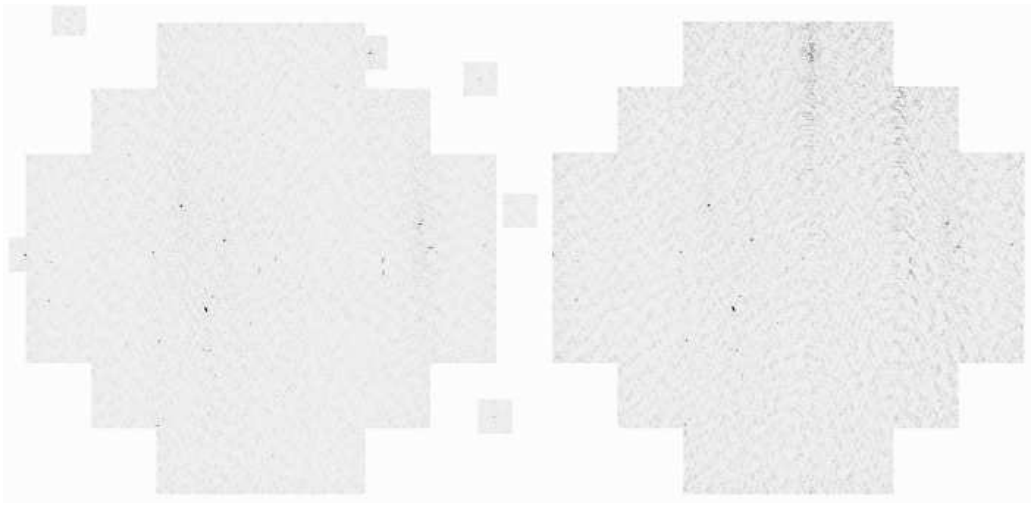

Figure B.6: The FLATNed images obtained from one pointing at 610 MHz in the SXDF. The outline clearly shows the polyhedron imaging approach. *Left* and *right* are the images obtained by including, or not including, bright outer sources in the IMAGR deconvolution, respectively. The inclusion of distant bright sources clearly improves the final imaging by eliminating sidelobe patterns, as those seen in the top-right of the right panel.

B.7 The final image

We use FLATN to knit together the central 37 slabs into a single map, correcting for the response of the primary beam which dies away as one moves away from the pointing centre. For GMRT we have used the PBCOR parameters from:

```
http://www.ncra.tifr.res.in/∼ngk/primarybeam/beam.html
```

throwing away data beyond the 30 per cent response point.

To sum all facets into one single field we combine them in a consistent way. The images are given in units of Jy beam^{-1}, then this means that we have to merge them using a common resolution-beam. In order to do this, we select the worst resolution (we run IMH for all images to find it) and convolve all the other images to this worst-case synthesised beam size using BMAJ, BMIN and BPA in the CONVL task. Since it has to be run 37 times, we prefer the creation of loops such as the one below:

```
>for j=ICL001:ICL037; getn j; outcl=incl; go convl; wait convl; end
```

We only consider the central 37 slabs that comprise the primary beam. During this process, we do not change the ICL number of the images.

We run IMEAN to determine the noise in each slab, and to write this noise in the header.

The noise is used in FLATN to weight any overlapping images. We now have created the final image.

From this final image, we can calculate a map of the clipped mean to remove large-scale RFI-induced ripples using RMSD (IMSIZE = 71, −1, OPCODE = 'MEAN', OPTYPE = 'HIST'). This can be subtracted using COMB to produce an image that is more pleasing to the eye.

B.8 Source extraction

To extract sources from the image, we prefer the use of a signal-to-noise criterion. For this we need a reliable estimate of the local noise in the different regions of the map, because the noise often has a complicated structure and is correlated on several different scales. It is possible to recognise three kinds of noise patterns. The first is due to the primary beam shape and depends on the distance from the pointing centre. The second is due to ripples produced by RFI that were not caught whilst editing the *uv* data. The third is isolated to the regions around bright sources, where the local r.m.s. increases due to sidelobes or deconvolution artifacts, hindering the detection of faint sources.

We recommend making a rough noise map, at first, using RMSD (IMSIZE = 71, −1, OPCODE = 'RMS', OPTYPE = 'HIST') followed by a rough source extraction of all bright ($> 5\,\sigma$) sources in the image. We used SAD for the source extraction, and went on to detect bright negative sources by inverting the map using COMB. This $5\,\sigma-$residual image (with no bright negative or positive sources) is then used to obtain the final noise map in RMSD – an estimate that does not become skewed by outliers in the histogram fits (OPTYPE = 'HIST').

This final noise noise map is then introduced as a secondary image in SAD to ensure reliable source extraction in signal-to-noise terms. For example, we use CPARM = 500, 100, 50, 10, 6, 4, 3, 2.5, DPARM(1) = 3, DPARM(2) as the r.m.s. in the image centre, ICUT = 0.1, and GAIN = 1, for a 3σ-peak extraction. The last CPARM parameter is lower than the first DPARM parameter because some sources may have peak flux densities (in Jy beam^{-1}) that exceed their measured integrated flux densities (in Jy) – a reflection of the increasing uncertainties in the source fits at low signal-to-noise ratios. We have found this provides reliable source extraction around bright sources and near the map edges (see Chapter 3 for more details).

Bibliography

Alexander D. M. et al., 2003, AJ, 126, 539

Alexander P., 1985, MNRAS, 213, 743

Alexander P., Leahy J. P., 1987, MNRAS, 225, 1

Antonucci R., 1993, ARA&A, 31, 473

Appleton P. N. et al., 2004, ApJS, 154, 147

Austermann et al. A., 2008, MNRAS, in preparation

Baade W., Minkowski R., 1954, ApJ, 119, 215

Barger A. J., Cowie L. L., Mushotzky R. F., Yang Y., Wang W.-H., Steffen A. T., Capak P., 2005, AJ, 129, 578

Barger A. J., Cowie L. L., Sanders D. B., Fulton E., Taniguchi Y., Sato Y., Kawara K., Okuda H., 1998, Nature, 394, 248

Barger A. J., Cowie L. L., Wang W.-H., 2007, ApJ, 654, 764

Barvainis R., 1987, ApJ, 320, 537

Beckert T., Duschl W. J., 2004, A&A, 426, 445

Beckmann V., Soldi S., Shrader C. R., Gehrels N., Produit N., 2006, ApJ, 652, 126

Beelen A., Cox P., Benford D. J., Dowell C. D., Kovács A., Bertoldi F., Omont A., Carilli C. L., 2006, ApJ, 642, 694

Beers T. C., Flynn K., Gebhardt K., 1990, AJ, 100, 32

Bell A. R., 1978, MNRAS, 182, 147

Bell E. F., 2003, ApJ, 586, 794

Bernet M. L., Miniati F., Lilly S. J., Kronberg P. P., Dessauges-Zavadsky M., 2008, Nature, 454, 302

Biggs A. D., Ivison R. J., 2006, MNRAS, 371, 963

Biggs A. D., Ivison R. J., 2008, MNRAS, 385, 893

Blain A. W., 1999, MNRAS, 309, 955

Blain A. W., Chapman S. C., Smail I., Ivison R., 2004, ApJ, 611, 52

Blain A. W., Ivison R. J., Smail I., 1998, MNRAS, 296, L29

Blain A. W., Jameson A., Smail I., Longair M. S., Kneib J.-P., Ivison R. J., 1999, MNRAS, 309, 715

Blain A. W., Longair M. S., 1993, MNRAS, 264, 509

Blain A. W., Smail I., Ivison R. J., Kneib J.-P., Frayer D. T., 2002, Phys. Rep., 369, 111

Blundell K. M., Kuncic Z., 2007, ApJ, 668, L103

Bohlin R. C., Savage B. D., Drake J. F., 1978, ApJ, 224, 132

Bondi M. et al., 2007, A&A, 463, 519

Bondi M. et al., 2003, A&A, 403, 857

Bower G. A., Heckman T. M., Wilson A. S., Richstone D. O., 1997, ApJ, 483, L33

Boyle B. J., Cornwell T. J., Middelberg E., Norris R. P., Appleton P. N., Smail I., 2007, MNRAS, 376, 1182

Boyle B. J., Shanks T., Croom S. M., Smith R. J., Miller L., Loaring N., Heymans C., 2000, MNRAS, 317, 1014

Brandl B. R. et al., 2006, ApJ, 653, 1129

Bridle A. H., Perley R. A., 1984, ARA&A, 22, 319

Brinkmann W., Laurent-Muehleisen S. A., Voges W., Siebert J., Becker R. H., Brotherton M. S., White R. L., Gregg M. D., 2000, A&A, 356, 445

Brodwin M., Lilly S. J., Porciani C., McCracken H. J., Le Fèvre O., Foucaud S., Crampton D., Mellier Y., 2006, ApJS, 162, 20

Brunner H., Cappelluti N., Hasinger G., Barcons X., Fabian A. C., Mainieri V., Szokoly G., 2008, A&A, 479, 283

Burch S. F., 1979, MNRAS, 186, 293

Burns J. O., Feigelson E. D., Schreier E. J., 1983, ApJ, 273, 128

Calzetti D., Armus L., Bohlin R. C., Kinney A. L., Koornneef J., Storchi-Bergmann T., 2000, ApJ, 533, 682

Carilli C. L., Perley R. A., Dreher J. W., Leahy J. P., 1991, ApJ, 383, 554

Carilli C. L., Yun M. S., 1999, ApJ, 513, L13

Carilli C. L., Yun M. S., 2000, ApJ, 530, 618

Carlstrom J. E., Kronberg P. P., 1991, ApJ, 366, 422

Casali M. et al., 2007, A&A, 467, 777

Chambers K. C., Miley G. K., van Breugel W. J. M., Bremer M. A. R., Huang J.-S., Trentham N. A., 1996, ApJS, 106, 247

Chandra P., Ray A., Bhatnagar S., 2004, ApJ, 612, 974

Chapman S. C., Ibata R., Lewis G. F., Ferguson A. M. N., Irwin M., McConnachie A., Tanvir N., 2005, ApJ, 632, L87

Chapman S. C., Smail I., Blain A. W., Ivison R. J., 2004a, ApJ, 614, 671

Chapman S. C., Smail I., Windhorst R., Muxlow T., Ivison R. J., 2004b, ApJ, 611, 732

Chapman S. C., Windhorst R., Odewahn S., Yan H., Conselice C., 2003, ApJ, 599, 92

Charlesworth M., Spencer R. E., 1982, MNRAS, 200, 933

Ciliegi P. et al., 1999, MNRAS, 302, 222

Ciliegi P. et al., 2005, A&A, 441, 879

Cirasuolo M. et al., 2007, MNRAS, 380, 585

Clemens M. S., Vega O., Bressan A., Granato G. L., Silva L., Panuzzo P., 2008, A&A, 477, 95

Comastri A., 2003, in American Institute of Physics Conference Series, Vol. 686, Centrella J. M., ed, The Astrophysics of Gravitational Wave Sources, p. 151

Condon J. J., 1984, ApJ, 287, 461

Condon J. J., 1992, ARA&A, 30, 575

Condon J. J., 2007, in Astronomical Society of the Pacific Conference Series, Vol. 380, Afonso J., Ferguson H. C., Mobasher B., Norris R., eds, Deepest Astronomical Surveys, p. 189

Condon J. J., Anderson M. L., Helou G., 1991, ApJ, 376, 95

Condon J. J., Cotton W. D., Yin Q. F., Shupe D. L., Storrie-Lombardi L. J., Helou G., Soifer B. T., Werner M. W., 2003, AJ, 125, 2411

Coppin K. et al., 2006, MNRAS, 372, 1621

Coppin K. et al., 2008, MNRAS, 384, 1597

Daddi E. et al., 2008, ArXiv e-prints

Daddi E. et al., 2005, ApJ, 631, L13

Dale D. A. et al., 2006, ApJ, 646, 161

Dole H. et al., 2006, A&A, 451, 417

Donley J. L., Rieke G. H., Rigby J. R., Perez-Gonzalez P. G., 2004, in Bulletin of the American Astronomical Society, Vol. 36, Bulletin of the American Astronomical Society, p. 1390

Donley J. L., Rieke G. H., Rigby J. R., Pérez-González P. G., 2005, ApJ, 634, 169

Downes A. J. B., Peacock J. A., Savage A., Carrie D. R., 1986, MNRAS, 218, 31

Downes D., Solomon P. M., 1998, ApJ, 507, 615

Drake C. L., McGregor P. J., Dopita M. A., van Breugel W. J. M., 2003, AJ, 126, 2237

Dunlop J. S., 2005, in Astrophysics and Space Science Library, Vol. 329, de Grijs R., González Delgado R. M., eds, Starbursts: From 30 Doradus to Lyman Break Galaxies, p. 121

Dunlop J. S., Peacock J. A., 1990, MNRAS, 247, 19

Dunne L., Clements D. L., Eales S. A., 2000, MNRAS, 319, 813

Dunne L., Eales S., Edmunds M., Ivison R., Alexander P., Clements D. L., 2000, MNRAS, 315, 115

Dunne L., Eales S. A., 2001, MNRAS, 327, 697

Dunne L. et al., 2008, ArXiv e-prints

Eales S., Bertoldi F., Ivison R., Carilli C., Dunne L., Owen F., 2003, MNRAS, 344, 169

Eales S., Lilly S., Gear W., Dunne L., Bond J. R., Hammer F., Le Fèvre O., Crampton D., 1999, ApJ, 515, 518

Eales S., Lilly S., Webb T., Dunne L., Gear W., Clements D., Yun M., 2000, AJ, 120, 2244

Elbaz D., 2005, Space Science Reviews, 119, 93

Elitzur M., Nenkova M., Ivezić Z., 2004, in Astronomical Society of the Pacific Conference Series, Vol. 320, Aalto S., Huttemeister S., Pedlar A., eds, The Neutral ISM in Starburst Galaxies, p. 242

Elvis M. et al., 1994, ApJS, 95, 1

Fanaroff B. L., Riley J. M., 1974, MNRAS, 167, 31P

Feigelson E. D., Nelson P. I., 1985, ApJ, 293, 192

Fermi E., 1949, Physical Review, 75, 1169

Furusawa H. et al., 2008, ApJS, 176, 1

Garn T., Green D. A., Hales S. E. G., Riley J. M., Alexander P., 2007, MNRAS, 376, 1251

Garn T., Green D. A., Riley J. M., Alexander P., 2008a, MNRAS, 383, 75

Garn T., Green D. A., Riley J. M., Alexander P., 2008b, MNRAS, 387, 1037

Garrett M. A., 2002, A&A, 384, L19

Garrett M. A., 2005, in EAS Publications Series, Vol. 15, Gurvits L. I., Frey S., Rawlings S., eds, EAS Publications Series, p. 73

Garrett M. A., Wrobel J. M., Morganti R., 2005, ApJ, 619, 105

Gebhardt K. et al., 2000, ApJ, 539, L13

Gehrels N., 1986, ApJ, 303, 336

Genzel R., Lutz D., Moorwood A. F. M., Rigopoulou D., Spoon H. W. W., Sternberg A., Sturm E., Tran D., 2000, in Lecture Notes in Physics, Berlin Springer Verlag, Vol. 548, Lemke D., Stickel M., Wilke K., eds, ISO Survey of a Dusty Universe, p. 199

Genzel R. et al., 1998, ApJ, 498, 579

Giacconi R. et al., 2002, ApJS, 139, 369

Ginzburg V. L., Syrovatskii S. I., 1965, ARA&A, 3, 297

Gopal-Krishna , Patnaik A. R., Steppe H., 1983, A&A, 123, 107

Granato G. L., Danese L., 1994, MNRAS, 268, 235

Greve T. R., Ivison R. J., Bertoldi F., Stevens J. A., Dunlop J. S., Lutz D., Carilli C. L., 2004, MNRAS, 354, 779

Gruppioni C., Mignoli M., Zamorani G., 1999, MNRAS, 304, 199

Haarsma D. B., Partridge R. B., Windhorst R. A., Richards E. A., 2000, ApJ, 544, 641

Harwit M., Pacini F., 1975, ApJ, 200, L127

Hasinger G., 2004, Nuclear Physics B Proceedings Supplements, 132, 86

Hasinger G. et al., 2001, A&A, 365, L45

Helou G., Soifer B. T., Rowan-Robinson M., 1985, ApJ, 298, L7

Hogg D. W., Baldry I. K., Blanton M. R., Eisenstein D. J., 2002, ArXiv Astrophysics e-prints

Holland W. et al., 2006, in Presented at the Society of Photo-Optical Instrumentation Engineers (SPIE) Conference, Vol. 6275, Society of Photo-Optical Instrumentation Engineers (SPIE) Conference Series

Holland W. S. et al., 1999, MNRAS, 303, 659

Hopkins A., Windhorst R., Cram L., Ekers R., 2000, Experimental Astronomy, 10, 419

Hopkins A. M., Afonso J., Chan B., Cram L. E., Georgakakis A., Mobasher B., 2003, AJ, 125, 465

Hughes D. H. et al., 1998, ArXiv Astrophysics e-prints

Hunt L. K., Maiolino R., 2005, ApJ, 626, L15

Ibar E. et al., 2008, MNRAS, 386, 953

Ibar E., Lira P., 2007, A&A, 466, 531

Ibar et al. E., 2009, MNRAS, in preparation

Ivison R. J. et al., 2007a, ApJ, 660, L77

Ivison R. J. et al., 2007b, MNRAS, 380, 199

Ivison R. J. et al., 2004, ApJS, 154, 124

Ivison R. J. et al., 2002, MNRAS, 337, 1

Ivison R. J., Smail I., Barger A. J., Kneib J.-P., Blain A. W., Owen F. N., Kerr T. H., Cowie L. L., 2000, MNRAS, 315, 209

Ivison R. J., Smail I., Le Borgne J.-F., Blain A. W., Kneib J.-P., Bezecourt J., Kerr T. H., Davies J. K., 1998, MNRAS, 298, 583

Jackson J. D., 1999, Classical electrodynamics. New York: Wiley, 1999, 3rd ed.

Jaffe W. et al., 2004, Nature, 429, 47

Jaffe W. J., Perola G. C., 1973, A&A, 26, 423

Jansky K., 1933, Nature, 132, 66

Jarvis M. J., Rawlings S., 2004, New Astronomy Review, 48, 1173

Jarvis M. J. et al., 2001, MNRAS, 326, 1563

Kantharia X., Rao X., 2001, GMRT Technical Note R00185

Kardashev N. S., 1962, Soviet Astronomy, 6, 317

Kasliwal M. M., Charmandaris V., Weedman D., Houck J. R., Le Floc'h E., Higdon S. J. U., Armus L., Teplitz H. I., 2005, ApJ, 634, L1

Katgert J. K., 1979, A&A, 73, 107

Katgert J. K., Spinrad H., 1974, A&A, 35, 393

Katgert-Merkelijn J. K., Windhorst R. A., Katgert P., Robertson J. G., 1985, A&AS, 61, 517

Kellermann K. I., Pauliny-Toth I. I. K., 1981, ARA&A, 19, 373

Kim D.-C., Sanders D. B., 1998, ApJS, 119, 41

Klein U., Wielebinski R., Thuan T. X., 1984, A&A, 141, 241

Kleinmann D. E., Low F. J., 1970, ApJ, 159, L165

Kovács A., Chapman S. C., Dowell C. D., Blain A. W., Ivison R. J., Smail I., Phillips T. G., 2006, ApJ, 650, 592

Kreysa E. et al., 2003, in Society of Photo-Optical Instrumentation Engineers (SPIE) Conference Series, Vol. 4855, Phillips T. G., Zmuidzinas J., eds, Society of Photo-Optical Instrumentation Engineers (SPIE) Conference Series, p. 41

Kreysa E. et al., 1999, Infrared Physics and Technology, 40, 191

La Franca F. et al., 2005, ApJ, 635, 864

Lagache G. et al., 2004, ApJS, 154, 112

Lagache G., Puget J.-L., Dole H., 2005, ARA&A, 43, 727

Laing R. A., Riley J. M., Longair M. S., 1983, MNRAS, 204, 151

Lawrence A. et al., 2007, MNRAS, 379, 1599

Le Floc'h E. et al., 2005, ApJ, 632, 169

Lilly S. J., Eales S. A., Gear W. K. P., Hammer F., Le Fèvre O., Crampton D., Bond J. R., Dunne L., 1999, ApJ, 518, 641

Liu R., Pooley G., Riley J. M., 1992, MNRAS, 257, 545

Lockman F. J., Jahoda K., McCammon D., 1986, ApJ, 302, 432

Longair M. S., 1994, High energy astrophysics. Vol.2: Stars, the galaxy and the interstellar medium. Cambridge: Cambridge University Press, —c1994, 2nd ed.

Lonsdale C. J. et al., 2003, PASP, 115, 897

Magliocchetti M., Andreani P., Zwaan M. A., 2008, MNRAS, 383, 479

Mainieri V., Bergeron J., Hasinger G., Lehmann I., Rosati P., Schmidt M., Szokoly G., Della Ceca R., 2002, A&A, 393, 425

Maiolino R., Salvati M., Bassani L., Dadina M., della Ceca R., Matt G., Risaliti G., Zamorani G., 1998, A&A, 338, 781

Matt G., 2002, Royal Society of London Philosophical Transactions Series A, 360, 2045

Matt G. et al., 1999, A&A, 341, L39

Matthews T. A., Morgan W. W., Schmidt M., 1964, ApJ, 140, 35

Menéndez-Delmestre K. et al., 2007, ApJ, 655, L65

Mitchell K. J., Condon J. J., 1985, AJ, 90, 1957

Miyazaki S. et al., 2002, PASJ, 54, 833

Morrison R., McCammon D., 1983, ApJ, 270, 119

Morrison et al. , in preparation

Mortier A. M. J. et al., 2005, MNRAS, 363, 563

Moss D., Seymour N., McHardy I. M., Dwelly T., Page M. J., Loaring N. S., 2007, MNRAS, 378, 995

Mushotzky R., 2004, in Astrophysics and Space Science Library, Vol. 308, Barger A. J., ed, Supermassive Black Holes in the Distant Universe, p. 53

Muxlow T. W. B. et al., 2005, MNRAS, 358, 1159

Nenkova M., Ivezić Ž., Elitzur M., 2002, ApJ, 570, L9

O'Dea C. P., 1998, PASP, 110, 493

Orienti M., Garrett M. A., Reynolds C., Morganti R., 2004, in Bachiller R., Colomer F., Desmurs J.-F., de Vicente P., eds, European VLBI Network on New Developments in VLBI Science and Technology, p. 129

Owen F. N. et al., 2008, ApJ, in preparation

Pacholczyk A. G., 1970, Radio astrophysics. Nonthermal processes in galactic and extragalactic sources. Series of Books in Astronomy and Astrophysics, San Francisco: Freeman, 1970

Padovani P., Mainieri V., Tozzi P., Kellermann K. I., Fomalont E. B., Miller N., Rosati P., Shaver P., 2007, in Astronomical Society of the Pacific Conference Series, Vol. 380, Afonso J., Ferguson H. C., Mobasher B., Norris R., eds, Deepest Astronomical Surveys, p. 205

Pier E. A., Krolik J. H., 1992, ApJ, 401, 99

Pier E. A., Krolik J. H., 1993, ApJ, 418, 673

Poglitsch A. et al., 2006, in COSPAR, Plenary Meeting, Vol. 36, 36th COSPAR Scientific Assembly, p. 215

Pope A. et al., 2006, MNRAS, 370, 1185

Prandoni I., Gregorini L., Parma P., de Ruiter H. R., Vettolani G., Wieringa M. H., Ekers R. D., 2001, A&A, 365, 392

Prieto M. A., Maciejewski W., Reunanen J., 2005, AJ, 130, 1472

Prieto M. A. et al., 2004, ApJ, 614, 135

Ramadurai S., Biswas S., 1972, Ap&SS, 17, 467

Ranalli P., Comastri A., Setti G., 2003, A&A, 399, 39

Richards E. A., 2000, ApJ, 533, 611

Risaliti G., Elvis M., Fabbiano G., Baldi A., Zezas A., 2005, ApJ, 623, L93

Robson , 1996, Journal of the British Astronomical Association, 106, 164

Rottgering H., Snellen I., Miley G., de Jong J. P., Hanisch R. J., Perley R., 1994, ApJ, 436, 654

Roy A. L., Norris R. P., Kesteven M. J., Troup E. R., Reynolds J. E., 1998, MNRAS, 301, 1019

Rybicki G. B., Lightman A. P., 1979, Radiative processes in astrophysics. New York, Wiley-Interscience, 1979. 393 p.

Sakamoto K., Scoville N. Z., Yun M. S., Crosas M., Genzel R., Tacconi L. J., 1999, ApJ, 514, 68

Sanders D. B., Mirabel I. F., 1996, ARA&A, 34, 749

Sanders D. B., Soifer B. T., Elias J. H., Neugebauer G., Matthews K., 1988, ApJ, 328, L35

Schinnerer E. et al., 2008, ArXiv e-prints

Schmidt M., 1963, Nature, 197, 1040

Schultz G. V., Wiemer W., 1975, A&A, 43, 133

Scott S. E. et al., 2002, MNRAS, 331, 817

Sekiguki et al. K., 2005, Multiwavelength mapping of galaxy formation and evolution. Springer-Verlag, 82P

Seyfert C. K., 1943, ApJ, 97, 28

Seymour N. et al., 2008, MNRAS, 386, 1695

Seymour N., McHardy I. M., Gunn K. F., 2004, MNRAS, 352, 131

Shupe D. L. et al., 2008, AJ, 135, 1050

Silva L., Granato G. L., Bressan A., Danese L., 1998, ApJ, 509, 103

Simpson C. et al., 2006, MNRAS, 372, 741

Smail I., Ivison R. J., Blain A. W., 1997, ApJ, 490, L5

Smail I., Ivison R. J., Blain A. W., Kneib J.-P., 2002, MNRAS, 331, 495

Smail I., Ivison R. J., Owen F. N., Blain A. W., Kneib J.-P., 2000, ApJ, 528, 612

Smith H. E., Lonsdale C. J., Lonsdale C. J., Diamond P. J., 1998, ApJ, 493, L17

Smolčić V. et al., 2008, ApJS, 177, 14

Snellen I. A. G., Schilizzi R. T., Miley G. K., de Bruyn A. G., Bremer M. N., Röttgering H. J. A., 2000, MNRAS, 319, 445

Soifer B. T., Sanders D. B., Madore B. F., Neugebauer G., Danielson G. E., Elias J. H., Lonsdale C. J., Rice W. L., 1987, ApJ, 320, 238

Spergel D. N. et al., 2007, ApJS, 170, 377

Stephens P. W., 1987, Ph.D. thesis, AA(Manchester Univ. (England).)

Streblyanska A., Hasinger G., Finoguenov A., Barcons X., Mateos S., Fabian A. C., 2005, A&A, 432, 395

Suganuma M. et al., 2006, ApJ, 639, 46

Surace J. A. et al., 2004, VizieR Online Data Catalog, 2255, 0

Svensson R., 1996, A&AS, 120, C475

Swain M. et al., 2003, ApJ, 596, L163

Szokoly G. P. et al., 2004, ApJS, 155, 271

Tasse C., Röttgering H. J. A., Best P. N., Cohen A. S., Pierre M., Wilman R., 2007, A&A, 471, 1105

Taylor G. B., Carilli C. L., Perley R. A., eds, 1999, Astronomical Society of the Pacific Conference Series, Vol. 180, Synthesis Imaging in Radio Astronomy II

Thompson T. A., Quataert E., Waxman E., Murray N., Martin C. L., 2006, ApJ, 645, 186

Tozzi P. et al., 2006, A&A, 451, 457

Treister E., Urry C. M., 2005, ApJ, 630, 115

Treister E. et al., 2004, ApJ, 616, 123

Trinchieri G., Fabbiano G., Canizares C. R., 1986, ApJ, 310, 637

Turner T. J., George I. M., Nandra K., Mushotzky R. F., 1997, ApJS, 113, 23

Ueda Y., Akiyama M., Ohta K., Miyaji T., 2003, ApJ, 598, 886

Ueda Y. et al., 2008, ApJS, 179, 124

Valentijn A. E., 1980, A&A, 89, 234

Valentijn E. A., Jaffe W. J., Perola G. C., 1977, A&AS, 28, 333

van der Horst A. J., Rol E., Wijers R. A. M. J., Strom R., Kaper L., Kouveliotou C., 2005, ApJ, 634, 1166

van der Kruit P. C., 1971, A&A, 15, 110

van der Kruit P. C., 1973, A&A, 29, 263

Vardoulaki E., Rawlings S., Simpson C., Bonfield D. G., Ivison R. J., Ibar E., 2008, MNRAS, 387, 505

Voellmer G. M. et al., 2003, in Society of Photo-Optical Instrumentation Engineers (SPIE) Conference Series, Vol. 4855, Phillips T. G., Zmuidzinas J., eds, Society of Photo-Optical Instrumentation Engineers (SPIE) Conference Series, p. 63

Wals M., Boyle B. J., Croom S. M., Miller L., Smith R., Shanks T., Outram P., 2005, MNRAS, 360, 453

Wang W.-H., Cowie L. L., van Saders J., Barger A. J., Williams J. P., 2007, ApJ, 670, L89

Warren S. J. et al., 2007, MNRAS, 375, 213

Werner M. W. et al., 2004, ApJS, 154, 1

Wiklind T., 2003, ApJ, 588, 736

Willott C. J., Rawlings S., Blundell K. M., Lacy M., Hill G. J., Scott S. E., 2002, MNRAS, 335, 1120

Wilman R. J., Fabian A. C., 1999, MNRAS, 309, 862

Wilson T. L., 2008, Ap&SS, 313, 13

Windhorst R., Mathis D., Neuschaefer L., 1990, in Astronomical Society of the Pacific Conference Series, Vol. 10, Kron R. G., ed, Evolution of the Universe of Galaxies, p. 389

Windhorst R. A., Miley G. K., Owen F. N., Kron R. G., Koo D. C., 1985, ApJ, 289, 494

Winter A. J. B. et al., 1980, MNRAS, 192, 931

Wrobel J. M., Taylor G. B., Rector T. A., Myers S. T., Fassnacht C. D., 2005, AJ, 130, 923

Xu C., Lisenfeld U., Volk H. J., Wunderlich E., 1994, A&A, 282, 19

Yamada T. et al., 2005, ApJ, 634, 861

Younger J. D. et al., 2007, ApJ, 671, 1531

Yun M. S., Reddy N. A., Condon J. J., 2001, ApJ, 554, 803

Zheng W. et al., 2004, ApJS, 155, 73